Ultrasensitive Microwave Near-Field Sensors For Detection, Imaging, and Material Characterization

by

Ali Mohammed Albishi

A thesis
presented to the University of Waterloo
in fulfillment of the
thesis requirement for the degree of
Doctor of Philosophy
in
Electrical and Computer Engineering

Waterloo, Ontario, Canada, 2018

Examining Committee Membership

The following served on the Examining Committee for this thesis. The decision of the Examining Committee is by majority vote.

External Examiner:	Samir Trabelsi Lead Scientist, US Department of Agriculture
Supervisor(s):	Omar M. Ramahi Professor, University of Waterloo
Internal Member:	Raafat Mansour Professor, University of Waterloo
Internal Member:	Chris Backhouse Professor, University of Waterloo
Internal-External Member:	Eihab Abdel-Rahman Professor, University of Waterloo

I hereby declare that I am the sole author of this thesis. This is a true copy of the thesis, including any required final revisions, as accepted by my examiners.

I understand that my thesis may be made electronically available to the public.

Abstract

Affordable, sensitive, selective, fast-responding, label-free sensors are currently in high demand for many of today's applications and technologies, particularly in the food industry, bio-sensing applications, and quality control. In addition, modern technologies such as a lab-on-a-chip involve microfluidic analysis, which requires highly accurate and miniaturized sensing systems. These systems can be implemented in biomedical applications such as point-of-care diagnostics, as well as in environmental monitoring, agriculture, biotechnology, and public health and safety. A need, therefore, exists for highly accurate and reliable sensing systems that can meet the requirements of these applications. This dissertation presents electrically-small planar microwave resonators for the design of near-field sensors that can satisfy the needs of the aforementioned applications. This thesis proposes a number of novel concepts related to miniaturization and the enhancement of the sensitivity of electrically-small sensors.

In the first part of the thesis, an analysis of the sensitivity of complementary split-ring resonators (CSRRs) with respect to changes in resonator topology is presented. Eigenmode solvers, circuit models, numerical simulations, and laboratory measurements were all employed for the analysis. The results show that the resonance frequency is adjustable and scalable. The second part of the thesis proposed an ultrasensitive near-field sensor for detecting submillimeter cracks in metallic materials. Experimental measurements revealed that a surface crack of 200 μm wide and 2 mm deep results in a 1.5 GHz shift in the resonance frequency. The results led to the idea of utilizing CSRRs for designing near-field sensors for crack detection in dielectric materials. The work was further extended to increase the sensitivity of planar CSRRs to detect the presence of dielectric materials. This concept is based on increasing the sensing areas per unit length and on the utilization of multiple, identical, and coupled resonators.

Although the electromagnetic energy stored in electrically-small planar resonators is concentrated primarily in an electrically-small volume, most of that energy is located in the host substrate, thus limiting the sensitivity required for detecting changes in the material under test (MUT), which differs from the host substrate. For this reason, a sensor designed for enhancing the EM energy stored in the sensing volume that is exposed to the

MUT is proposed. The design concept is based on the use of a three-dimensional capacitor. For validation purposes, a complementary electric-LC resonator (CELCR) and two metallic bars were utilized for designing the sensor for dielectric materials. Furthermore, by adopting the concept of three-dimensional capacitors, microwave sensors based on planar SRRs are introduced in order to 1) enhance the sensitivity, 2) allow for flexible tunability, and 3) create novel sensors for fluidic applications. For validation purposes, an SRR-based sensor was designed and tested using numerical simulation and experiments to detect fluid materials and fluid levels. The SRR with the three-dimensional capacitors was also utilized to design probes for the near-field scanning microscopy. An additional component of this research was, therefore, an exploration of the miniaturization of CELCR sensing areas so that these devices could be loaded with three-dimensional capacitors in order to design a sensitive near-field sensor for microscale-based technologies. The ability of the sensor to detect the presence of magnetic materials was also investigated numerically. For applications in which flatness or compactness is a relevant factor, enhancing sensitivity with the use of three-dimensional capacitors is not an ideal solution.

Although classical planar antennas such as patch antennas are subject to a lack of EM energy localization in small areas, the adoption of the split concept, utilized in electrically-small resonators, can improve these antennas for use in designing near-field microwave sensors. This thesis proposed a planar microwave sensor based on an annular ring resonator loaded with a split, thus enabling it to operate at lower frequencies and to enhance the quality factors. The sensor was tested experimentally with respect to characterizing dielectric slabs and detecting the presence of fluidic materials.

The last part of the thesis introduced the concept of an intelligent sensing technique based on the modulation of the frequency responses of near-field microwave sensors for the characterization of material parameters. The concept is based on the assumption that the physical parameters being extracted are uniform over the frequency range of the sensing system. The concept is derived from the observation of the sensor responses as multidimensional vectors over a wide frequency range. The dimensions are then considered as features for a neural network. The concept has been demonstrated experimentally for the detection of the concentration of a fluid material composed of two pure fluids.

Acknowledgments

All praises are due to Allah for giving me the ability to write this dissertation. All praises are due to Allah for giving me the honor of helping the humanity by contributing to enrich its knowledge.

I would like to express my deepest gratitude to my supervisor Professor Omar M. Ramahi. I cannot thank him enough for his thoughtful guidance, generous supports, and friendly discussions that helped me to improve not only my academic knowledge but also my understanding of the real message of life. I believe that having a discussion with him is a peerless privilege. I am also grateful to my committee members, Professor Raafat R. Mansour and Professor Chris Backhouse, Professor Eihab Abdel-Rahman, and Dr. Samir Trabelsi for serving in my examination committee and for their valuable comments and feedback.

Special thanks to Babak Alavikia for his support and assistance during my graduate studies.

I would like to acknowledge my colleagues during my Ph.D. studies at the University of Waterloo. Specifically, I would like to thank Ahmed Ashoor, Abdulaziz Alqahtani, Mohammed AlShareef, Mohamed El Badawe, Miguel Ruphuy, Dawood Alsaedi, Seyed Mirjahanmardi, Mohammed Aldosari, Vahid Nayyeri, Humayra Naosaba, and Melad Olaimat. Their friendly discussion always inspires new ideas. My apologies to those whom I forgot to mention here. Their friendship will always be remembered.

Special thanks to my best friends Saud Wasly and Omar Alarfaj for the discussion we had every Wednesdays "Idea's Coffeeshop" about physics and life in general.

I would like to thank my family for their support, patience, and for believing in me, my father (Mohammed) and my mother (Salihah), my brothers (Ayed, Abdullah, and Bandar) and my sisters (Shara, Kazma, Rana, Haya, Hoda, Maram).

Atha, my dear wife, is always my source of inspiration. I owe Atha my deepest gratitude for her infinite patience that accompanies me along this long journey to fulfill my goals. Atha and my twins (Mohammed and Abdulaziz) are my source of strength. Their love is my motivation, and their happiness is my ultimate goal.

This research work was financially supported by King Saud University, Saudi Arabia.

Dedication

To my parents for their unconditional love and support,
To my beloved wife Atha and twins Mohammed and Abdulaziz who give color to my life,
And to all people that are trying to make the world a better place

Table of Contents

List of Tables

List of Figures

Chapter 1

Introduction

1.1 Research Motivation

The requirements of many of today's applications and technologies have created an enormous demand for affordable, sensitive, selective, fast-responding, and label-free sensors [4]. These technologies include food industry and bio-sensing applications, microfluidic technologies for biomedical applications such as point-of-care diagnostics, and surface inspection for crack detection in metallic materials, to name but a few [1, 2, 4–9]. A need thus exists for sensing systems that can meet the needs of such applications.

For example, according to a recent report [10], in Europe alone, 70 % of steel bridges have been in service for more than 50 years, and about 30 % have been in service for more than 100 years. Metallic structures, such as steel bridges, aircraft fuselage, and nuclear power plant steam generator turbines, can be compromised by cracking. The detection and inspection of cracks, especially when covered by paint (or any dielectric coating in general), is critical for the quality assessment and maintenance of these structures. Several nondestructive testing and evaluation (NDE) techniques have been investigated and utilized for the detection of cracks in metallic materials. These techniques include Eddy current, acoustic emission, ultrasonic, dye penetrant, magnetic particle, radiographic, and microwave testing [11, 12]. The effectiveness of these methods is marred by limitations

that include low levels of sensitivity to changes in the materials under test (MUTs), the requirement that they be applied directly on the surfaces of metallic and magnetic materials, the necessity of removing surface coatings (e.g., paints) from the materials prior to testing, and the short stand-off distance needed [13].

In addition, modern technologies such as a lab-on-a-chip are attractive in many applications such as point-of-care diagnostics, which enable data to be measured and collected and an immediate diagnosis to be provided during a regular clinic visit, in an ambulance, or even at home. These types of technologies involve fluidic and microfluidic analysis, which requires highly accurate sensing systems. To be suitable for in-the-field applications, such as environmental monitoring, agriculture, biotechnology, and public health and safety, these systems must be miniaturized, inexpensive, extremely sensitive and selective, and able to provide very fast responses [14]. From an engineering perspective, since microfluidic technologies operate at the microscale [15], the need for smaller (miniaturized) devices is an essential objective.

Generally speaking, a sensor is a device designed to interact with materials in order to detect changes or to characterize pure materials. The sensing mechanism in these devices is dependent on the interactions between the sensor and the MUT. For example, the electromagnetic (EM) interactions between the MUTs and sensors designed for any regime are fundamentally dependent on three constitutive parameters: permittivity (ϵ), permeability (μ), and conductivity (σ), which can be correlated with physical quantities, such as temperature, water content, water in soil, and cracks in materials, or even with a biochemical molecule such as a particular DNA sequence or a specific protein. Sensor-based techniques are thus essential for many real-field applications, and microwave frequencies can be utilized for the design of the necessary sensors.

1.2 Microwave Frequency Based Sensors

In the EM spectrum, the microwave regime refers to frequencies ranging from 3 GHz to 300 GHz, or 10 cm and 1 mm, respectively, in terms of wavelength [16]. There are many applications of microwave-based technologies including wireless networking and communi-

cations systems, wireless security systems, radar systems, environmental remote sensing, and medical systems [16]. At the low range of microwave frequencies, microwaves can penetrate dielectric materials, with the penetration depth being related to skin depth as follows:

$$\delta_s = \frac{1}{\alpha} \qquad \text{(m)} \tag{1.1}$$

where α is the attenuation constant of the medium. The attenuation constant (α) is a function of the excitation frequency and of the complex permittivity of the medium ($\epsilon = \epsilon^{'} + \epsilon^{''}$), expressed as follows [17]:

$$\alpha = w\{\frac{\mu\epsilon^{'}}{2}[\sqrt{1 + (\frac{\epsilon^{''}}{\epsilon^{'}})^2} - 1]\}^{\frac{1}{2}} \tag{1.2}$$

From equation (1.2), it is clear that the higher the frequencies and dielectric constant, the greater the attenuation. Thus, based on equation (1.1), the skin depth is decreased. Therefore, for applications involving a substantial penetration depth, lower microwave frequencies are desirable. Microwave sensors can hence provide solutions for the challenges and requirements associated with modern technologies such as nondestructive (contactless) testing and evaluation (NDE) because of the deep penetration of the MUTs provided by EM fields. More detail and a general review of the state of the art of NDE techniques that are based on microwave frequencies can be found in [18]. Microwave sensors also have a simpler measurement setup and are easier to design and less costly to fabricate than high-frequency sensors, which are characterized by design and measurement complexity.

Among microwave-frequency-based techniques, near-field microwave sensors can be considered strong candidates because of their following key advantages. The MUTs are in close proximity to the sensors, where the perturbation of the EM fields is maximized, thus enhancing sensitivity. Near-field techniques can also provide high-resolution sensors that break the diffraction limit; a resolution in the order of $\lambda/10^6$ has in fact, already been verified experimentally [19]. Generally speaking, near-field microwave sensors can be categorized as either resonant or non-resonant.

Resonant microwave structures, or resonators, have been utilized in many applications including filters, oscillators, frequency meters, tuned amplifiers, and sensors [16]. Based on observed changes in the resonance frequencies, the sensing mechanism of the resonators

in the sensing systems offers a number of benefits compared to sensors based on measured changes in the magnitude of the reflection coefficient (non-resonant sensors). Resonant sensors help reduce inaccuracies associated with the signal-to-noise ratio since measurements are not performed at a single or very narrow range of frequencies [20]. In addition, detecting changes in the magnitude and phase of the reflection coefficients at a single frequency requires sensitive and accurate measurement setups which add complexity to the detection procedure. Of course, resonant sensors require vector network analyzers (VNAs), which make the application of these types of sensors difficult from a practical point of view. Nevertheless, the rapid growth in the development of portable and inexpensive VNAs is expected to make resonant-probe-based technologies more suitable than other microwave techniques in the near future. Despite the key advantages of near-field microwave techniques, miniaturizing sensors for microscale applications in a microwave regime can introduce a number of design challenges. The many beneficial features of near-field microwave sensors based on electrically-small planar resonators are indicators of their significant potential.

1.3 Background

1.3.1 Electrically-Small Resonators

Electrically-small resonators are those whose lengths are electrically small compared to the excitation wavelength. Such resonators include split-ring resonators (SRRs) [21] and their complements (CSRRs) [22]. It could be argued that the first-proposed SRRs date back to 1952 [23] and that they were subsequently applied to metamaterials by Pendry in 1999 [21].

When SRRs are illuminated by external oscillating magnetic fields, a resonant surface electric current density (J) is generated and circulates, producing an inductance in the SRRs whereas the accumulated charges at the edge of the splits at each cycle generate a capacitance. Both the capacitance and the inductance create a resonance phenomenon at specific frequencies: the resonance frequencies. Figure 1.1 shows an SRR placed on a dielectric substrate, where g is the size of the gap, t is the thickness of the metallic trace, and L is the length of the resonator.

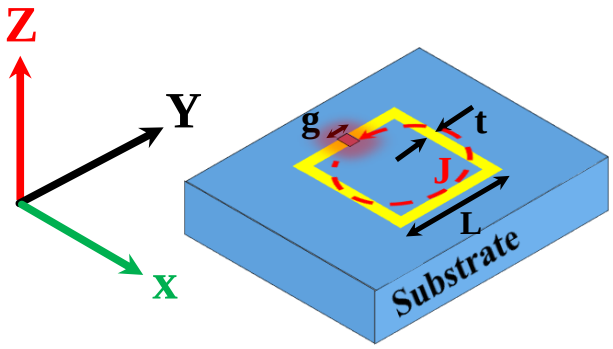

Figure 1.1: An SRR placed on a dielectric substrate, where g is the size of the gap, t is the thickness of the metallic trace, and L is the length of the resonator

Since the resonators are miniaturized compared to the excitation wavelength, so that the EM fields can be concentrated into a smaller, closely proximate volume [21]. Electrically-small resonators-based sensors are thus highly sensitive to changes in their surrounding environment. By disturbing such fields with the MUTs, the resonators can then be utilized for designing different sensing modalities [15, 24]. Among electrically-small resonators, SRRs and their complements (CSRRs) have been utilized for designing near-field sensors for numerous applications, including bimolecular sensors [9, 25–27], crack detection in metallic and nonmetallic materials [1, 2, 28], microfluidic sensors [8, 29], bioassay sensors [30], and dielectric characterization [25, 31–33].

1.3.2 Planar Electrically-Small Resonators as Near-Field Sensors for Detection, Characterization, and Imaging

Electrically-small planar resonators exhibit many features that make them strong candidates for designing near-field sensors for a number of techniques, including detection, imaging, and characterization. From a fabrication technology point of view, these resonators are easy to fabricate using printed circuit board technology (PCB), so that, with mass production, the fabrication of such resonator-based sensors is less expensive. Second, the resonators are electrically small (miniaturized) compared to the excitation wavelength, which means that they are highly compact for applications (e.g., a lab-on-a-chip) that

involve limited physical space. Since these resonators are printed on substrates, they can also be easily integrated with current electronics technologies.

To create sensing systems, planar resonators must be coupled to external circuitries. A variety of techniques are available for exciting microwave planar resonators [16]. The sensing systems used in the research for this dissertation are based on two-port microstrip-line systems that excite the planar resonators. Two-port microstrip-line systems have no need for the matching networks that can increase system complexity. For example, a two-port system is designed to have an approximately flat 50-Ω characteristic impedance. A resonator is then coupled to the system. Any change in the fields surrounding the resonator thereby creates, in theory, another resonator, which interestingly, is coupled to the microstrip line, without the need for a matching network, which would, of course, be within the frequency band of the designed characteristic impedance. The coupled resonators in fact create a band gap that is a function of the frequency. The response of the system can be observed using two-port VNAs, which extract the transmission coefficient ($|S_{21}|$).

In two-port systems, an SRR is designed using a copper ring with a split (gap) that is placed beside a microstrip line so that the magnetic field generated excites the surface of the rings, creating a circulating current and voltage difference at the gap. The frequency at which the electric and magnetic energies are equal is the resonance frequency. Figure 1.2(a) provides a schematic of an SRR in a two-port system. Electrically-small resonators such as SRRs can be considered quasi-static resonators. The effects of the circulating surface current can therefore be represented by an inductance whereas the effects of the voltage that develops at the gap can be denoted by a capacitance. The SRRs can thus be considered to be series RLC resonators. Figure 1.2(b) illustrates an SRR circuit model, where C_r, L_r, and R_r are the capacitance, inductance, and resistance of the resonator, respectively; L is the inductance of the transmission line per unit length; and M is the mutual coupling [3]. It should be noted that the motivation for the use of lumped-element models is that this type of model can help provide an intuitively deep understanding of the nature of the resonance phenomenon. For the resonant circuit shown in Figure 1.2(b), the frequency at

which the transmission is minimal can be expressed as follows:

$$f_0 = \frac{1}{2\pi\sqrt{L_r C_r}} \tag{1.3}$$

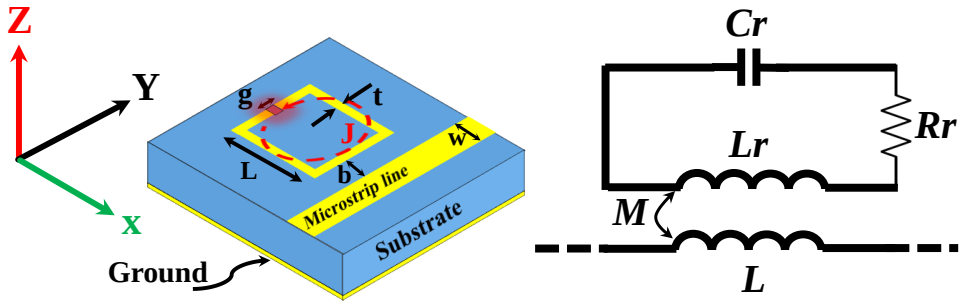

Figure 1.2: (a) The schematic of an SRR in a two-port microstrip-line system, L is the length of the resonator, g is the size of the gap, t is the thickness of the trace, w is the thickness of the microstrip line, and b is the distance between the resonator and the microstrip line (b) the circuit model of the SRR in the two-port system, where C_r, L_r, and R_r are the capacitance, inductance, and resistance of the resonator, respectively, L is the inductance of the transmission line per unit length, and M is the mutual coupling

CSRRs can be designed by creating a complement of the SRRs, with copper replacing air and vice versa. A CSRR is etched out in the ground plane of a microstrip line where the electric field is exciting the surface of the resonator. Figure 1.3(a) presents a schematic of a CSRR in a two-port system. The voltage difference between the centre island and the rest of the ground plane can be represented by a capacitance whereas the surface current circulating through the small bridge (a) can be denoted as an inductance. Based on the excitation mechanism and the topology of the CSRR, it can be regarded as a parallel RLC resonator. Figure 1.3(b) depicts the CSRR circuit model, where C_r, L_r, and R_r are the capacitance, inductance, and resistance of the resonator, respectively, and L and C are the inductance and the capacitance (the coupling capacitance) of the transmission line per unit length. The frequency at which the transmission is at a minimum is the resonance frequency of the circuit, which can be expressed mathematically as follows:

$$f_0 = \frac{1}{2\pi\sqrt{L_r(C_r + C)}} \tag{1.4}$$

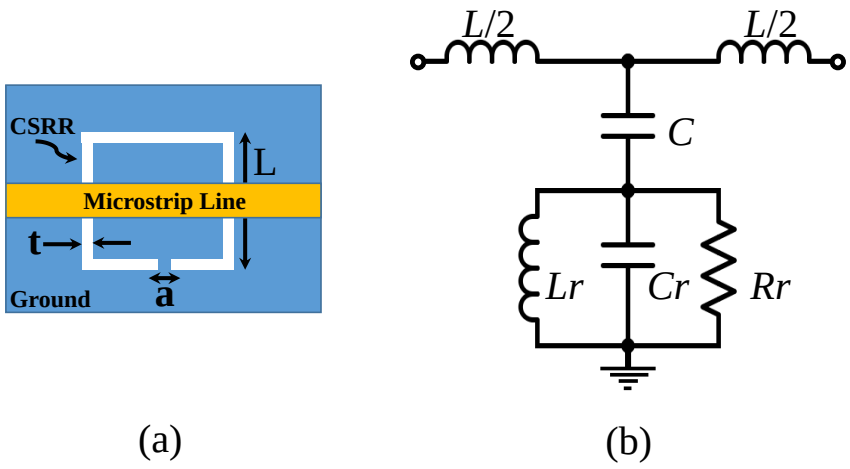

Figure 1.3: (a) The schematic of a CSRR in a two-port microstrip-line system, L is the length of the resonator, g is the size of the gap, t is the thickness of the trace, w is the thickness of the microstrip line, and b is the distance between the resonator and the microstrip line (b) the circuit model of the SRR in the two-port system, where C_r, L_r, and R_r are the capacitance, inductance, and resistance of the resonator, respectively, L and C are the inductance and the capacitance (the coupling capacitance) of the transmission line per unit length

In near-field sensors for dielectric materials, the SRR sensing elements are the splits (gaps) in the rings, where the electric field develops, whereas, with CSRRs, the sensing elements are the gaps between the centre islands and the rest of the ground planes. When the MUTs disturb the distribution of closely proximate EM fields, the resonance frequencies of the resonators exhibit a shift to a lower frequency since the loaded MUTs provide a capacitance parallel to that of the resonators. Observation of the changes in the resonance frequency is, in fact, the fundamental sensing mechanism underlying the work presented in this thesis. Figure 1.4 shows the sensing mechanism where the shift in the resonance frequency (Δf_r) can be observed. The words "reference" or "a priori knowledge" mean creating a reference point based on reference materials that have previously been characterized before the testing is conducted[1]. The procedure for obtaining the reference point

[1]Note that the concept of *priori knowledge* is so fundamental to the point that without it, it is difficult to apply the techniques including *detection*, *imaging*, and *material characterization*

is thus an essential element of the sensing procedure. Without it, the shift in resonance frequency is meaningless. The detection procedure therefore enables the observation of the shift in resonance frequency that results from changes in the MUTs. The sensing procedure is based on a binary decision being detected (1) or not being detected (0). Utilizing the sensing system for imaging techniques such as near-field scanning microscopy requires additional information (a priori knowledge) so that the data can be processed in order to construct an image. Further constraints are also required so that the sensing systems can resolve the space.

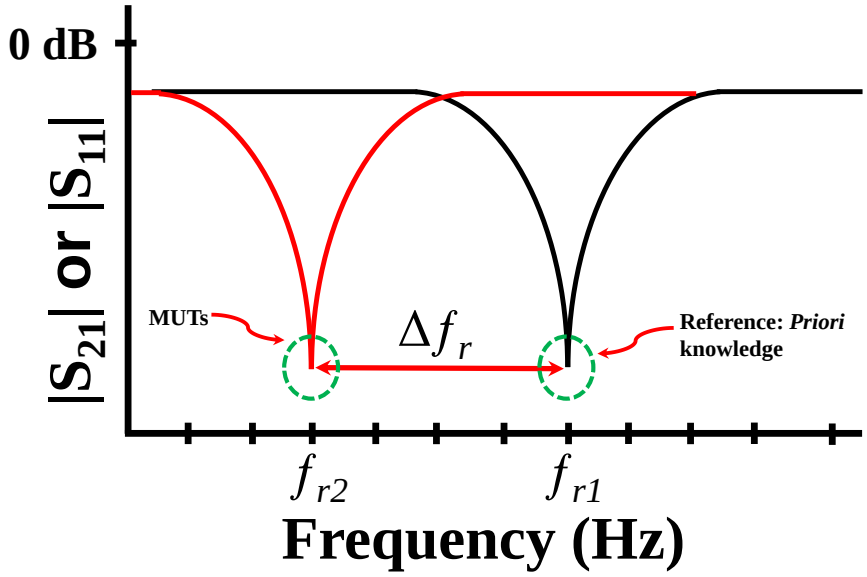

Figure 1.4: The typical response of the resonant-sensing based systems when encountering changes in the surrounding environment

Figure 1.5 shows an arbitrary near-field probe with a specific thickness, with the probe being utilized for imaging closely spaced objects that are separated by a distance (d). The response (changes in resonance frequency) is observed using the reading systems. In electrically-small resonators, the size of the probe as well as that of the objects is electrically small compared to the excitation wavelength. The strength of the perturbation in the EM field due to the interaction between the probe and the objects determines the sensitivity, with the strength of the perturbation being a function of the stand-off distance. In near-

field scanning microscopy, the resolution is more important than the sensitivity. Of course, the sensitivity determines the dynamic range. However, without greater resolution, a very highly sensitive system is useless for imaging techniques. In electromagnetism, the limitation of the resolution is related to the Abbe diffraction limit, which stipulates that the distance between two points must be approximately greater than or equal to $\lambda/2$.

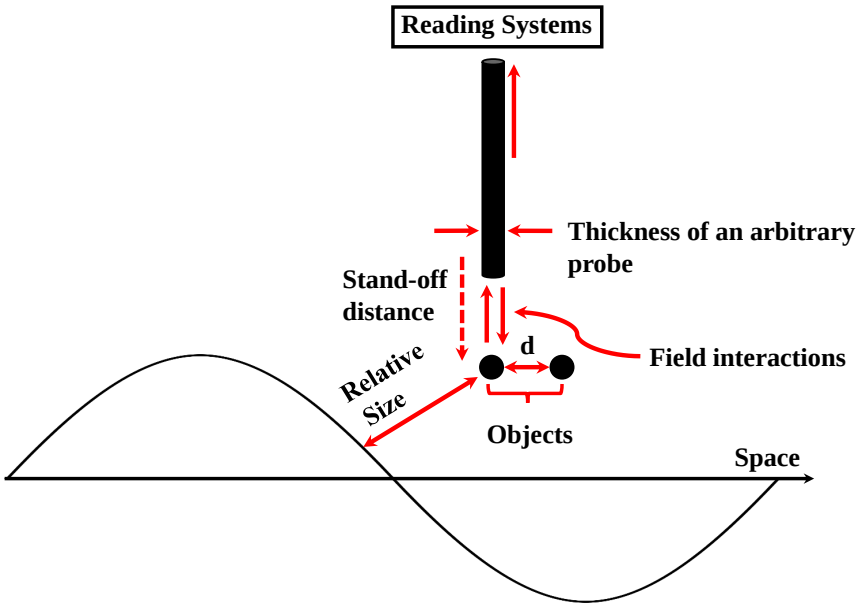

Figure 1.5: An arbitrary near-field probe with a certain thickness, where the probe is utilized to image closely spaced objects that are separated by a distance (d)

In near-field microscopy, although the systems operate in a microwave regime, the probes can be characterized by high resolution that breaks the diffraction limit [19]. Figure 1.6 shows an arbitrary near-field probe with a varying distance between the probe and the object to be resolved (stand-off distance). The dashed lines are visual aids used for plotting the variations in the field over the space. The closer the dashed line to the head of the probe, the more the field is confined in the spatial dimensions. The Fourier series can be used for decomposing the field over the space into spatial harmonics, as indicated in figure 1.7. The high spatial-harmonic components are responsible for the greater resolution and sensitivity. A high-resolution probe can be used for performing a two-dimensional scan

(e.g., in the x and y planes), where the shift in the resonance frequency can be observed by the reading systems at each step. Ultimately, a two-dimensional matrix is constructed and can be processed for plotting the image of the scanned objects. The scanning procedure is illustrated in figure 1.8, where d is the scanning step.

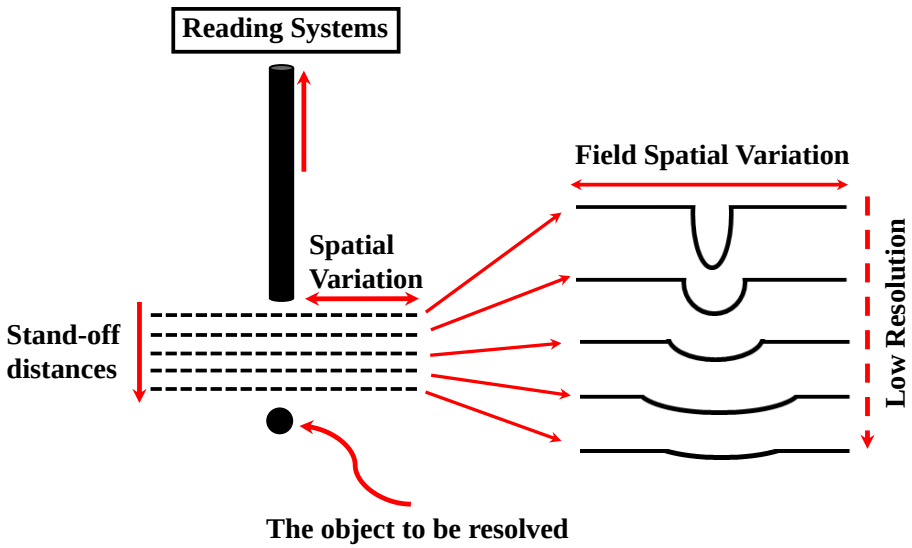

Figure 1.6: An arbitrary near-field probe where the distance between the probe and the object to be resolved (stand-off distance) are varied. The dashed lines are visual aids used for plotting the variations in the field over the space

Moreover, the procedure is more difficult to implement in material characterization techniques than in detection and imaging techniques. The relation between multiple independent parameters must be constructed either mathematically or with the use of data extracted either numerically or experimentally. In electrically-small planar resonators, the response curves relate the output of the sensing system (the shift in the resonance frequency) to a targeted MUT parameter (e.g., permittivity), as shown in figure 1.8. Generally speaking, the slope of the response curve is a measure of the sensitivity of the sensing systems, which determines the smallest variations in the materials targeted for detection [4]. With the use of fitting function techniques, the relation can be constructed mathematically.

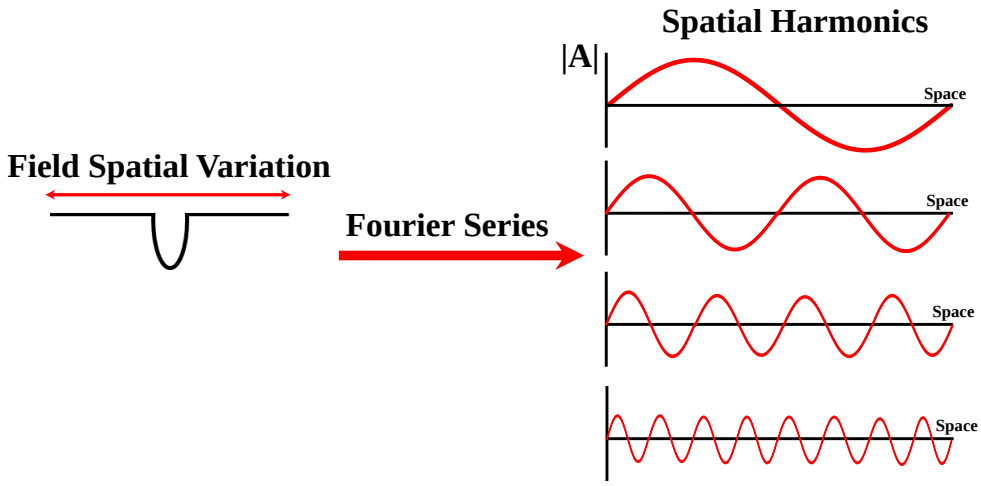

Figure 1.7: An arbitrary confined field distribution over space, where it can be decomposed into spatial harmonics using the Fourier series

1.4 Research Objectives

Although electrically-small planar resonators have been utilized for designing near-field sensors, with respect to suitability for micro and submicro technologies, planar sensors still provide relatively low sensitivity due to the concentration of the field in the substrates and reduced resolution due to the size of the probes. It is in this area that the research presented in this thesis plays a role: the investigation of a variety of possibilities for enhancing the sensitivity and resolution of sensors that are based on electrically-small planar resonators for detection, imaging, and material characterization based techniques. Therefore, the main objectives in this thesis are summarized as follows:

1. **Provide** an analysis of the sensitivity of planar CSRRs based on the approximation of lumped-circuit models, in which resonators are viewed as parallel RLC circuits.

2. **Propose** an ultrasensitive sensor based on resonators inspired by planar CSRRs to detect and image surface cracks in metallic materials.

3. **Propose** a novel sensor for surface crack detection in dielectric materials.

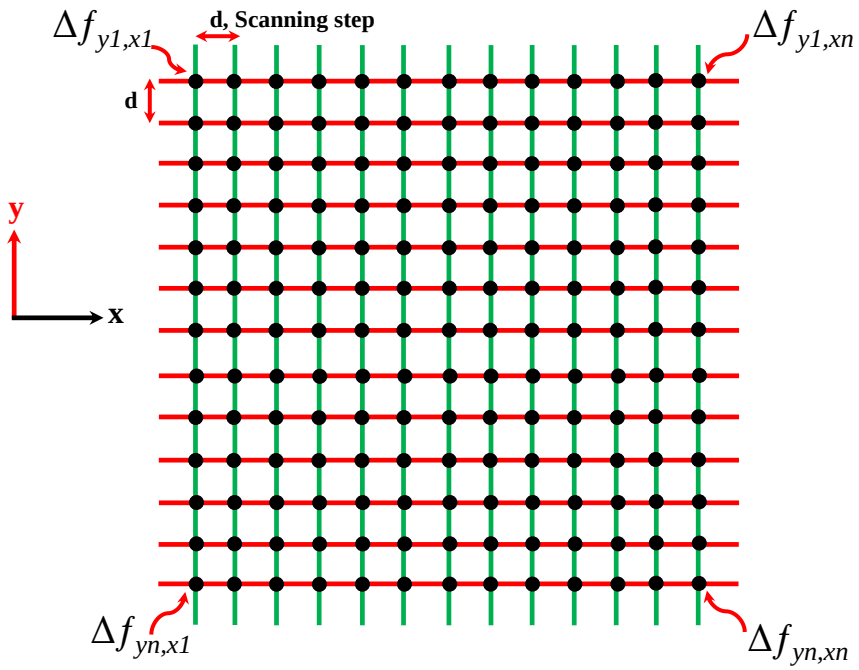

Figure 1.8: The scanning procedure, where d is the scanning step and at each step, the shift in the resonance frequency is observed

4. **Propose** a novel concept to enhance the sensitivity of planar CSRRs based on the utilization of multiple resonators.

5. **Propose** a sensitive sensor based on three-dimensional capacitors and CELCRs for fluidic and microfluidic based technologies.

6. **Enhance** the sensitivity and tunability of SRRs fluidic and microfluidic technologies, fluid-Level detection, and near-field scanning microscopy.

7. **Enhance** the sensitivity of CELCRs for fluidic and microfluidic technologies, fluid-Level detection.

8. **Propose** a high-Q split-annular-ring resonator based sensor for material characterization and microfluidic technologies.

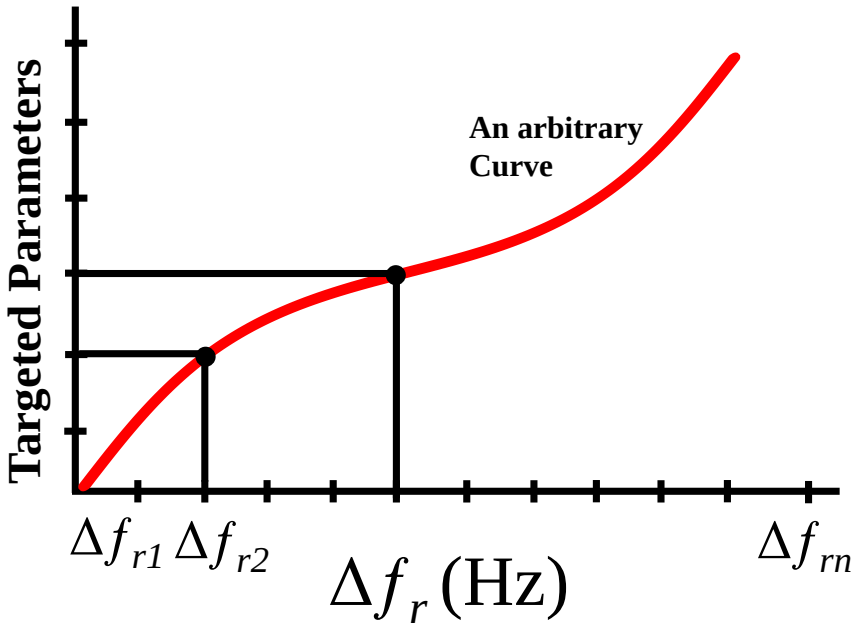

Figure 1.9: The response curves relate the sensing system's output (the shift in the resonance frequency) to a targeted parameter of the MUTs

9. **Propose** an integrated system technique for material characterization, with the sensing techniques being based on electrically-small resonators and modeling and data processing being based on artificial intelligence.

1.5 Dissertation Outline

Chapter 2 presents an analysis of the sensitivity of CSRRs with respect to changes in resonator topologies, such as gaps and length. The analysis is based on the utilization of eigenmode solvers, approximated circuit models, a numerical simulation tool (using ANSYS HFSS [34]), and experimental studies.

Chapter 3 introduces an ultrasensitive near-field sensor for detecting submillimeter cracks in metallic materials. The sensor design relies on physics-based modelling, lumped-element models, and EM field distribution using numerical simulation (HFSS). This chapter

also describes the utilization of the resonator for designing near-field scanning microscopy for imaging a finite crack in a metallic materials.

In **chapter 4** a near-field sensor based on planar CSRRs for crack detection in dielectric materials is proposed. The results reported in Chapter 2 and analysis of the distribution of the total electric field on the resonators enabled a determination of sensitive areas that interact with a crack in dielectric materials.

Chapter 5 explains a novel concept for increasing the sensitivity of planar CSRRs for the detection of the presence of dielectric materials. The concept is based on the utilization of multiple resonators coupled to one another perpendicularly to the direction of the wave propagation in the structure.

Chapter 6 introduces a novel concept for addressing the sensitivity limitations of complementary structures such as CSRRs and CELCRs. The concept is based on the idea of extracting the electric field from the substrate and concentrating it in the sensing area (the free space). For the realization of this idea, three-dimensional capacitors are loaded into the CELCRs since they are more suitable for microfluidic technologies from a topological perspective.

Chapter 7 presents the implementation of three-dimensional capacitors for enhancing SRR tunability and sensitivity. In addition, the sensor was utilized for designing near-field microscopy for imaging the surface of dielectric materials.

Chapter 8 focusses on the miniaturization of CELCR sensing areas, with the goal of enabling them to be loaded with three-dimensional capacitors for designing a sensitive near-field sensor for microscale applications such as detection and material characterization. The sensor is utilized for detecting the presence of dielectric and magnetic materials.

Chapter 9 describes a novel planar structure based on an annular ring resonator loaded with a cut in order to miniaturize the ring so that it operates at a lower frequency and to enhance the quality factor. The proposed structure can be utilized for designing near-field sensors for material characterization. The sensor was also tested with respect to designs for microfluidic technologies.

In **chapter 10**, an integrated system technique is proposed for material characterization, with the sensing techniques being based on electrically-small resonators and the

modelling and data processing relying on artificial intelligence. In particular, the system can be utilized for detecting the concentration of fluid materials.

Chapter 9 offers conclusions, list of publications, and suggestions for future research.

Chapter 2

Sensitivity Analysis of Microwave Planar CSRRs based Sensors

2.1 Introduction

Despite the fact that microwave planar SRRs sensors have been utilized to design near-field sensors, CSRRs sensors are more sensitive for detecting the presence of dielectric materials [8, 29, 31]. In [35], the sensitivity and limitation of planar SRRs sensors were investigated. The analysis was based on the approximated lumped circuit (RLC circuit model). The analysis can thus be adopted to analyze the sensitivity of planar CSRRs sensors.

This chapter presents the sensitivity analysis of CSRRs sensors. In particular, the length of CSRRs as a "*footprint*" was fixed for the analysis to determine the sensitive elements in the resonators' topologies such as gaps and bridges that play important roles in determining the resonators' capacitance, hence, the resonance frequency. First, an approximated lumped element model was used to find the relationship between the shifts in resonance frequency and the resonators' capacitance. Then, the results numerically was tested using the numerical simulation tool (HFSS). Then, the predicted results from both approximated and numerical models were experimentally validated.

2.2 CSRRs as Near-field Sensors

Generally speaking, CSRRs are quasi-static resonators and can be modeled using an approximated lumped element model. The loops and gaps can thus be represented by an inductance and capacitance, respectively, and the resonance frequency can be written as

$$w_0 = \frac{1}{\sqrt{L_r C_r}} \tag{2.1}$$

where L_r and C_r are the inductance and capacitance, respectively, of the resonator. Electrically-small resonators have flexibility in terms of topologies and structures. Figure 2.1 shows the footprint of the CSRR where L is the length of the resonators, b is the size of the gap, and a is the size of the bridge that connecting the centre island the rest of the ground plane. For the excitation, figure 2.2(a) shows the CSRRs coupled to a two-port microstrip line system. Figure 2.2(b) shows the lumped element model, with the CSRR being excited by the microstrip line through the line capacitance (C).

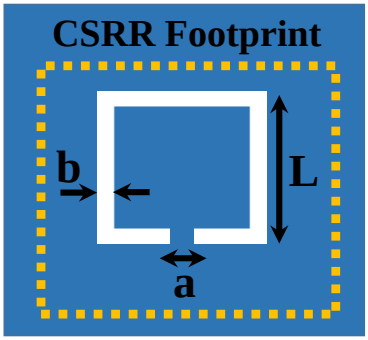

Figure 2.1: The schematic of the footprint of a CSRR where L is the length and a and b are the size of bridge and gap, respectively.

Electromagnetic fields are concentrated in close proximity of the CSRRs, and the sensing mechanism is based on disturbing the fields by the MUTs. The disturbance in the fields can be correlated to changes in the inductance and the capacitance presented in equation (2.1). In the CSRRs, electric fields are distributed between the centre island and the rest of the ground plane. Disturbing the fields by the MUTs causes the resonance

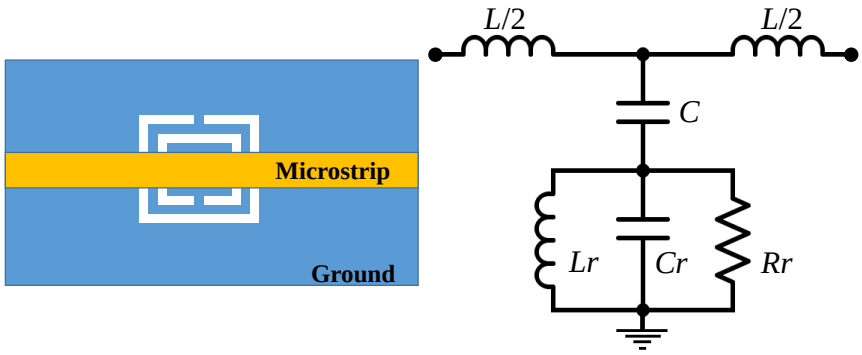

Figure 2.2: (a) A microstrip line exciting a CSRR that is etched out in the ground plane (b) The equivalent lumped circuit model where L and C are inductance and capacitance of the microstrip line per unit length, respectively, and L_r, C_r, R_r are the inductance, capacitance, and resistance of the CSRR, respectively.

frequency to exhibit a shift which explains the underlying sensing mechanism of electrically-small resonators to design planar microwave near-field sensors. Since the lumped elements model such as the inductance and the capacitance, hence the resonance frequency, are related to the topology of the resonators, the model can be utilized to investigate the sensitivity.

2.3 Sensitivity Analysis based on an Approximated Lumped Element Model

In microwave planar CSRRs sensors, the sensitivity is directly related to many parameters including the dielectric constant of substrates and their thicknesses, and CSRRs' topologies such as length, gaps, and bridges (L, b, and a in figure 2.1). The limitations and effects of the substrates on the performance of electrically-small resonators as near-field sensors, which includes CSRRs, can be found in [35,36]. In this chapter, investigation focuses on the effect of topologies parameters, in particular, the length, gaps, and bridges. By fixing the square length of a CSRR and regarding it as a "*footprint*", the sensitivity of the resonance

frequency with respect to the length, gaps, and bridge can be investigated.

The CSRRs is quasi-static resonators where there is no analytic formula to directly relate the design parameters to the resonance frequency. Generally speaking, the resonance frequency of electrically-small resonators is proportional to the largest dimensions of the resonators and can be found either numerically or experimentally [31,37,38]. In this work, the CSRRs are modeled numerically using eigenmode solver in ANSYS HFSS, where L is = 4.5 and 5.3 mm and both a and b are varied from 0.1 to 1.7 mm. When a is varied, the b is fixed and vice versa. The planar resonator and the substrate are placed inside a cavity with the enforced perfect electric conductor. The cavity is designed to have a resonance frequency higher than the resonance frequency of the CSRR by making the size of the cavity larger, so it will not affect the resonance frequency of the resonator. For the aforementioned dimensions, the resonance versus the a and b is presented in figure 2.3.

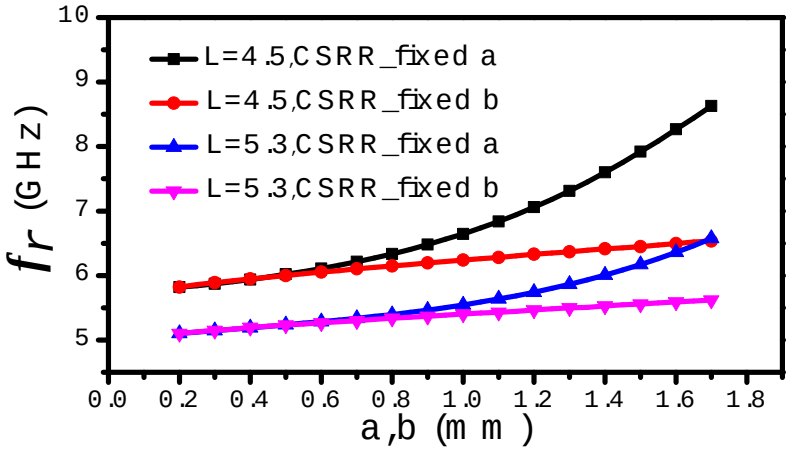

Figure 2.3: The resonance frequency versus the gap (b) and bridge (a) of a CSRR, where L = 4.5 and 5.3 mm and a and b are varied from 0.1 to 1.7 mm. When a is varied, the b is fixed and vice versa. The result is extracted using the HFSS

Since the eigenmode solver is utilized, the frequency shown in figure 2.3 is the natural resonance frequency where the CSRR is regarded as parallel LCR resonator. Equation (2.1) can thus be used to analyze the behavior of the resonance frequency as a function of a and b. Note that, equation (2.1) is valid only around the resonance frequency. To analyze

the sensitivity of the CSRR to the changes in the topology parameters (a, b, and L), the changing rate of the resonance frequency versus the changing in the capacitance (C_r) can be utilized. To find the changing rate of the change close to the resonance, the partial derivative of the resonance function with respect to C_r can be calculated as

$$\frac{dw_0}{dC_r} = \frac{-1}{2}\frac{1}{\sqrt{L_r}\sqrt[3]{C_r}} \tag{2.2}$$

Equation (2.2) shows that the negative changing in the resonance frequency with respect to the C_r is proportional to $1/\sqrt[3]{C_r}$. The increase in the value of b (the gap) will cause the capacitance (C_r) to decrease, hence, increasing the resonance frequency as illustrated in figure 2.3. In addition, equation (2.2) can be used to find the ratio of the change in close to the resonance frequency where the change in the capacitance is small as

$$\frac{dw_0}{w_0} = \frac{-1}{2}\frac{dC_r}{C_r} \tag{2.3}$$

It is clear that decreasing the capacitance (C_r) by increasing the value of b will increase the rate of the change, hence, the sensitivity. In addition, varying the size of a are not highly affecting the capacitance of the resonator (C_r), which means the resonance frequency is more sensitivity to the changes in b as presented in figure 2.3. In addition, figure 2.3 can be utilized to analyze the effects of the length (L) on the changes in the resonance frequency. If equation (2.3) is rewritten in the following form as

$$\frac{dw_0}{dC_r} = \frac{-1}{2}\frac{w_0}{C_r} \tag{2.4}$$

The increment in the length will increase the inductance (L_r), hence, lowering the resonance frequency (w_0). Equation (2.4) shows that the sensitivity will be degraded. In addition, the increment in L will affect the capacitance (C_r) of the resonators, which will degrade the sensitivity since the C_r is in the numerator of equation (2.4).

So far, it has been shown that decreasing the length (L) and increasing gap (b) will enhance the sensitivity of the resonance frequency, yet the quality factor has to be investigated since it has the information of the electromagnetic field of the resonators, which is responsible for determining the bandwidth of the response. Note that, it is desirable to

have a sharper dip of the profile around the resonance frequency to detect smaller changes in the resonance (readable). For parallel LCR resonator, the quality factor can be written as

$$Q_{resonator} = R\sqrt{\frac{C_r}{L_r}} \tag{2.5}$$

Equation (2.5) shows that decreasing the C_r by increasing the gap (b) will decrease the quality factor. In addition, the quality factor is increased by increase the length of the resonator since the C_r will increase. However, the sensitivity of the resonance frequency will be degraded. From an engineering point of view, one can find an intermediate point between higher quality factor and sensitivity by choosing the right C_r that is controlled by the CSRRs gaps (b) and lengths (L).

2.4 Sensitivity Analysis Based on Numerical Simulations

In the two-port systems, the CSRRs can be coupled to microstrip lines where the CSRRs are etched in the ground plane. Since the response of the system (the scattering parameters) will be measured by a 50 Ω vector network analyzer (VNA), a microstrip line is designed with a characteristic impedance of 50 Ω. Using Rogers RO4350 substrate with a thickness of 0.75 mm, the permittivity of 3.66, loss tangent of 0.0031, the designed line width is 1.7 mm.

The numerical simulation can be used to compare the sensitivity of the planar CSRRs and SRRs by studying the losses in the resonators, which is the fundamental factor for degrading the quality factor of the resonators. Two resonators (CSRR and SRR) with the length of 7.5 mm are designed. Note that, the SRR is placed beside the transmission line excited by the magnetic field. Figures 2.4 and 2.5 show the response of the CSRR and SRR, respectively. In the case of CSRR, the loses due to conductor loss, substrate loss, and radiation loss can be calculated as $|S_{21}|^2 + |S_{11}|^2 - 1$ = -0.123. The numerical result shows that 36% is the radiation efficiency at the resonance frequency of 3.35 GHz, which indicates that the CSRRs sensors will be sensitive to changes in close proximity since the field are

not highly confined in the substrate, which is the case in planar resonators. However, in the case of the SRR, the field is confined in the substrate and most of the power is lost as a dielectric loss. From figure 2.3, it is clear that the SRR sensor has higher quality factor than the CSRR sensor yet less sensitivity, which has been shown in the literature [8,29,31]. In addition, the radiation loss of the SRR is numerically calculated as 1.6% compered 36% of the CSRR, which means that the losses are mostly due to the dielectric loss and ohmic loss.

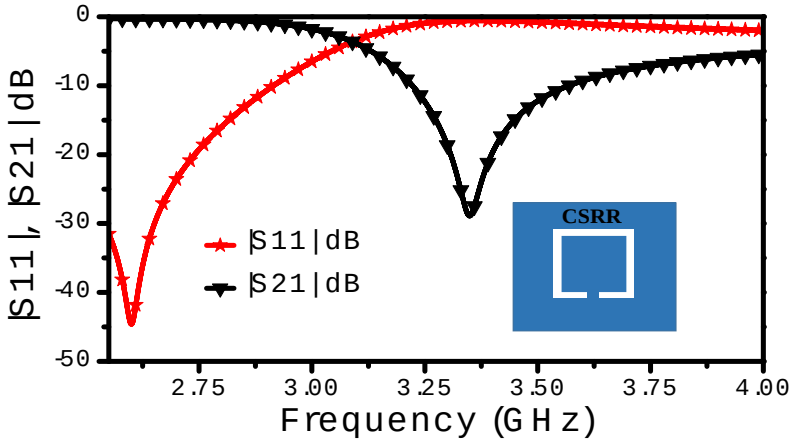

Figure 2.4: The scattering parameters of a 7.5 mm CSRR extracted using the HFSS

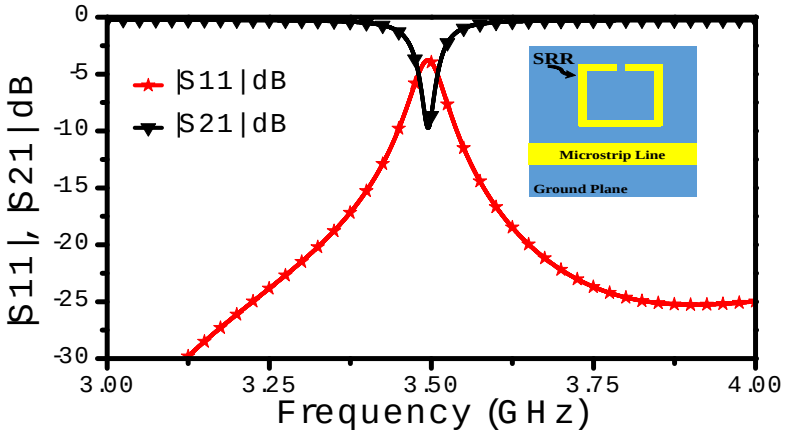

Figure 2.5: The scattering parameters of a 7.5 mm SRR extracted using the HFSS

Furthermore, in the two port systems, the numerical simulation can be used to find a relation between the resonance frequency and the size of the gap (b) and the bridge (a). Two CSRRs with the length of L = 4.5 and 5.3 mm excited by microstrip lines are designed. The gap (a) and bridge (b) are varied from 0.1 to 1.7 mm, with a being fixed and b being varied and vice versa. Figure 2.6 shows the response of the system. Compared to the eigenmde solution, both figures. 2.4 and 2.5 have the same profile except the resonance frequency are different. The main reason can be attributed to the fact that in the two-port system, there is an addition factor related to the coupling capacitance (C) between the transmission line and the resonator, where the resonance frequency (transmission zeros) can be written as [39]

$$w_0 = \frac{1}{\sqrt{L_r(C_r + C)}} \tag{2.6}$$

Taking the partial derivative of equation (2.6) with respect to C_r,

$$\frac{dw_0}{dC_r} = \frac{-1}{2}\frac{w_0}{C_r + C} \tag{2.7}$$

The quality factor can be written as follows:

$$Q_{resonator} = R_r\sqrt{\frac{C_r + C}{L_r}} \tag{2.8}$$

Sine the sensitivity is highly effected by the change in b, the CSRRs sensors with L = 4.5 and 5.3 mm, a = 0.2 mm and b = 0.2 and 1.3 mm are utilized to detect the present of a dielectric slab with the permittivity of 2.33 and thickness of 3 mm. Figures 2.7 and 2.8 show the response of the sensors (the transmission coefficient $|S_{21}|$). In the case of L = 4.5 mm and a = 0.2 and b = 0.2 and 1.3 mm, the shift in the resonance frequency is 780 MHz and 580 MHz, respectively, which means that the sensitivity is enhanced with the value of 34.5 % when the b changes from 0.2 to 1.3 mm (reduction in C_r), whereas in the case of L = 5.3 mm and a = 0.2 and b = 0.2 and 1.3 mm, the shift in the resonance frequency is 556 MHz and 487 MHz, respectively, which means that the sensitivity is enhanced with the value of 14.2 % when the b changes from 0.2 to 1.3 mm. By comparing the two results, the sensitivity is enhanced in the case of smaller length (L = 4.5 mm) with the difference of 20.3%.

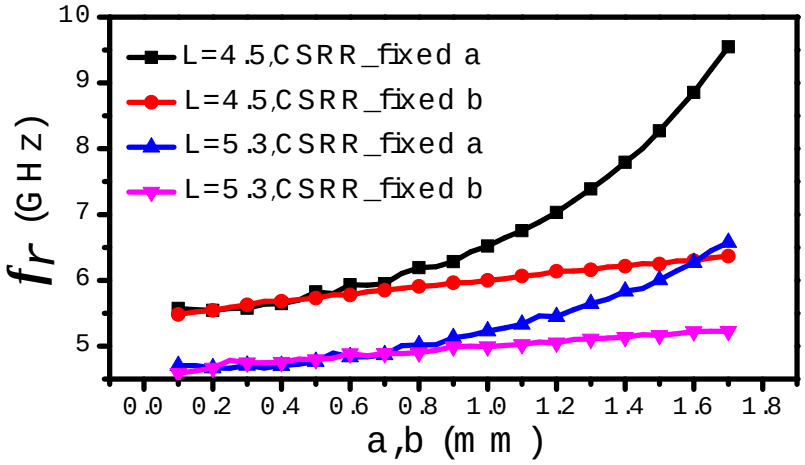

Figure 2.6: The resonance frequency versus the gap (b) and bridge (b) of a CSRR coupled to a microstrip line, where L = 4.5 and 5.3 mm and a and b are varied from 0.1 to 1.7 mm. The result is extracted using HFSS

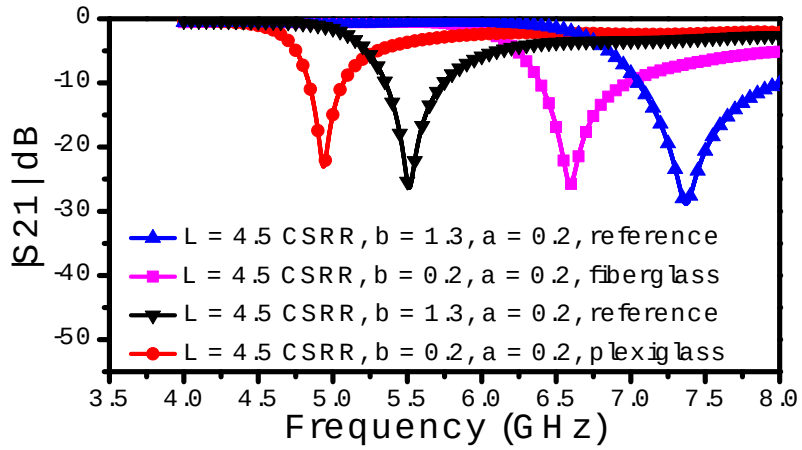

Figure 2.7: The transmission coefficient of a 4.5 mm CSRR sensor utilized to detect the presence of a dielectric slab with the thickness of 3 mm and dielectric constant of 2.33 using the HFSS, where a = 0.2 mm and b = 1.3 and 0.2 mm

By carefully analyzing equations (2.6) and 2.7, the sensitivity of the changes in the resonance frequency is also related to the coupling capacitance (C), which is in the numer-

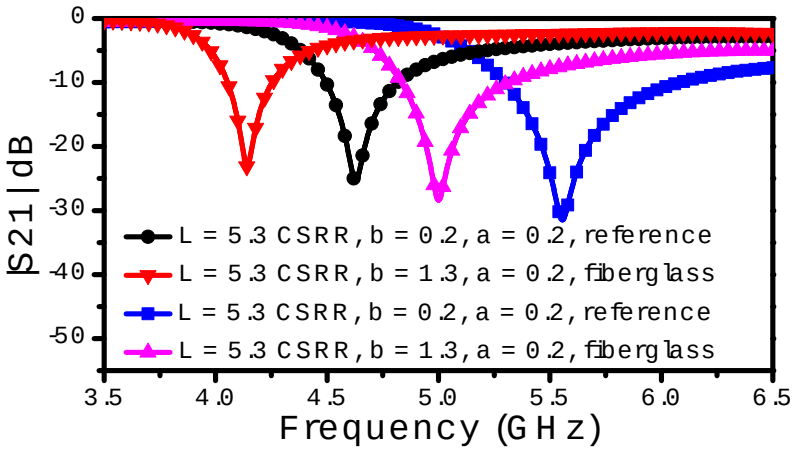

Figure 2.8: The transmission coefficient of a 5.3 mm CSRR sensor utilized to detect the presence of a dielectric slab with the thickness of 3 mm and dielectric constant of 2.33 using the HFSS, where a = 0.2 mm and b = 1.3 and 0.2 mm

ator (inside w_0) and denominator $(C_r + C)$. If the MUTs will affect the coupling factor, the transmission zeros will be vanished. In addition, although the effect of the MUTs will be presented in the form of a capacitance parallel to the C_r, which means higher quality factor, the losses of the MUTs will reduce R in equation (2.7). To investigate the effect of the MUTs, a CSRR with L = 7.5 mm, b = a = 0.5 mm is coupled to a microstrip line for designing a near-field sensor to detect the presence of a lossless dielectric slab where its dielectric constant is varied from 1 to 100. The slab will add a parallel capacitance to C_r (increasing the total capacitance of the resonators), yet the coupling capacitance will be affected since the electric field will eventually start to concentrate in the half space of the MUTs. From figure 2.9, it can be noticed that the coupling factor is reduced with higher dielectric constant, which means the CSRR is suitable for low dielectric materials. Thinner substrates to increase the coupling capacitance can be utilized [35, 36].

Since the CSRRs are electrically-small and complement structures, the circuit model shown in 2.2 and the equation (2.6) can be generalized to any other electrically-small complementary resonators such as CSRRs and CELCRs. To investigate the effects of resonator's length on the shift in the resonance frequency of complementary structures such as CSRRs and CELCRs, the length of the resonators are varied from 5.5 to 7.5 mm

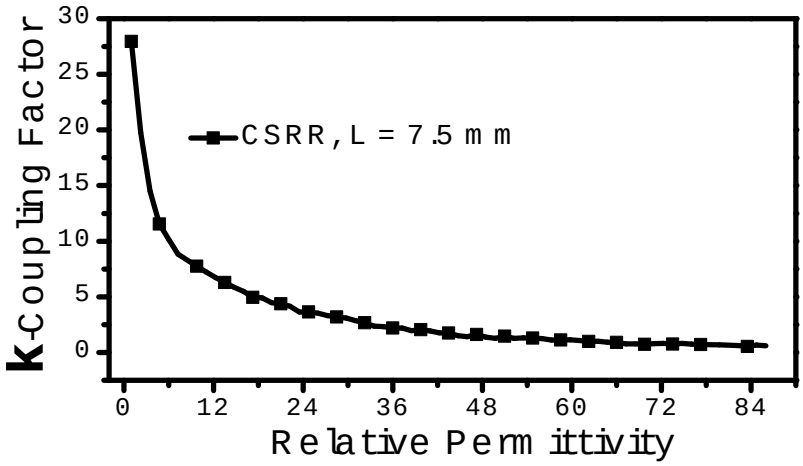

Figure 2.9: The transmission coefficient of a 5.3 mm CSRR sensor utilized to detect the presence of a dielectric slab with the thickness of 3 mm and dielectric constant of 2.33 using the HFSS, where a = 0.2 mm and b = 1.3 and 0.2 mm

and utilized to design near-field sensors to detect the presence of the dielectric slab with the thickness of 3 mm and dielectric constant of 4.81. Figure 2.10 shows the shift in the resonance frequency versus the resonator length. Based on the equation (2.7) and the fact that the increment in the length will increase the inductance (L_r), the sensitivity of the resonance frequency shift is decreased.

2.5 Sensitivity Analysis Based on Experimental Results

To validate the numerical results, four CSRRs sensors were fabricated using printed circuit board technology (PCB), where L = 4.5 and 5.3 mm, a = 0.2 mm, and b = 0.2 and 1.3 mm. The fabricated sensors are shown in figure 2.11. The sensors were tested to detect the presence of a dielectric slab with the thickness of 3 mm and dielectric constant of 2.33. Note that higher dielectric materials can be tested, yet the main idea here is to prove the concept. Figures 2.12 and 2.13 show the experimental results of 4.5 and 5.3 CSRRs,

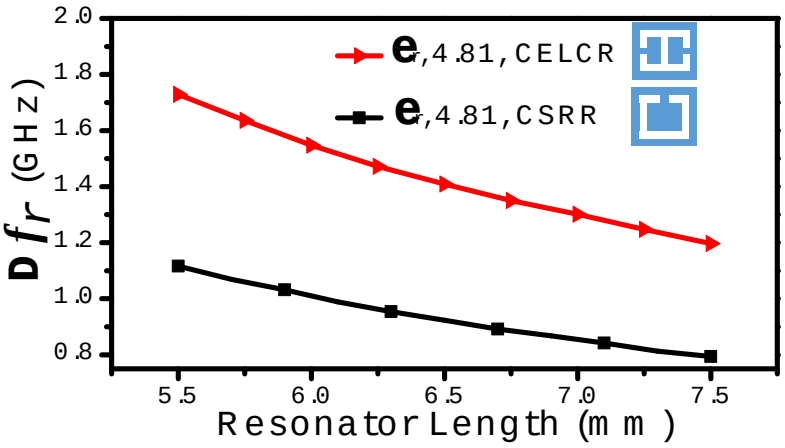

Figure 2.10: The transmission coefficient of CSRR and CELCR sensors where the length of the resonators are varied from 5.5 to 7.5 mm. The sensors are tested to detect the presence of a dielectric slab with the thickness of 3 mm and dielectric constant of 4.81 using the HFSS

respectively.

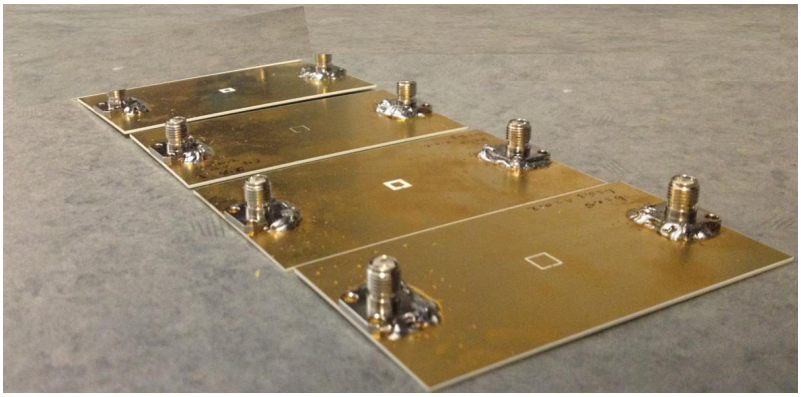

Figure 2.11: The transmission coefficient of a 4.5 mm CSRR sensor utilized to detect the presence of a dielectric slab with the thickness of 3 mm and dielectric constant of 2.33 extracted experimentally, where a = 0.2 mm and b = 1.3 and 0.2 mm

In the case of L = 4.5 mm and a = 0.2 and b = 0.2 and 1.3 mm, the shift in the resonance

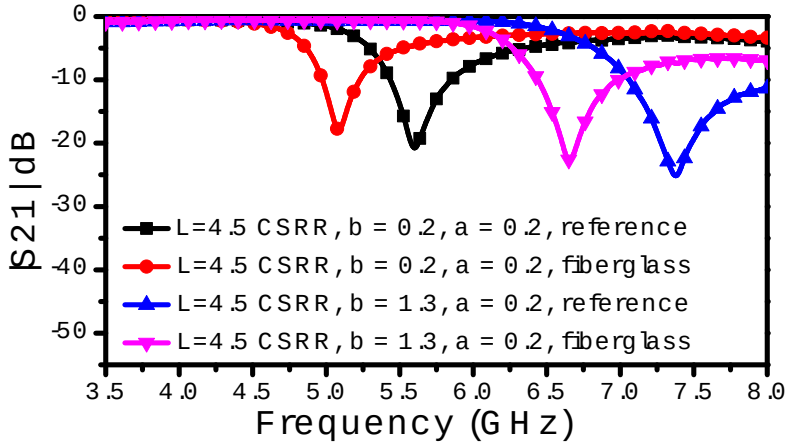

Figure 2.12: The transmission coefficient of a 4.5 mm CSRR sensor utilized to detect the presence of a dielectric slab with the thickness of 3 mm and dielectric constant of 2.33 extracted experimentally, where a = 0.2 mm and b = 1.3 and 0.2 mm

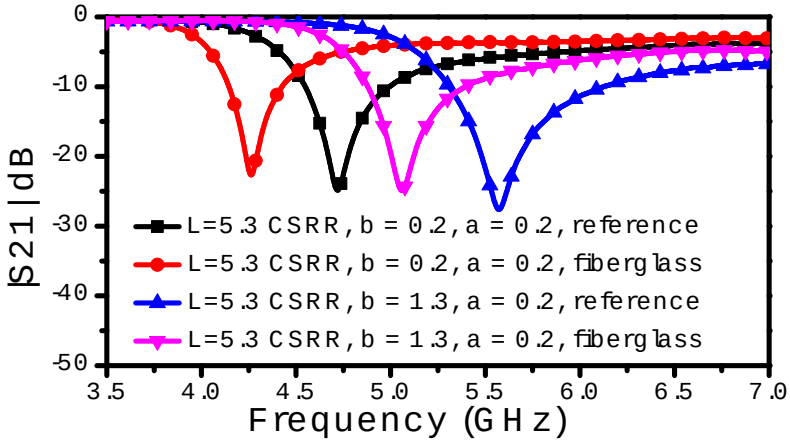

Figure 2.13: The transmission coefficient of a 5.3 mm CSRR sensor utilized to detect the presence of a dielectric slab with the thickness of 3 mm and dielectric constant of 2.33 extracted experimentally, where a = 0.2 mm and b = 1.3 and 0.2 mm

frequency is 725 MHz and 520 MHz, respectively, which means that the sensitivity is enhanced with the value of 39.4 % when b changes from 0.2 to 1.3 mm (reduction in C_r). In the case of L = 5.3 mm and a = 0.2 and b = 0.2 and 1.3 mm, the shift in

the resonance frequency is 515 MHz and 458 MHz, respectively, which means that the sensitivity is enhanced with the value of 12.4 % when the b changes from 0.2 to 1.3 mm. By comparing the two results of L = 4.5 and 5.3 mm, the sensitivity is enhanced in the case of smaller length (L = 4.5 mm) with the difference value of 27%. The results prove that the sensing system is sensitive to the gap and length of the resonators. Although the area of the interaction in the case of larger resonators is higher, the smaller resonators are more sensitive to the presence of the MUTs.

2.6 Conclusion

In this chapter, the sensitivity of planar CSRRs to the topologies such as gaps and length was analyzed. Since the resonators are electrically small compared to the excitation wavelength, the analysis was based on the circuit model and the full-wave simulation (HFSS). The results show that the CSRRs are sensitive to the changes in the gap and length which determine the sensitivity of the CSRRs to detect the presence of dielectric materials. The CSRRs can thus be utilized to design near-field sensors. Many prototypes with different gaps and length were fabricated to validate the result of the numerical analysis. A dielectric slab with the permittivity of 2.33 was used to test the sensitivity of the CSRRs sensors. The CSRRs with larger gaps or smaller lengths are more sensitive to the changes in the MUTs. Moreover, the numerical analysis shows that the coupling between the planar CSRRs and microstrip lines are reduced for high dielectric MUTs. Consequently, the planar CSRRs sensors are suitable to design near-field sensors for low dielectric materials. Indeed, electrically-small resonators such as CSRRs are flexible and scalable structures to design near-field sensors for detection, imaging, and material characterization.

Chapter 3

Microwaves-Based High Sensitivity Sensors for Crack Detection in Metallic Materials

3.1 Introduction

Microwave techniques have unique characteristics over other techniques. For instance, microwave frequencies can penetrate dielectric coating materials and detect changes in metallic surfaces without the need for surface cleaning or removing some of covering materials, which is difficult from a practical point of view. In real-world situations, cracks in metallic materials may be concealed by paint, composite laminates, corrosion protection substances, and rust, which are easier to be detected using microwave techniques compared to other techniques. In addition, microwave near-field probes are highly sensitive to the changes in MUTs. For more details and a general review of the state of the art of NDE techniques based on microwave frequencies, the readers are referred to [18].

Microwave near-field probes provide resolution beyond the Abbe diffraction limit. A resolution on the order of $\lambda/10^6$ was reported [19]. Microwave near-field probes for crack detection in metallic materials can be categorized into two groups: reflection coefficient

based and resonance frequency based. Reflection coefficient probes include open-ended waveguide and open-ended coaxial probes.

In [12], an open-ended waveguide operating at 20 GHz was utilized as a sensor to detect an 840-μm-wide surface crack by direct correlation with changes in the reflection coefficient. Open-ended waveguide techniques are capable of detecting smaller cracks such as fatigue cracks, yet the change in standing wave measurement (measured voltage using a detector) is very small [40]. It can thus easily be affected by many factors such as noise, air gap, and error introduced by the measurement setup. To overcome this limitation, the open-ended waveguide technique has been investigated to optimize some critical parameters such as the frequency of operation, detector diode location, an intentionally introduced dielectric layer at the waveguide aperture and the incident power level [41]. In addition, open-ended waveguide techniques are sensitive to the orientation of the cracks with respect to the broad dimension of the apertures, which add limitations from a practical point of view. Furthermore, in open-ended waveguide techniques, the spatial resolution depends on the apertures sizes, so to obtain higher resolution, the open-ended waveguide techniques must work at higher frequencies [13]. This limitation has been addressed using a technique that is based on open-ended coaxial probes [42]. Alternatively, resonant probes have been utilized to design near-field sensors for crack detection in metallic materials.

Several technologies based on resonant probes for crack detection were reported including a microstrip linear resonator loaded with an aperture [43], a quarter-wavelength microstrip line terminated with an electric dipole [20], dual-behavior resonator filter [20], and CSRRs [1, 44]. In [43], a microstrip linear resonator was used to excite an aperture that induces evanescent waves in free space. Thus, the resolution of the detection is determined by the size of the aperture. When a MUT is placed in close proximity of the aperture, the resonance frequency of the resonators exhibits a change. However, change in the resonance frequency is small requiring a highly accurate and sensitive measurement setup especially for very small cracks [43]. Since the change in the resonance frequency is small, perturbation theory was used to calculate small changes in the stored energy. On the other hand, the microstrip resonator can be more flexible and inexpensive than other techniques.

In recent years, near-field sensors were developed based on electrically-small resonators.

Such resonators include the SRR and the CSRR. The sensing mechanism in electrically-small resonators is based on disturbing the electromagnetic fields around the resonators. At the resonance frequency of a CSRR, a relatively high magnetic field is confined in close proximity of the small bridge between the center island and ground plane and a relatively high electric field is confined between the strips and the ground plane [1]. Generally, disturbing the fields in close proximity of the CSRR by metallic or dielectric materials cause the resonance frequency to shift, which is the underlying sensing mechanism. In recent work, a sensor based on a CSRR excited by a microstrip line was introduced to detect sub-millimeter size cracks in metallic surfaces [1, 44]. In [1], the sensor was able to resolve a sub-millimeter crack with a frequency shift of approximately 260 MHz for a 200-μm crack in a metallic block[1]. The CSRR sensor was also used to detect cracks in non-metallic surfaces [2]. One of the advantages of electrically-small sensors is that they can be easily incorporated into large arrays [45, 46]. In [45], an array of SRRs was embedded with a near-field waveguide probe for sensitivity enhancement for crack detection in metallic materials. The probe was able to detect a crack as small as 25 μm. In addition, the same system was improved by introducing artificial intelligence [47].

In this chapter, the proposed sensor is investigated for sensitivity enhancement and tested experimentally to detect sub-millimeter cracks in metallic surfaces. The sensitivity of the proposed sensor is appreciably higher than what was achieved earlier [1, 2]. Furthermore, the rationale behind the sensor topology design is shown by using circuit models and qualitative understanding of the electromagnetic field distribution in close proximity of the sensor. The resonator-based sensor is designed and tested numerically and validated by building and testing a physical prototype [48].

3.2 Sensor Design Based on Physics-Based Modeling

In [1, 2], CSRRs sensors could be used to detect sub-millimeter cracks in metallic materials. In [1, 2], the largest dimension of the CSRR resonator was 3 mm, and the length of the

[1]The caption of Figs. 3 and 4 of [1] stated incorrectly that the crack depths were 100 μm and 200 μm while the correct values of 1 mm and 2 mm were stated correctly in the legend of the figures

sensing element (a small bridge in CSRRs) was 0.2 mm. The sensor was able to detect a surface crack of 0.2 mm and 2 mm in width and depth, respectively. The resonance frequency of the sensor exhibited a change with respect to the faultless metal from 5.0625 GHz to 4.796 GHz with a shift of more than 260 MHz. Figure 3.1 presents the transmission coefficient ($|S_{21}|$ in dB) of the CSRR sensor when it was used to interact with three different materials: air, an aluminum block without a crack (a reference case), and an aluminum block with a crack. In order to understand qualitatively the response in figure 3.1, a lumped element model derived in [3] can be utilized for modeling a single CSRR excited by a transmission line. Figure 3.2 shows the circuit model of the CSRR sensor where L and C are the per-unit-length inductance and capacitance of the microstrip line, and L_r, C_r, and R_r are the inductance, capacitance, and resistance of the CSRR, respectively. The resonance frequency of the sensor at the transmission zero can be written as [39]

$$f_0 = \frac{1}{2\pi\sqrt{L_r(C_r + C)}} \tag{3.1}$$

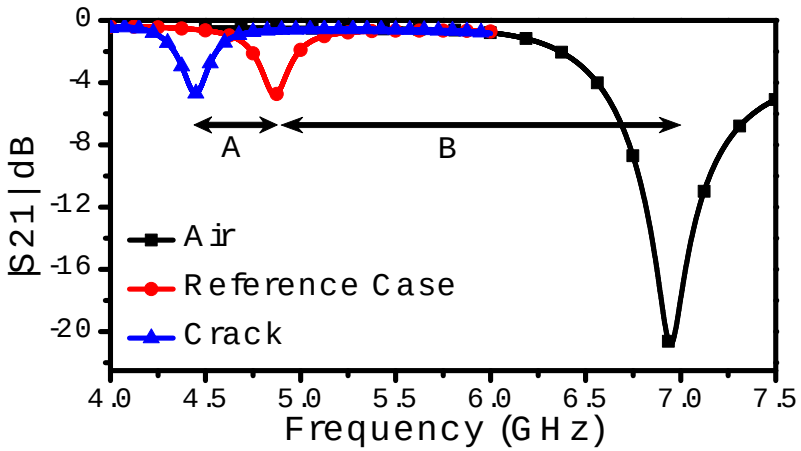

Figure 3.1: Scattering parameter of a 3 mm CSRR proposed in [1, 2] obtained from the full-wave simulation when encountering three different materials: air, an aluminum block without crack (a reference case), and an aluminium block with a crack. The shift B in the resonance frequency is due to a faultless aluminum block. The shift A in the resonance frequency is due to a crack of 0.2 mm in the width and 2 mm in the depth.

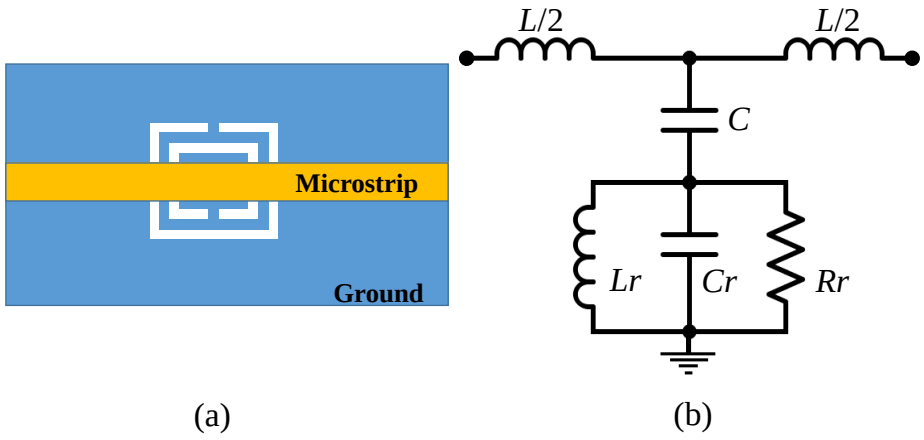

Figure 3.2: (a) A microstrip line used to excite a CSRR (etched in the ground plane) as proposed in [1,2]. (b) The equivalent lumped element model where L and C are inductance and capacitance of the microstrip line, and L_r, C_r, R_r are the inductance, capacitance, and resistance of the CSRR, respectively.

Next, a physics-based model is constructed to understand factors that affect the sensitivity of the CSRR sensor and the class of sensors that are based on removing part of the ground plane in a highly localized area (defect in the ground plane). Figure 3.3 presents a physical multi-layer model of a generic sensor when encountering an aluminium block without a crack (the reference case). By considering the reference planes (1) and (2) shown in figure 3.3, there will be a discontinuity (frequency dependent) in the field caused by the defect (resonator). Note that the discontinuity is frequency dependent. This discontinuity enforces the electric field between the strip line and ground plane to have new distributions in order to satisfy the new boundary conditions, thus creating the displacement current J_{D1}. In addition, in the sensor, two different current densities are developed, J_{D2} representing the effect of the potential difference (related to the electric field distribution) developed between the resonator and the rest of the ground plane, and J_{C3} representing the circulating conduction current density in the resonator. In the region between the sensor and the aluminium block (Teflon region), most of the electric field components will be perpendicular on the surface of the aluminium block, thus creating the displacement current densities J_{D3} while some will be horizontal leading to J_{D4}. The displacement current

J_{D3} will excite a conduction current on the surface of the aluminium block J_{C4}. Based on the circuit model and the physical multi-layer based model presented in figures 3.1 and 3.3, respectively, an equivalent lumped element model can be predicted. Figure 3.4 presents the equivalent lumped element model the for physical multi-layer model shown in figure 3.3. When the sensor encounters a faultless metallic block, a new capacitance, C_b, is created that increases the total capacitance of the sensor. The C_b depends on the surface area of the sensor and the metallic block, the dielectric materials in between, and the standoff distance.

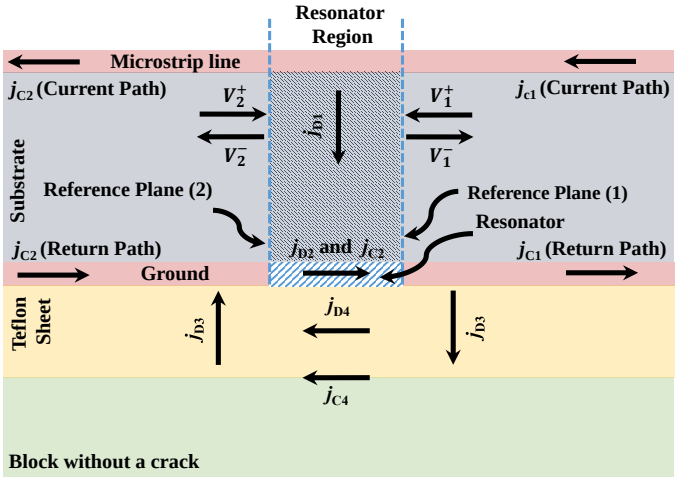

Figure 3.3: The physical multilayer model of a defect based sensor. The resonator region shows the discontinuity region caused by the defect. The disturbance in the electric field distribution in the resonator region is modeled by a displacement current density J_{D1}. J_{D3} models the effect of the electric field distribution between the defect and the aluminum block (through the Teflon layer). J_{C4} is the conduction current density excited by J_{D3} on the metallic surface.

In the case when a crack is present in the aluminium block, figure 3.5 shows the physical multi-layer model with current densities. The model presented in figure 3.5 is similar to the model shown in figure 3.3 except that there are two additional current densities, J_{D5} and J_{C5}, representing the discontinuity caused by the crack. Figure 3.6 shows the equivalent lumped element model for the physical multi-layer model shown in figure 3.5.

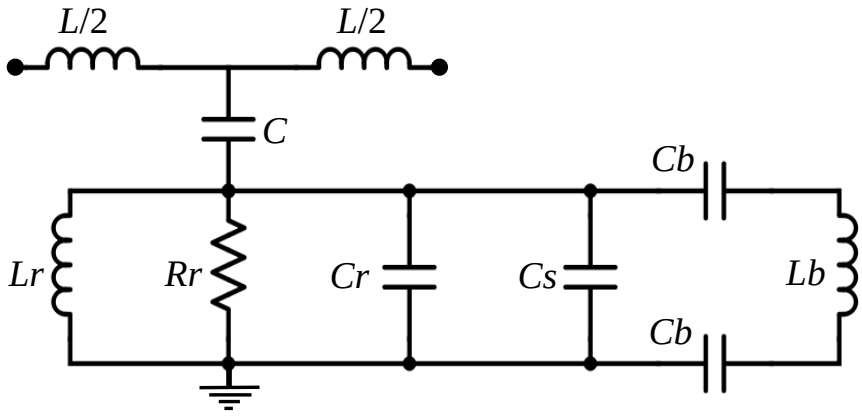

Figure 3.4: The proposed equivalent lumped circuit model for the sensor encountering a faultless block where L and C are the inductance and capacitance of the microstrip line, L_r, C_r, R_r are the inductance, capacitance, and resistance of the defect, respectively. C_b and L_b are the capacitance and inductance, respectively, induced by the presence of the block.

The main objective of the lumped element circuit model in this work is to help understand the factors that contribute to the sensitivity (the resonance frequency shift with respect to the crack width) of the sensor, and, therefore, design new sensors with higher sensitivity. One approach to increase the sensitivity consists of decreasing the capacitance, C_b, between the sensor and the block. This can be obtained by reducing the surface area of the sensor by etching out strips in the area near to the small sensing bridge, not in a random orientation but in the same direction of the current traveling on the small sensing bridge. Without employing systematic optimization, the sensor design shown in figure 3.7 is proposed. Etching out strips as suggested helps to decrease the capacitance, C_b). The orthogonal strips, while also contributing to decrease the capacitance, provide a longer current path, which increases the inductance, thus leading to additional enhancement of the sensitivity.

Without loss of generality, the sensor operates in the vicinity of 8 GHz. The reason behind using this specific frequency comes from the intention to make the comparison between the proposed sensor and the sensors in [1] and [2] having identical footprints (3×3 mm). Generally, the resonance frequency of quasi-static resonators (such as the

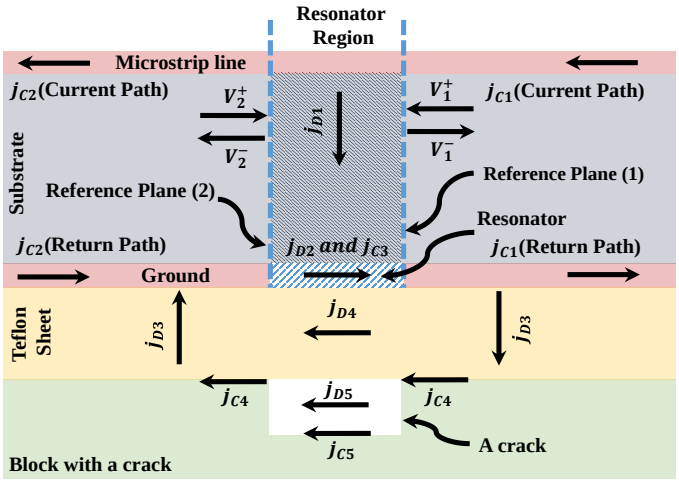

Figure 3.5: The physical multilayer model of a defect based sensor. The resonator region shows the discontinuity region caused by the defect. The disturbance in the electric field distribution in the resonator region is modeled by a displacement current density J_{D1}. J_{D3} models the effect of the electric field distribution between the defect based sensor and the block aluminum (through the Teflon layer). J_{C4} is the conduction current density excited by J_{D3} on the metallic surface. J_{D5} and J_{C5} model the discontinuity effects caused by the crack in the metallic material.

sensor introduced in this work) is proportional to the overall size. For such resonators, the resonance frequency can be found either numerically or experimentally [31, 37, 38]. Here, the design process was based on the Eigenmode solver in ANSYS HFSS. First, a cavity with perfect electric conductor walls was designed in such a way that its resonance frequency was higher than the resonance frequency of the designed resonator but with the larger size so it will not effect the resonance frequency of the resonator. For the dimension chosen, the numerical results of the Eigenmode solver gave a resonance frequency of 8.55 GHz. The dimensions were optimized to achieve this objective (see figure 3.7) resulting in L = 3 mm and S = t = 0.2 mm. It should be emphasized that the sensor can be scaled to operate at other frequencies depending on the size of the targeted crack.

In this work, the MUT, which in our case is the metallic block, was used to determine the reference resonance frequency of the sensor. The frequency shift due to the presence of

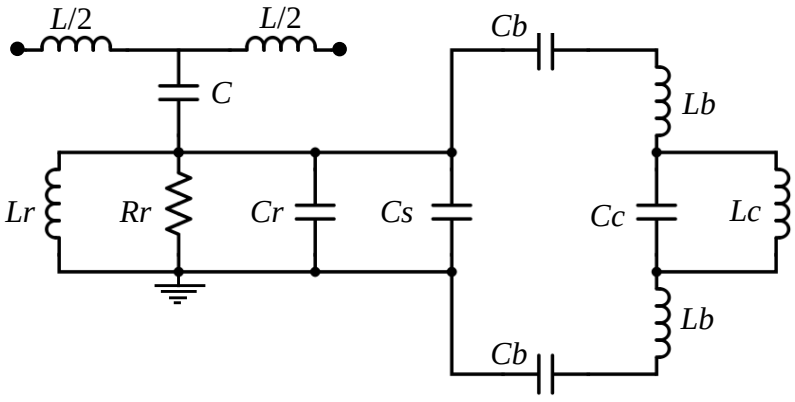

Figure 3.6: The proposed equivalent lumped circuit model for the sensor encountering a crack in a block where L and C are the inductance and capacitance of the microstrip line, L_r, C_r, R_r are the inductance, capacitance, and resistance of the defect, C_b and L_b are the capacitance and inductance, respectively, induced by the block, and C_c and L_c are the capacitance and inductance induced by the crack.

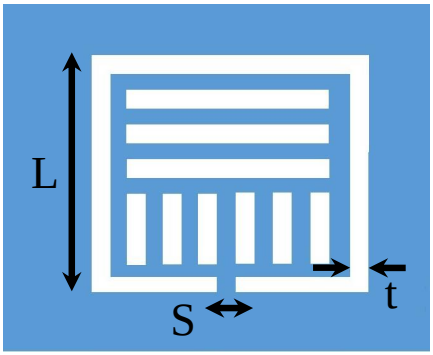

Figure 3.7: The schematic of the sensor proposed in this work. The white areas represent etched-out copper whereas the dark areas (blue in color version) represent copper.

cracks was measured with respect to the reference frequency. Figure 3.8 shows the scanning procedure used to detect surface cracks in metallic materials.

A vector network analyzer (VNA) was used to measure the scattering parameters of the sensor. In the measurement setup, a VNA with an internal impedance of 50 Ω was utilized. To match the VNA used in the measurement procedure, the microstrip line that

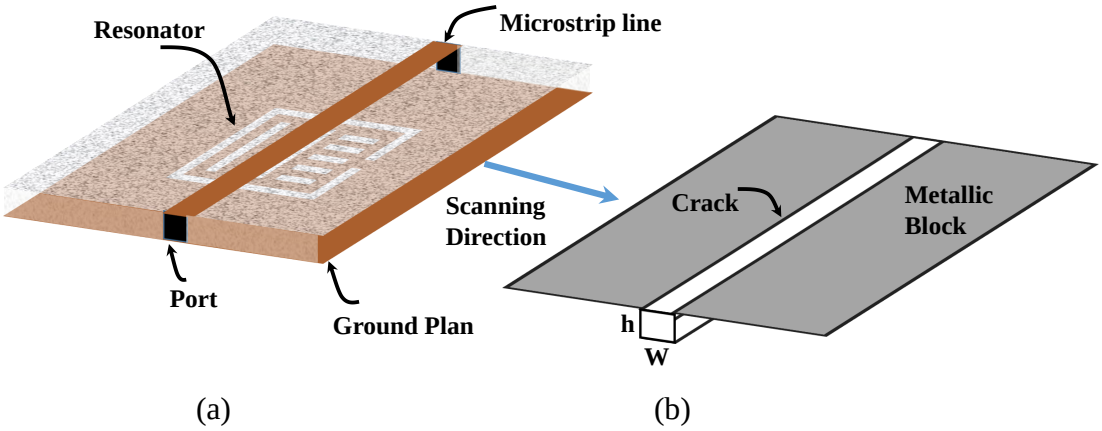

Figure 3.8: The scanning procedure using the proposed sensor to detect a crack in a metallic block. (a) The proposed sensor (the microstrip line and the proposed resonator). (b) The metallic block to be scanned for cracks where w and h are the width and depth of a crack, respectively.

excites the sensor (see figure 3.8) was designed to have a characteristic impedance of 50 Ω. Using Rogers RO4350 substrate with a thickness of 0.75 mm, the relative permittivity of 3.66, a loss tangent of 0.003, a line width of 1.7 mm was required. Figure 3.9 shows the fabricated sensor. Figure 3.10 shows the transmission coefficient of the sensor obtained from measurement and the full-wave numerical simulation. All the numerical simulation results presented in this chapter were obtained using the full-wave numerical simulation package ANSYS HFSS. The strong agreement between the measurement and the numerical simulation in figure 3.10 provides a validation of the numerical simulation, which consequently provides a strong rationale for using the numerical simulation only to test the sensitivity of the sensor over a wide range of crack parameters, as will be demonstrated below.

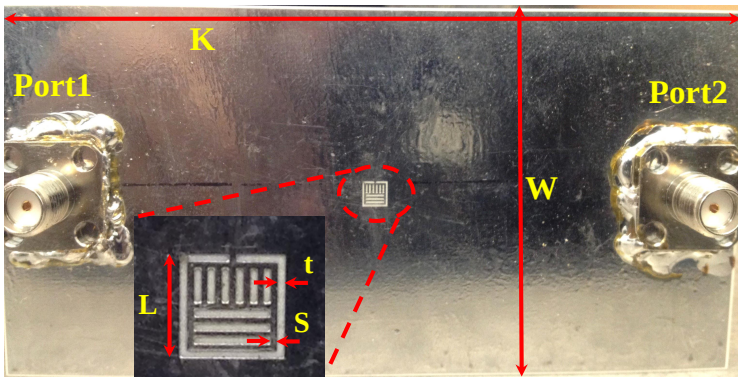

Figure 3.9: The proposed sensor fabricated using printed circuit board technology where L= 3 mm, S=t= 0.2 mm, K= 87.7 mm, and W= 43.8 mm. The microstrip line feeding the sensor is on the other side of the board and thus cannot be seen in the photo.

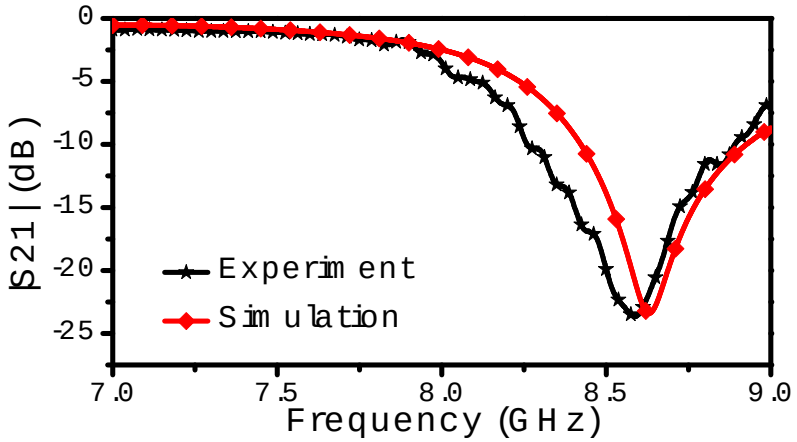

Figure 3.10: Scattering parameter ($|S_{21}|$) response of the proposed sensor obtained from measurement and the full-wave simulation. The sensor is operating in free space without any metallic surface in its close proximity.

3.3 Quantitative Analysis of the Sensitivity of the Proposed Sensor

For testing, the metallic block was covered by a thin dielectric sheet to mimic thin dielectric material such as paint that in practical scenarios might cover the crack. Teflon was considered as the dielectric sheet with a thickness of 0.076 mm (over the frequency range of interest in this work, Teflon has a dielectric constant of 2.1 and loss tangent of 0.001). A block having a surface crack of 200 μm in width and 2 mm in depth was considered. The resonance frequency of the sensor was recorded by placing the metallic block above the sensing element.

Figure 3.11 shows the numerical results of the frequency response of the proposed sensor when encountering three different materials: air, an aluminum block, and an aluminum block with a crack. The aluminum blocks with and without the crack were scanned using the sensor, and the minimum transmission coefficient ($|S_{21}|$) were recorded. A shift in the resonance frequency of more than 1.5 GHz was observed. In addition, the proposed sensor to detect a crack with a width of 10 μm was tested. Figure 3.12 shows the numerical simulation results when the sensor was used to detect a crack of 10 μm in width and 2 mm in depth. Even for such very narrow crack, a shift in the resonance frequency of 180 MHz was realized.

While the new sensor provides dramatic enhancement in the sensitivity as exhibited by a comparatively significant shift in the resonance frequency, the response of the sensor without any MUT is virtually identical to that of a simple CSRR sensor, as shown in figure 3.13. This signifies the importance of designing sensors while incorporating the MUT in the design process.

The increase in the shift in the resonance frequency (sensitivity) was analyzed using two approaches: (1) current density distribution approach, and (2) circuit model approach. It was started by investigating the surface current density distribution on the sensor. Figure 3.14 shows the surface current density distribution on the sensor and the faultless aluminum block at the resonance frequency of 7.7 GHz. Very high current density was observed, with being concentrated in a small region on the aluminum block which identifies

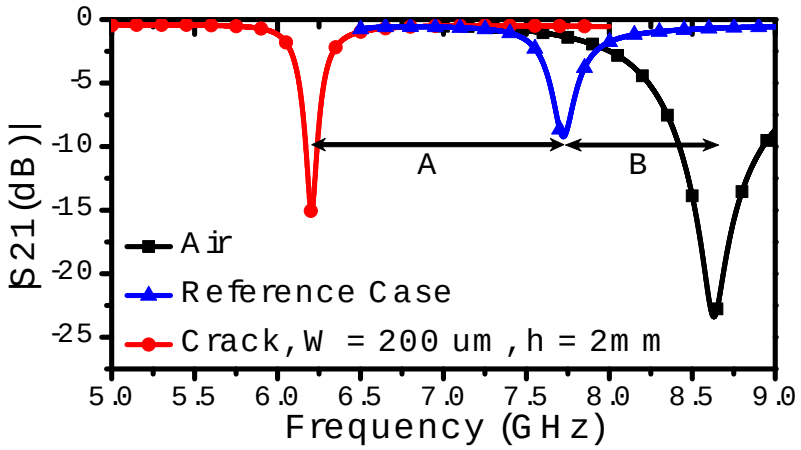

Figure 3.11: The response of the proposed sensor obtained from the full-wave simulation for air, an aluminum block without crack (the reference case), and an aluminium block with a crack. The shift illustrated in the figure as a region B is due to a faultless aluminum block. The shift A is due to a crack of 0.2 mm and 2 mm in width and depth, respectively.

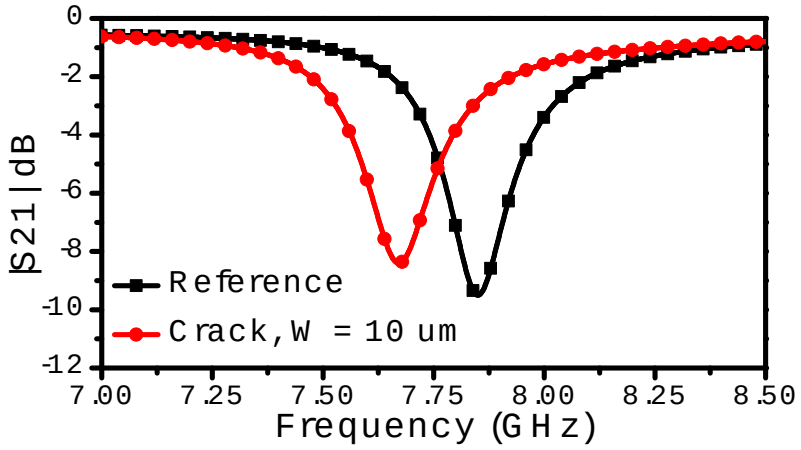

Figure 3.12: The response of the proposed sensor obtained from the full-wave simulation for a crack of 10 μm and 2 mm in width and depth, respectively. The Reference Case is for a faultless aluminum block. The crack resulted in a 180 MHz shift in the resonance frequency.

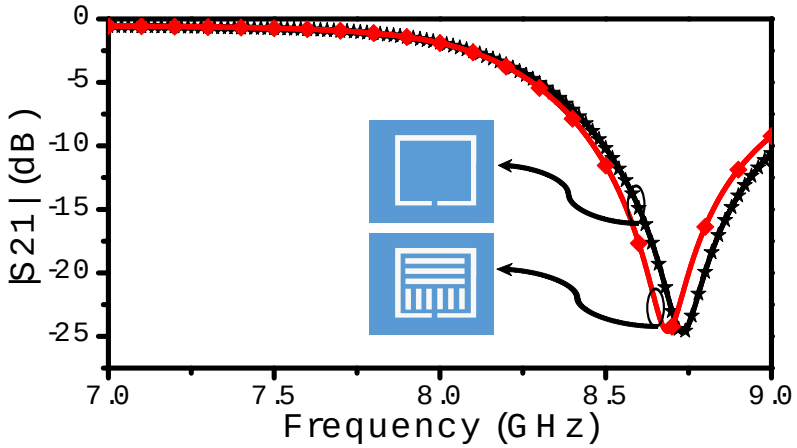

Figure 3.13: $|S_{21}|$ response of the proposed sensor (red curve in the color version) and a simple CSRR sensor (black in the color version) shown in the inset both occupying identical footprint and trace width of 3 mm and 0.2 mm, respectively

the sensing element in the sensor. Figure 3.15 shows the top-side of the surface current density distribution at the resonance frequency on a block with a crack of 0.2 mm in width and 2 mm in depth.

The circuit models (see figures 3.4, 3.6, and 3.2) were validated by extracting their circuit elements (capacitance, inductance, and resistance) and comparing resultant scattering parameters with scattering parameters obtained using HFSS. First, the scattering parameters obtained using HFSS were imported to the circuit simulator (ADS by Keysight). In ADS, the scattering parameters were used to set two objective functions; one for $|S_{21}|$ dB and the other one for $|S_{11}|$ dB. The objective functions were used by the optimization toolbox in ADS to find the optimal value of the circuit elements. After that, the extracted circuit elements were substituted in the circuit models to find the corresponding scattering parameters. For the case of the sensor placed in the free space, the scattering parameters for both the full-wave numerical simulation and circuit model are shown in figure 3.16, which show good agreement. However, the circuit model is only valid near the resonance frequency. In other words, the circuit models are not correct for the whole frequency spectrum. Based on the set objective functions, the optimal value for the circuit elements are L = 0.59 nH, C = 0.25 pF, C_r = 0.6 pF, R_r = 2.2 kΩ, and L_r = 0.36 nH. It can be observed

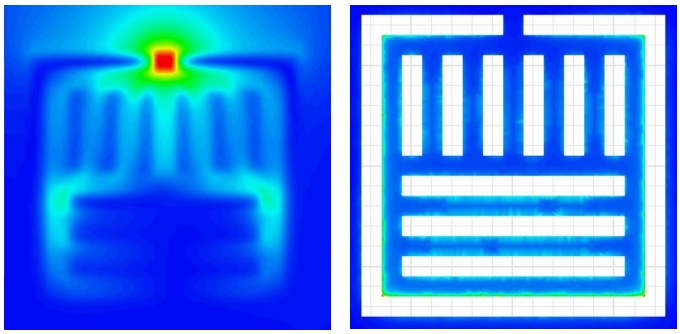

(a) (b)

Figure 3.14: The Simulated surface current density distribution on (a) the faultless aluminum block and (b) the proposed resonator at the resonance frequency of 7.7 GHz. For the current density distribution, the highest red intensity corresponds to 400 A/m, and the highest blue intensity corresponds to 230 uA/m.

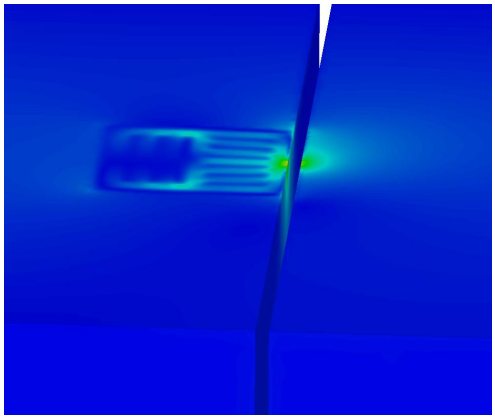

Figure 3.15: Top-side view of the surface current distribution at the resonance frequency of 7.7 GHz on a block with a crack of 200 μm width and 2 mm depth

that at the resonance frequency, the resonator create a large resistance ($R_r = 2.2$ kΩ) that leads to a bandgap apparent in figure 3.16.

For the second case of the sensor encountering a faultless block, the scattering parameters are shown in figure 3.17(a). The extracted optimal value of the circuit elements are

$L = 0.25$ nH, $C = 0.17$ pF, $C_r = 0.47$ pF, $R_r = 0.97$ kΩ, $L_r = 0.39$ nH, $C_s = 0.075$ pF, $C_b = 0.54$ pF, and $L_b = 0.37$ nH. By comparing the extracted circuit elements of the circuit models shown in figures 3.2 and 3.4, it can be noticed that the resistance value of the resonator R_r is reduced from 2.2 to 0.97 kΩ. The effect of this reduction can be observed in terms of rejection level shown in figures 3.16 and 3.17(a). In addition, the strips in the resonator minimize the effect of the capacitance C_b between the metallic block and the resonator. Thus, by comparing the circuit elements in the case of the free space and metal without the circuit elements exhibit small variations, except for R_r, which explains the small shift in the resonance frequency shown in region B in figure 3.11.

Furthermore, to observe the effect of the strips in the resonators, it is needed to extract the circuit elements in the case of metals with a crack and make a comparison between the two cases of the sensor encountering a block with and without a crack. For the third case of the sensor encountering the faulty block with a crack, the scattering parameters are shown in figure 3.17(b). The extracted circuit elements are $L = 0.42$ nH, $C = 0.20$ pF, $C_r = 0.88$ pF, $R_r = 5.24$ kΩ, $L_r = 0.75$ nH, $C_s = 0.18$ pF, $C_b = 4.77$ pF, $L_b = 0.43$ nH, $C_c = 0.43$ pF, and $L_c = 4.79$ nH. The effect of the slots can be noticed by observing the changes in C_r, C_b, and L_r. C_r and C_b exhibit an increase from 0.47 to 0.88 pF and from 0.54 to 4.77 pF, respectively. By consistent with our prediction, an increase in the inductance L_r from 0.39 nH to 0.75 nH can be observed. For all cases, strong agreement between the circuit model and the scattering parameters can be observed. It has been noticed that the slight differences between the circuit model and the full-wave simulation results can be attributed to the fact that the circuit models did not take into account radiation losses and coupling between the elements in the circuit models. Furthermore, the experiment result (see figure 3.20) shows that the sensitivity of the sensor to detect the presence of a faultless block is reduced. This was expected since the slots in the sensor will reduce the effective capacitance (C_b) between the sensor and the block. On the other side, the slots in the sensor help to increase the sensitivity to detect cracks in metals due to the increase in the value of L_r, C_r, and C_b. Thus, the sensitivity and dynamic range of the sensor to detect the cracks were enhanced.

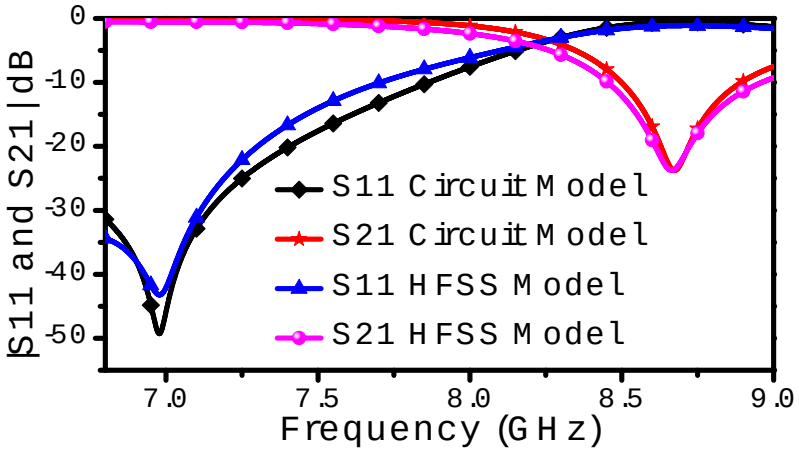

Figure 3.16: The response of the proposed sensor obtained using the full-wave simulation and the circuit model for the case of the sensor present in the air without any metallic surface in its close proximity.

3.4 Numerical Study of the Effect of the Sensor Orientation

Although the sensitive region shown in figure 3.14 that gives the maximum shift in the resonance frequency is utilized to detect a crack in a metallic material, the direction of the crack with respect to the sensor topology plays an important role in the detection. To study the effect of different orientations, a crack in two-different directions (x and y) was scanned. The scanning step in each direction is 0.2 mm. Figures 3.18 and 3.19 show the numerical results for the scans in the x and y directions. These results clearly show that the sensor is not sensitive when scanned in the x direction but very sensitive when scanned in the y direction. In fact, maximum sensitivity when scanned in the y direction was observed at y = 1.4 mm (see figure 3.19). Notice that y =1.4 mm corresponds to the location of the bridge having the high-density current shown in figure 3.14.

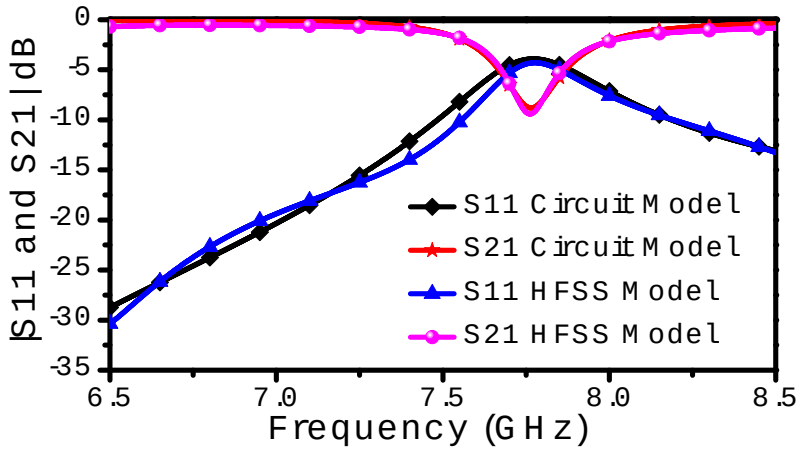

(a)

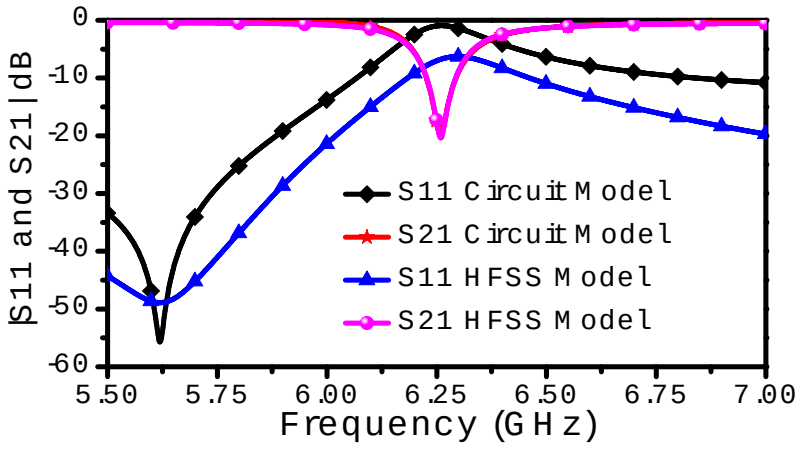

(b)

Figure 3.17: (a) The response of the proposed sensor obtained from the full-wave simulation and the equivalent circuit model (figure 3.4) for the reference case (sensor positioned next to a block without a crack) and (b) Response of the proposed sensor obtained from the full-wave simulation and the equivalent circuit model (figure 3.6) for the case of the sensor in the presence of a block with a crack of 200 μm and 2 mm in width and depth, respectively.

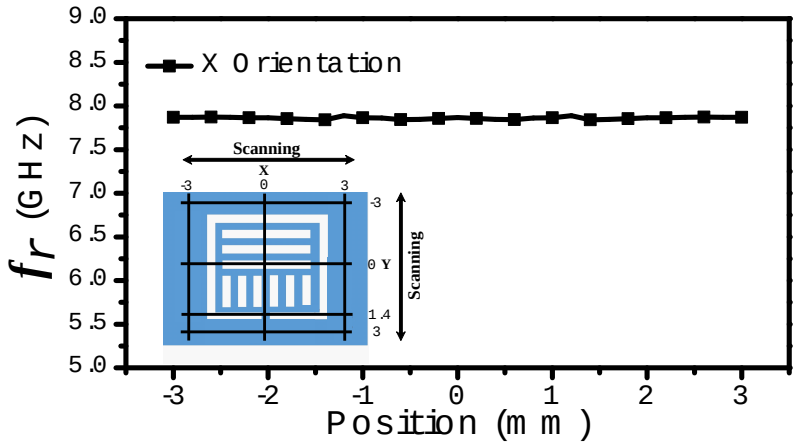

Figure 3.18: The resonance frequency of the sensor for scanning the crack in the x direction

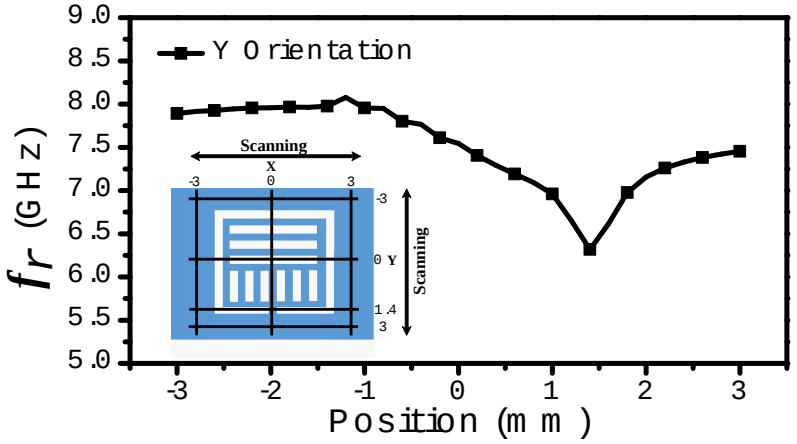

Figure 3.19: The resonance frequency of the sensor for scanning the crack in the y direction

3.5 Experimental Study

Aluminum blocks with and without a crack were fabricated to validate the sensitivity of the sensor. A block having a surface crack of 200 μm in width and 2 mm in depth was considered. (Due to fabrication limitation and cost, cracks having width below 200 μm were not available for testing). Figure 3.20 shows the experimental results of the sensor where a shift of more than 1.8 GHz was achieved. It can be noticed that a difference between the resonance frequencies obtained from simulations and measurements. This discrepancy can be analyzed by studying the effect of the standoff distance (air gap between the sensor and the sample) on the resonance frequency. By using the numerical simulation, the stand-off distance was varied from 0 to 0.05 mm in steps of 0.002 mm for a block with and without a crack. Figure 3.21 shows the numerical simulation results for the dependence of the resonance frequency on the standoff distance. These results indicate that in real-world applications, the standoff distance needs to be maintained constant throughout the testing process.

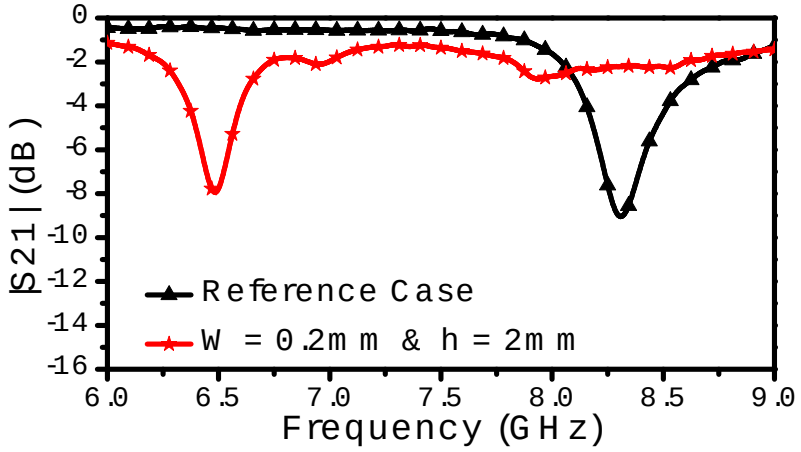

Figure 3.20: The measured performance of the proposed sensor.

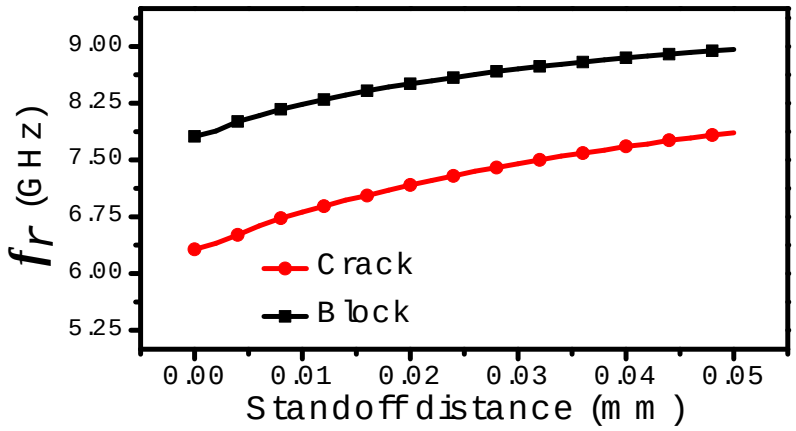

Figure 3.21: The numerical simulation showing the resonance frequency shift versus the standoff distance for the cases of an aluminum block with and without a crack of 200 μ m wide and 2 mm deep scanned by the sensor. The standoff distance was varied from 0 to 0.05 mm in steps of 0.002 mm.

3.6 A Numerical Study of the Sensitivity of the Sensor to Width and Depth

To evaluate the sensitivity of the sensor for crack detection, a numerical study was conducted where the width of the crack was varied over the range 0 to 0.2 mm while keeping the crack depth fixed at 2 mm. Another study was conducted where the crack depth was varied over the range 0 to 3 mm while keeping the crack width constant at 0.2 mm. The change and shift in the resonance frequency for both cases are shown in figures 3.22. It can be observed that the change in the resonance frequency and its shift from the reference, for the case of varying crack depth, while keeping the width a constant, has strong exponential behavior. These results provide guidelines to use the proposed sensor when the primary objective is gauging a crack depth for a crack with fixed width. In particular, figure 3.22(b) shows that if the objective were to gauge the depth of the crack (for a crack width of 0.2 mm), the sensitivity to differential different crack depths (not width) decreases substantially beyond a crack depth of 2 mm.

In comparison to the performance of the CSRR sensors proposed in earlier work [2],

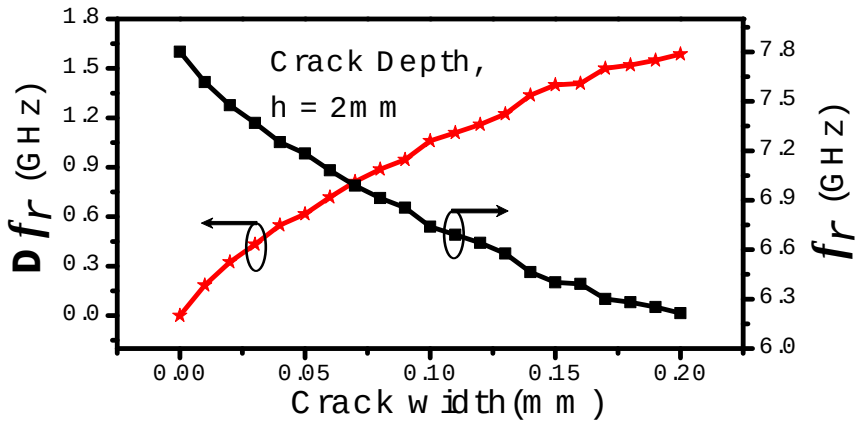

(a)

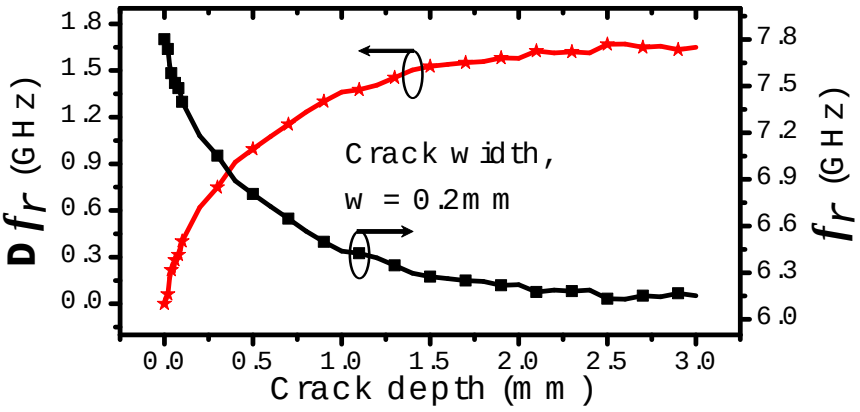

(b)

Figure 3.22: (a) The shift in the resonance frequency and resonance frequency of the sensor as a function of the crack width. (b) The shift in the resonance frequency and resonance frequency of the sensor as a function of the crack depth.

the sensor proposed here shows a substantial improvement in the sensitivity. For the case analyzed in both works (this work and [2]), namely, a crack with 0.2 mm in width and 2 mm in height, the sensor in this work gave a resonance frequency shift of 1.8 GHz which is more than 6 times higher than the resonance frequency shift realized by the CSRR sensor (of 275 MHz). Based on the numerical simulation, a more comprehensive comparison between the two sensors is presented in figures 3.23(a) and 3.23(b), which show the shift in the resonance frequency versus the width and depth, respectively.

3.7 The Sensor as Near-Field Scanning Microscopy: Crack Imaging

In the near-field scanning microscopy, the spatial resolution depends on the size of the probe. Although the size of the CSRR is 3 mm, the sensor is able to detect micro-cracks, 200 μm. With the strips etched out in the center island of the CSRR, the small bridge (S) is the probe, not the whole CSRR. Figure 3.19 shows that the sensor has a high spatial resolution, where the shift in the resonance frequency is the minimal around the position of the crack in the y direction (1.4 mm). In addition, the resolution of the probe depends on the stand-off distance (0.0762 mm in our case). To investigate the effect of the stand of distance, the thickness of the teflon sheet is varied from 0.0762 to 2 mm with the step value of 0.08 mm. Figure 3.24 shows the shift in the resonance frequency versus the thickness of the teflon when the sensor is utilized to detect the presence of a crack with the width and the depth of 200 μm and 2 mm, respectively. Up to 0.88 mm, the sensor is able to detect the presence of the cracks with the shift in the resonance frequency of 50 MHz.

However, since the sensitivity is related to the shift in the resonance frequency, other parameters that play important roles in determining the resolution have to be investigated. From figure 3.14, it is clear that the current surface distribution is highly concentrated in an area equivalent to the size of the S (0.2×0.2 mm). The concentrated surface current in the smaller area can be attributed to be one of the important parameters that can be utilized to investigate the resolution. Thus, it is expected that the sensor will not only detect the crack, but it will also detect with high resolution. In addition, based on the

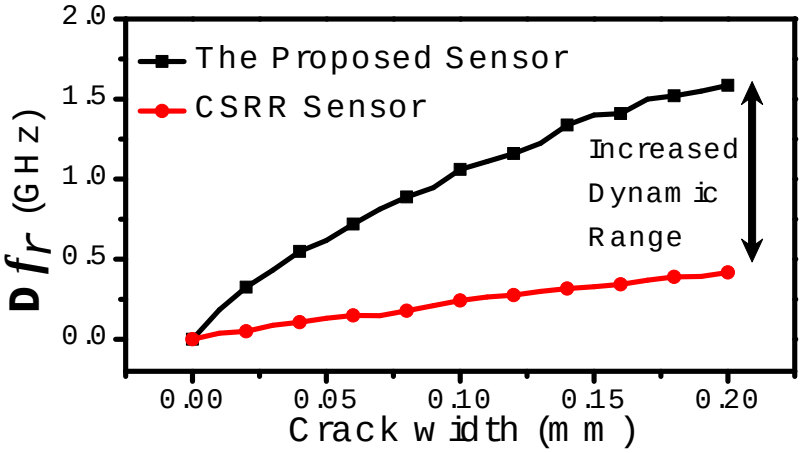

(a)

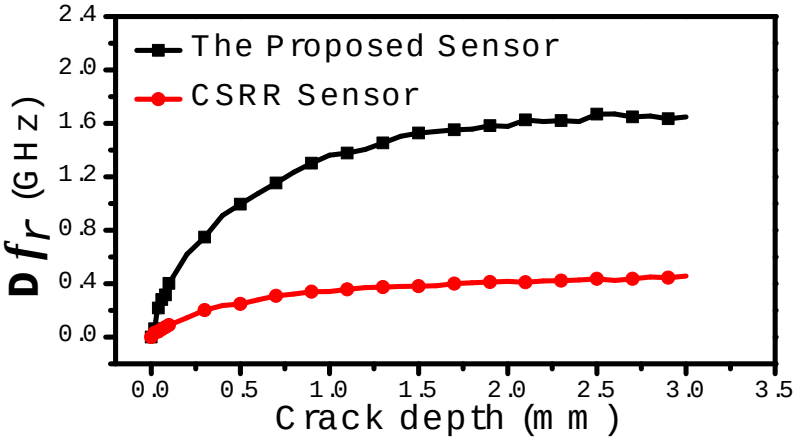

(b)

Figure 3.23: (a) The shift in the resonance frequency as a function of the crack width for the sensor proposed in this work and the CSRR sensor in [1]. (b) the shift in the resonance frequency as a function of the crack depth for the sensor proposed in this work and the CSRR sensor in [1].

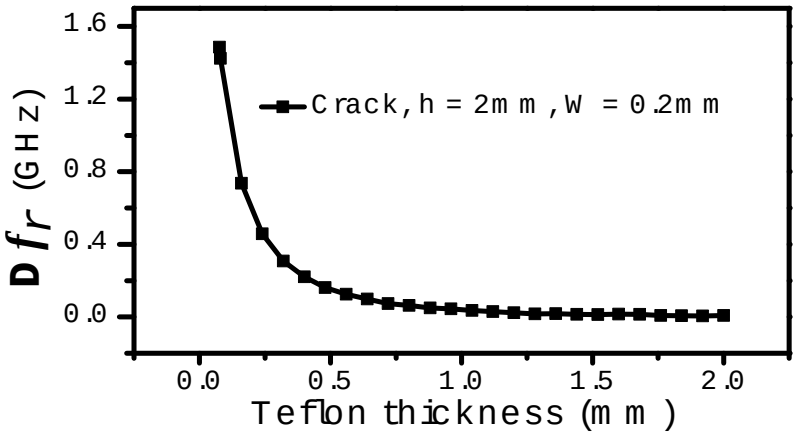

Figure 3.24: The shift in the resonance frequency versus the teflon thickness (varied from 0.0762 to 2 mm) when the sensor is utilized to detect the presence of a crack with the width and the depth of 200 μm and 2 mm, respectively

sensitivity analysis in chapter 2, the sensitivity of the CSRR is a function of the length (L). Thus, it is expected that the surface current distribution on the faultless metallic cause by the interaction with the sensor will have higher magnitude. Figure 3.25 shows the spatial variation of the surface current distribution on the aluminum slab with the teflon thickness of 0.0762 mm. The length of the CSRRs is 3 (our sensor) and 3.4 mm. Changing the length by 13.33 % enhances the magnitude of the current (in the area of the sensing element, the small bridge), with 2.73 % enhancement.

Furthermore, the total electric and magnetic field can be investigated, where the field can be numerically calculated on the surface of the faultless aluminum along the dotted line shown in figure 3.26). The magnetic field distribution along the line is calculated where the thickness of the teflon is varied from 0.0762 to 0.5 mm. Fig 3.27 shows that the spatial variation of the total magnetic field, which explains the underlying reason for the high resolution of the resonator. The spatial variation of the magnetic field (the resolution) is diminished with the increase in the stand-off distance (the teflon thickness). It is worthwhile to plot the spatial variation of the total electric field as well since both fields (magnetic and electric) can help to understand the expected high resolution of the sensor. Figure 3.28 shows the spatial variation of the electric field along the line shown in

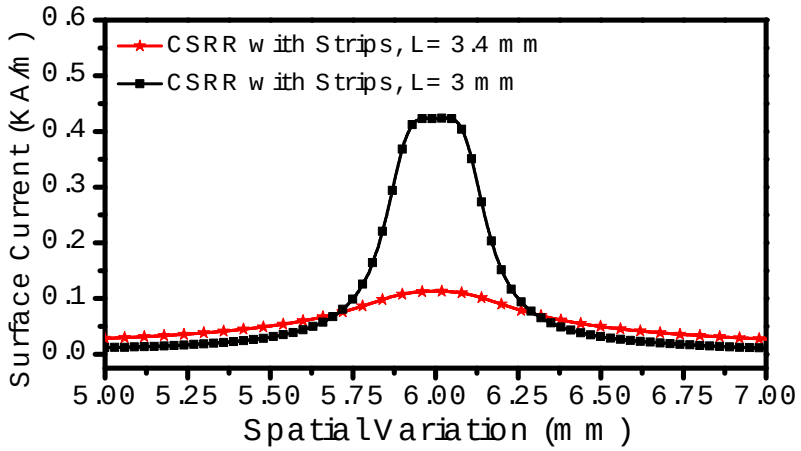

Figure 3.25: The spatial variation of the surface current distribution at the teflon thickness of 0.0762 mm, where the length of the resonator is 3 and 3.4 mm

figure 3.26. This is another evidence that the stand-off distance plays an important role in determining the resolution of near-field microscopy based techniques as explained earlier in figure 1.6.

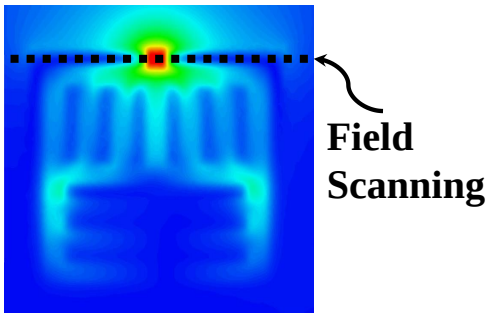

Figure 3.26: The scanning field line, where the electric and magnetic field will be calculated on the surface of the faultless aluminum

Since the CSRR with strips has high sensitivity and resolution, the sensor can be used to image a finite crack (limited length) in metallic materials. To test the idea, an aluminum slab with the thickness of 3 mm, length and width of 15 mm was designed. The crack has the following design specification: the width of 200 μm, depth of 2 mm, and length of 3 mm. The thickness of the teflon (the stand-off distance) is 0.0762 mm. The surface

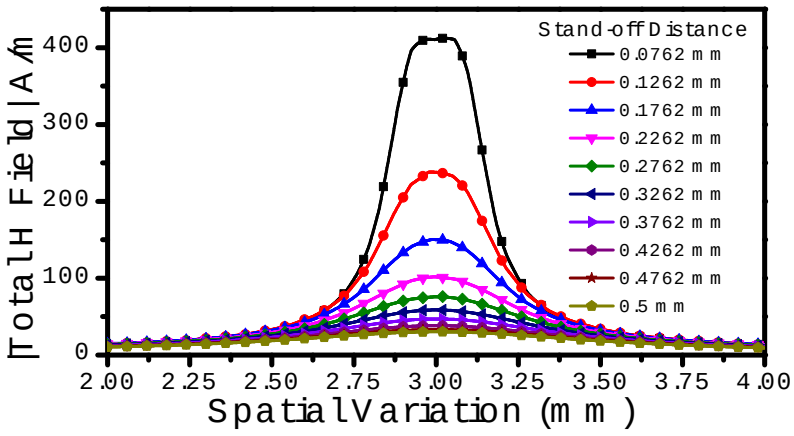

Figure 3.27: The spatial variation of the magnetic field at different distances from the sensors (the teflon thickness)

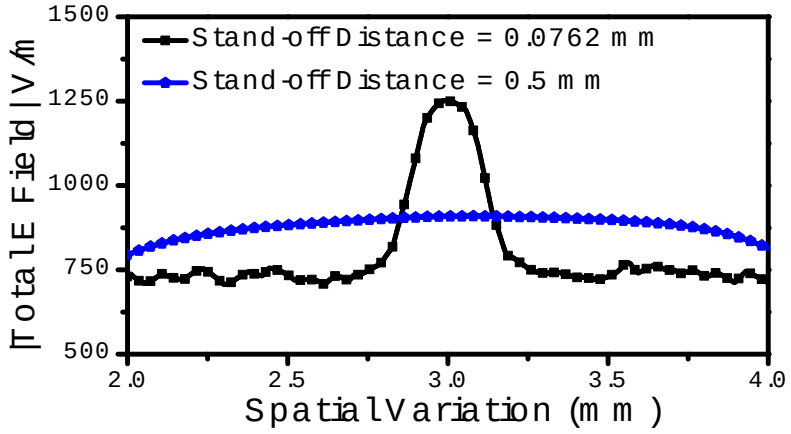

Figure 3.28: The spatial variation of the electric field at two stand-off distance = 0.0762 and 0.5 mm

scanning is in y and x plane with 1406 scanning point(38×37 pixels). Observing the shift in the resonance frequency is the underlying sensing mechanism. The shift in the resonance frequency where there are no cracks is the reference points and will be used to normalize the data between 1 and 0. 1 is for the maximum shift whereas 0 is for the minimum shift in the resonance frequency. For processing the information, the raw data can be brought to

any numerical computing program, MATLAB in our case. Figures 3.29 and 3.30 show the images of raw and interpolated data (for smother edges), respectively. From figure 3.29, one can notice a gradient blue color far from the crack. It can be explained by observing the change in the resonance frequency as shown in figure 3.19 that the scanning in y direction is not symmetrical.

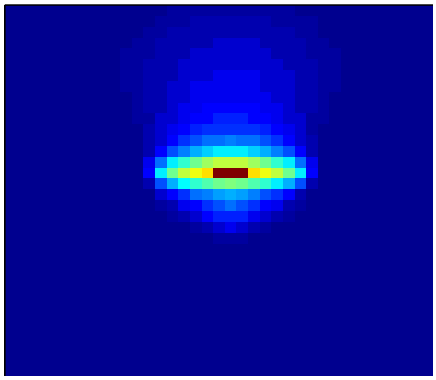

Figure 3.29: The image of the raw data of the scanned crack on the surface of metallic materials

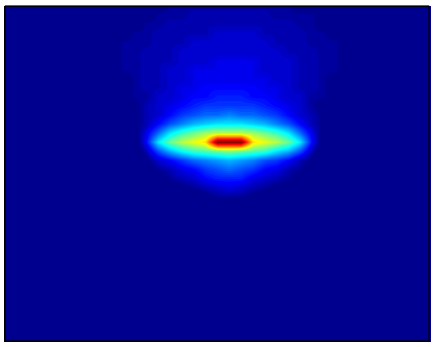

Figure 3.30: The image of the interpolated data of the scanned crack on the surface of the metallic material

3.8 Sensitivity Enhancement Utilizing Strips and Larger Gaps

In chapter 2, the sensitivity of the resonance frequency of the complement structures such as CSRRs with respect to the gap (b) was analyzed. One can design sensitive sensors by increasing the gap, hence, the capacitance (C_r). By increasing the gap and utilizing the strips etched in the ground plane, it is expected that the sensitivity of the CSRR will be further enhanced to detect micro-cracks in metallic materials. The increase in the sensitivity is crucial for increasing the dynamic range of the sensor to be able to detect smaller cracks. However, there is a constraint regarding the size of the small bridge (S). Since the CSRR is designed for the near-field scanning microscopy and the resolution is related to the size of the probe, the small bridge (S) needs to be kept small (0.2 mm). Thus, the length of the resonator (L) and the size of the small bridge (S) will be kept the same, 3 mm and 0.2, respectively. Taking into account the constraint, the final schematic of the proposed unit cell is presented in figure 3.31.

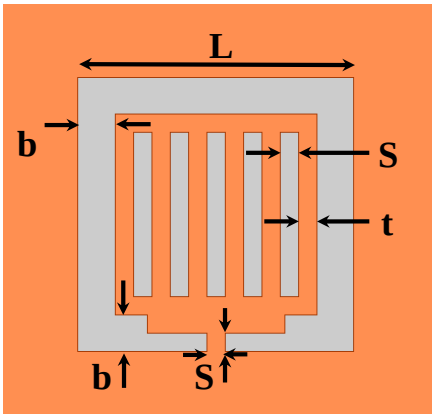

Figure 3.31: The schematic of the sensor where L = 3 mm, S = t = 0.2 mm, b = 0.4 mm

With the modification in the topology, the resonance frequency of the CSRR is increased from 8.687 GHz to 9.889 GHz. Note that based on the result presented in figure 3.13, the increase in the resonance frequency is only due to the increase in the gap (b), hence, lower C_r. In addition, the strips play important roles in the presence of the metallic materials.

Figure 3.32 shows the response of the sensor, where L = 3 mm, and b = 0.2 mm and 0.4 mm. It worth noticing, as predicted by equation (2.5), that quality factor is decreased from 33.15 to 25.02 with the increase in the b (lower C_r).

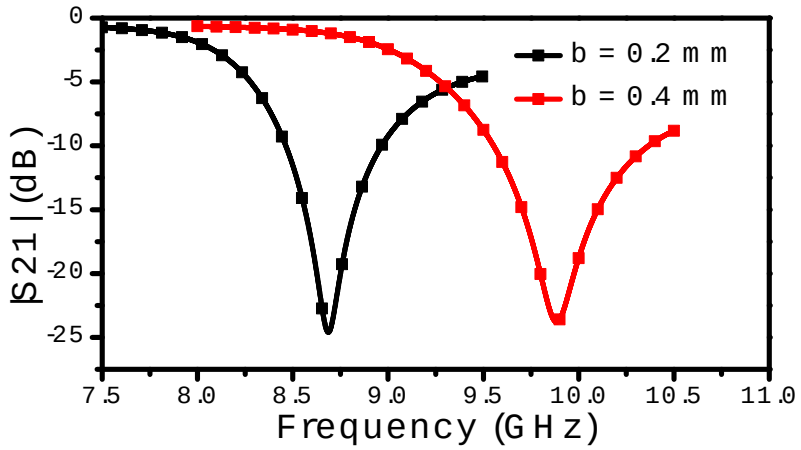

Figure 3.32: The response of the sensor L = 3 mm and b = 0.2 and 0.4 mm

The sensor is tested to detect a surface crack in metallic materials using the numerical simulation, HFSS. With a crack with the width of 200 μm and depth of 2 mm. Figure 3.33 shows the response of the sensor when is utilized to detect the presence of the crack, with the shift in the resonance frequency of almost 2 GHz. Compared to 1.5 GHz (the sensor with b = 0.2 mm), the sensitivity is enhanced with 33.33 %. Furthermore, the sensor is tested to detect the presence of the crack when the crack thickness and depth are varied. Figure 3.34(a) shows the resonance and the shift in the resonance frequency of the sensor where the depth of the crack is fixed to 2 mm and the width is varied from 0 to 0.2 mm, whereas figure 3.34(b) shows the resonance frequency and the shift in the resonance frequency of the sensor where the width of the crack is fixed to 0.23 mm and the depth is varied from 0 to 3 mm. To characterize the enhancement in the dynamic range of the sensor when detecting the changes in the crack width (figure 3.35(a)) and depth (figure 3.35(b)), the CSRR without strips (b = 0.2 mm), CSRR with strips (b = 0.2 mm), and CSRR with strips (b = 0.4 mm) are compared together. Figure 3.35(a) proves that the dynamic range of the sensors with strips and b = 0.4 mm is enhanced. This enhancement is essential to detect smaller cracks. Thus, the sensor is utilized to detect the presence of a crack with

the width of 10 μm and depth of 2 mm. The shift in the resonance frequency is 200 MHz. Compared to the CSRR (strips and b = 0.2 mm), the enhancement in the sensitivity with b = 0.4 mm is 11.11 %.

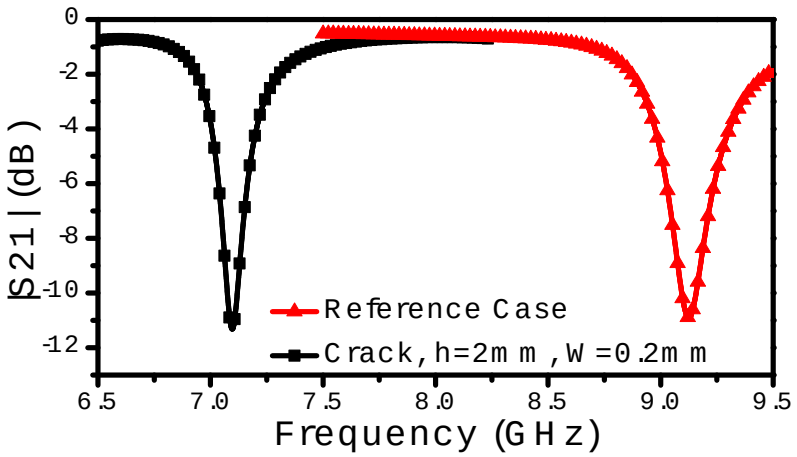

Figure 3.33: The response of the sensor using the numerical simulation, HFSS.

Since the CSRRs can be utilized to design near-field scanning microscopy, the new CSRR with the strips and the gap (b = 0.4 mm) are compared to the CSRR with strips and b = 0.2 mm with respect to the magnitude of the total magnetic and electric field variation on the aluminum slab, where the thickness of the teflon is 0.0762 mm. Figures 3.37 and 3.38 show the total magnetic field and electric field. It is clear that the increase in the magnitude of the magnetic and electric field is the underlying reason for the increase in the sensitivity to detect the presence of the crack (W = 200 μm and h = 2 mm) with enhancement in the shift in the resonance frequency from 1.5 to 2 GHz.

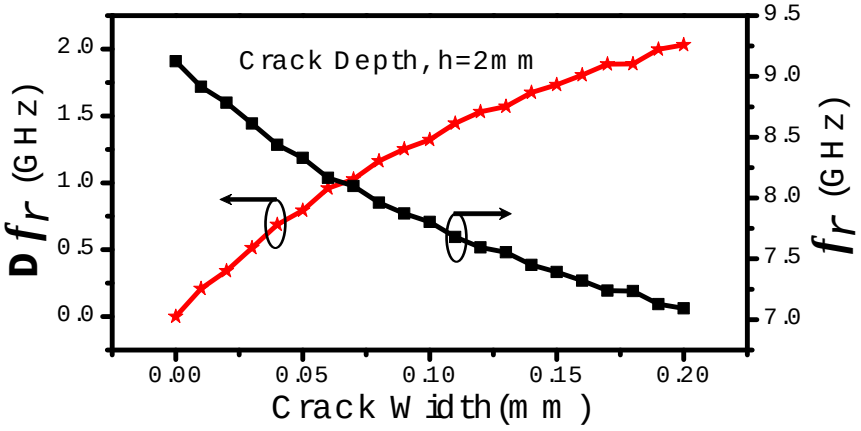

(a)

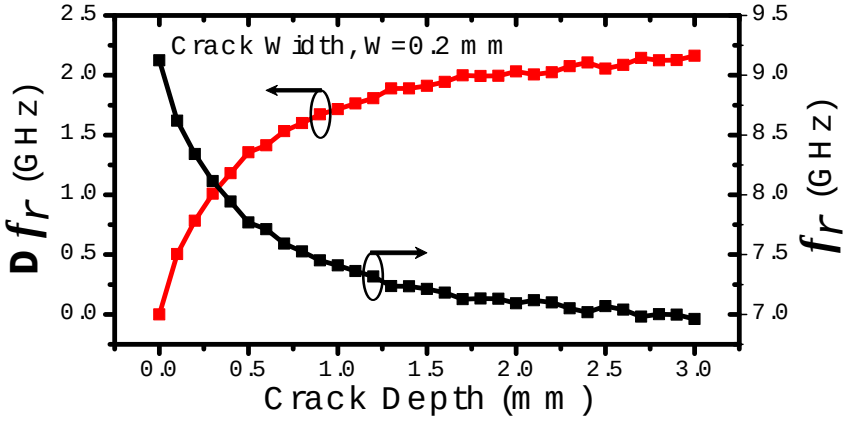

(b)

Figure 3.34: (a) The shift in the resonance frequency and resonance frequency of the sensor as a function of the crack width. (b) The shift in the resonance frequency and resonance frequency of the sensor as a function of the crack depth.

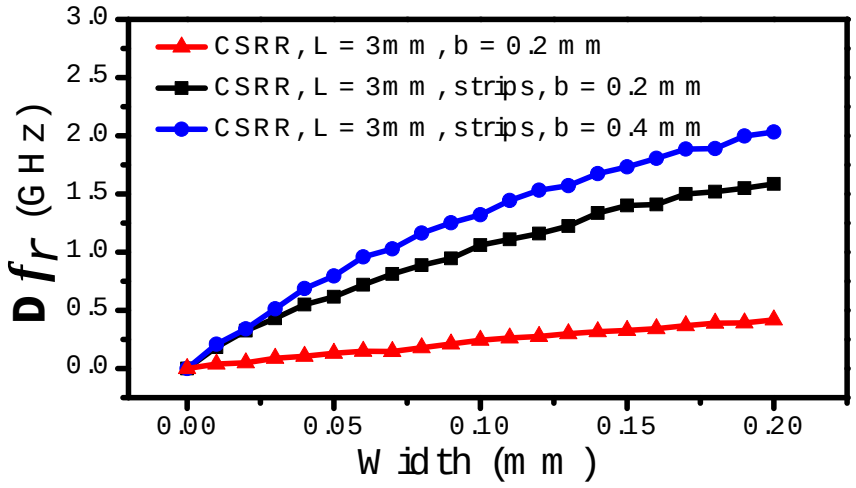

(a)

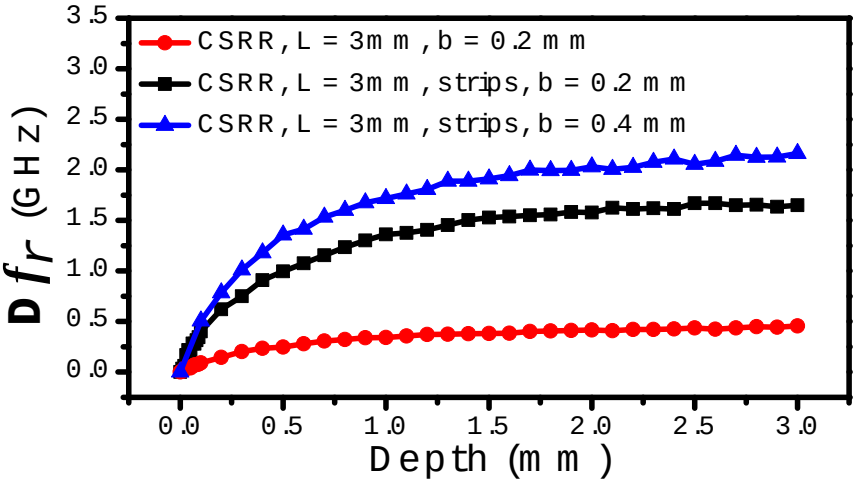

(b)

Figure 3.35: (a) The shift in the resonance frequency as a function of the crack width (fixed depth of 2 mm) for three cases: CSRR, L = 3 mm, b = 0.2 mm, CSRR, L = 3 mm, strips, b = 0.2 mm, and CSRR, L = 3 mm, strips, b = 0.4 mm (b) Shift in the resonance frequency as a function of the crack depth (fixed width of 0.2 mm) for for three cases: CSRR, L = 3 mm, b = 0.2 mm, CSRR, L = 3 mm, strips, b = 0.2 mm, and CSRR, L = 3 mm, strips, b = 0.4 mm

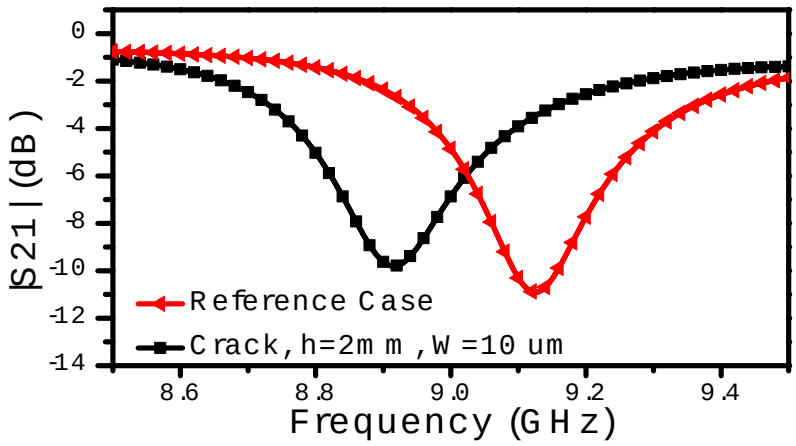

Figure 3.36: The response of the proposed sensor obtained from the full-wave simulation for a crack of 10 μm and 2 mm in width and depth, respectively. The Reference Case is for a faultless aluminum block. The crack resulted in a 200 MHz shift in the resonance frequency.

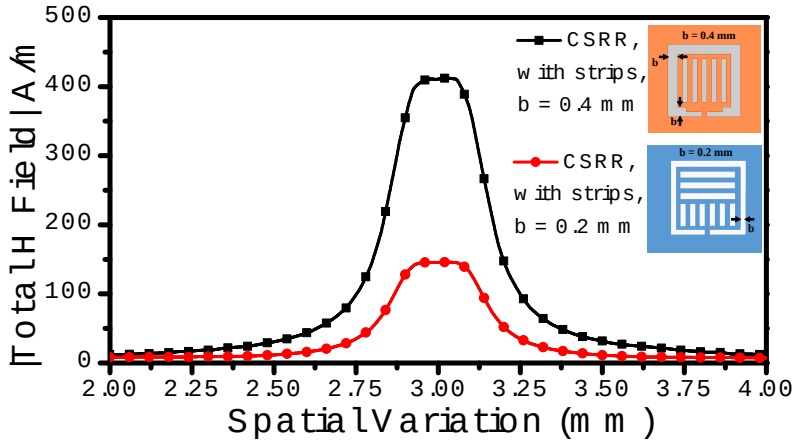

Figure 3.37: The spatial variation of the magnetic field at the stand-off distance = 0.0762 mm

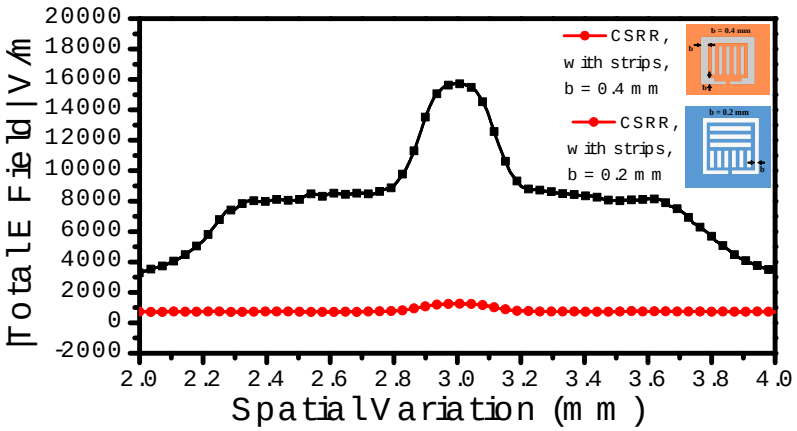

Figure 3.38: The spatial variation of the electric field at the stand-off distance = 0.0762 mm

3.9 Conclusion

In this chapter, a new near-field microwave sensor based on a ground plane defect was presented . The sensor was designed based on a physics based model in order to increase the overall effective capacitance and inductance of the sensor. The entire sensor was fabricated using inexpensive and readily available printed circuit board technology. The full-wave simulation was used in the design process with laboratory measurements used for full validation. For a crack width of 200 μm and depth of 2 mm, the sensor achieved a resonance shift of 1.8 GHz, which is significantly higher than what was achieved by any other microwaves sensor, including the highly sensitive CSRR sensor, operating in the low microwaves regime. The ultra high sensitivity of the sensor makes it a strong candidate for the detection of sub-millimeter size cracks, and also for other applications such as material sensing and characterization including the crack detection in dielectric materials.

Chapter 4

Detection of Surface Cracks in Dielectric Materials Using CSRRs

4.1 Introduction

Dielectric material based composites such polymer composites have been utilized in the space industries, aerospace and automotive. The composites can undergo harsh environmental conditions causing mechanical, thermal and chemical damages [49]. The damages can cause the composites based structures to develop macro and microscopic cracks. Thus, inspection for surface and subsurface cracks in non-metallic materials (dielectric materials) is critical for quality assessment and maintenance. Electromagnetic fields in the microwave regime can penetrate and interact with dielectric materials, provided that the permittivity of the media is not excessively high.

Several microwaves techniques for crack detection in non-metallic materials have been reported. In [50], an open-ended waveguide antenna was used to detect flaws (holes) ranging in diameters from 0.025 and 0.59 mm in ceramic materials (Si_4N_4) used in fabricating gas turbines. Since the technique in [50] is based on the far field, which is based on reflection and refraction, the perturbation in the size of the defects or anomalies in the MUT needs to be proportional to the wavelength, thus requiring operation in the W band (75

GHz to 110 GHz). Such operation frequency makes the measurement setup expensive and complex.

To overcome this problem, microwave near-field techniques were introduced to detect cracks in non-metallic materials. Near-field techniques are dependent on the evanescent type of fields having effective wavelengths much higher than the wavelength in free space, which makes detection of particles having sub-wavelength features possible. In [51], an open-ended waveguide, similar to the one reported in [12], was used to detect cracks in cement-based materials where the basic detection principle is the complex interaction between the near field at the end of the waveguide and the MUT. To the best knowledge of the author and based on the available literature, the available detection techniques for crack detection in non-metallic materials have at least one of the following challenges: (1) working at a relatively high frequency; (2) requiring a complex measurement setup; (3) a relatively high manufacturing cost; (4) low sensitivity; and (5) low resolution.

In [1], a method for sub-millimeter surface cracks in metallic material based on the near-field microscopy technique using a CSRR was introduced for the first time and was validated experimentally. The technique used a CSRR as a sensor, which was able to detect sub-millimeter surface cracks with a resolution of $\lambda/600$ and to resolve two adjacent cracks separated by 1 mm. A recent paper by Taehwa *et al.* [52] used the same CSRR reported in [1] for crack detection in metallic material, but with a substrate integrated waveguide (SIW) for excitation. Although the strips, presented in chapter 2, increases the sensitivity to detect defects in metallic materials, the strips do not affect the sensitivity in the case of dielectric materials as shown figure 3.13.

In this chapter, a planar CSRR sensor for crack detection in non-metallic materials is proposed. First, design formulae that can be used by engineers and scientists to easily design CSRR sensors and predict their resonance frequencies are introduced. The total electric field distribution as the underlying physical mechanism behind the CSRR sensor for dielectric materials is investigated. It can be shown that the CSRR sensor is effective, not only for sensing cracks in metallic surfaces [1], but also non-metallic material, such as fiberglass, plastics, carbon fibers, amongst other dielectric materials that are increasingly used in aircraft structures and high-performance applications.

4.2 CSRRs as a Near-field Sensor for Dielectric Materials

Quasi-static resonators are designed such that the resonators' structures are electrically small compared with the electromagnetic field wavelength of the excitation source. The resonance phenomenon in quasi-static resonators is based on the effective tightly-distributed capacitance and inductance of the structure, unlike resonators of dimensions comparable to the wavelength, where the resonance phenomenon is based on phase propagation. Several works provided circuit models for CSRRs [37, 39, 53]. Generally, the resonance frequency can be formulated as follows:

$$f_0 = \frac{1}{2\pi\sqrt{L_r C_r}} \tag{4.1}$$

where L_r and C_r are the inductance and capacitance of the resonator, respectively. There have been many designs used to realize quasi-static resonators, where loops create current circulations that directly contribute to the effective inductance and gaps affect the net capacitances. Examples include SRRs [21], spiral resonators [3] and Hilbert curves [54]. Like SRRs, CSRRs are quasi-static resonators that were originally conceived of based on Babinet's principle. The CSRRs can be designed by creating the complement of the SRR, whereby copper is replaced by air and *vice versa*. Strictly speaking, the CSRR etched on a substrate is semi-complementary to the SRR due to the presence of the dielectric substrate essential for the construction of the sensor. At the resonance frequency of a resonator, the electric and magnetic energy densities are enhanced significantly at certain locations in close proximity of the resonator [21]. Any disturbance of the electromagnetic fields around the resonator causes the resonance frequency to shift.

When the electrodynamic near field of a resonator is disturbed due to the presence of either new material or deformation (such as topological anomalies) in the original material, the resonance frequency exhibits a shift that can be used as a signature for detection or for characterizing the new environment in general. In this chapter, CSRR excited by a microstrip line as a near-field sensor was used. Figure 4.1 shows a CSRR sensor that is used to detect defects in non-metallic surfaces, such as cracks. The sensor is a planar CSRR excited by a microstrip line, which produces an electric field perpendicular to the surface

of the sensor. The sensor has a conducting center island surrounded by a conducting plane that connects the center island through two narrow bridges, as shown in figure 4.2.

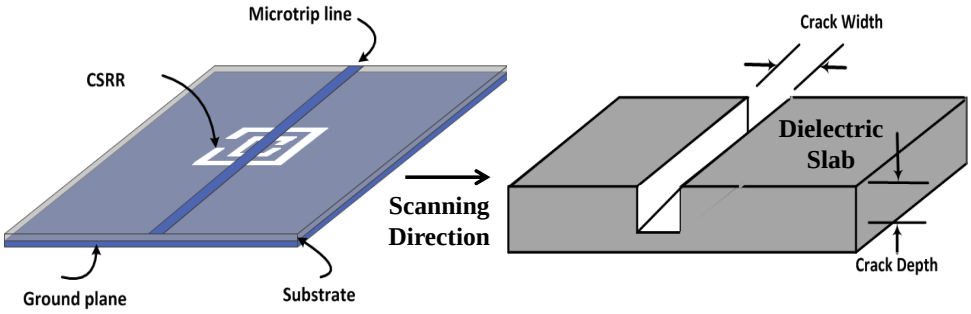

Figure 4.1: A schematic of a CSRR excited by a microstrip line as a near-field sensor to detect defects in dielectric surfaces.

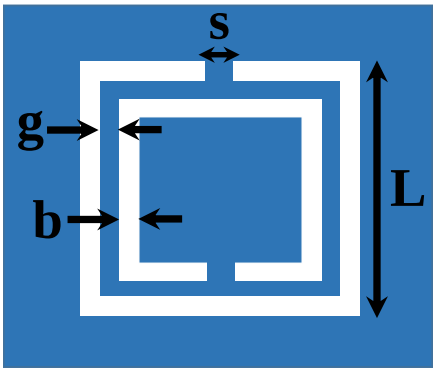

Figure 4.2: a CSRR topology, where L = 3 mm, g = 0.2 mm, s = 0.2 mm and b = 0.2 mm.

The primary objective when designing a sensor is to obtain a high measurement sensitivity, reduce measurement setup complexity and use widely available relatively inexpensive microwave components. Since the near field of any electromagnetic source occupies a space directly proportional to the size and frequency of the radiator, to effectively sense small changes, such as sub-millimeter cracks in materials in the near field of the sensor, the overall size of the CSRR must be sufficiently small so as not to be much larger than the features to be detected. In the examples considered here, the gap separations and trace widths of

the sensor were chosen to be 0.2 mm as the smallest feature in this design. Generally, there is flexibility in designing a CSRR sensor at a wide range of frequencies associated with a target crack size.

4.3 CSRR Sensor Design Approach

Unlike conventional wire antennas, where the resonant frequency is directly proportional to the length of the radiator, the resonant frequency of electrically-small resonators, such as CSRR and SRR resonators, is typically found through measurement or simulation [1,31, 37,38,53]. In general, however, the larger the overall size of the electrically-small resonator, the lower its resonant frequency. Here, correlating the topological dimensions of a CSRR element to its resonant frequency for the purpose of obtaining useful design guidelines is considered. Because the sensor is a two-port microstrip line exciting a CSRR, a vector network analyzer (VNA) is used to measure the reflection and transmission parameters. In order to match the internal impedance of the VNA in our measurement setup, the microstrip line was designed to have a characteristic impedance of 50 Ω (the microstrip line can be designed to match the internal impedance of other measurement setup devices). To achieve a 50Ω characteristic impedance for the microstrip line using Rogers RO4350 substrate with a thickness of 0.75 mm, the permittivity of 3.66 and a loss tangent of 0.0031, the width of the microstrip line was 1.7 mm.

For the purpose of developing CSRR sensor design guidelines, the CSRR length was varied from 2 to 4 mm. Two different values of 0.1 mm and 0.2 mm were considered for the gap separations and trace widths of the structure. The resonance frequencies *versus* the size of CSRRs (considered to be its length) are plotted in figure 4.3. An exponential fitting function was used to find the resonance frequency of a CSRR as a function of its length, expressed as:

$$f_r = e^{a+bL+cL^2} \tag{4.2}$$

where L is the length of the resonator and a, b and c are the fitting function constants. For gap separations and trace widths of 0.1 mm, the constants were a = 4.041, b = -1.085 and

c = 0.104. In the case of the gap separations and trace widths of 0.2 mm, the constants were a = 4.34, b = -1.093 and c = 0.098.

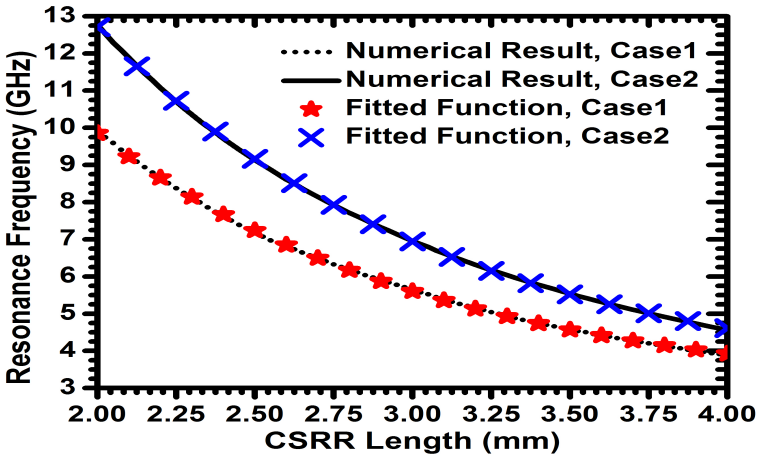

Figure 4.3: The resonance frequency *versus* the CSRR length obtained form full-wave numerical simulation and from the fitting exponential function for gap separations and trace widths of 0.1 mm and 0.2 mm labeled as Case 1 and Case 2, respectively.

Figure 4.3 shows that the resonance frequencies decrease exponentially by increasing the overall lengths of the resonator. Of course, lowering of the resonant frequency is expected due to the increase in the effective inductance of the SCSR; however, the exponential relationship could not have been intuitively predicted.

A CSRR sensor was designed to resonate at around 6.95 GHz with resonator dimensions of L = 3 mm and b = s = g = 0.2 mm (see figure 4.2). For the purpose of crack detection, designing a sensor to operate at a specific resonance frequency is unnecessary as long as the resonance frequency and dimensions of the sensor are chosen to detect cracks with dimensions falling within a specific range. Figure 4.4 shows a photo of the designed CSRR with dimensions of L = 0.27 mm and b = s = g = 0.16 mm.

Figure 4.5 shows a comparison between the simulation and measurements for a sensor with L = 0.27 mm and b = s = g = 0.16 mm. The feeding microstrip line had a width of 1.7 mm on Rogers RO4350 substrate with a thickness of 0.75 mm, the permittivity of 3.7 and a loss tangent of 0.003. The agreement between the full-wave simulation and measurements

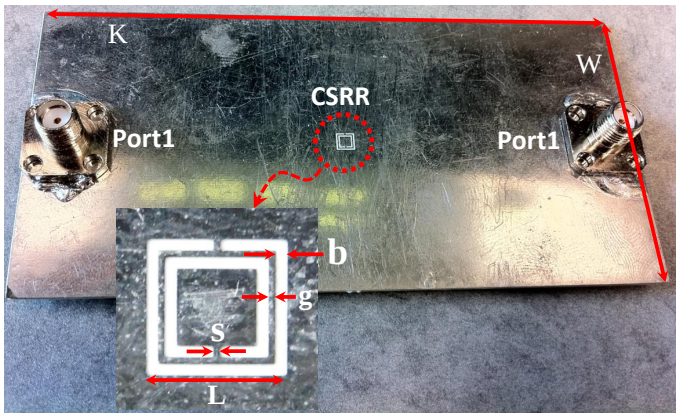

Figure 4.4: The CSRR printed on the ground plane of a microstrip line with its fabricated dimensions, L = 0.27 mm, b = s = g = 0.16 mm, K = 100 mm and W = 50 mm.

is observed to be very strong, especially at the frequency of minimum transmission. This gives strong confidence in the capability of numerical simulation to determine the response of different sensors and different crack topologies.

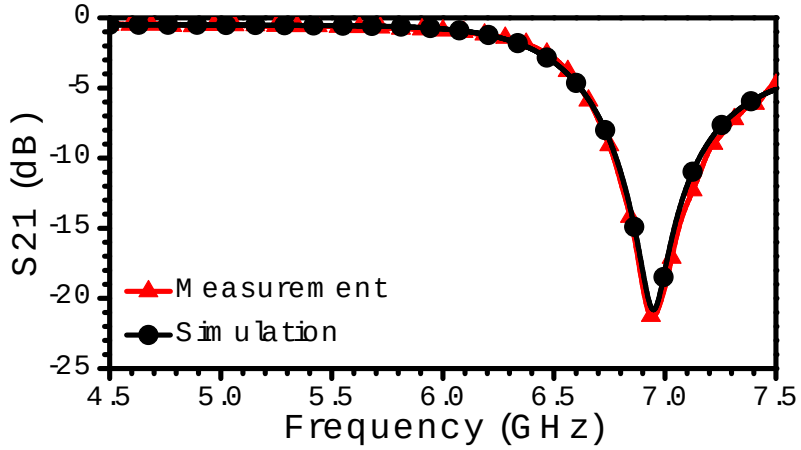

Figure 4.5: THe frequency response of the sensor obtained from full-wave simulation using HFSS and measurements for the CSRR sensor.

4.4 Crack Detection in Non-Metallic Materials

Detection of anomalies, such as cracks in the dielectric materials, is based on a change in the electric field due to the presence of the anomaly. Therefore, the sensing element for the near-field detection of anomalies, such as cracks in dielectric surfaces, needs to have a dominant electric field. By investigating the total electric field on the surface of the CSRR sensor, a dominant electric field along one side of the CSRR was observed. Figure 4.6 shows the maximum electric field distribution on a 3-mm CSRR at the resonance frequency. The sensing element for the purpose of detecting dielectric anomalies, therefore, can be considered as the side depicted by the letter C in figure 4.6.

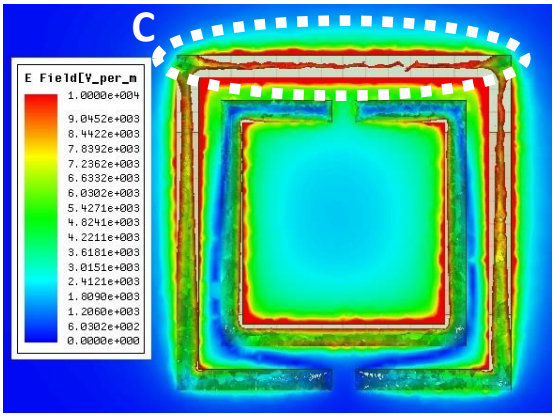

Figure 4.6: The total electric field distribution on the CSRR at the resonance frequency. The red color indicates the highest field magnitude.

For validation purpose, a CSRR of a length of 3 mm is used to detect sub-millimeter cracks in dielectric materials. Fiberglass (thickness of 3 mm and length and width of 50 mm) and ceramic materials (thickness of 6 mm and length and width of 50 mm) with dielectric constants of 2.3 and 9.8, respectively, were used. Figure 4.7 shows the frequency of minimum transmission coefficient obtained experimentally when the sensor passes over a fiberglass material with different crack widths of 150 μm and 200 μm (depths of 1.5 mm). A maximum shift of more than 312 MHz was observed with respect to the reference case. For the ceramic material considered, figure 4.8 shows a maximum shift of more than 477 MHz for the two crack topologies considered. These results indicate that the

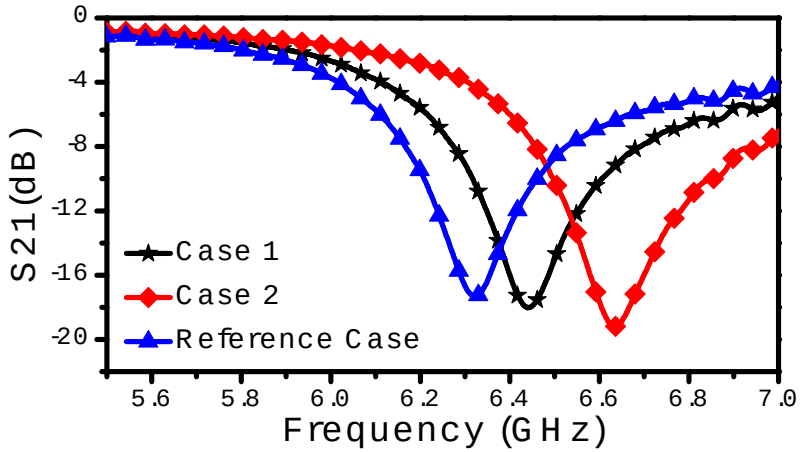

Figure 4.7: The minimum transmission of the sensor for a crack width (w) of 150 μm (Case 1) and 200 μm (Case 2) compared with the solid dielectric material (fiberglass) with a dielectric constant of 2.3 (reference case). The crack depth (h) is 1.5 mm.

sensitivity increases with the dielectric constant of the MUT. Based on figures 4.7 and 4.8, it can be observed that the cracks result in an upward shift in the resonance frequency (in contrast to the downward shift observed in the case of detecting cracks in metallic surfaces), which is consistent with the prediction of Equation (4.1), due to the decreased capacitance experienced by the sensor.

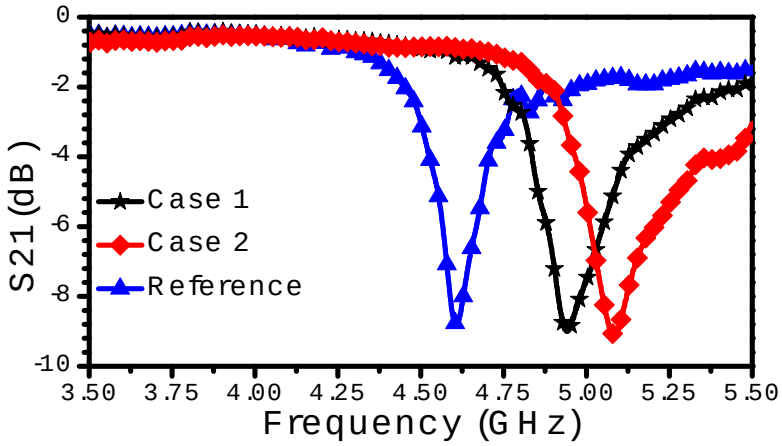

Figure 4.8: Minimum transmission of the sensor for a crack width (w) of 150 μm (Case 1) and 200 μm (Case 2) compared with a solid dielectric material, ceramic (ceramic material), with a dielectric constant of 9.8 (reference case). The crack depth (h) is 1.5 mm.

4.5 Conclusions

In this chapter, a planar CSRR sensor for crack detection in non-metallic materials was reported. Design formulae were derived based on full-wave numerical simulation to provide the designers with guidelines that can eliminate expensive full-wave numerical simulations. The analysis of the total electric field distribution on the CSRR revealed important clues for the active sensing element that is most sensitive to changes in the surface of MUTs. The CSRR sensor was found to be highly effective for detecting sub-millimeter cracks in dielectric surfaces. Finally, since the strips, presented in chapter 2 (figure 3.13), do not affect the response of the CSRR in the presence of dielectric materials, a new concept to increase the sensitivity of the planar CSRRs sensors is needed.

Chapter 5

Sensitivity Enhancement Using a Novel Transmission Line Coupling Mechanism to Multiple Resonators

5.1 Introduction

Electrically-small resonators show enhanced localized electric fields, yet most of the enhanced fields are concentrated in the substrates (host materials) [55], especially if the substrates are designed using high dielectric materials. The interactions with MUTs are thus limited. To overcome such limitation, a channel used for carrying dielectric materials can be embedded inside the substrate of a microatrip line loaded with an SRR [55]. The interactions between the dielectric materials and the electric fields will be increased. The sensitivity is hence increased as well. However, fabricating a channel inside dielectric substrates can produce many challenges from the practical point of view. It is not easy taking into account different fabrication tolerance as well as different resonators' size and frequency range of operation to locate the channel precisely in the sensitive region inside the substrate. In fact, an optimization process was followed to find the optimal location of the channel (tube) inside the substrate [55].

In this chapter, a novel microstrip line coupling mechanism to multiple resonators is proposed for sensitivity enhancement. It can be shown that when the resonators are coupled in perpendicular to the direction of propagation of a microstrip line (axial plane), the sensing areas are increased. In addition, the electric fields per unit length are increased as well. The sensitivity to detect changes in dielectric materials is thus enhanced. Note that, when resonators coupled to transmission lines are in perpendicular to the direction of propagation, namely a *parallel configuration* whereas if resonators in the same direction of propagation, we can call a series or *cascade configuration*. The resonators are based, not limited, on CSRRs. The concept using splitter-combiner microstrip sections loaded with coupled resonators (CSRRs) was demonstrated. The splitter utilized to excite the resonators has a characteristic impedance of 100 Ω whereas the combiner has a characteristic impedance of 50 Ω, which makes the design much easier. There is no need to design precisely the length of splitter-combiner microstrip sections and no need to use quarter wavelength transmission line for the combiner [56]. Detecting changes in dielectric constants of MUTs, the parallel configuration shows higher sensitivity compared to a single CSRR and cascade configuration. In addition, increasing the number of resonators can create more sensitive modes (minimum transmission zeros) was shown. These modes can be useful for many applications to detect many parameters simultaneously including the detection of complex permittivity and thickness of dielectric slabs, and the estimation of the air gap during measurements [33]. The sensitivity enhancement was tested with the numerical simulation tool (ANSYS HFSS) and verified experimentally by detecting the dielectric constant of two dielectric slabs.

5.2 Theory of Sensitivity Enhancement Using a System of Microwave Multiple Resonators

Electrically-small resonators including CSRRs are one of the main constitutive building blocks of metamaterials [22]. The resonators can be considered as quasi-static resonators and approximately modeled using lumped circuit elements (inductance, capacitance, and resistance). This model is acceptable near the resonance frequency. With respect to their

topologies, the gaps and metallic traces of the CSRRs can be represented as capacitances and inductances, respectively. Based on the effective inductances and capacitances, resonance frequencies of CSRRs can be predicted. In general, the self-resonance frequency of a CSRR can be expressed as follows:

$$f_0 = \frac{1}{2\pi\sqrt{L_r C_r}} \tag{5.1}$$

where L_r and C_r are the effective inductance and capacitance, respectively. A general footprint of a CSRR is shown in figure 5.1. For planar microwave near-field sensors, CSRRs are coupled to microstrip lines, and transmission zeros (bandgaps) occur. In a two-port network, the transmission zeros can be represented in the form of the scattering transmission coefficient $|S_{21}|$ dB. Figure 5.2 shows the lumped circuit model of a CSRR coupled to a microstrip line. At the minimum transmission zero, the resonance frequency can be expressed as follows:

$$f_{z0} = \frac{1}{2\pi\sqrt{L_r(C_r + C)}} \tag{5.2}$$

where C is the capacitance of the transmission line per unit length. At the resonance frequency, the CSRR sensor is sensitive to changes in MUTs if placed close proximity. However, the sensitivity is limited since the electromagnetic fields are concentrated in the substrate. To overcome this limitation, one can increase the sensing area using a system of multiple resonators.

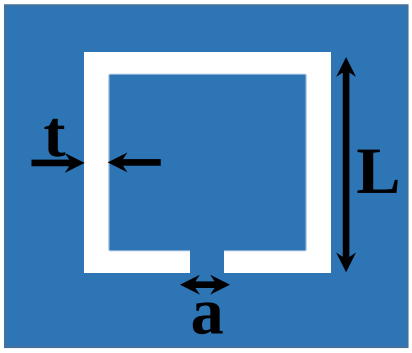

Figure 5.1: The schematic of a general footprint of a CSRR etched out in a ground plane

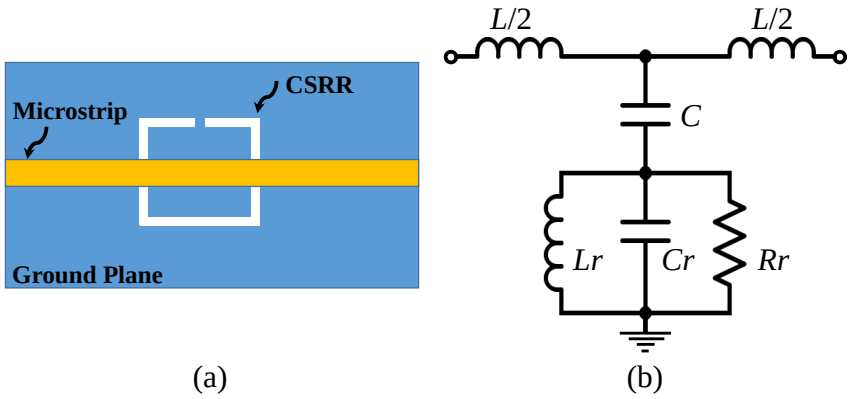

Figure 5.2: (a) A microstrip line exciting a CSRR that is etched out in the ground plane, (b) The equivalent lumped circuit model where L and C are inductance and capacitance of the microstrip line per unit length, respectively, whereas L_r, C_r, R_r are the inductance, capacitance, and resistance of the CSRR, respectively.

In order to keep the sensing areas electrically small compared to the guided wavelength (λ_g) of microstrip lines, multiple CSRRs can be coupled to the microstrip lines in the parallel configuration. Note that, if the resonators are coupled in the cascade configuration, the sensor suffers from sensitivity degradation [56, 57]. Figure 5.3 shows the footprint of two-coupled CSRRs. For exciting the resonators, there are two suggested ways. One way is to excite both resonators using a single transmission line shown in figure 5.4 whereas the other one is to excite each resonator individually using two-transmission lines shown in figure 5.5. To attain a qualitative understanding of what is happening, Figures 5.6 and 5.7 show lumped circuit models for the single and two transmission lines, respectively. In the case of the two transmission lines (figure 5.5), the coupling capacitance (C) is higher because the transmission lines are exciting the center island of the resonators [58]. The high-coupling capacitance becomes more significant in the case of exciting more than two resonators. If the coupling capacitance is weaker in the case of a single transmission line, coupling more resonators to the transmission line in the parallel configuration will further be weaker. Thus, in this work, the two transmission lines excitation in the form of splitter-combiner microstrip sections will be utilized. Note that, the distance (k) between the two-100-Ω-transmission lines is carefully chosen to eliminate any coupling between

them. Thus, first, the transmission lines shown in figure 5.5 without CSRRs is designed. Figure 5.8 shows the scattering parameters, with the transmission coefficient (S_{21}) being almost 0 dB (maximum transmission).

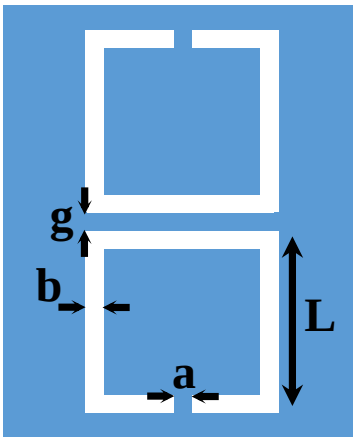

Figure 5.3: The schematic of a general footprint of two-coupled CSRRs etched out in a ground plane

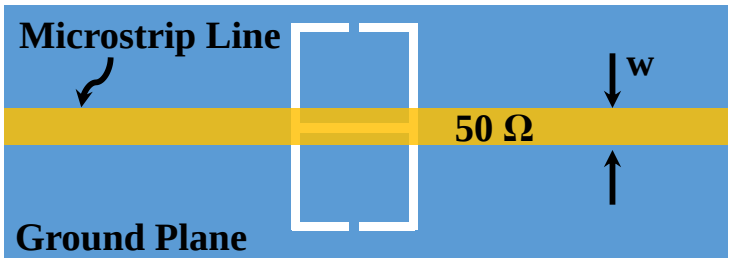

Figure 5.4: A two-port system using a microstrip line loaded with two-coupled resonators (CSRRs)

It is clear from figures 5.6 and 5.7 that the sensing area of the multiple resonators in the parallel configuration are increased due to the enhancement in the resonators' capacitances C_r. Although the sensing areas are increased, the resonators are still electrically small with respect to the guided wavelength. To increase the sensing areas further, four resonators are coupled to two transmission lines as shown in figure 5.9. Figure 5.10 shows the lossless

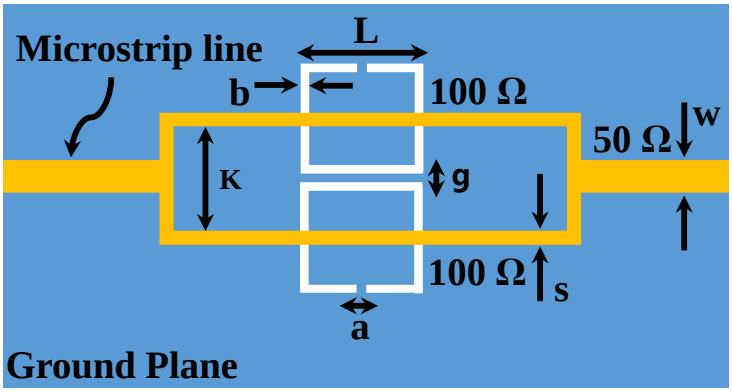

Figure 5.5: A two-port system using splitter-combiner microstrip sections loaded with two-coupled resonators (CSRRs) where each resonator is excited by a 100 Ω microstrip line

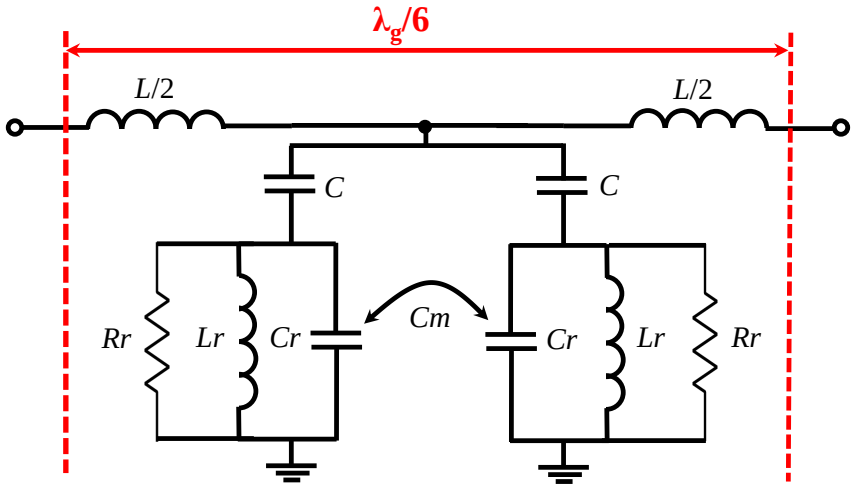

Figure 5.6: The equivalent lumped circuit model of a two-port system using a microstrip line loaded with two-coupled resonators (CSRRs), where C_m is the mutual capacitance

lumped circuit model in the case of four resonators. Since the two-transmission lines are not in the center islands the two-added resonators, it is expected that the coupling capacitance will become weaker (C_2) as well as the mutual capacitance (C_{m2}). In addition, since there are two sets of coupling capacitances (C_1 and C_2) as well as two mutual capacitances, it is

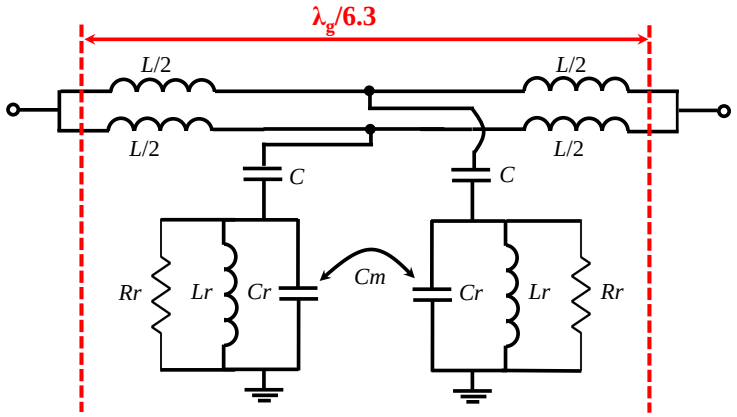

Figure 5.7: The equivalent lumped circuit model of a two-port system using splitter-combiner microstrip sections loaded with two-coupled resonators (CSRRs) where each resonator is excited by a 100 Ω, where C_m is the mutual capacitance

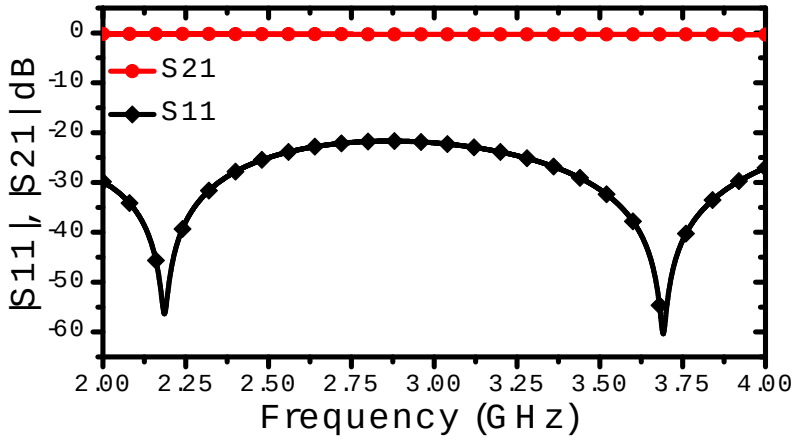

Figure 5.8: The scattering parameters of the transmission lines shown in figure 5.5 without CSRRs

expected that the sensor will have dual-band rejection (minimum transmission coefficients).

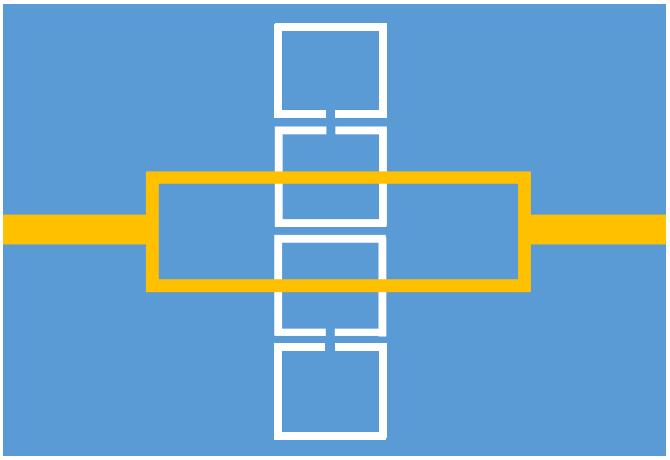

Figure 5.9: A two-port system using splitter-combiner microstrip sections loaded with four-coupled resonators (CSRRs) where every two sets of resonators are excited by a 100 Ω microstrip line

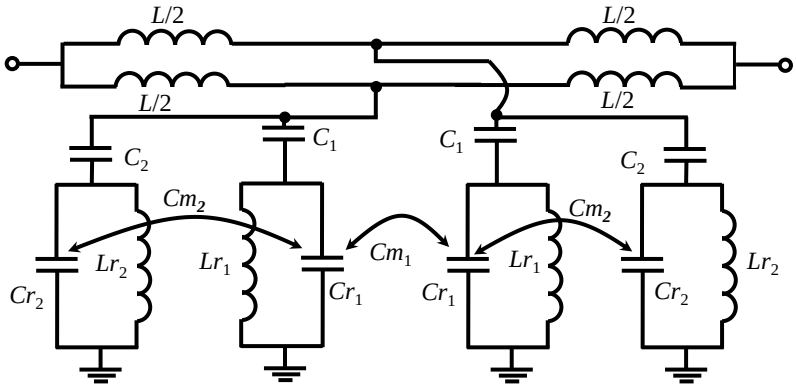

Figure 5.10: The equivalent lumped circuit model of a two-port system using splitter-combiner microstrip sections loaded with four-coupled resonators (CSRRs) where each resonator is excited by a 100 Ω, where C_{m1} and C_{m2} are the mutual capacitances

5.3 The Sensing System Design and Excitation

Since scattering parameters of the sensors will be extracted using a VNA with an internal impedance of 50 Ω, the single microstrip line and the splitter-combiner microstrip sections

are designed as follows. The two-lines splitter has a characteristic impedance of 100 Ω whereas the single microstrip line and the combiner have the characteristic impedance of 50 Ω. Using Rogers RO4350 substrate with a thickness of 0.75 mm, a relative permittivity of 3.66, and a loss tangent of 0.0031 to design microstrip lines with characteristic impedances of 100 Ω and 50 Ω, two-line widths of 0.37 mm and 1.63 mm, respectively, are required.

The main objective of the proposed sensors is to increase the sensing areas interacting with MUTs for sensitivity enhancement. The investigation is conducted by analyzing sensing areas of a single CSRR, with the electric field distribution being numerically calculated. Generally speaking, resonance frequencies of electrically-small resonators are directly proportional to largest dimensions, so taking into account many factors such as the field penetration and fabrication cost, the largest dimensions in the CSRR is chosen to be L = 7.5 mm, and the air and metallic traces is b = a = 0.5 mm as shown in figure 5.1, which resulted in a resonance frequency of 3.35 GHz. By using the numerical simulation (HFSS), the single CSRR sensor shown in figure 5.2 is modeled. Figure 5.11 shows the scattering parameters of the sensor extracted using the numerical simulation (HFSS) and the circuit model. To evaluate the electromagnetic fields, figure 5.12 shows the total electric field distribution on a virtual sheet placed horizontally inside the dielectric substrate and underneath the ground plane (the free space). The maximum electric-field distribution is 500 V/m. However, the electric field is concentrated inside the substrate and limited to certain regions, hence, reducing the sensitivity of the CSRR to detect changes in dielectric materials.

For the case of the two CSRRs sensor (the proposed sensor), the dimensions of the sensor as shown in figure 5.5 are a = b = g = 0.5 mm, L = 7.5 mm, K = 7.626 mm. With these design specification, the resonance frequency of the proposed sensor is 3.8 GHz. By comparing the resonance frequency of the single CSRR and the two CSRRs sensors, the resonance frequency is increased from 3.35 GHz to 3.8 GHz. By using the numerical simulation (HFSS), the electric field enhancement of the two CSRRs sensor is compared to the single CSRR sensor. Figure 5.13 shows the total electric field distribution that is calculated on a virtual sheet inside the substrate and underneath the resonators (in the free space). The maximum electric field is 35 KV/m. In fact, with respect to the single

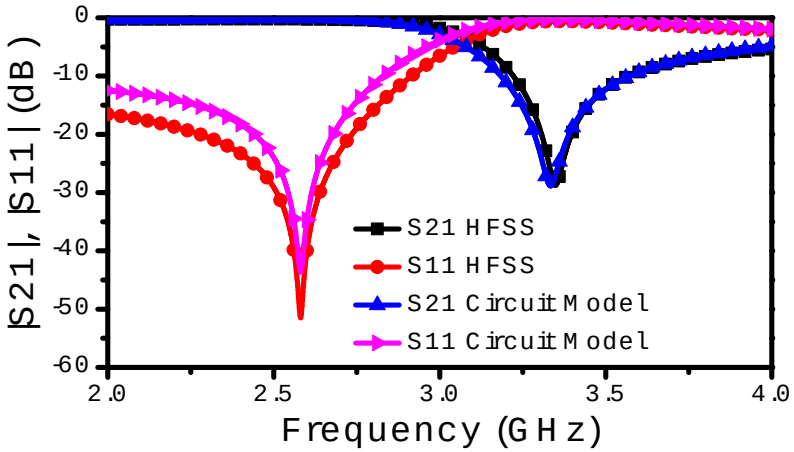

Figure 5.11: The scattering parameters ($|S_{11}|$ and $|S_{21}|$ dB) extracted using the numerical tool (HFSS) and circuit model of the single CSRR sensor

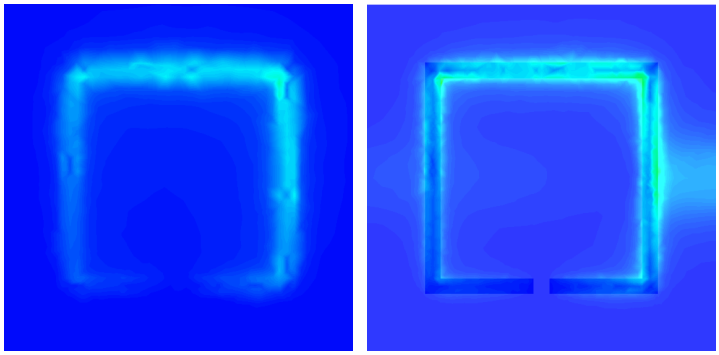

(a) (b)

Figure 5.12: Simulated electric field distribution on a virtual sheet (a) the field distribution underneath the CSRR (in the free space)(b) the field distribution inside the dielectric substrate. Note that for both figures, the highest red intensity corresponds to 1 KV/m and the highest blue intensity corresponds to 77 mV/m.

CSRR sensor, the electric field is dramatically enhanced with a percentage of 7000%. The enhanced electric field gives an inference that the two-CSRRs sensor will be more sensitive

to detect the changes in dielectric materials.

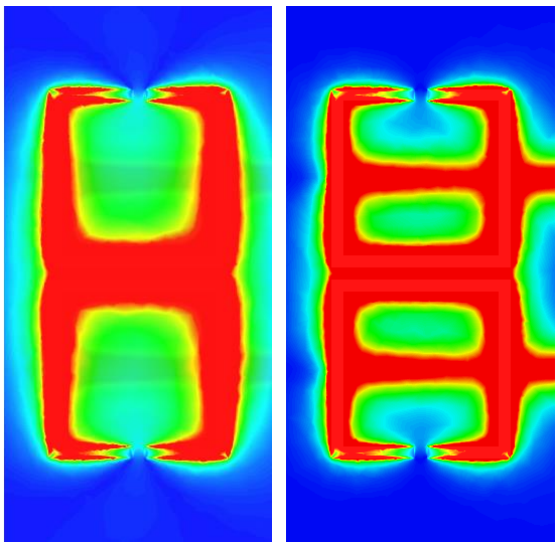

(a) (b)

Figure 5.13: The numerical result of electric field distribution on a virtual sheet of the two-CSRRs sensor (a) the field distribution underneath (in the free space) the multi-CSRRs sensor where the highest red intensity corresponds to 1 KV/m and the highest blue intensity corresponds to 45 mV/m. (b) the field distribution inside the dielectric substrate.

To extract the lumped circuit parameters shown in figure 5.7, first, the scattering parameters of the two-CSRRs sensor are extracted using HFSS, then using the optimization tool box in the circuit model simulator of ADS by Keysight, the circuit parameters are calculated. Figure 5.14 shows the scattering parameters of two-CSRRs sensor that are extracted using the numerical simulation (HFSS) and the circuit model. Since the coupling between the splitter section is very low, the resonance frequency at the minimum transmission zero can be approximated according to the following equation [56]

$$f_z = \frac{f_{z0}}{2\pi\sqrt{1-\frac{Cm}{Cr+C}}} \tag{5.3}$$

where f_{z0} is the resonance in the case of zero interresonator coupling between the CSRRs. Form equation (5.3), C_m will cause the transmission zero frequency to increase. From the

circuit model extraction of the two CSRRs sensor, the f_{z0} is 3.469 GHz. Based on the mutual capacitance, $C_m = 0.0195$ pF, and using equation (5.3), the resonance frequency, f_z is 3.786 GHz as expected from the numerical simulation. In addition, the mutual capacitance will help to increase the shift in the resonance frequency when the two CSRRs sensor interacts with MUTs.

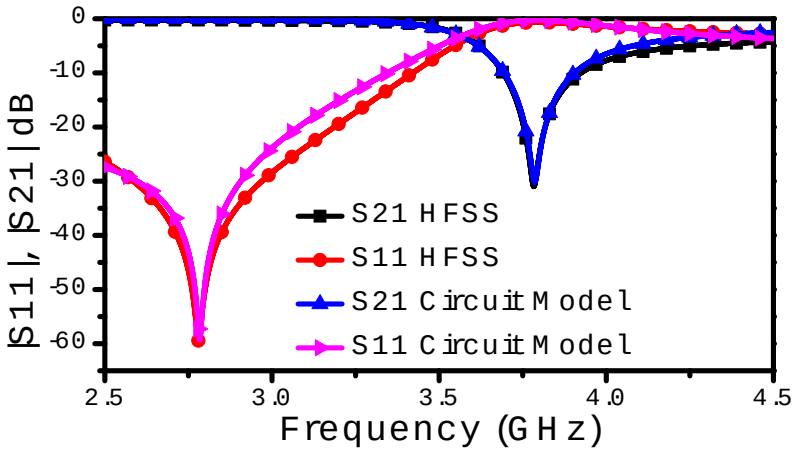

Figure 5.14: The scattering parameters ($|S_{11}|$ and $|S_{21}|$ dB) extracted using the numerical tool (HFSS) and circuit model of the two CSRRs sensor

To analyze the sensitivity of the single CSRR compared to the two CSRR sensor, it is assumed that with small changes in the resonance frequency due to the perturbation of MUTs. From equations (5.2), the change in the angular resonance frequencies can be written as

$$\frac{dw_z}{dC_r} = -\frac{L}{2\left(l\left(C_r + C\right)\right)^{\frac{3}{2}}} \tag{5.4}$$

or

$$\frac{dw_z}{dC_r} = -\frac{w_z}{2\left(C_r + C\right)} \tag{5.5}$$

whereas from equations 5.3, the angular resonance frequencies of two-CSRRs can be written as

$$\frac{dw_z}{dC_r} = -\frac{L}{2\left(L\left(C_r + C\right)\right)^{\frac{3}{2}}\left(1 - \frac{C_m}{C_r + C}\right)^{\frac{3}{2}}} \tag{5.6}$$

or

$$\frac{dw_z}{dC_r} = -\frac{w_z}{2\left(C_r + C\right)\left(1 - \frac{C_m}{C_r + C}\right)} \tag{5.7}$$

Compared to the changes in the resonance frequency of the single CSRR sensor, the new factor in equation (5.7) that contains the mutual capacitance (C_m) will make the angular resonance frequency of the two CSRR sensor to exhibit more changes.

In the case of four CSRRs, figure 5.15 shows the scattering parameters of the four-CSRRs sensor. By adding two more resonators, the coupling capacitances as well as the mutual capacitances have exhibited changes. Consequently, the sensor has two modes: mode 1 and 2. In addition, the sensing areas are increased, which will increase the sensitivity.

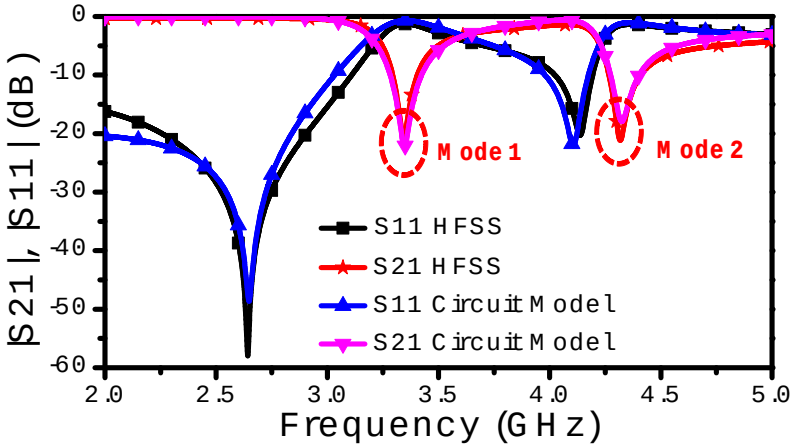

Figure 5.15: The scattering parameters ($|S_{11}|$ and $|S_{21}|$ dB) extracted using the numerical tool (HFSS) and circuit model of the four CSRRs sensor

5.4 The Multi-CSRRs as Near-Field Sensors for Dielectric Materials

By using the numerical simulation (HFSS), the dielectric constant of a dielectric slab with a thickness of 3 mm was varied from 1 to 30 with a small variation step of 0.2. Figure 5.16

shows the shifts in the resonance frequencies of the single CSRR and two CSRRs sensors. As expected, the proposed two CSRRs sensor shows a higher sensitivity. In case of the four CSRRs sensor, mode 2 shows higher sensitivity to changes in the dielectric constant of the slab. Figure 5.17 shows the shift in the resonance frequencies of four sensors: Mode (1) (four CSRRs), Mode (2) (four CSRRs), two CSRRs, and a single CSRR.

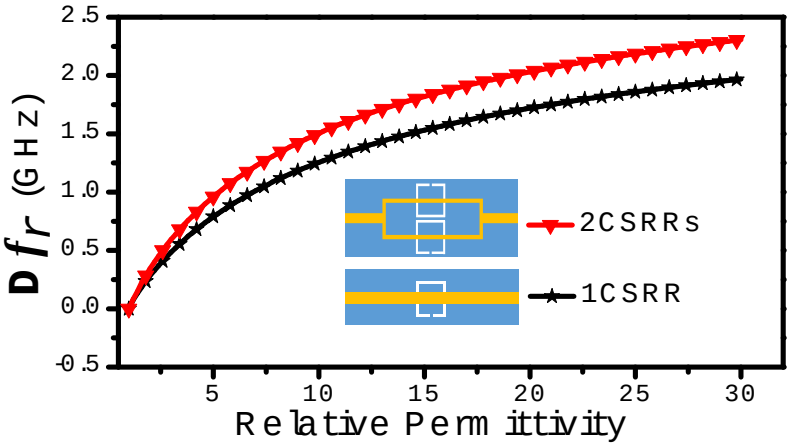

Figure 5.16: The resonance frequency shifts versus the dielectric constant of the slab that is varied from 1 to 30 with a step size of 0.2 of the single CSRR and two CSRRs sensors

.

5.5 The Multi-CSRRs baed Sensors: Fabrication and Experimental Results

For the purpose of experimental verification, a single CSRR and two CSRRs sensors were fabricated using the printed circuit board technology (PCB). Figure 5.18 shows the fabricated sensors, where figures 5.18(a) and 5.18(c) are for the single CSRR sensor and figure 5.18(b) and 5.18(d) are for the proposed two CSRR sensor.

The sensors were tested to detect two-dielectric slabs. The two dielectric slabs were prepared with dielectric constants of 2.3 and 9.8. As shown in figures 5.19 and 5.20, the experimental results (the transmission coefficients, $|S21|$ dB) of the sensors were extracted

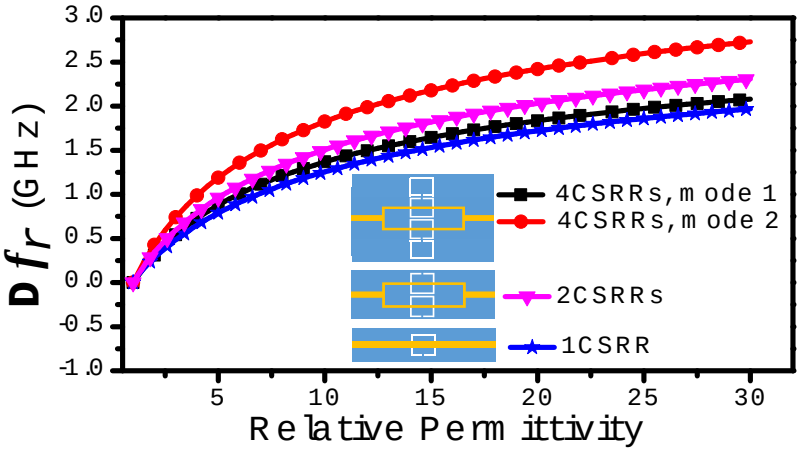

Figure 5.17: The resonance frequency shift versus the dielectric constant of the slab that is varied from 1 to 30 with a step size of 0.2 of Mode 1 (four CSRRs), Mode 2 (four CSRRs), two CSRRs, and a single CSRR sensors

.

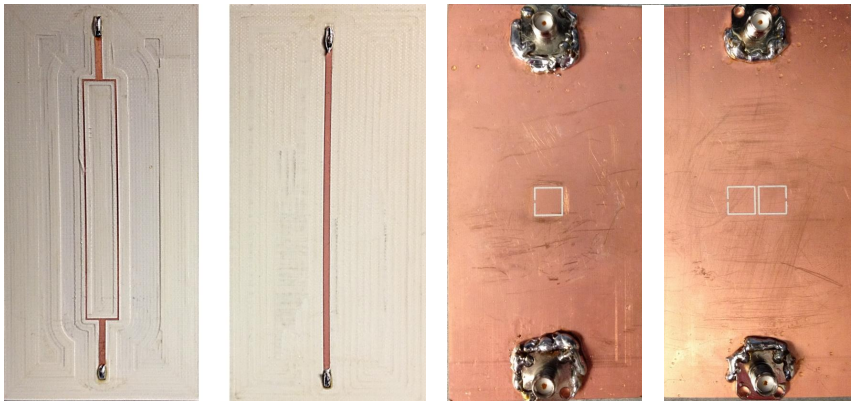

Figure 5.18: The fabricated CSRRs sensors. (a) and (C) are the single CSRR sensor. (b) and (d) are the proposed two CSRR sensor

using a VNA. First, the single CSRR were utilized to interact with three materials: the free space (used as a reference case) and dielectric slabs of the dielectric constants of 2.3

and 9.8. The resonance frequencies of the sensor for the three cases are 3.38, 3.067, and 2.137 GHz, respectively. Compared to the reference case (the free space), the shifts in the resonance frequency are 0.313 and 1.243 GHz for the dielectric constants of 2.3 and 9.8, respectively. On the other hand, the resonance frequencies of the proposed two CSRR sensor encountering the free space and dielectric slabs of the dielectric constants of 2.3 and 9.8 are 3.926, 3.507, and 2.507 GHz, respectively. Compared to the reference case, the sensor shows shifts in the resonance frequency of 0.42 and 1.42 GHz for the dielectric constant of 2.3 and 9.8, respectively. When the two sensors compared to each other for the two-dielectric slabs with the dielectric constants of 2.33 and 9.8, the increase in the shifts in the resonance frequencies is 107 and 180 MHz, respectively. This results were predicted numerically and here experimentally proven.

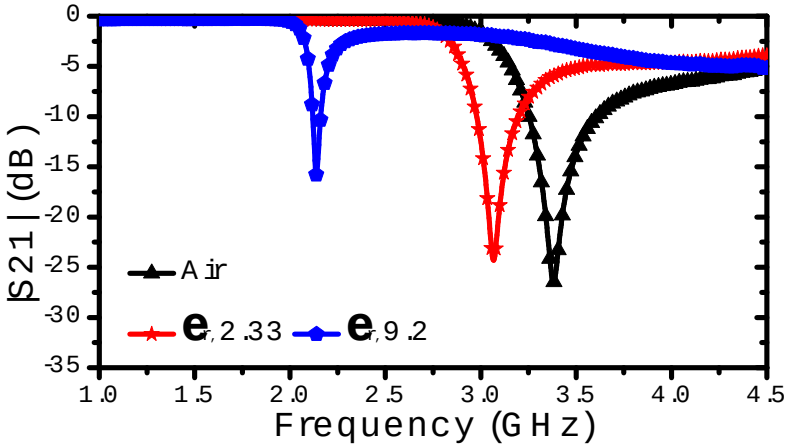

Figure 5.19: The experiment result of the minimum transmission coefficient ($|S_{21}|$ dB) of a fabricated 50 Ω microstrip line exciting a single CSRR shown in Figure 5.18, a and c

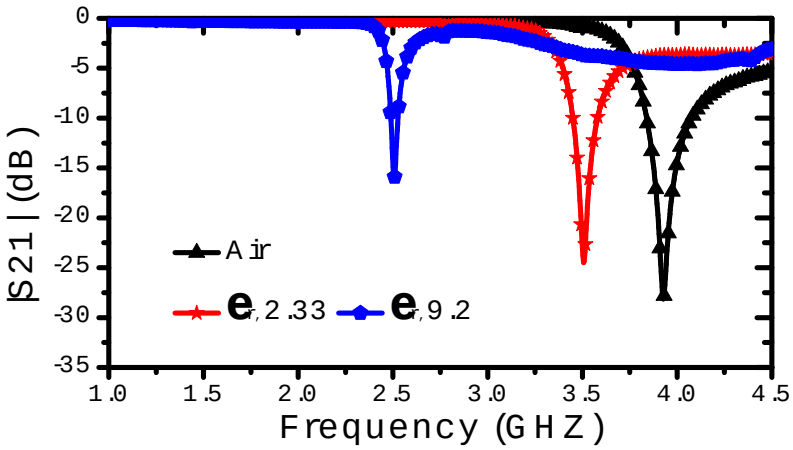

Figure 5.20: The experiment result of the minimum transmission coefficient ($|S_{21}|$ dB) of a fabricated two-port system using splitter-combiner microstrip sections loaded with four-coupled resonators (CSRRs) shown in figure 5.18, b and d

5.6 Conclusion

In this chapter, a novel microstrip line coupling mechanism to multiple resonators was presented for sensitivity enhancement. The resonators are based, not limited, on CSRRs and coupled to the microstrip line in perpendicular to the direction of the propagation. The coupled CSRRs are thus kept electrically small and the sensing areas are increased. Consequently, the sensitivity of CSRRs sensors to detect dielectric materials has enhanced. The sensor is based on splitter-combiner microstrip sections loaded with coupled resonators (CSRRs). The proposed concept was tested numerically using a numerical tool to detect two-dielectric slabs. The sensor was fabricated using a cheap technology based on the printed circuit board technologies (PCB). For experimental verification, the sensor was utilized to sense two dielectric slabs with the dielectric constant of 2.33 and 9.8, respectively. The proposed sensor shows higher sensitivity compared to a single CSRR sensor. Although the concept of multi-resonators increases the sensitivity to detect the presence of dielectric materials, the sensing area is relatively large for microscale-based applications such as microfluidic technologies.

Chapter 6

Highly Sensitive Microwaves Sensors for Fluid Concentration Measurements

6.1 Introduction

Planar electrically-small resonators have been used for designing sensitive near-field sensors. Since the resonators are electrically small compared to the excitation wavelength, the sensors are scalable to a very wide range of frequency from microwaves to THz. At the resonance frequencies of such resonators, the electromagnetic fields are concentrated in small areas surrounding the resonator structure [21]. When the fields are disturbed due to topological or material change in the environment, the impedance profile of the sensor changes thus leading to physical measurable changes that in turn reflects the change in the dielectric or magnetic properties of the surroundings [59]. The SRRs and their complement (CSRRs) have been used to design a variety of sensors (see [28] and references therein). However, planar electrically-small resonators show inherent sensitivity limitation [35]. This chapter aims to address these limitations.

6.2 Increased Capacitance for Sensitivity Enhancement

Figure 6.1 shows a CELCR etched out in a ground placed on a dielectric host substrate. At the resonance frequency, the stored-electric energy within sensor proximity is enhanced. The fringing flux in the substrate and the free space can be accounted for by an effective capacitance C_{sub} and C_{air}, respectively (see figure 6.1(b)). However, since most of the fringing flux will be concentrated in the material with the highest dielectric constant (the substrate), the effective capacitance C_{sub} will be the dominant contributor to the total capacitance of these type of resonators [35]. The MUT, which will be placed on the opposite side of the substrate, will minimally interact with the resonators, thus minimizing the shift in the resonance frequencies, and consequently, the sensitivity. To increase the interaction with the MUTs, sharp tips and breaking the symmetry of the resonators (e.g., SRRs) have been proposed where the sensing volume remains small, however, most of the stored energy remains in the substrate [60]. Since most of the electromagnetic energy is stored in the substrate, creating a channel inside the substrate to contain the MUT can substantially increase the interaction with the resonators and consequently, the sensitivity [55]. However, from a practical point of view, designing a channel inside the substrate in the sensitive volume can be challenging [55].

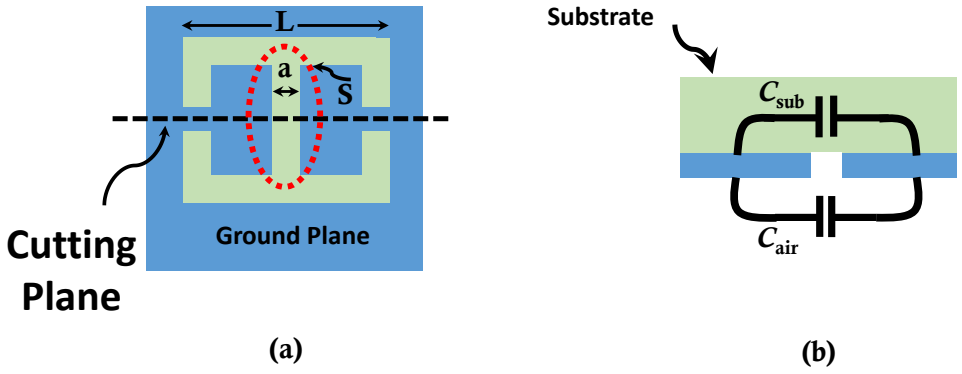

Figure 6.1: The schematic of the CELCR etched out in a ground plane. (a) Top view. (b) Side view through the cutting plane.

In this chapter, a concept for enhancing the electromagnetic-stored energy in the sensing volumes of electrically-small resonators is proposed. The concept is based on increasing the capacitance experienced by the MUT. One possible way of doing this is by adding a capacitor, three-dimensional capacitor (C_{pp}), on the top of a CELCR. However, the concept can be generalized to other types of electrically-small resonators and other types of top capacitors. Referring to figure 6.1, the middle gap labeled as S in the CELCR is the most sensitive part of the resonator, yet most of the electromagnetic energy is stored in the substrate. By introducing C_{PP}, which models a three-dimensional capacitor, the effective capacitance C_{air} in the free space will be increased leading to an increase in interaction with the MUT. This is expected to result in increased sensitivity. By using the CELCR, a two-port system is designed whereby a microstrip line excites the sensor. The concept was tested using numerical simulations and experiments to detect changes in the dielectric properties of materials.

The CELCR is electrically small compared to the excitation wavelength. The resonator can thus be analyzed using lumped circuit models. Figure 6.2 shows the circuit model of the CELCR connected to a two-port microstrip line that enables excitation and measurements. The resonance frequency at the minimum transmission zero can be written as follows:

$$f_z = \frac{1}{2\pi\sqrt{L_r(C_r + C)}} \tag{6.1}$$

where L_r and $C_r = C_{sub} + C_{air}$ are the inductance and capacitance of the resonators, respectively, and C is the capacitance per unit length of the microstrip line. The stored-electric energy in the resonator is represented by the effective capacitance (C_r). Disturbing the stored-electric energy affects the capacitance, and consequently the resonance frequency will exhibit a change. Notice that C_r represents the summation of two capacitances: C_{sub} and C_{air}. C_{air} is the capacitance that senses the change in the surrounding environment. However, the contribution of C_{air} to the total capacitance C_r is very small, especially for higher dielectric substrates, which, in general, limits the sensitivity of such electrically-small resonators [35]. When a capacitor is placed on the CELCR, this limitation is mitigated (see figure 6.3). The added three-dimensional capacitor, C_{PP}, increase the contribution of C_{air} to the total capacitance of the resonator C_r, which is expected to increase the overall sensitivity of the entire sensor. Figure 6.4 shows the circuit model with C_{pp} in parallel to

C_r.

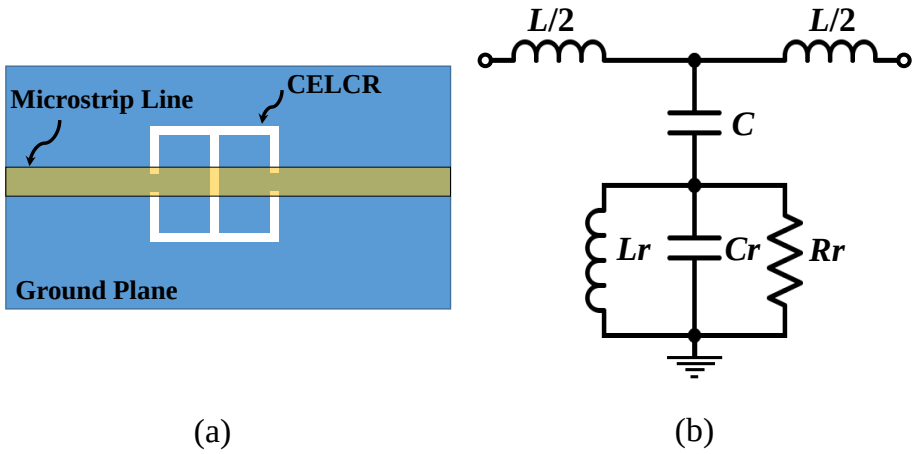

Figure 6.2: The circuit model of a CELCR connected to a two-port microstrip line. C_r, L_r, and R_r are the capacitance, inductance, and resistance, respectively, and C and L are capacitance and inductance per unit length of the microstrip line.

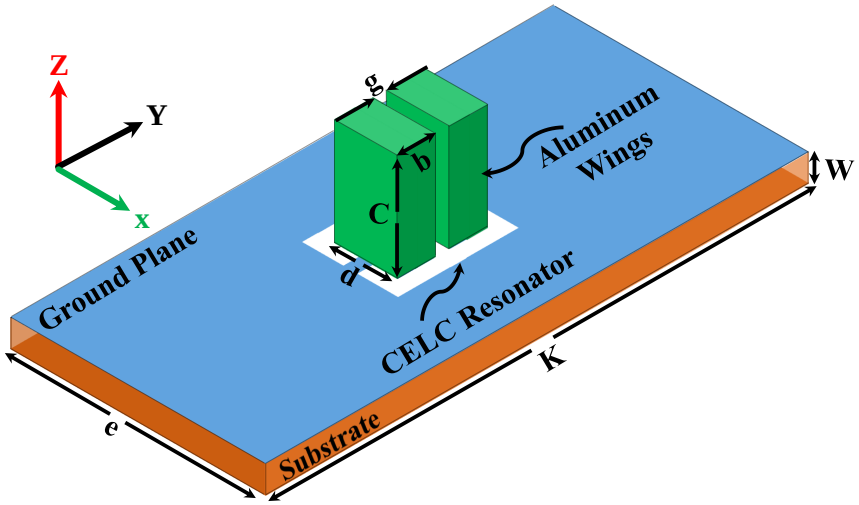

Figure 6.3: A schematic of the proposed sensor showing the CELCR etched out in the ground plane of a microstrip line with an inserted three-dimensional capacitor. The microstrip line used for port measurements is on the other side of the substrate (not shown).

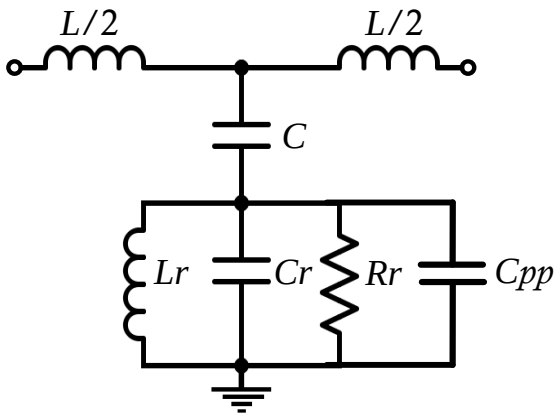

Figure 6.4: The circuit model of a CELCR loaded with C_{pp}

6.3 Sensor Design and Validation

By making close attention to figure 6.2(b), one can notice that the circuit model is identical to the circuit model of the CSRR (see figure 2.2). Since the circuit model is being utilized to understand and investigate the sensitivity enhancement, it has to be validated. First, the scattering parameters ($|S_{11}|$ and $|S_{21}|$ in dB) are calculated using the numerical simulation, HFSS. Then, the scattering parameters are brought to the circuit simulation (ADS) to extract the circuit parameters (the inductance, capacitance, and resistance). Following the similar steps, the circuit models shown in figure 6.4 can be validated as well. Figures 6.5(a) and 6.5(b) present the scattering parameters of the circuit models and the numerical simulation of the sensor with and without the C_{pp} in the presence of the free space. Generally speaking, although circuit models using lumped elements are valid close to the resonance frequency since the structure might have distribution elements that make the inductance and the capacitance functions of the frequency, Figures 6.5(a) and 6.5(b) shows that it is not the case. In addition, despite the fact that the circuit simulation is utilizing coarse models (not taking the coupling and radiation into account), the scattering parameters of the circuit models and the full-wave simulation are identical over a wide band. The result shows that the electrically-small resonators have confined electromagnetic fields suitable to design near-field sensors, which will be less sensitive to the background noise.

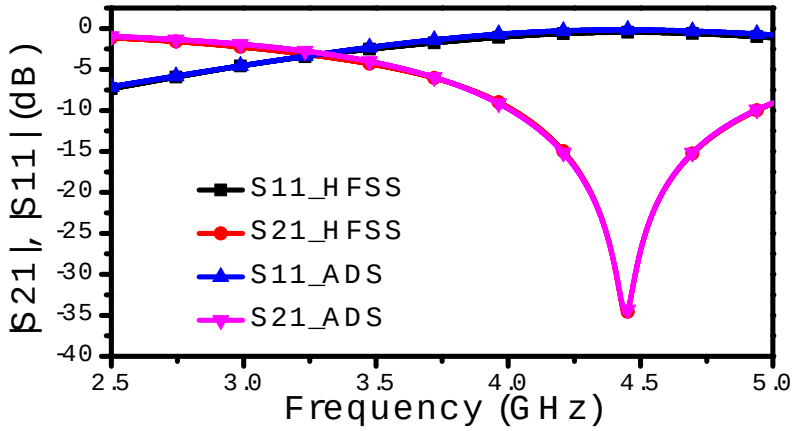

(a)

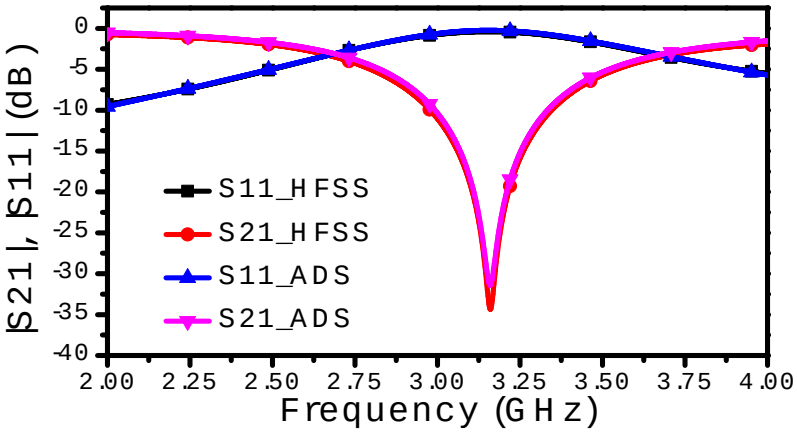

(b)

Figure 6.5: (a) The scattering parameters of the circuit models and the numerical simulation of the sensor without the C_{pp} in the presence of the free space and (b) with the C_{pp}

The response of the sensor is quantified using the scattering parameters which are measured using a vector network analyzer (VNA) with an internal impedance of 50 Ω. Therefore, a 50 Ω microstrip line was used for the excitation of the sensor. This impedance was achieved with a line width of 1.63 mm on a Rogers RO4350 substrate with a thickness of W = 0.75 mm and a relative permittivity of 3.66 and a loss tangent of 0.0031. With

the design specification L = 7.5 mm, a = 0.5, K = 100 mm and e = 50 mm, the resonance frequency of the sensor corresponding to the minimum transmission zero was 4.434 GHz. (Of course, there is no particular reason for selecting this specific frequency aside from being within a suitable range for our testing equipment.) The three-dimensional capacitor had the following dimensions which were chosen purely for practical reasons and to keep the overall footprint and profile limited: d = 6.5 mm, c = 3 mm, and the channel gap g = 0.5 mm. The C_{pp} causes the CELCR to store more electric energy at the new sensor resonance frequency given by

$$f_z = \frac{1}{2\pi\sqrt{L_r(C_{r0} + C_{pp} + C)}} \tag{6.2}$$

where C_{r0} is the capacitance of the CELCR before the inserted C_{PP}. The new resonance frequency shifted lower to 3.17 GHz (see figure 6.6). The new sensor, therefore, is expected to be more sensitive to detect changes in the surrounding environment since the inserted C_{PP} becomes the dominant capacitance of the resonator. Additionally, the quality factor at -10 dB is increased from 5 to 8.7, which is expected to yield a higher resolution. Note that, the increase in the quality factor of the resonator is critical since the inserted C_{PP} is exposed to the surrounding environment. Hence, any disturbance of the stored energy in the C_{pp} caused by the MUTs can lead to a higher frequency shift.

The sensor was utilized to detect changes in a dielectric slab inserted in the channel gap shown in figure 6.3. The relative permittivity of the slab was varied from 1 to 10 with an increment of 0.2. Figure 6.7 shows the simulation results extracted using the commercial three-dimensional full-wave simulation (ANSYS HFSS). The maximum enhancement in the sensitivity to detect changes in a dielectric slab from 1 to 1.2 increased from 165 kHz/Δ to 755 MHz/Δ, where Δ is a relative permittivity unit. The increase in sensitivity exceeded 450%.

6.4 Fabrication and Experimental Results

The sensor was fabricated using printed circuit board technology (PCB) and a three-dimensional capacitor constructed using two-aluminum cubes. The channel was created

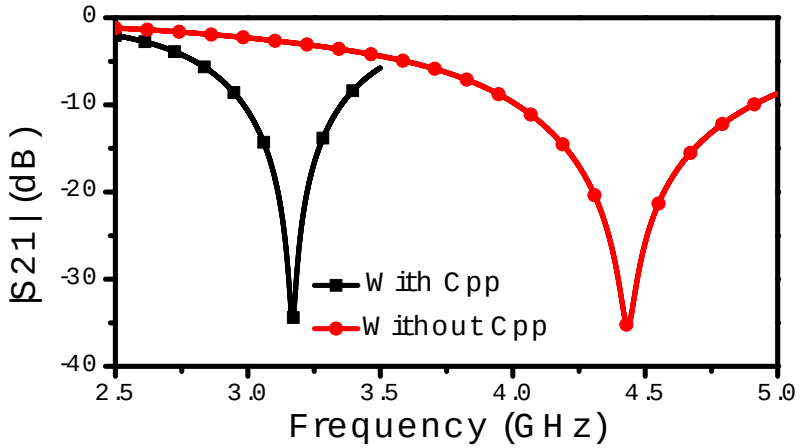

Figure 6.6: The scattering parameter $|S_{21}|$ dB of the sensor with and without the inserted C_{pp}

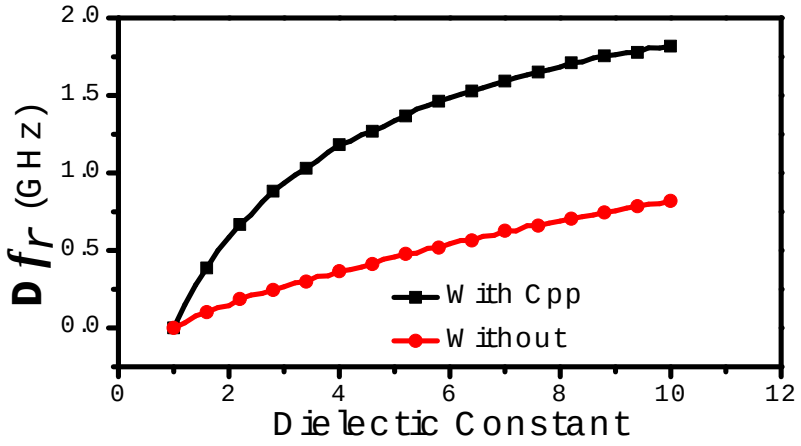

Figure 6.7: The shift in the resonance frequency as a function of the permittivity of a dielectric slab obtained using full-wave numerical simulation. The relative permittivity of the slab was varied from 1 to 10 in increments of 0.2.

using a dielectric glue that prevents any liquid material from flowing outside the channel. Note that the calibration of the sensor which entails determining the minimum transmission frequency without the presence of the MUT was performed after the channel was made. The fabricated sensor is shown in figure 6.8. The sensor was tested to detect the changes in

the concentration of two-dielectric fluids: Cyclohexane and Chloroform with permittivities of 2.02 and 4.81, respectively (taken from [61]). The concentration of the mixture of the two fluids was prepared as the following. The volume of the mixture is 1 mL where the chloroform was the reference. To create 60% concentration, 0.6 mL of chloroform is mixed with 0.4 mL of Cyclohexane. The concentration was varied from 0% to 80% in increments of 10%. Figure 6.9 shows the shift in the resonance frequency versus the changes in the fluid concentrations. The sensor was able to detect a concentration of 5% with an enhancement of 304% compared to the sensor without the C_{PP}. Additionally, as figure 6.9 shows, the new sensor is significantly more sensitive than the one without the three-dimensional capacitor. It can be noticed that the rate of change of the resonant frequency shift with respect to the concentration is similar for the two sensors (with and without the additional capacitor), however, the absolute shift in the resonant frequency in the new design is considerably higher and hence the sensitivity. Therefore, in field applications where the VNA needs to be replaced by compact microwave circuitry, the higher sensitivity feature enables the use of less expensive devices requiring smaller dynamic range.

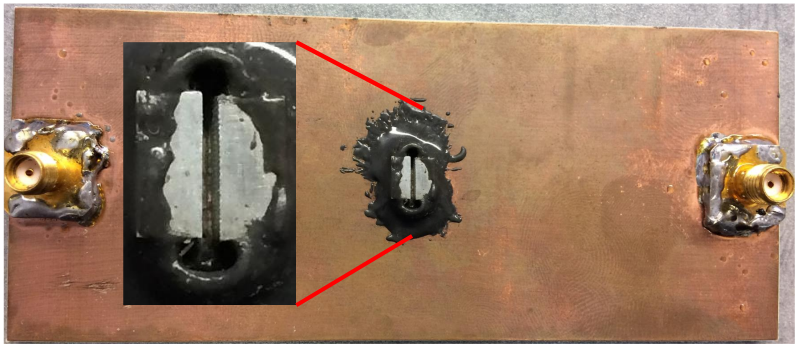

Figure 6.8: The fabricated CELCR sensor with the three-dimensional capacitor made of two-aluminium cubes. The dark grey material is the glue used to contain any liquid material within the capacitor channel. The feed microstrip line is on the other side (not shown.)

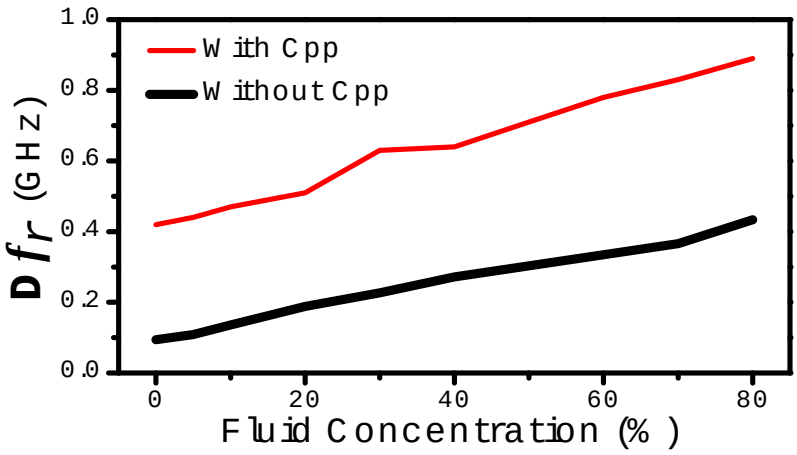

Figure 6.9: The experimental results show the shift in the resonance frequency as a function of the fluid concentration.

6.5 Conclusion

In this chapter, a concept to increase the sensitivity of planar electrically-small resonators when used as near-field sensors was introduced. The concept is based on increasing the overall capacitance of the sensor and especially the capacitance that interacts with the MUTs. One possible realization that was adopted in this chapter was the placement of a capacitor on top of a planar sensor. As a validation, the sensor was fabricated using PCB technology and verified experimentally to detect the concentration of fluid materials. The sensor presented here is expected to be useful in the a-lab-on-a chip and other quality control and environmental monitoring applications. Moreover, three-dimensional capacitors with planar structures then triggered the idea of implementing the concept for split-ring resonators (SRRs) since such resonators offer the advantage of miniaturized sensing areas (the splits).

Chapter 7

Sensitivity and Tunability Enhancement of SRRs for Fluidic and Microfluidic Technologies, Fluid-Level Detection Applications, and Near-Field Scanning Microscopy

7.1 Introduction

Although the SRRs show higher quality factors, the CSRRs show higher sensitivities to detect the presence of dielectric materials [31] since the CSRRs have larger sensing areas (maximum concentrated electric fields based areas) compared to the SRRs. However, the small sensing areas in the SRRs can be considered as more attractive in fluidic and microfluidic applications if the size of sensing areas has higher priority from an application point of view. Furthermore, although the splits (the gaps) in the SRRs create capacitances that are responsible for making normal-resonating-closed loops to exhibit resonance phenomena at lower frequencies, it is difficult to tune the resonance frequency without changing the

lengths of the resonators [62]. Alternatively, the gap capacitance can be increased, yet the miniaturization process will be limited by fabrication capabilities. In addition, increasing the capacitance of series resonators such as SRRs will decrease the quality factors. In fact, it is difficult to design on demand a new sensor for a specific band of frequency, which might be required by applications such as point-of-care lab applications. Of course, varactor-loaded split ring resonators can be utilized to tune the resonance frequencies [63], but the concept can add some difficulty from the practical point of view, especially in the sensing applications.

In this chapter, a novel microwave sensor based on SRRs and three-dimensional capacitors (C_{pp}) is proposed to enhance the sensitivity and make the tunability (working at a specific resonance frequency) much easier and flexible. In fact, by using C_{pp} with the resonant structures (SRRs), three objectives in the same time were achieved, enhancing tunability and the sensitivity, creating a new probe that can be utilized for sensing fluid materials and detecting their levels, and designing probes for near-field scanning microscopy based technologies. In addition, the sensing area is no longer in the same plane with transmission lines that are used for the excitation. The interactions between the MUTs and the transmission lines [64] are thus totally eliminated. The proposed sensor is designed and evaluated using the full-wave simulation (ANSYS HFSS). Then, two sensors are fabricated with and without C_{pp} for making a comparison by detecting the presence of two fluid materials. The proposed sensor shows the higher sensitivity of almost 700%. In addition, the proposed sensor is utilized to detect the levels of the fluid materials.

7.2 The Utilization of Three-Dimensional Capacitors with SRRs

Figure 7.1(a) shows an SRR with the length (L) coupled to a two-port microstrip line system. Having the right frequency associated with the design specification of the SRR, the microstrip line, and the host material (substrate), the system will exhibit a band-gap response, which can be called as a quasistatic resonance since the SRR is a quasi-static resonator compared to the excitation wavelength. At the resonance frequency, the devel-

oped circulating current path creates magnetic fields that can be modeled as an inductance (L_r), whereas the developed voltage difference creates electric fields at the gap (S) that can be modeled as a capacitance (C_r).

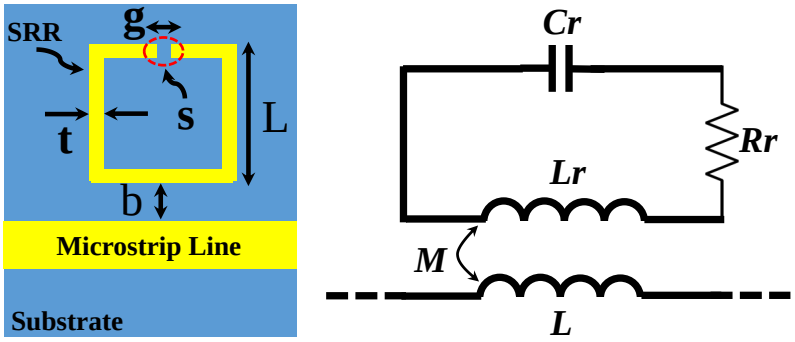

Figure 7.1: (a) The schematic of an SRR mutually coupled to a microstrip line (b) Circuit model of the SRR [3], where M represents the mutual coupling. Lr, C_r, and R_r represent the inductance, capacitance, and the resistance of the SRR, respectively. L is the inductance of the transmission line per unit length.

Disturbing the electric fields at the gap by dielectric materials, the system can be used as near-field sensors. However, most of the electric fields are concentrated in the substrate, thus, weakening the interactions with the MUTs, hence, limiting the sensitivity [48]. Therefore, utilizing a C_{pp} as shown in figure 7.2(a) will enhance the total electric field dramatically in the sensing area (the free space), hence, the sensitivity. The resonance frequency of the SRR occurring at the minimum magnitude of the transmission coefficient ($|S_{21}|$) will thus exhibit a change. Since the C_{pp} will be in parallel to C_r, the overall capacitance of the new resonator will increase; it is expected that the resonance frequency will be shifted to a lower frequency to satisfy the new enforced boundary condition by C_{pp} that is given by

$$f_z = \frac{1}{2\pi\sqrt{L_r(C_{r0} + C_{pp})}} \tag{7.1}$$

where C_{r0} is the capacitance of the SRR before the inserted C_{PP}. However, for the overall

quality factor for the new configuration is not intuitive to be predicted since the quality factor of the SRR as a series resonator is a function of many parameters, L_r, C_{pp}, and R_r that is given by

$$Q = \frac{1}{R_r}\sqrt{\frac{L_r}{C_r}} \tag{7.2}$$

Thus, by using one of the implications of Eq. 7.2, it might be concluded that the quality factor will decrease, which is not necessarily to be a valid conclusion unless the quality factor is evaluated numerically or experimentally. However, from the Eq. 7.2, it can be noticed that the quality factor will be more sensitive to changes in the R_r than the changes in C_r since the ratio of L_r/C_r is under the square root. Since the insertion of the C_{pp} will add a resistance R_{pp} parallel to the R_r, the new quality factor is given by

$$Q = \frac{R_r R_{pp}}{R_r + R_{pp}}\sqrt{\frac{L_r}{C_r + C_{pp}}} \tag{7.3}$$

Thus, if the R_{pp} will be smaller than R_r, the quality factor will be improved. Moreover, since the C_{pp} is a function of the metal bars' length (d), the resonance frequency of the new resonator will be a function of the length as well that is given by

$$f_z(d) = \frac{1}{2\pi\sqrt{L_r(C_{r0} + C_{pp}(d))}} \tag{7.4}$$

Therefore, one of the implications of Eq. 7.4 is that a new degree of freedom is added to the system vertically in the **Z** direction, which makes the tunability of the resonance frequency is flexible. In addition, since the C_{pp} is a function of the gap between the bars (g), it can also be utilized to tune the resonance frequency. In addition, the C_{pp} can be used as a sensitive probe to detect the levels of fluids. Since the material between the metallic bars will affect the C_{pp}, the resonance frequency is expected to exhibit a shift.

7.3 Sensor Design and Validation

In this work, the proposed sensor is based on a two-port microstrip line system designed based on a 50-Ω characteristic impedance, which is utilized to excite a loaded SRR with C_{pp}.

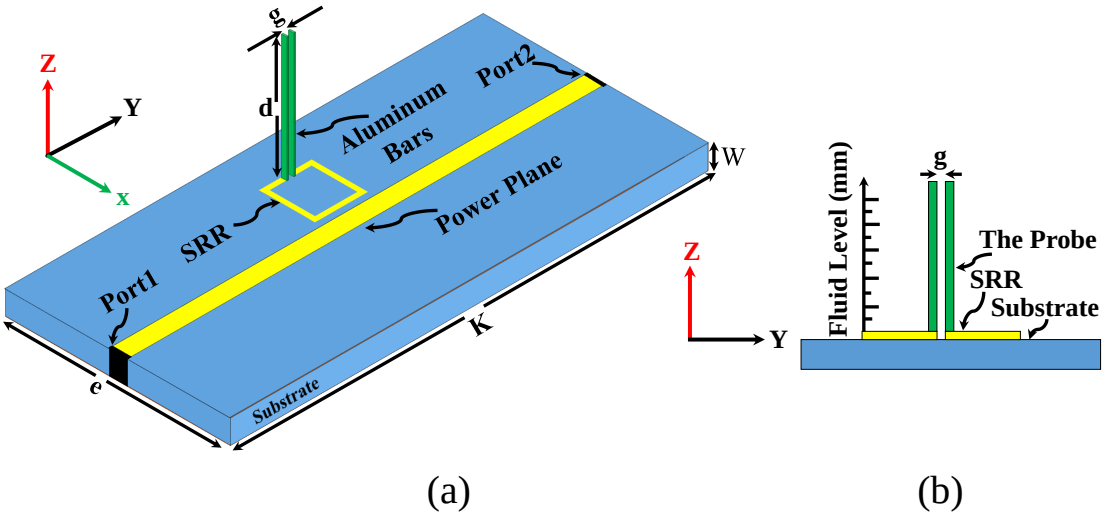

Figure 7.2: (a) The schematic of the sensor where the SRR excited by two-port microstrip line system. (b) The side view of the sensor where the shown probe can be divided into a small distance to measure the fluid level

Since the response of the system will be measured in terms of the minimum transmission coefficient ($|S_{21}|$), the response will be extracted using a 50-Ω vector network analyzer (VNA). For designing the microstrip line with the 50-Ω characteristic impedance, the line width is 1.63 mm on a Rogers RO4350 substrate with a thickness of W = 0.75 mm and a relative permittivity of 3.66 and a loss tangent of 0.0031. The design specification shown in figures 7.1(a) and 7.2(a) are L = 7.5 mm, t = a = b = g = 0.5 mm, K = 100 mm, and e = 50 mm. The length (d) in figure 7.2(a) will have two different values 1 and 4 mm to show the changes in the resonance frequency as a function of the length (d).

Figure 7.3 shows the response of the sensor with and without C_{pp}. Without the C_{pp}, the resonance frequency is 3.458 GHz. Note that, there is no particular reason for choosing this frequency except for being within a suitable range of frequency of our VNA. In the case of C_{pp} with two different values of d (1 and 4 mm), the resonance frequency exhibits changes to lower frequencies 3.282 and 2.828 GHz, respectively. Based on Eq. 7.4 and figure 7.3, it is an evident that the resonance frequency is inversely proportional to the length d. The change in d from 1 to 4 mm makes the resonance frequency to exhibit a change of 546 MHz

or 16.6%. The resonance frequency can thus be tuneable using a different length of the C_{pp}. Figure 7.4 shows the resonance frequency (f_z) and the minimum of the $|S_{21}|$ versus the length of the C_{pp} (bars length). The length (d) is varied between 1 to 29 mm with the step value of 0.5 mm. It has been noticed that the minimum of $|S_{21}|$ and the length of the C_{pp} are inversely proportional, which makes the minimum of $|S_{21}|$ decreased with the increase in the length.

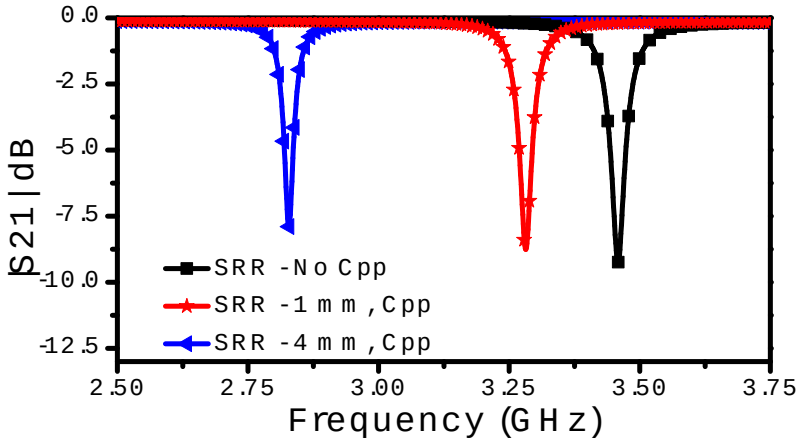

Figure 7.3: The transmission coefficient of the sensor for two-different length (d), 1 and 4 mm in the presence of the free space medium. The results are extracted using the numerical simulation (HFSS)

To investigate the relation between the minimum of $|S_{21}|$ and the length of the C_{pp}, one can extract the coupling factor (κ) versus the length of the C_{pp} using the information of the scattering parameter $|S_{21(f_z)}|$ at the resonance frequency. In two-port systems coupled to SRRs, the transmission powers to the output ports are minimal at the resonance frequencies. These type of resonators are categorized under the band-gap based resonators where the coupling factor can be calculated as [65]

$$\kappa = \frac{1 - |S_{21(f_z)}|}{|S_{21(f_z)}|} \tag{7.5}$$

Figure 7.5 shows the coupling factor versus the length of the C_{pp} that can reveal the underlying reason of the decrease in the magnitude of $|S_{21(f_z)}|$ with the increase in the

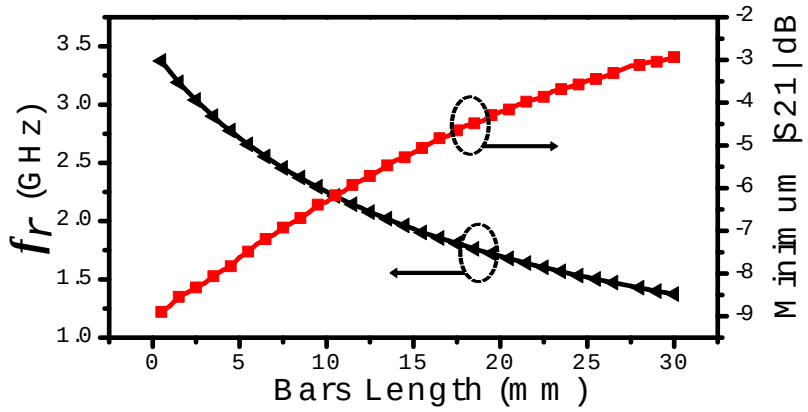

Figure 7.4: The resonance frequency (f_z) and the minimum of the $|S_{21}|$ versus the length of the C_{pp} (bars length)

length of C_{pp} as shown in figure 7.4. The coupling factor becomes smaller with the increase in the length.

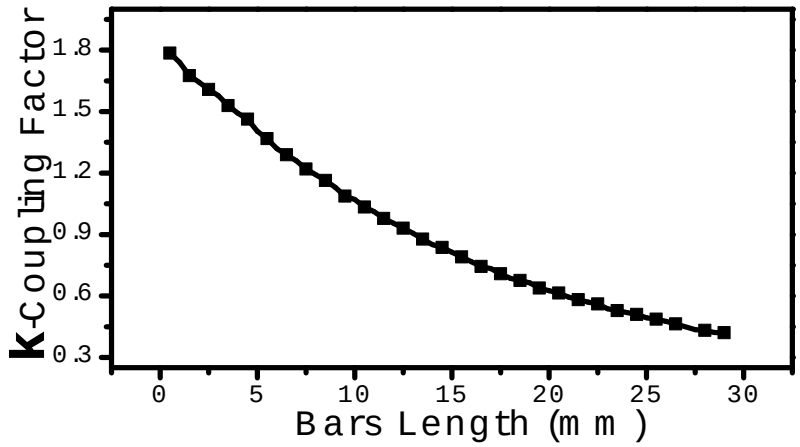

Figure 7.5: The coupling factor (κ) versus the length of the C_{pp}.

Moreover, the quality factor is evaluated at -3 dB based on the following equation

$$Q_L = \frac{f_z}{f_2 - f_1} \tag{7.6}$$

where f_z is the resonance frequency and f_1 and f_2 are the frequencies where a line is crossing the $|S_{21}|$ at -3 dB. The quality factor for the SRR without C_{pp} is 70.6, whereas

in the case of C_{pp} with the lengths 1 and 4 mm, the quality factor is increased to 78.14 and 97.5, respectively. If the increase in the total capacitance of the SRR is responsible for improving the quality factor of the proposed sensor, this implies that these results might contradict the implication of Eq. 7.3. However, this can be resolved from a different prospective. Since the quality factor is more sensitive to changes in the total resistance of the resonator, the increase can be attributed to the decrease in the overall resistance. The C_{pp} will make the electric fields to concentrate more in the free space, which it is a lossless medium. It is thus expected that the implementation of C_{pp} will increase the quality factor. However, the coupling factor will be decreased. Figure 7.6 shows the loaded and unloaded quality factor for the proposed sensor versus the length of C_{pp}. The unloaded quality factor is given by

$$Q_0 = Q_L(\kappa + 1) \tag{7.7}$$

When the length d is 29 mm, the loaded and unloaded quality factor are 1555.5 and 2209, respectively. Based on our knowledge, the improvement in the quality factor of 1555 compared to 70.6 of the planar SRR is significantly higher than what can be achieved using planar resonators working in the same range of frequency.

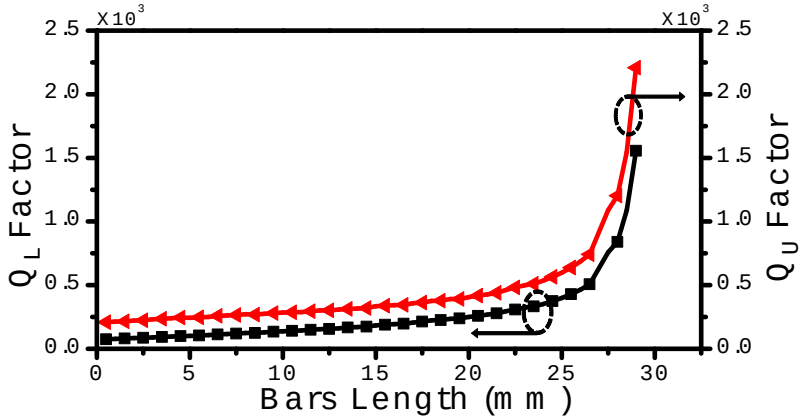

Figure 7.6: The loaded and unloaded quality factor of the proposed sensor versus the length of C_{pp}

Generally speaking, the improvement in the quality factors in microwave resonators from sensing applications point of view has only beneficial use if and only if the enhanced

fields associated with the quality factor are in the sensing areas. Otherwise, the increase in the quality factors in different areas, e.g., substrates, will be beneficial for other applications such as microwave filters, which is not our interests in this work. Therefore, evaluating the total electric fields in the region between the metal bars (C_{pp}) is essential to investigate the correlation between the quality factor and a possible increase in the sensitivity. Figure 7.7 shows the magnitude of the total electric field of the SRR with and without C_{pp} at the resonance frequency in the **Z** direction where the length of the probe increases. In addition, figure 7.7 shows the field enhancement in term of the difference in the total electric field of the SRR with and without C_{pp}. It is an evident that the field is enhanced dramatically inside the C_{pp} (the sensing area for fluid materials).

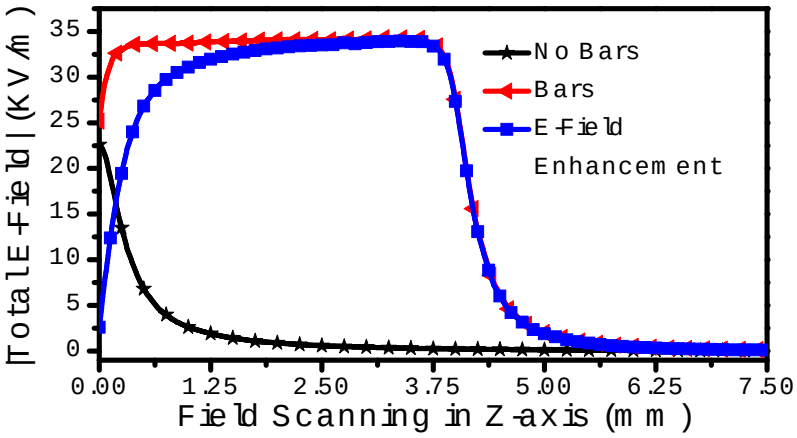

Figure 7.7: The magnitude of the total electric field in the **Z** direction where the length of the probe increases versus the frequency

7.4 Fabrication and Experimental Results

For experimental evaluation of the proposed sensor, an SRR coupled to a two-port microstrip line is fabricated using printed circuit board technology (PCB). Then, two aluminum bars are implemented on the top of SRR at the small channel S presented in figure 7.1 using conductive glue. Note that a calibration where the altered resonance frequency occurs as a result of the fabrication tolerance will be taken into account through

the measurement procedure to create a reference (the free space). Figures 7.8(a) and 7.9 show the fabricated sensor with the aluminum bars and its response ($|S_{21}|$), respectively. Also, to evaluate the sensitivity enhancement of the proposed sensor, a sensor without C_{pp} is fabricated as shown in figure 7.8(b) where a plastic glue shown in figure 7.8(b) is only to contain the fluids during the measurement. The glue effects will be calibrated as well. Figure 7.10 shows the experimental results the fabricated SRR sensor with and without the plastic glue container in the presence of the free space.

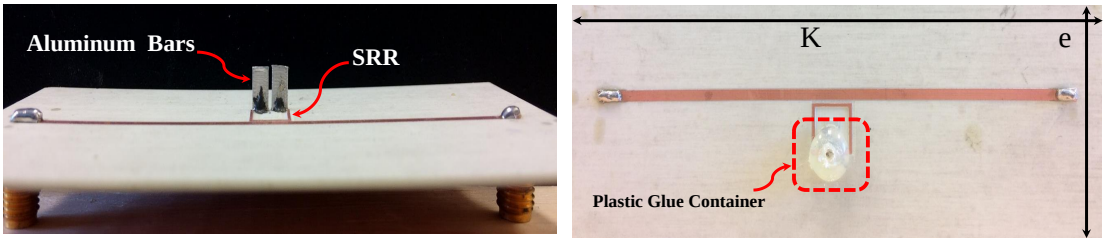

(a) (b)

Figure 7.8: (a) The fabricated sensor with the three-dimensional capacitor, C_{pp} made of two aluminum bars (b) The sensor without the three-dimensional capacitor, where K and e are 100 and 50 mm, respectively. The plastic glue container was used to contain any liquid material within the capacitor channel

Furthermore, the proposed sensor is used to detect the presence of two-dielectric fluids: chloroform and dichloromethane with permittivities of 4.81 and 8.93, respectively (taken from [61]). Compared to the SRR without C_{pp}, the proposed sensor shows higher sensitivities of 700 % and 374.5 % to detect the present of chloroform and dichloromethane, respectively. The experimental result is shown in figure 7.11 for the two sensors with and without C_{pp}. Moreover, the proposed sensor is tested to detect the levels of fluid materials. Moreover, since the C_{pp} has a length normal to the surface of the SRR, the sensor can be used as a probe to detect the level of fluids. The probe (aluminum bars) shown in figure 7.8(a) is immersed in the fluids with a step of 0.25 mm, which would be difficult or impossible to achieve without C_{pp}. Figure 7.12 shows the experimental result of the proposed sensor that is used to detect the change in the levels of the two fluid materials, chloroform and dichloromethane. The sensor can have potential applications in

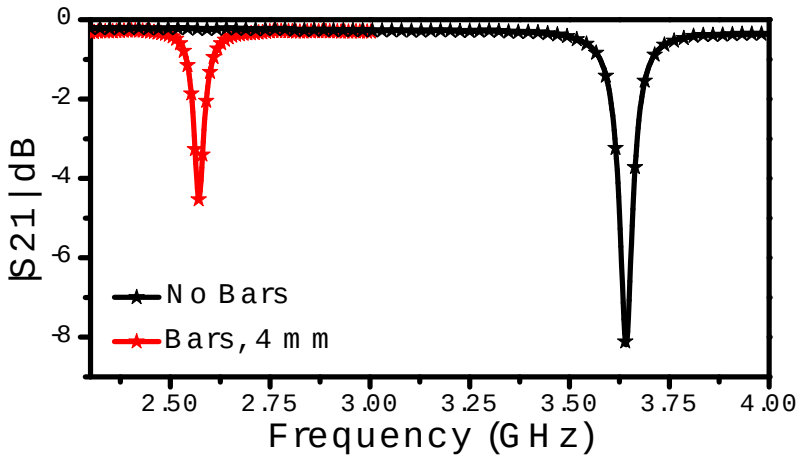

Figure 7.9: The experimental results of the fabricated SRR sensor with and without the three-dimensional capacitor C_{PP} of the sensor response in the presence of the free space medium

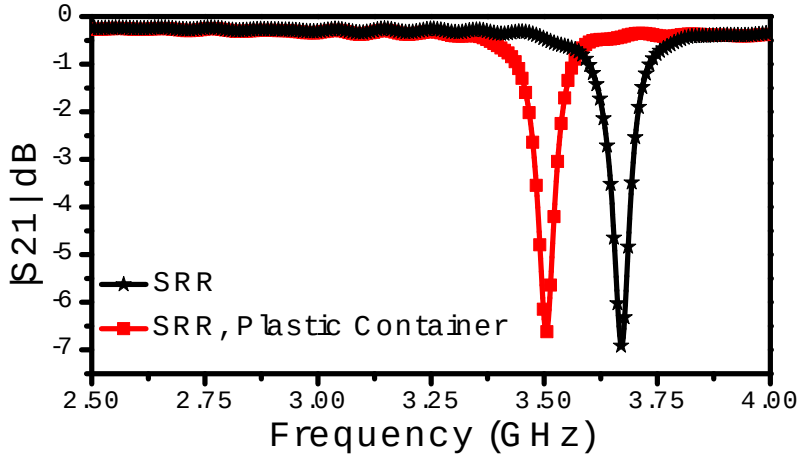

Figure 7.10: The experimental result of the fabricated SRR sensor with and without a plastic glue container in the presence of the free space

technologies that depend on measuring the level of fluids.

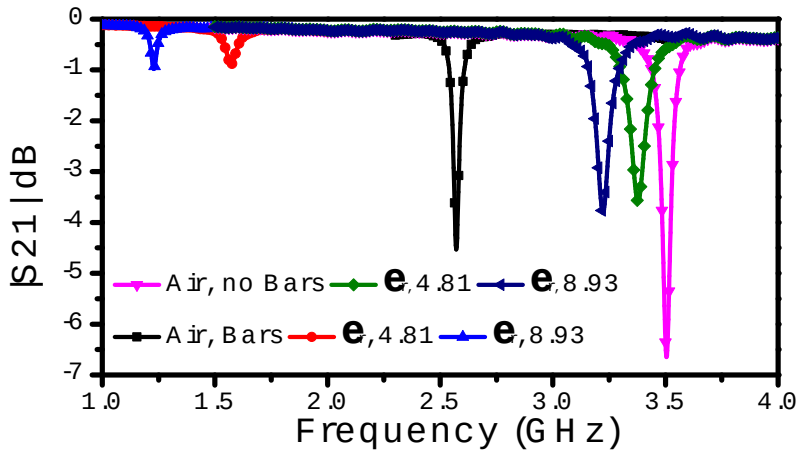

Figure 7.11: The experimental result for the two sensors with and without C_{pp} detecting the two fluid materials, chloroform and dichloromethane

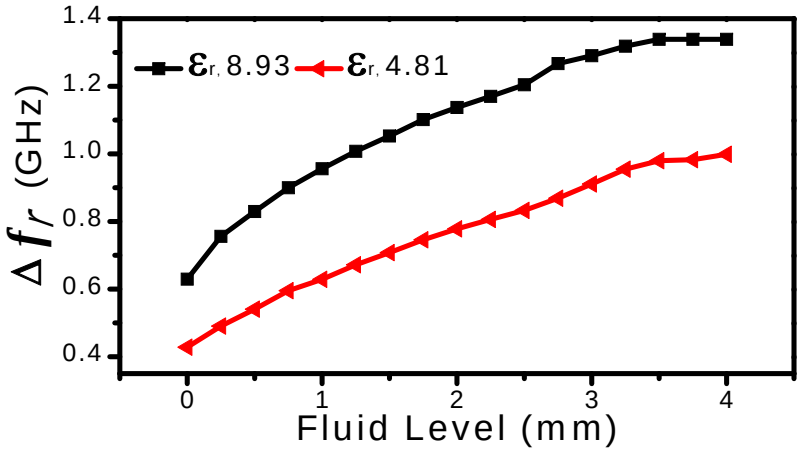

Figure 7.12: The experimental result of the shift resonance frequency versus the fluid levels for the two fluid materials, chloroform and dichloromethane

7.5 Coupling Factor Enhancement for SRRs

So far, it has been proven that the three-dimensional capacitance (C_{pp}) enhances the sensitivity and improves the tunability of the SRR sensor. However, from figures 7.4 and 7.5, we can understand that the increase in the resonator's capacitance C_{pp} either through the

utilization of C_{pp} or by loading the SRR with the MUTs can exponentially reduce the coupling between the microstrip line and the resonator. Therefore, the use of such resonator as a sensor in applications such as material characterization and detection will suffer from the poor coupling, especially for the higher dielectric materials.

Fundamentally, the SRR are inductively and capacitively coupled to the transmission line through the generated magnetic and electric fields as shown in figure 7.5. Since the SRR is a loop, it is expected that the SRR is dominantly coupled to the line through the magnetic field. If the capacitive coupling can be enhanced, the general coupling will be improved.

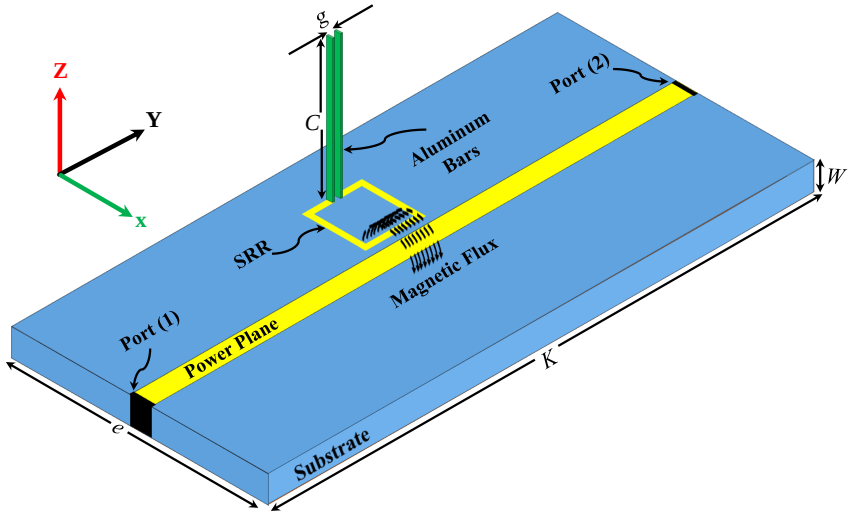

Figure 7.13: The schematic of the sensor where the SRR coupled to the two-port microstrip line system by the magnetic flux

For enhancing the capacitive coupling, the metallic edge (b in figure 7.1) between the SRR and the microstrip line can be increased vertically in the z direction, which will increase the cross area for the enhanced field. Figure 7.14 shows the proposed SRR with the edge coupling, where m and t are the height and the thickness of the edge. To test the concept, the design specification of the coupling edge is m varied from 0 to 1 mm with the step value of 0.05 mm and b = t = 0.5 mm, whereas the length of the arm of the probe is C = 4 mm. Figure 7.15 shows the minimum $|S_{21}|$ in dB versus the edge-coupling height (m).

It is clear that the minimum $|S_{21}|$ is improved with the increase in the height of the edge, which is the result of the enhancement in the coupling factor. By using equation (7.5), the coupling factor (κ) versus the edge-coupling height (m) can be extracted as shown in Fig 7.16. To observe the enhancement in the coupling factor, figure 7.17 shows the coupling factor for the sensor without and with the coupling edge (m = 1 mm and t = 0.5 mm), where the length of the probe (C) is varied from 0.5 to 29 mm with the step value of 0.5 mm. It is clear that the sensitivity of the changes in the coupling factor is less in the case of the utilization of the edge coupling.

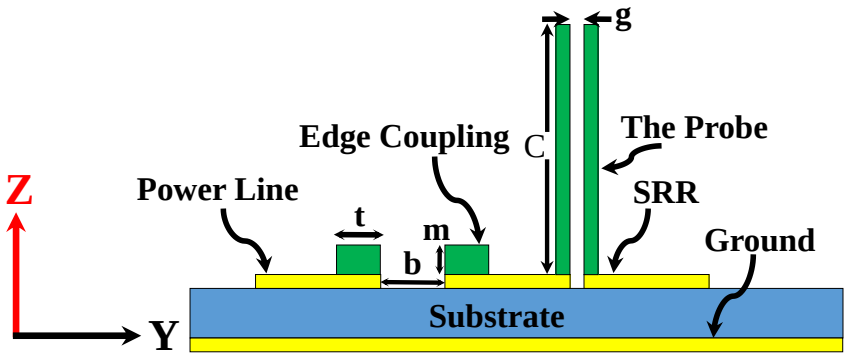

Figure 7.14: The schematic of the sensor where the SRR coupled to the two-port microstrip line system by the magnetic flux

To observe the difference in the scattering parameters ($|S_{11}|$ and $|S_{21}|$), the sensor without and with the coupling edge (m = 1 mm and t = 0.5 mm) is compared. By using the numerical simulation (HFSS), the scattering parameters are extracted as shown in figure 7.18. For a lossless two-port network, the unitary condition can be stated as [16]

$$|S_{11}|^2 + |S_{21}|^2 = 1 \tag{7.8}$$

By applying equation 7.8 on the results shown in figure 7.18, the following results are extracted. Applying the unitary condition in the case of no coupling edge (m = 0) gives

$$|0.6|^2 + |0.4|^2 = 0.5 \neq 1$$

which means the system is not lossless and the total losses are 0.5. On the other hand,

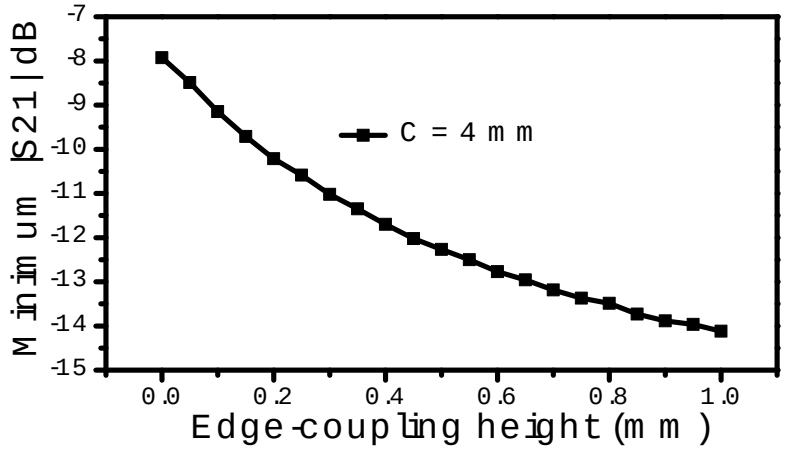

Figure 7.15: The minimum $|S_{21}|$ in dB versus the edge-coupling height (m), where m is varied from 0 to 1 mm with the step value of 0.05 mm and b = t = 0.5 mm, whereas the length of the arm of the probe is C = 4 mm

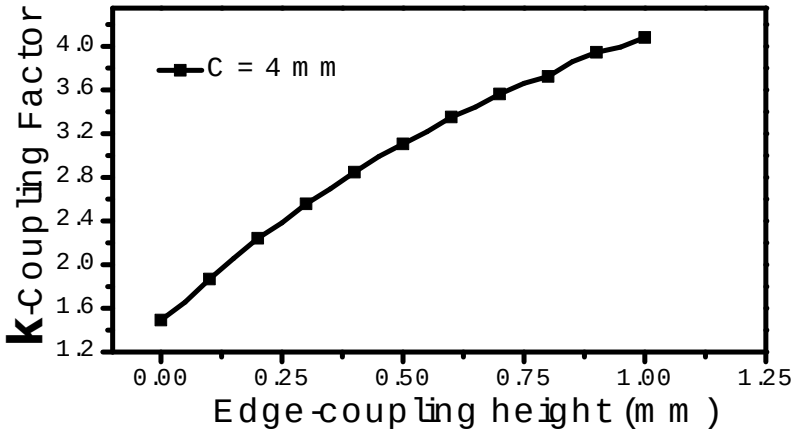

Figure 7.16: The coupling factor (κ) versus the edge-coupling height (m)

applying the unitary condition in the case of coupling edge (m = 1) gives

$$|0.8051|^2 + |0.1835|^2 = 0.68 \neq 1$$

which means the total losses are reduced to 0.318. It shows that the coupling edge enhances the field concentration in the probe volume (the free space). It is thus expected that the sensitivity of the sensor will be enhanced. To test the sensitivity enhancement, the sensor

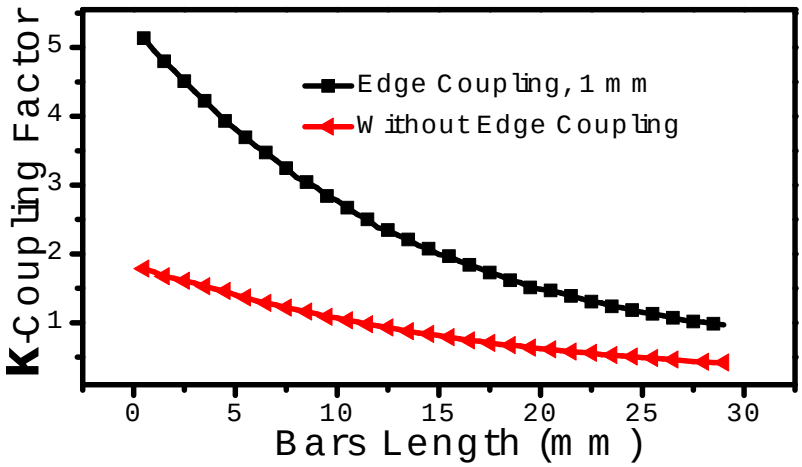

Figure 7.17: The coupling factor (κ) versus the probe length (C), where the C is varied from 0.5 to 29 mm with the step value of the 0.5 mm

is utilized to detect the presence of a dielectric material, where the dielectric constant is varied from 1 to 10 with the step value of 0.5. Four cases are compared: 1- the SRR without the probe 2- the SRR with the probe (C = 1 mm) 3- the SRR with the probe (C = 4 mm) 4- the SRR with the probe (C = 4 mm) and the coupling edge (m = 1 mm). It is clear that the edge coupling enhances the sensitivity and the dynamic range of the sensor.

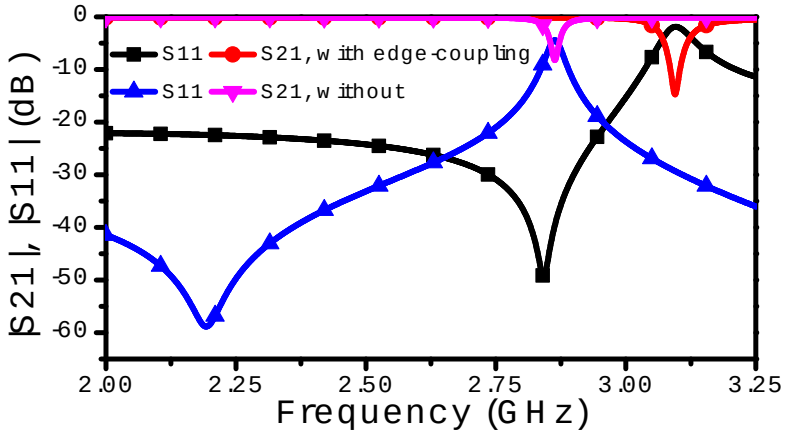

Figure 7.18: The scattering parameters ($|S_{11}|$ and $|S_{21}|$), the sensor without and with the coupling edge (m = 1 mm and t = 0.5 mm)

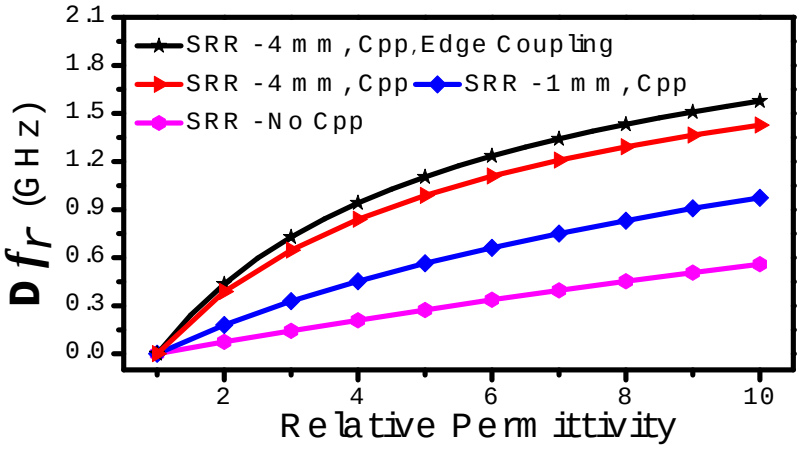

Figure 7.19: The shift in the resonance frequency versus the relative permittivity

7.6 SRRs and Three-Dimensional Capacitors for Near-Field Microscopy

In near-field scanning microscopy based techniques, the stand-off distance between the probes and the MUTs determines the spatial resolution (see figure 1.2). However, it has been shown that reducing the stand-off distance will increase the interaction between the MUTs and the microstrip lines used for the excitation. Thus, as mentioned in the introduction, the three-dimensional capacitors (C_{pp}) will reduce the interaction between the MUTs and the microstrip lines used for the excitation. Not only that, the size of the probe will not be anymore the whole size of the SRRs. The probe will be the size of the separation between the parallel capacitors (C_{pp}), which can be easily controlled. Furthermore, the C_{pp} will help to tune the resonance frequency of the probe since the length of the probe is in the vatical z direction (a new degree of freedom). This tuning flexibility is not available for the planar SRRs.

For designing near-field scanning microscopy based probes, the numerical simulation (HFSS) is utilized to study the spatial variation of the electric field in close proximity. Figure 7.20 shows the schematic of the probe, where the dashed lines is visual aids used

for plotting the variations in the field over the space, z is the the stand-off distance, and t is the thickness of the probe's arm, and g is the gap. Two SRRs with and without C_{pp} are designed where C = 4 mm, L = 7.5 mm, g = t = 0.5 mm, and z = 5 μm. The length of the dashed line is 11 mm. Figures 7.21(a) and 7.21(b) show the total electric field variation along the dashed line for the SRR without and with C_{pp}, respectively. In the two figures, there are four peaks in the total electric field corresponding to the edge effects.

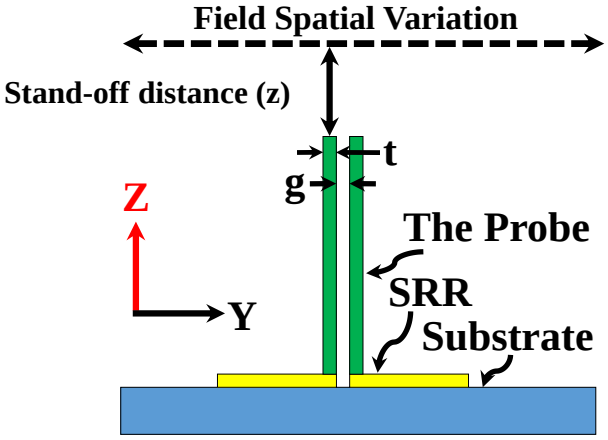

Figure 7.20: The schematic of the probe, where the dashed lines is visual aids used for plotting the variations in the field over the space, z is the the stand-off distance, and t is the thickness of the probe's arm, and g is the gap

Although the total electric field is higher for the case of the SRR without the C_{pp}, the total electric field of SRR with C_{pp} has the total electric field localized in close proximity of the probe. Since the resolution in the near-field scanning microscopy depends on the spatial variation of the field to be localized in the space, the SRRs with C_{pp} is suitable for designing the sensor. In addition, the new probe will be isolated from the surface of the resonators, hence, minimizing the interaction. Thus, these features make the SRRs with C_{pp} strong candidates for designing the sensor to image the surface of the dielectric materials.

Furthermore, the spatial variation and the localization of the total electric field are investigated with respect to different variations in the design specifications as shown in figure 7.20 (L, t, and g), where the stand-off distance is kept the same (5 μm) and the arm

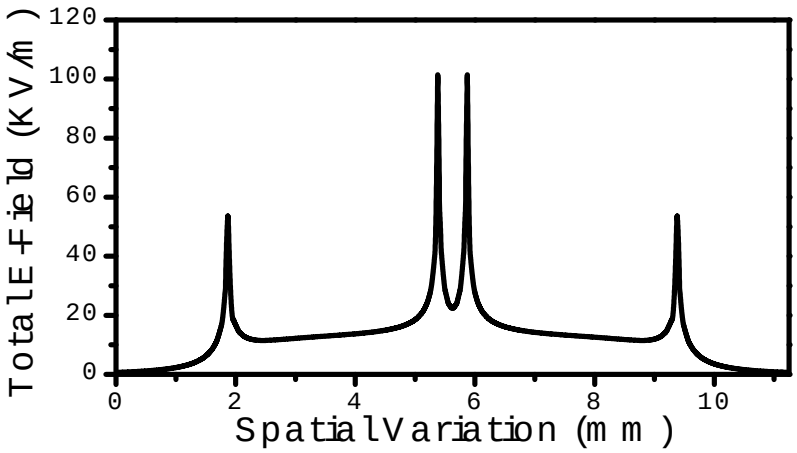

(a)

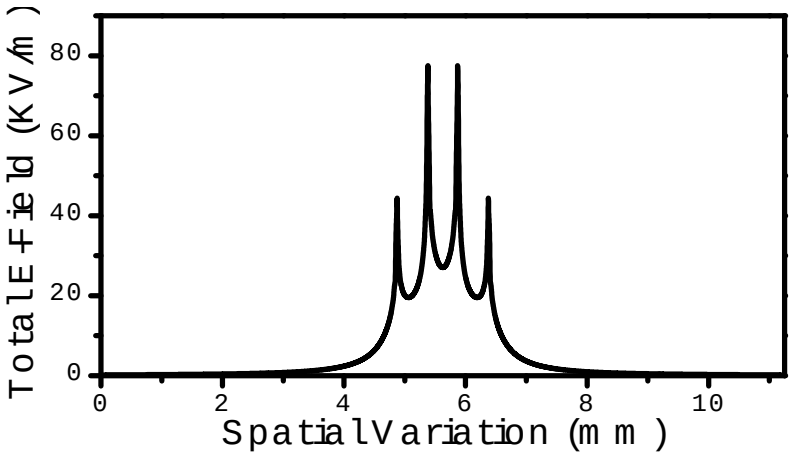

(b)

Figure 7.21: (a) The total electric field variation along the dashed line shown in figure 7.20 for the SRR without C_{pp} (b) for the SRR with C_{pp}

length (C) = 4 mm. By shortening the lengths of the SRRs, the magnetic field is reduced, hence, the inductance. Based on the equation. (7.1), the resonance frequency will shift to higher frequencies. It is thus expected that the magnitude of the electric field will be enhanced. Two general cases are considered. For L = 5.5 mm, three cases are studied, 1) g = 0.5 mm and t = 0.5 mm shown in figure 7.22 2) g = 0.05 and t = 0.5 mm shown in

figure 7.23 3) g = 0.05 and t = 0.05 mm shown in figure 7.24, whereas for L = 3.5 mm, one case is studied that g = 0.05 mm and t = 0.5 mm shown in figure 7.25.

By comparing the spatial variation of the electric field shown in figure 7.21(b) (for L = 7.5 mm) and figure 7.22 (for L = 5.5 mm), it can be observed that the magnitude of the maximum field (the middle-two peaks) is enhanced [1]. This enhancement can be attributed to the fact that the resonance frequency of L = 5.5 mm is higher due to the reduction in the inductance. In addition, by comparing the three cases shown in figures 7.22, 7.23, and 7.24 (for L = 5.5 mm), the smaller the probe arms' thickness (t) and the gap (g) are, the higher the magnitude of the total electric field.

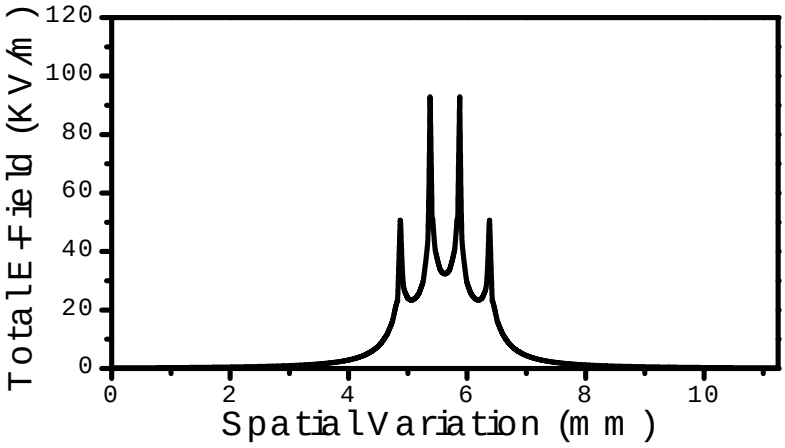

Figure 7.22: The total electric field versus the spatial variation for L = 5.5 mm, g = 0.5 mm and t = 0.5 mm

[1] This can explain the reason behind the higher sensitivity for electrically-small resonators when the lengths of the resonators are becoming smaller (see figure 2.10)

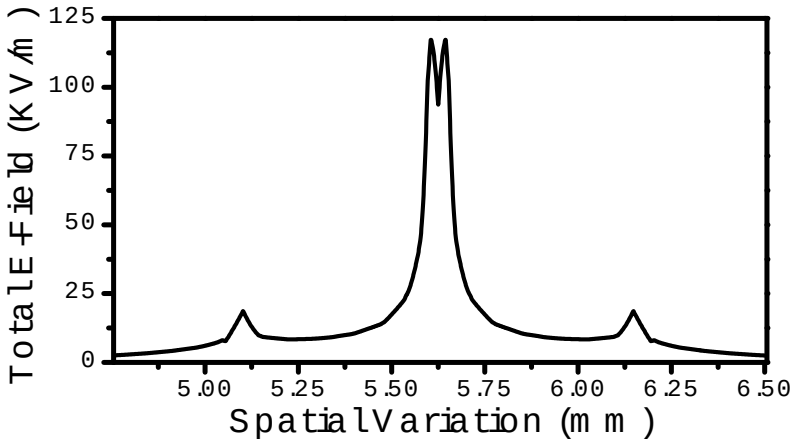

Figure 7.23: The total electric field versus the spatial variation for L = 5.5 mm, g = 0.05 mm and t = 0.5 mm

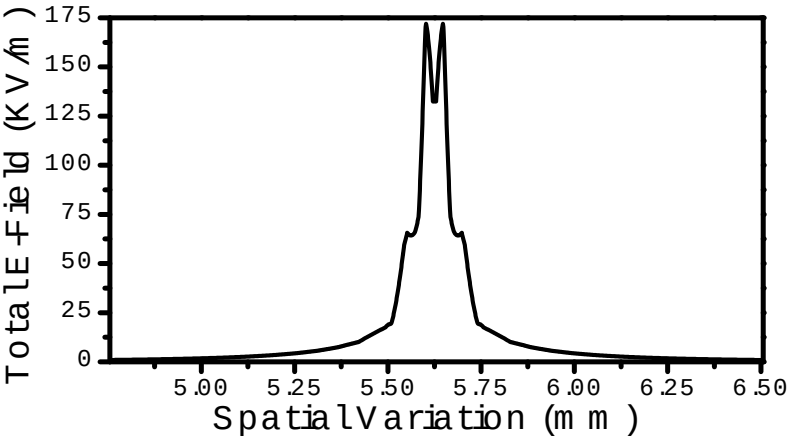

Figure 7.24: The total electric field versus the spatial variation for L = 5.5 mm, g = 0.05 mm and t = 0.05 mm

7.7 SRRs with Three-Dimensional Capacitors and Flanges

The sensing areas of SRRs are limited to the size of the gaps (the splits). Increasing the gap size (g) to cover more surface areas of the MUTs will increase the resonance frequency to higher frequencies, which make the resonators becoming electrically large. By utilizing

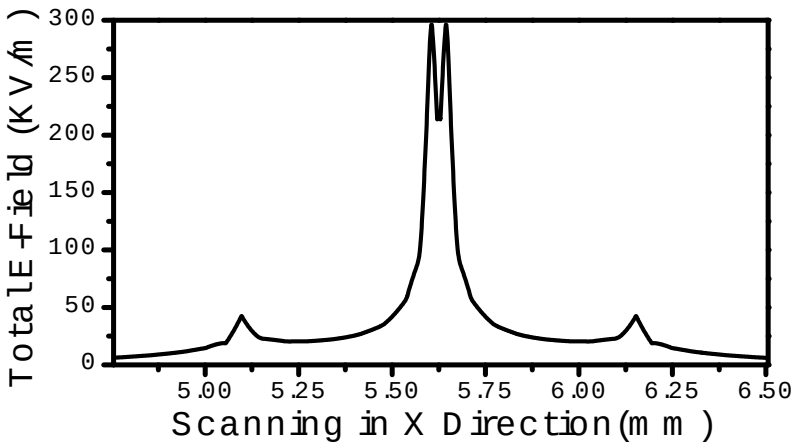

Figure 7.25: The total electric field versus the spatial variation for L = 3.5 mm, g = 0.05 mm and t = 0.5 mm

the three-dimensional capacitors and adding flanges, the sensing area can be enlarged and simultaneously the resonance frequency can be tune to lower frequencies. The schematic of the proposed sensor with the flange is shown in figure 7.26, where R is the length of the flange. To test the effects of the flange on the resonance frequency of the SRRs, an SRR with L = 7.5 mm, C = 4 mm, and g = 0.5 mm is modeled. The flange length is varied from 0.5 mm to 8 mm with the step value of 0.5 mm. The effects of the flange on the resonance frequent are minimal at the lower length as shown in figure 7.27. It might appear from figure 7.27 that the flange has minimal effects on the sensitivity of the SRRs. However, when the flange are placed close to the dielectric materials, the electric field distribution that was presented in figures 7.21 to 7.25 will be disturbed to satisify the new boundary condition. In particular, there will be a new parallel capacitors between the flange and the dielectric materials. To investigate that, the SRR with the C_{pp} and flange is tested to detect the presence of a dielectric slab with the thickness of 3 mm and relative permittivity of 4. Similarly, the flange length is varied from 0.5 mm to 8 mm with the step value of 0.5 mm. The response of the sensor is extracted using the numerical simulation (HFSS). Figure 7.28 shows the shift in the resonance frequency versus the flange length detecting the presence of the dielectric slab. One can observe that the sensitivity of the probe is increased since the flange will provide larger areas for the interaction to occur.

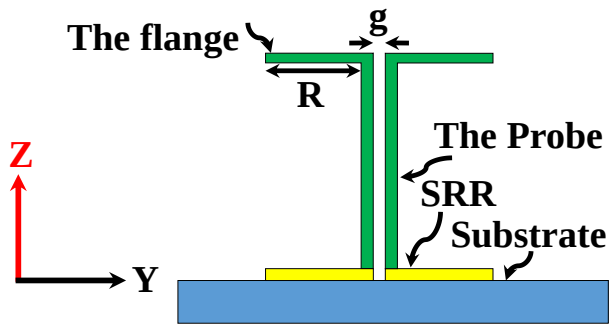

Figure 7.26: The schematic of the proposed sensor with the flange, where R is the length of the flange

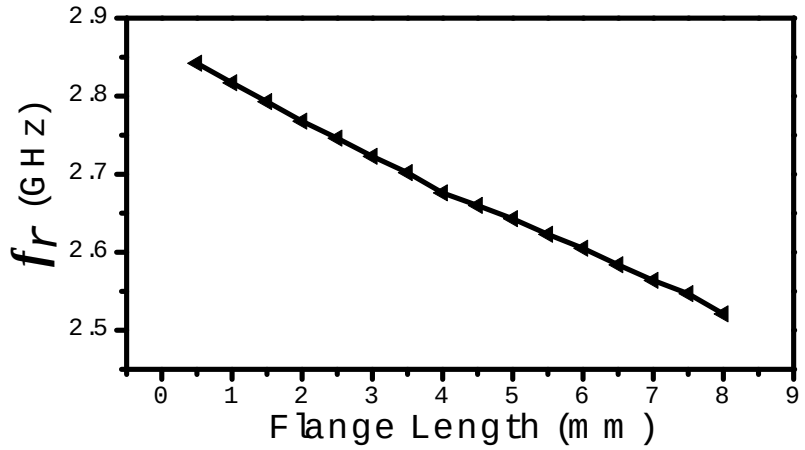

Figure 7.27: The resonance frequency versus the length of the flange, where L = 7.5 mm, C = 4 mm, and g = 0.5 mm with the step value of 0.5 mm

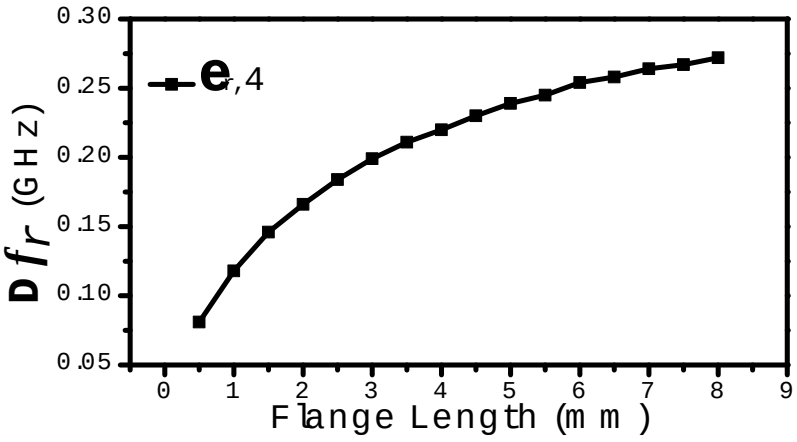

Figure 7.28: The shift in the resonance frequency versus the flange length, where L = 7.5 mm, C = 4 mm, and g = 0.5 mm with the step value of 0.5 mm

7.8 SRRs with Three-Dimensional Capacitors for Near-Field Scanning Microscopy: Experimental Results

For the experimental evaluation, a SRR with L = 7.5, C = 3 mm, g = 0.25 mm, and t = 0.25 mm was fabricated. For the MUTs, a dielectric slab with the height of 6 mm, the length of 105 mm, width of 60 mm, relative primitivity of 9.2 was utilized. Then, a hollow-cylindrical cavity with the diameter (u) of 4 mm was fabricated through the dielectric slab as shown in figure 7.29. The response of the sensor ($|S_{21}|$) was extracted using the VNA. Figure 7.30 shows the response of the sensor in the presence of the free space.

To perform the two-dimensional scanning, an XYZ-manual positioner was utilized. First, the system was calibrated by touching the dielectric slab with the probe. Then, the stand-off distance between the probe and the slab was set to be 0.005 mm to have a maximum sensitivity and resolution. The scanning step in XY plane was 0.25 mm with the total of 28×32 pixels. The maximum shift in the resonance frequency corresponds to the detection of the highest dielectric constant (9.2 in our case) and is utilized as a reference to normalize the shift in the resonance frequency in all the scanning procedure (see figure 1.4). Figure 7.31 shows the normalized resonance frequency shift versus the scanning in x direction where the y is fixed at 3.5 mm. The asymmetric of the response

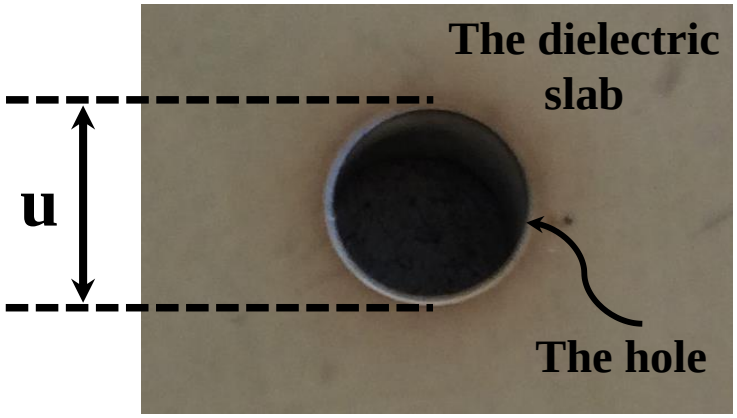

Figure 7.29: A hollow-cylindrical cavity with the diameter (u) of 4 mm fabricated through a dielectric slab (ceramic) with the permittivity of 9.2

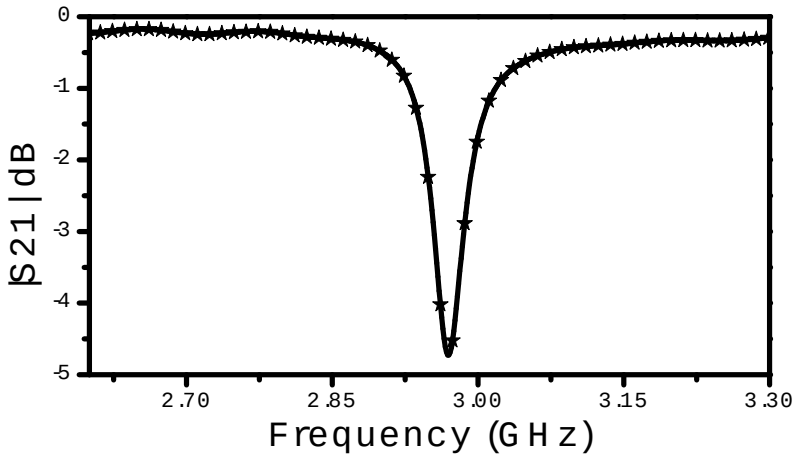

Figure 7.30: The response of the sensor in the presence of the free space.

can be attributed to the fabrication tolerance of the planar SRR and the three-dimensional capacitors. Figures 7.32(a) and 7.32(b) show the images of raw and interpolated data (for smother edges), respectively of the scanned hole. By counting the number of the blue pixels and multiple them in the scanning step of the 0.25 mm, the resolved diameter is approximately 4 mm, which shows the resolution of the probe.

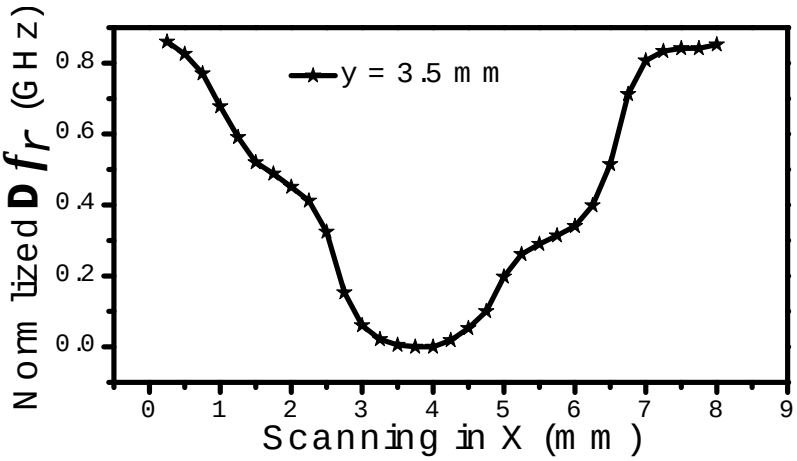

Figure 7.31: The normalized resonance frequency shift versus the scanning in x direction where the y is fixed at 3.5 mm

Furthermore, the probe was utilized for detecting the surface of different materials, an aluminum slab and two dielectric slabs with the relative permittivity of 2.2 and 9.2. For the aluminum slab, figures 7.33(a) shows the resonance frequency and the shift in the resonance frequency versus the stand-off distance, where the stand-off distance is varied from 5 μm (the reference to calculate the shift) to 8.35 mm. Figures 7.33(b) and 7.33(c) show the resonance frequency and the shift in the resonance frequency versus the stand-off distance, where the stand-off distance is varied from 0 to almost 8.35 mm for the dielectric slab of 2.2 and 9.2, respectively.

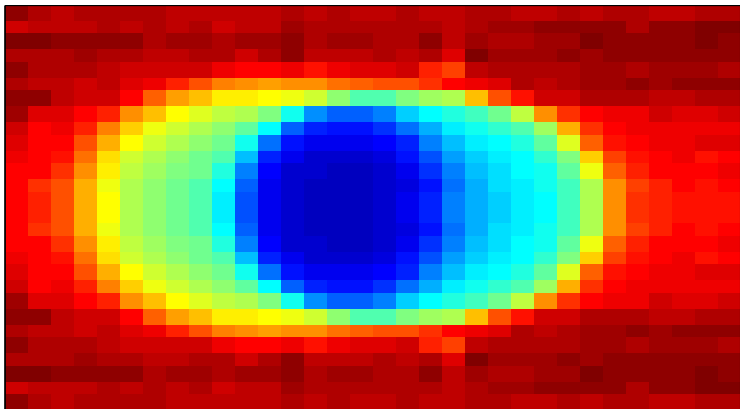

(a)

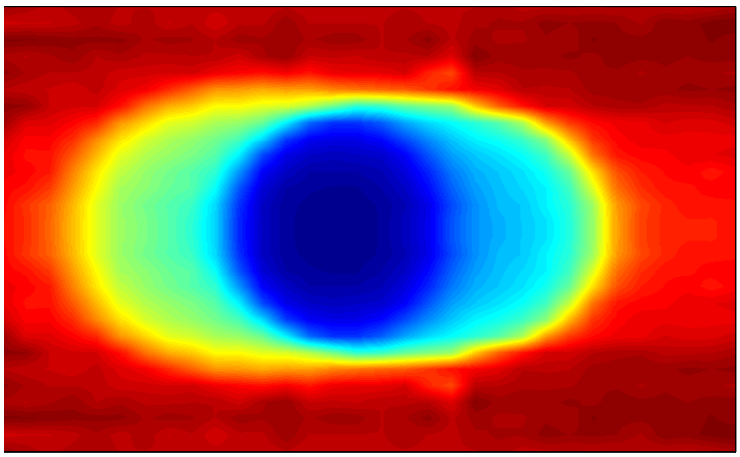

(b)

Figure 7.32: The processed experimental results (a) The images of raw data of the scanned hole (b) The images of interpolated data of the scanned hole

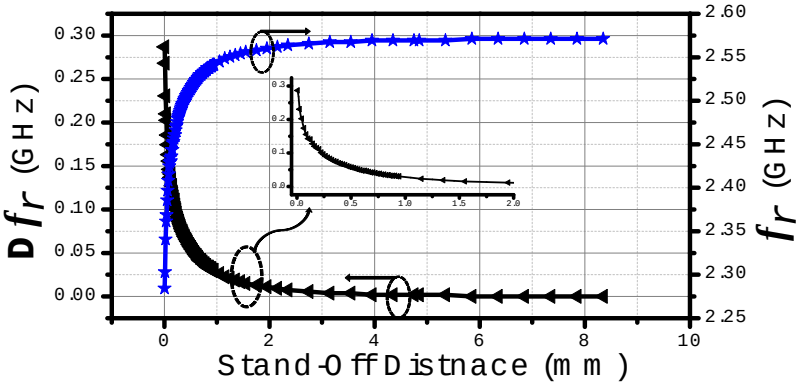

(a)

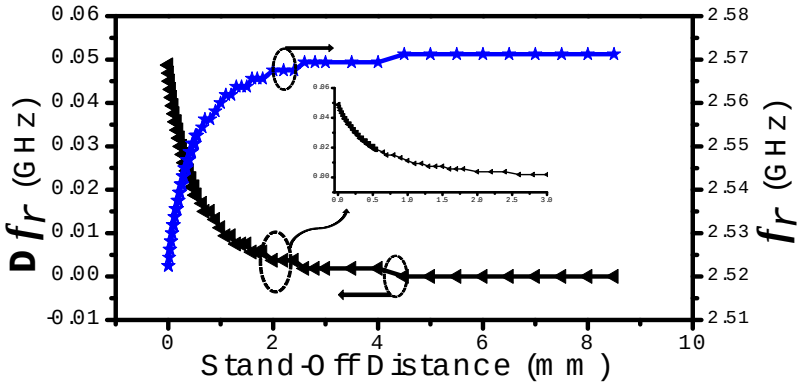

(b)

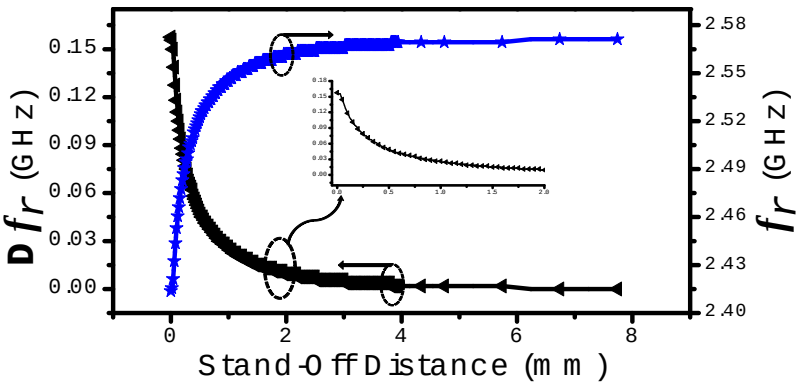

(c)

Figure 7.33: (a) The resonance frequency and the shift in the resonance frequency versus the stand-off distance, where the stand-off distance is varied from 5 μm (the reference to calculate the shift) to 8.35 mm (b) and (c) The resonance frequency and the shift in the resonance frequency versus the stand-off distance, where the stand-off distance is varied from 0 to almost 8.35 mm for the dielectric slab of 2.2 and 9.2, respectively

7.9 Conclusion

In this chapter, novel planar microwave sensors based on SRRs and three-dimensional capacitors were introduced. The three-dimensional capacitors increase the stored-electric field in the sensing areas that interact with the MUTs. The loaded quality factor of 1555 or 2102% compared to 70.6 of the planar SRR is achieved using the numerical simulation. Thus, compared to the SRR without three-dimensional capacitors, 700% sensitivity enhancement when detecting changes in dielectric materials is experimentally achieved. In addition, the concept design is utilized to fabricate a sensor for fluid level detection. Since the resonance frequency is a function of the length of the three-dimensional capacitors, the presented concept can be utilized to design sensors for fluidic and microfluidic technologies. Thus, applications such as a lab on a chip and other quality control and environmental monitoring can find these type of sensor attractive. Moreover, one of the essential features of the SRRs compared to the complements structures such as CELCRs is that the sensing areas are smallers, which is an advantage for applications such as microfluidic technologies. However, the sensing areas of the CELCRs can be miniaturized to smaller areas.

Chapter 8

Sensitivity Enhancement of CELCRs for fluidic and Microfluidic Technologies and Fluidic Level Detection Applications

8.1 Introduction

It has been shown that CSRRs sensors are higher sensitive than SRRs sensors [8, 29, 31]. As stated early that complement structures such as the CSRRs can be modeled as parallel resonators, where as the SRRs can be modeled as series resonators. From sensing point of view where the MUTs loading the resonators, the parallel resonators have some advantageous over the series resonators. The MUTs will add shunt capacitances to the resonators and based on the equations (2.8), the quality factor of the resonators will be enhanced. Of course, the enhancement in quality factor can be correlated to the sensitivity if one has access to the sensing area (concentrated field).

In chapter 7, near-field sensors for detecting changes in microscale dimensions were designed based on the SRRs and the three-dimensional capacitance (C_{pp}) since the sensing

area in the SRRs (the splits) are in microscale. On the contrary, the sensing area for dielectric materials in CSRRs are not in microscale (see figure 8.7). It is not thus the suitable choice to utilize the CSRRs to design a near-field sensor for microscale-based applications such as microfluidic technologies.

Alternatively, the complement structures such as CELCRs can be adopted (see figure 6.1). The sensing area (S) can be miniaturized, where the thickness (a) is kept the same, whereas the length of the channel is shrunk to the same size of a so that the sensing area (S) will have the area a×a. In this chapter, a near-field sensor based on a CELCR and the C_{pp} for microscale-based applications is proposed. In particular, the sensor is demonstrated to detect the presence of dielectric and magnetic materials.

8.2 Sensor Design and Excitation

Figure 8.1(a) shows the proposed topology, where the sensing area (S) is a×a. Since the resonator is working at the microwave regime, the dimensions of the resonator are L = 7.5 mm and b = a = 0.5 mm. Figure 8.1(b) shows the equivalent circuit diagram. The circuit diagram helps to analyze the proposed topology and to test if it will be working as a parallel resonator. The shrink in the sensing area will cause a reduction in the capacitance of the resonators. Based on the equation (2.1), the resonance frequency will increase to a higher frequency. For a two-port microstrip line, the lumped-elements circuit model is presented in figure 8.2. The resonance frequency can thus be written as the equation (2.6), where the C in the coupling capacitance between the microstrip line and the resonator.

Since the electric fields are highly concentrated in the dielectric substrates (sensitive areas) [66], the adoption of the concept of three-dimensional capacitors will help to design sensitive near-field sensors since the sensitive areas can be accessed. Figure 8.3 shows the system loaded with the C_{pp}. The C_{pp} will increase the total capacitance of the resonators, hence, the increment in the shift of the resonance to a lower frequency according to equation (2.6).

For the reason that the response of the system ($|S_{21}|$ dB) will be measured by a 50-Ω vector network analyzer (VNA), a 50-Ω microstrip line is utilized to excite the resonator

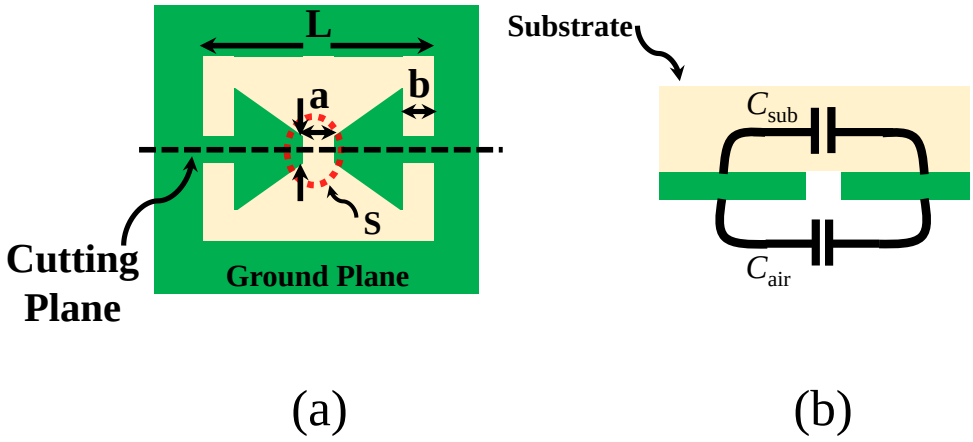

Figure 8.1: The schematic of the CELCR etched out in a ground plane. (a) Top view. (b) Side view through the cutting plane.

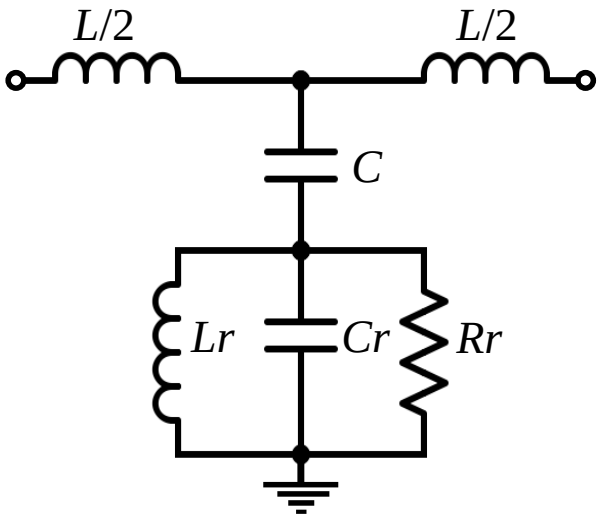

Figure 8.2: The circuit model of a proposed CELCR topology coupled to a microstrip line

and is achieved with a line width of 1.63 mm on a Rogers RO4350 substrate with a thickness of W = 0.75 mm and a relative permittivity of 3.66 and a loss tangent of 0.0031. Figure 8.4 shows the synthesized sensor with the three-dimensional capacitor probe, representing the added capacitance, where the C is the length of the capacitive probe, X is the marks for measuring the fluid level, g and a are the thickness of the channel and the probe,

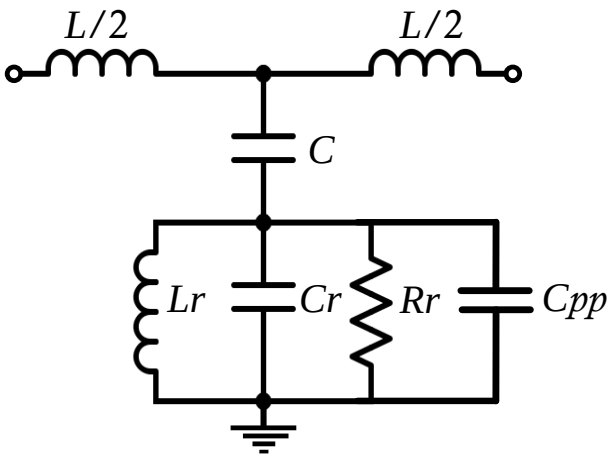

Figure 8.3: The circuit model of a proposed CELCR topology with the C_{pp}

respectively.

By using the numerical simulation (HFSS), the response of the sensor can be extracted. With the length of the probe (C) is 30 mm, figure 8.5 shows the response of the sensor with and without the C_{pp}, where the resonance frequency is 1.824 GHz. The following can be observed. First, the resonance frequency is shifted from a high frequency (6.281 GHz) to a lower frequency (1.824 GHz). Second, the response of the sensor becomes very sharp around the resonance, which is the result of the enhancement in the quality factor according to equation (2.8) since the total capacitance of the sensor is increased (C_r+C_{pp}). By using equation (7.6), the loaded quality factors for the sensor without and with C_{pp} can be calculated. From figure 8.5, it can be noticed that in the case of the sensor without C_{pp}, the quality factor at -3 dB nor -10 dB cannot be evaluated. Thus, to be able to calculate the quality factor of the resonator, two frequencies points f_1 and f_2 at -15 dB (no particular reason for chosen - 15 dB except to evaluate the quality factor) has been determined form figure 8.5.

$$Q(loaded)_{|without\ C_{pp}} = \frac{6.284}{7.054 - 5.697} = 4.63$$

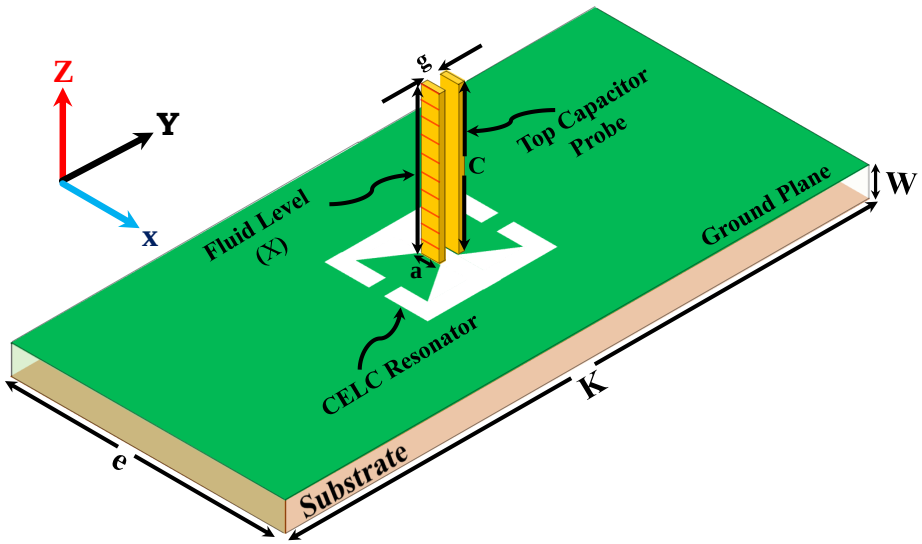

Figure 8.4: The synthesized sensor with the three-dimensional capacitor probe, representing the adding capacitance, where the C is the length of the capacitive probe, X is the marks for measuring the fluid level, g and a are the thickness of the channel and the probe, respectively

$$Q(loaded)_{|C_{pp}} = \frac{1.824}{1.845 - 1.8} = 40.53$$

The enhancement in the quality factor is around 775.4 %. Since there is access to the enhanced-stored energy, it is expected that the sensitivity will be enhanced as well.

Moreover, since the changes in the resonance frequency and the quality factor were analyzed using the lumped elements models, it is worthwhile to validate the circuits shown in figures 8.2 and 8.3. The circuit parameters of the CELCR were extracted by importing the scattering parameters $|S_{21}|$ dB and $|S_{11}|$ dB from the numerical simulation (HFSS), and then by using the optimization tool box, the circuit elements can be extracted. Figures 8.6(a) and 8.6(b) show the scattering parameters of the CELCR sensor without and with the C_{pp}, respectively. The length of the probe (C) is 10 mm.

In chapter 7, the coupling factor (κ) of the SRR with C_{pp} was calculated. It can be noticed that the κ is decreased with the increase in the length of the capacitive probe. Similarly, the κ of the CELCR with C_{pp} based sensor can be extracted. First, the response

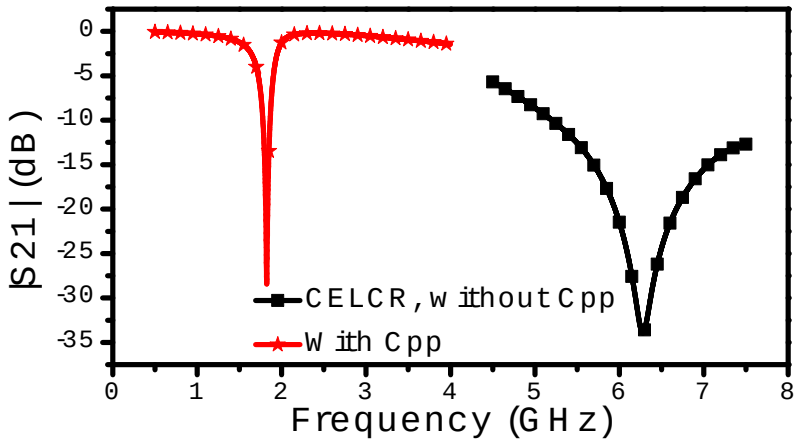

Figure 8.5: The transmission coefficient of the sensor with and without the C_{pp}, where the length of the probe is 30 mm

of the sensor versus the length of the probe is extracted using the numerical simulation. Figure 8.7 shows the resonance frequency and minimum $|S_{21}|$ dB versus the probe length (C). The length is varied from the 0.5 to 29 mm with the step value of 0.5 mm. Compared to the response of the coupling factor of the SRR shown in figure 8.4, the function that expresses the relation between the minimum $|S_{21}|$ dB and the probe's length is not monotonic, which will affect the function of the coupling factor with respect to the length. By using equation (7.5), the κ can be extracted. The κ for the SRR and CELCR with the C_{pp} are compared as shown in figure 8.8. Although the trend of the coupling factor versus the length is not monotonic, the coupling between the microstrip line and the CELCR are stronger, which is the clue that the CELCR sensors are suitable for high dielectric materials based applications.

8.3 Numerical Simulations for the Sensitivity Analysis

The measure of the sensitivity of the CELCR sensor is based on the measurement of the changes in the resonance frequency in the presence of dielectric materials. To investigate

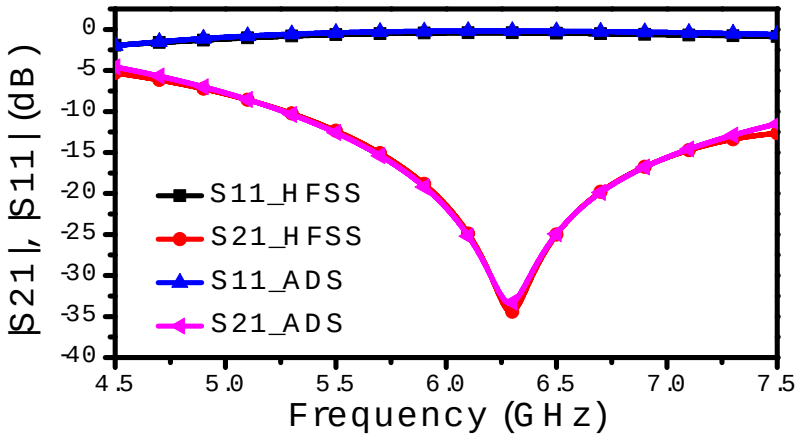

(a)

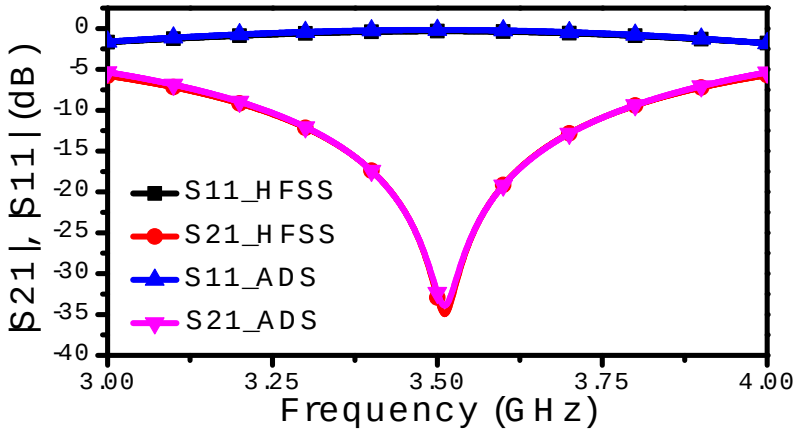

(b)

Figure 8.6: (a) The scattering parameters of the circuit models and the numerical simulation of the CELCR sensor without the C_{pp} in the presence of the free space and (b) with the C_{pp}, where the length of the probe (C) is 10 mm

the sensitivity enhancement, the CELCR sensor with and with C_{pp} is utilized to detect the presence of a dielectric material, where the dielectric constant is varied from 1 to 10 with the step value of 0.5. The probe is immersed inside a dielectric cylinder to mimic real-field applications for fluidic testing as shown in figure 8.9. Figure 8.10 shows the shift in the resonance frequency versus the relative permittivity of the CELCR sensor with and

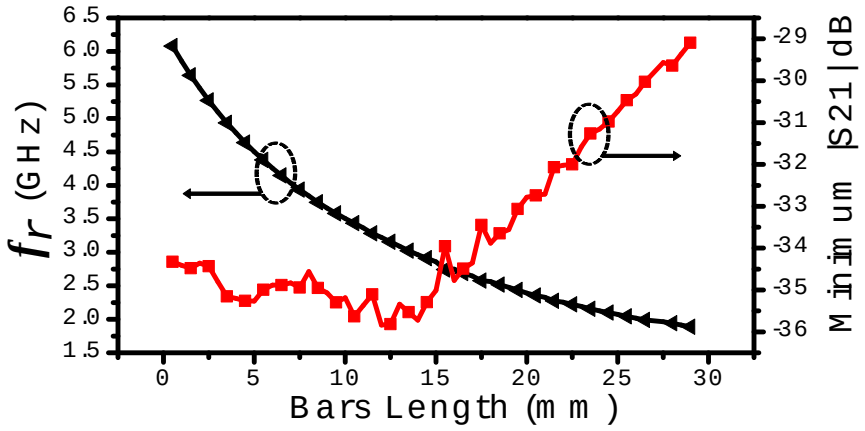

Figure 8.7: The resonance frequency and minimum $|S_{21}|$ dB versus the probe length (C). The length is varied from the 0.5 to 29 mm with the step value of 0.5 mm

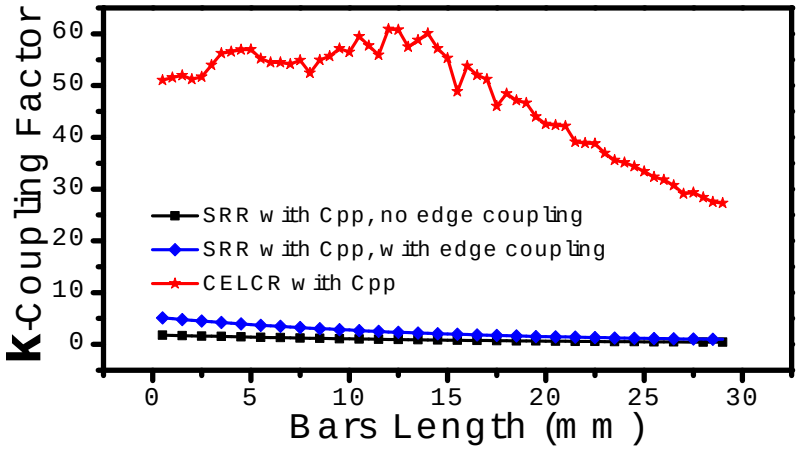

Figure 8.8: The coupling factor for the SRR (with and without coupling edge) and CELCR with the C_{pp}. The length (C) is varied from the 0.5 to 29 mm with the step value of 0.5 mm

without C_{pp}, where the sensitivity, as well as the dynamic range of the sensor, is enhanced. Furthermore, the sensitivity enhancement utilizing the C_{pp} is compared for the CELCR (figure 8.4) and SRR (figure 7.2) based sensors, where C = 4 mm. Figure 8.11 shows the sensors utilized to detect the dielectric cylinder, where the result shows that the CELCR

with the C_{pp} based sensor is more sensitive than the SRR with the C_{pp} based sensor.

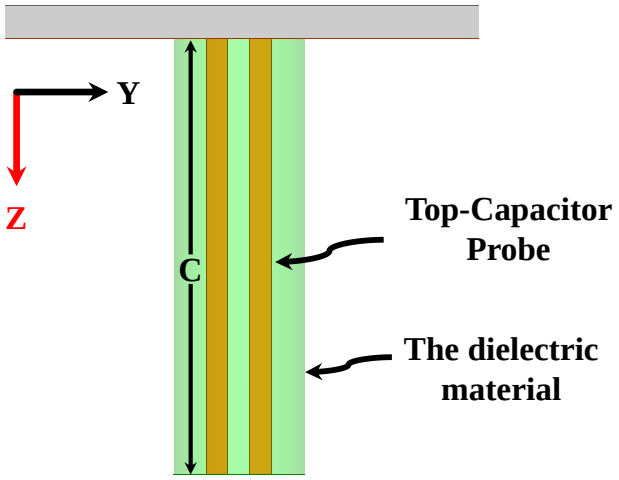

Figure 8.9: The probe is immersed inside a dielectric cylinder, where the length of the probe (C) is 10 mm

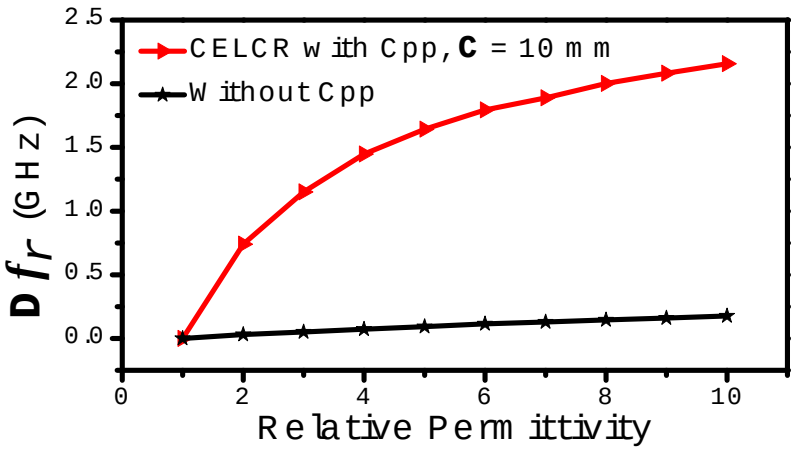

Figure 8.10: The shift in the resonance frequency versus the relative permittivity of the CELCR sensor with and without C_{pp}, where the length of the probe (C) is 10 mm

Moreover, the proposed sensor with C = 10 mm is used to detect the level of the fluid materials. The sensor is immersed with different level (X) inside a dielectric cylinder. The level of the immersion (X) is varied from 1 to 10 mm with the step value of 1 mm.

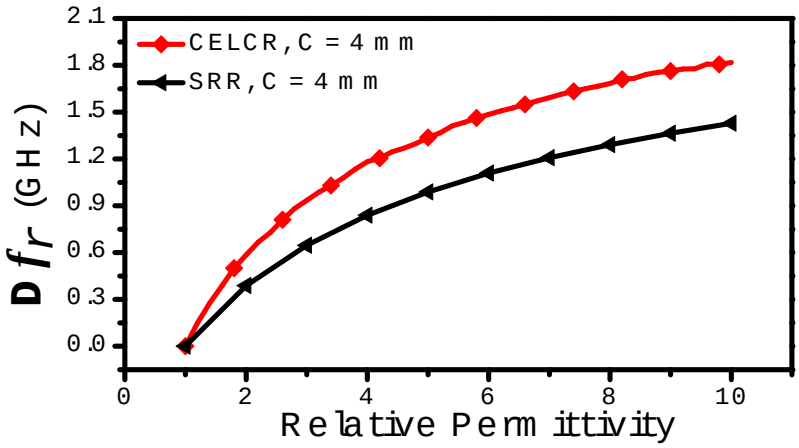

Figure 8.11: The shift in the resonance frequency versus the relative permittivity of the CELCR and SRR sensors where the length of the probe (C) is 4 mm

Figure 8.12 shows the shift in the resonance frequency versus the relative permittivity that is varied from 1 to 100. The sensitivity (the shift in the resonance frequency) is increased due to two factors: the increase in the immersion level (X) and the increase in the relative permittivity.

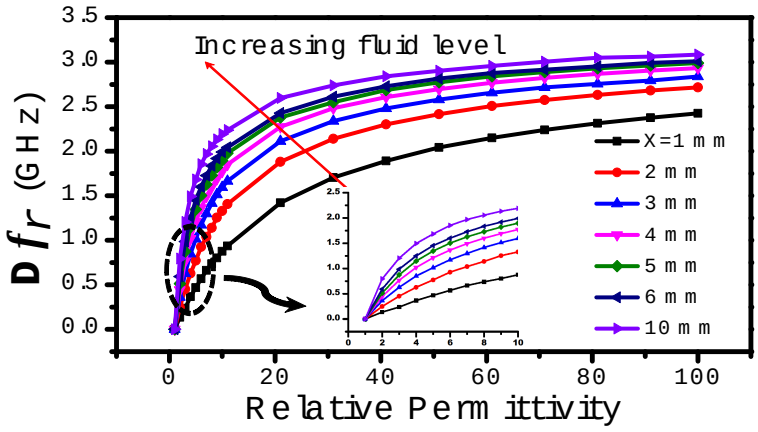

Figure 8.12: The shift in the resonance frequency versus the relative permittivity varied from 1 to 100, where the level of the immersion (X) is varied from 1 to 10 mm with the step value of 1 mm

8.4 Fabrication and Experimental Results

For the experimental validation, a CELCR sensor was fabricated using the printed circuit board technology (PCB). Figure 8.13 shows the fabricated sensor without (figure 8.13(a)) and with (figure 8.12(b)) the capacitive probe, where the length of the probe (C) is 30 mm, K = 100 mm, and e = 50 mm. The capacitive probe is made of two aluminum bars. Note that there is no particular reason for choosing the aluminum except for its availability in our lab. Other metallic material can be tested to design the probe. Figure 8.14 shows the response of the sensor ($|S_{21}|$ dB) in the presence of the free space. Since the sensing mechanism is based on the shift in the resonance frequency, it is expected that the small discrepancy between the simulation and the experiment will be minimal. In fact, the effects will appear when using the sensor for material characterization. For level detection, the sensor will be experimentally calibrated before the use.

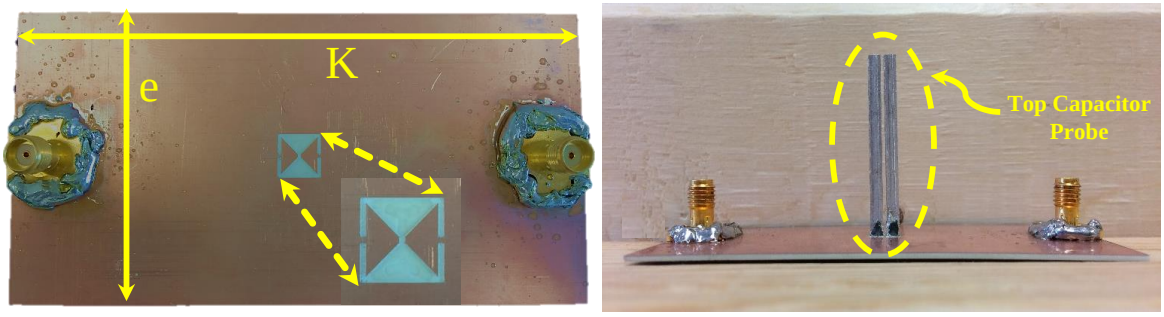

Figure 8.13: (a) The fabricated sensor without the capacitive probe, where K and e are 100 and 50 mm, respectively (b) The sensor with the capacitance probe, where the length of the probe (C) is 30 mm

To validate the sensitivity enhancement of the proposed sensor, the sensor with and without the capacitive probe is compared for detecting detect the presence of two-dielectric fluids: chloroform and dichloromethane with permittivities of 4.81 and 8.93, respectively (taken from [61]). Figure 8.15 shows the sensor without the capacitive probe, where a

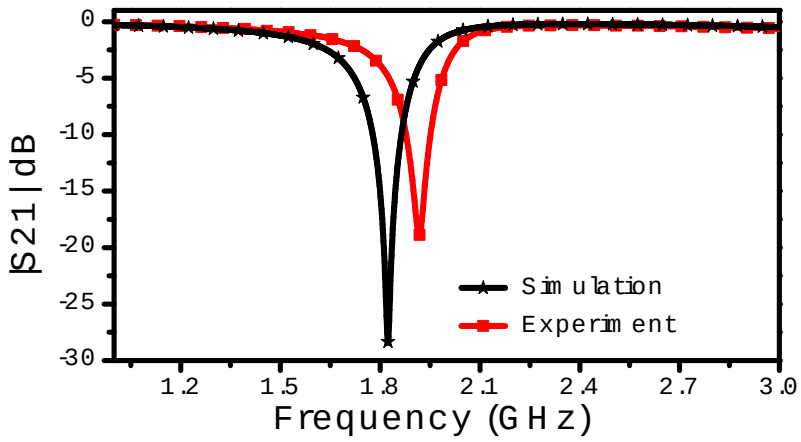

Figure 8.14: The experimental result of the fabricated CELCR sensor with the three-dimensional capacitor C_{PP} in the presence of the free space medium

plastic glue container is fabricated to contain the fluids. Figures 8.16 and 8.17 show the response of the sensors without and with the capacitive probe, respectively, detect the fluidic materials. In the case of the sensor without C_{pp}, the shift in the resonance frequency is

$$\Delta f_r = 6.0607 - 5.848 = 212.7 \text{ MHz for } \varepsilon_r = 4.81$$

$$\Delta f_r = 6.0607 - 5.745 = 315.7 \text{ MHz for } \varepsilon_r = 8.93$$

whereas in the case of the sensor with C_{pp}, the shift in the resonance frequency is

$$\Delta f_r = 1.915625 - .88375 = 1.031875 \text{ GHz for } \varepsilon_r = 4.81$$

$$\Delta f_r = 1.915625 - .65125 = 1.26437 \text{ GHz for } \varepsilon_r = 8.93$$

Thus, the enhancement in the sensitivity of the sensor to detect the chloroform and dichloromethane is 385.13 % and 300.475 %, respectively.

Moreover, the sensor with the C_{pp} is tested to detect the changes in the level of fluidic materials. The probe was immersed gradually into a cylindrical glass containing the chloroform, with the value of each step of 0.762 mm. The resonance frequency versus the fluid

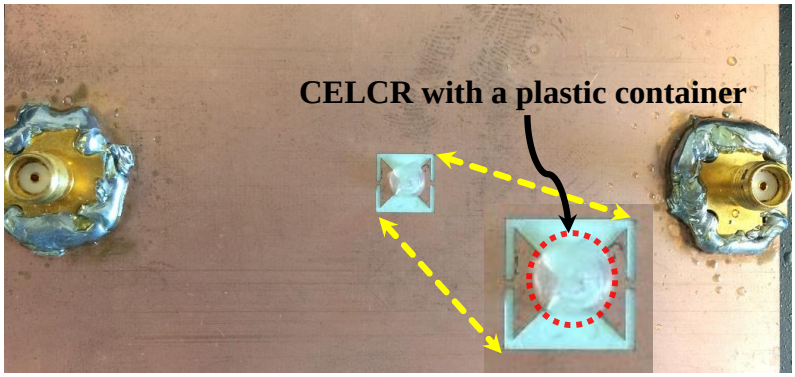

Figure 8.15: The fabricated sensor without the capacitive probe, where a plastic glue container is fabricated to contain the fluids

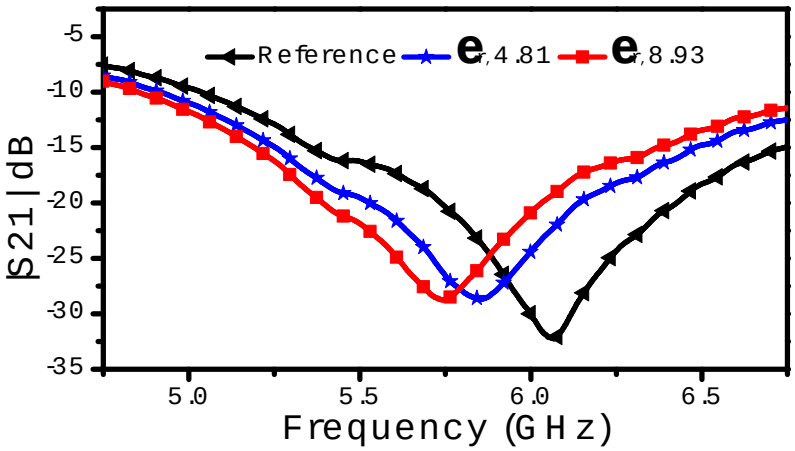

Figure 8.16: The experimental result of the fabricated CELCR without the three-dimensional capacitor C_{PP} detecting the presence of the fluidic materials, chloroform and dichloromethane

level (X) was extracted numerically and experimentally. Figure 8.18 shows the extracted experimental and numerical results of the sensor detecting the fluid level of the chloroform. In addition, the sensor was utilized to detect the level of the dichloromethane as shown in Figure 8.19. Furthermore, in figure 8.8, it is was expected that the sensor with the capacitive probe could be utilized to detect the presence of high dielectric materials, such as the distilled water with the relative permittivity of 81. Figure 8.20 shows the resonance

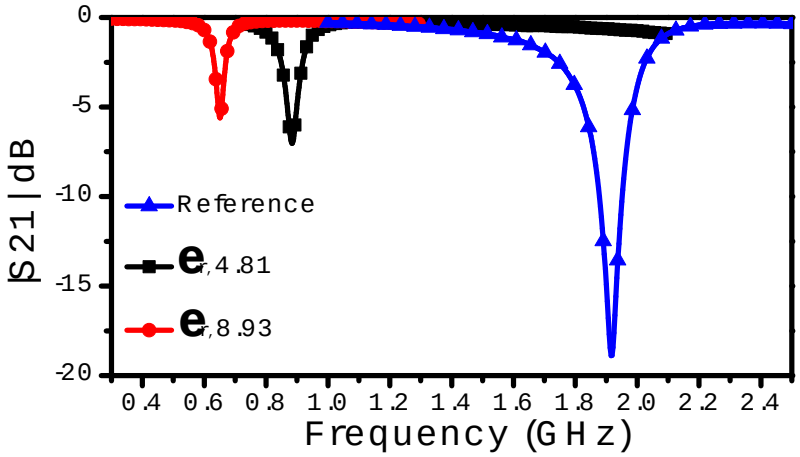

Figure 8.17: The experimental result of the fabricated CELCR with the three-dimensional capacitor C_{PP} detecting the presence of the fluidic materials, chloroform and dichloromethane

frequency versus the distilled water.

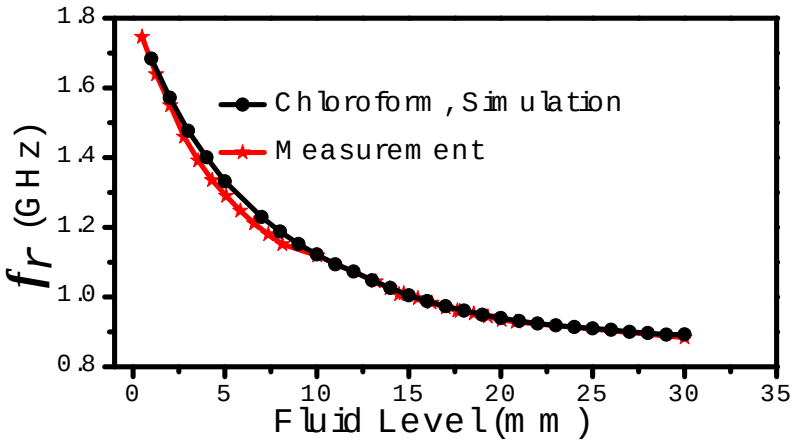

Figure 8.18: The numerical and experimental results of the resonance frequency versus the fluid level (X) of the chloroform

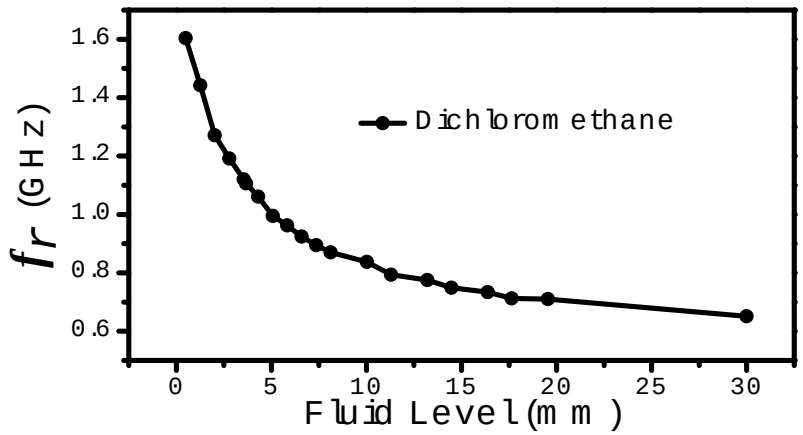

Figure 8.19: The experimental results of the resonance frequency versus the fluid level (X) of the dichloromethane

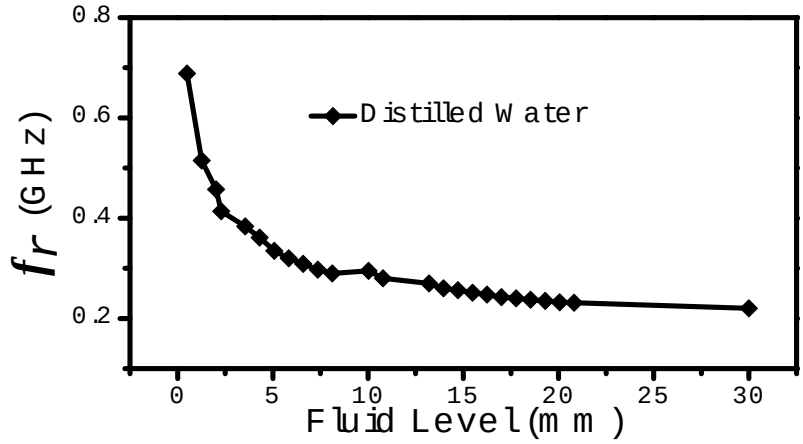

Figure 8.20: The experimental results of the resonance frequency versus the fluid level (X) of the distilled water

8.5 CELCRs and Three-Dimensional Capacitors for Magnetic Materials Detection: Numerical Results

Since modern technologies such as the RFID tag based technology need compact and miniaturized devices, the use of magneto-dielectric substrates can open a new degree of

freedom for the miniaturization to meet the requirement by the technologies [67–69]. Thus, there is a need for modern sensing technologies to detect and characterize the magnetic materials. The CELCRs with the C_{pp} based sensor is a strong candidate.

Investigating the surface current distribution on the three-dimensional capacitor (C_{pp}) shows the sensitive area that can be used to interact with the magnetic materials. A CELCR with L = 7.5 mm, C = 10 mmm, and g = a = 0.5 mm is utilized to plot the surface current distribution at the resonance frequency of 3.5 GHz as shown in figure 8.21. For the validation, the sensor is used to detect the presence of the magnetic slab, where the permeability is varied from 1 to 5 with the step value of 0.2. Similar to figure 8.9, the probe is immersed inside a magnetic cylinder, where the length of the probe (C) is 10 mm

Figure 8.22 shows the resonance-frequency shift versus the relative permeability, which shows the sensitivity of the sensor for detecting magnetic materials.

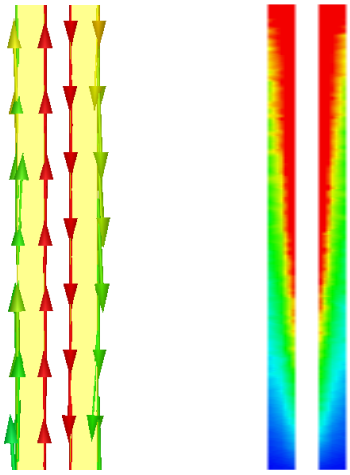

Figure 8.21: The surface current distribution is plotted at the resonance frequency of 3.5 GHz. The red color is corresponding to the 1.5 A/m, and blue to 2.1 mA/m

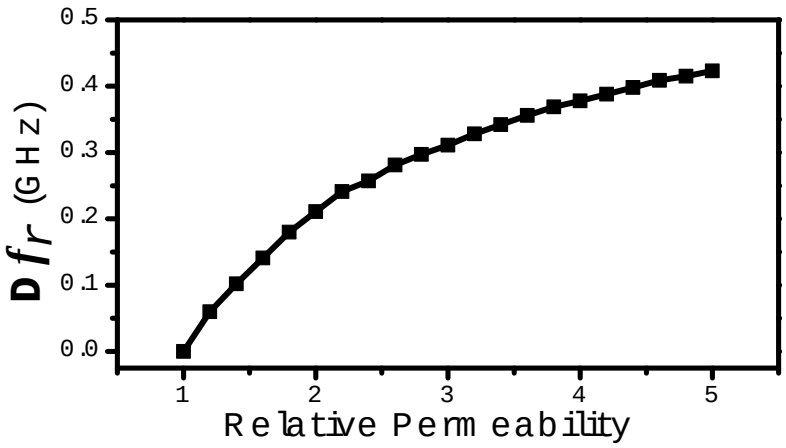

Figure 8.22: The resonance-frequency shift versus the relative permeability extracted numerically using the numerical simulation (HFSS)

8.6 Conclusion

In this chapter, a novel microwave near-field sensor based on CELCR and three-dimensional capacitors was proposed. The sensing area was shrunk to a microscale so that the three-dimensional capacitor can be utilized to design probes for microscale-based applications such as microfluidic technologies. The sensor was tested using the numerical simulation to detect the presence of fluid materials. In addition, the sensor was utilized to detect the fluid levels of the chloroform, dichloromethane, distilled water, which shows that the sensor can be utilized to detect the presence of high dielectric materials. Furthermore, the proposed sensor can be utilized to design near-field microscopy. The sensor was tested numerically to detect the topography of materials. Furthermore, the sensor was investigated using the numerical simulation to detect the presence of magnetic materials. Moreover, for applications that are concerning the flatness or compactness, the three-dimensional capacitors are not the ideal solution for sensitivity enhancement.

Chapter 9

High-Q Split-Annular-Ring Resonators for Detection Applications

9.1 Introduction

In recent years, microwave planar electrically-small resonators such as SRRs and their complement (CSRRs) have been utilized to design different sensing modalities [15,24]. Thanks to the printed circuit board technology (PCB) that makes the possibility for such planar resonators to be fabricated with very low cost and mass production. The sensing modalities can be implemented in many technologies including fluidic and microfluidic technologies, solid dielectric material characterization, and biosensing technologies. Since the resonators are electrically small compared to the operating wavelength, the electromagnetic (EM) fields are concentrated in small volumes in the structures [21].

Although the EM energies are stored in the small volumes, most of the energies are concentrated in higher dielectric substrates of the planar structures, limiting the interactions with MUTs [48]. In addition, the resonators suffer from the radiation loss that causes the resonators to exhibit low-quality factors [70], which can be correlated with the possibility

of sensitivity degradation. Resolving such limitations can be achieved by exploiting the sensing area by implementing a channel inside the substrates [55], yet such solution can be considered as another challenge from the practical point of view. In chapter 6, the proposed solution was presented that based on utilizing three-dimensional capacitors to transfer the higher sensing area out of the substrate to the free space where the quality factor can be enhanced as well [48]. If a particular application is concerning the flatness or the compactness of the sensor, the three-dimensional capacitors are not the ideal solution.

Alternatively, classical antennas such as planar dipole, patch, and loop antennas can be utilized since the antennas are usually made on low dielectric substrates making the input impedance sensitive to changes in the background. In addition, the antennas have the advantage to be excited and read using one-port systems. However, compared to electrically-small resonators, the antennas suffer from the field localization (concerning space) that is necessary for near-field sensing techniques. In addition, compared to one-port systems, electrically-small resonators based sensors excited using two-port systems do not require matching networks since the MUTs is loading the resonators not the load impedance (the termination) of the systems. As an intermediate solution between the classic antennas and electrically-small resonators, the split (cut) concept in SRRs can be adopted in the antennas' structures [66] as parasitic elements to 1- miniaturize the antennas 2- localize the EM fields in smaller volumes to enhance the quality factors 3- make the split with the MUTs acting as an adaptive matching network.

In this chapter, a microwave high-Q near-field sensor for solid dielectric material and microfluidic detection applications is presented. The sensor is based a planar annular-ring resonator loaded with a split as a parasitic element, henceforth referred to as a split-annular-ring resonator (SARR). The split makes the structure compact resonating at a lower frequency than the fundamental frequency. The resonator shows a high loaded (at -3 dB) and unloaded-quality factor of 138.5 and 304.2, respectively. For the demonstration, the sensor is tested using numerical simulation tools to detect changes in the relative permittivity of 1- a dielectric slab placed on the whole resonator and 2- fluid materials filling a channel placed on the split. Then the sensor was fabricated and tested experimentally to characterize solid-dielectric materials and to detect the presence of fluid materials suitable for microfluidic technologies.

9.2 Annular-Ring Resonators Loaded with Splits As Near-Field Sensors

Figure 9.1(a) shows an annular-ring resonator where b and t are the otter and inner radius, respectively, whereas X_0 and Y_0 are the excitation-position coordinates in the x-y plane. With the ring design specification of b = 15 mm and t = 6.5 mm placed on a Rogers RT/duroid 5870 substrate with a thickness of W = 1.575 mm and a relative permittivity of 2.33 and a loss tangent of 0.0012 and excited by a coaxial probe positioned at $X_0 = 0$ mm and Y_0 = -10 mm, where the ring is placed at the centner, the TM11 mode is excited [71]. The annular-ring resonators suffer from a poor impedance matching to 50-Ω systems. [71]. Figure 9.2 shows the input impedance and the reflection coefficient of the ring extracted using a numerical simulation (ANSYS HFSS) where the fundamental resonance frequency is 3.263 GHz.

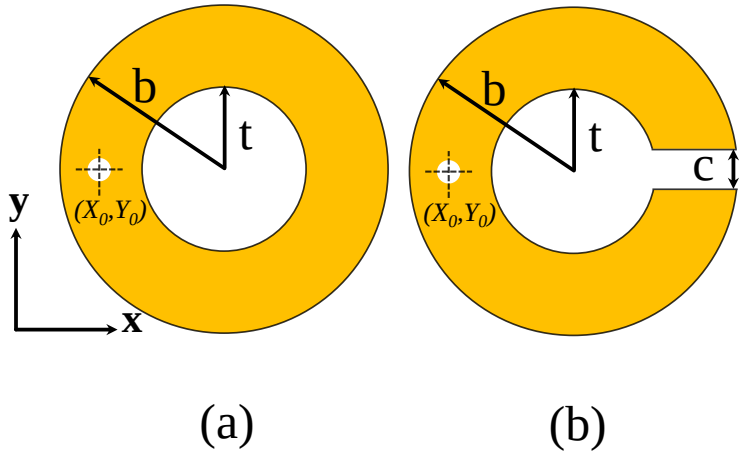

Figure 9.1: The schematic of the annular-ring antenna (a) without the split (b) with the split.

Now, the task is to investigate the possibility to make the resonator compact resonating at lower frequencies where the EM energies are concentrated in smaller volumes, hence, enhancing sensitivity to detect changes in the near environment. Working at the lower frequencies will allow regarding the resonator as an electrically-small resonator where the

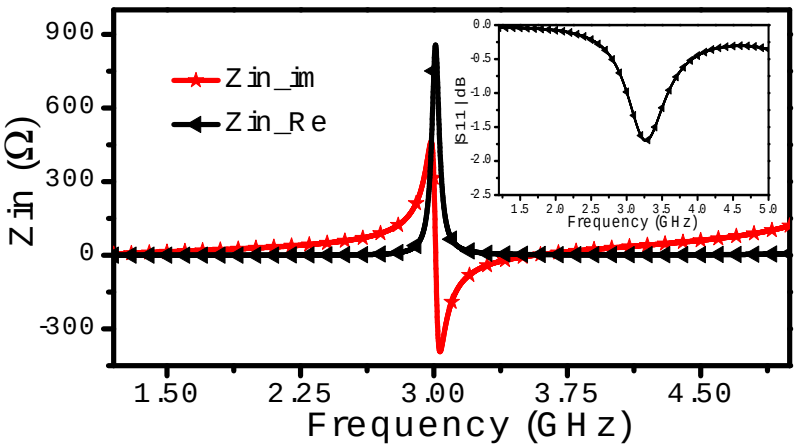

Figure 9.2: The input impedance and the reflection coefficient of the annular-ring antenna without the split.

highest length in the resonator (b in our case) is electrically small compared to the operating wavelength. The input impedance can thus be modeled using lumped elements, which will be utilized in the analysis and to predict the resonance frequencies and quality factors. By carefully investigating the input impedance of the resonator lower than 3 GHz (see figure 9.2), the input impedance is entirely inductive with almost no real part impedance that manifests the possibility to design a high-quality factor structure. If the goal is to match the resonator at the lower frequencies, it is intuitive to anticipate that a capacitive load will achieve the goal since the capacitive load will adjust the ratio between the stored electric and magnetic energies so that the input impedance will match the source impedance at specific frequencies.

The matching condition at a certain frequency depends fundamentally on the new boundary condition enforced by the capacitive load. Thus, by disturbing the capacitive load with MUTs, the resonance frequencies will exhibit changes to lower frequencies since the capacitance of the MUTs will be in parallel with the capacitive load. Since the resonator will be used as a near-field sensor, the concept of the split (cut) that have been utilized in electrically-small resonators to design near-field sensors is adopted. In fact, with the MUTs, the capacitive load can be seen as an adaptive matching network. Figure 9.1 shows the resonator loaded with the split (c). Since the ratio (b-t)/(b+t) is larger than

0.5 [24], it is expected that the higher order modes will be excited. However, since the resonator is a quasi-static resonator working at lower frequencies, one can expect that the higher order modes will be diminished. Thus, the microstrip line theory to calculate the effective permittivity to find the guided wavelength can be used. Since the thickness of the microstrip line (b-t) is 8.5 mm, the calculated ϵ_{eff} is 2.06.

By loading the resonator with the split (c) of 0.5 mm, the structure exhibits a resonance frequency of 1.593 GHz. Thus, the guided wavelength (λ_0/ϵ_{eff}) is 131.21 mm, and the electric length of the ring diameter (30 mm) is $\lambda_g/4.4$. By utilizing the lumped elements, the resonator is an LCR series resonator coupled to the source through an inductive element L_c (coaxial probe). Using the numerical simulation tool of HFSS, the circulating surface current (figure 9.3(a)) and localized electric field (figure 9.3(b)) distributions are extracted. The effects of the current are represented in the form of the inductance (L_r), whereas the electric field effects are represented in the form of the capacitance (C_r). In addition, the resonator is coupled to the ground plane through a capacitive element (C_g). Figure 9.4 shows the proposed circuit model of the SARR. The resonance frequency of the proposed circuit of the SARR can be expressed as follows:

$$w_0 = \frac{1}{\sqrt{L_r(C_r + C_g)}} \tag{9.1}$$

Taking the partial derivative of equation (9.1) with respect to C_r, the sensitivity of the resonance frequency with respect to the changes in C_r can be found as

$$\frac{dw_0}{dC_r} = \frac{-1}{2}\frac{w_0}{C_r + C_g} \tag{9.2}$$

$$Q_u = \frac{1}{R_r}\sqrt{\frac{L_r}{(C_r + C_g)}} \tag{9.3}$$

Since the capacitance C_g is symmetric with respect to C_r, the capacitance C_g is divided by 2. The extracted circuit elements are $L_c = 0.7$ nH, $L_r = 2.202$ nH , $C_r = 4.353$ pF , $R_r = 0.072$ Ω, and $C_g = 0.183$ pF. Based on the extracted elements, the resonance frequency and the quality factor are 1.593 GHz and 304.232, respectively. By utilizing the numerical simulation, the loaded quality factor at -3 dB is 138.5.

By analyzing equation (9.3), the quality factor is a function of two factors: $1/R_r$ and $(L_r/(C_r + C_g))^{1/2}$. Since the second factor is under the square root, the quality factor is expected to be more sensitive to changes in the R_r. Simultaneously, the second factor $(L_r/(C_r+C_g))^{1/2}$ is a function of the C_r and C_g, so the high-dielectric MUTs and substrates will reduce the quality factor. In addition, equation (9.2), shows that the sensitivity can be increased by reducing the capacitance, C_g by choosing low-dielectric substrates. Thus, the sensor will be suitable for low-loss and low-dielectric materials. Furthermore, since the sensing mechanism is based on the shift in the resonance frequency, the sensitivity (equation (9.2)) for the changes in the resonance frequency will be reduced with the increase in C_r as a result of loaded MUTs. Figure 9.5 shows the sensor utilized to detect the presence of a lossless-dielectric slab where the dielectric constant is varied from 1 to 10 with the step value of 0.5. The sensor is able to detect the changes with higher quality factor (high sharp response around the resonance frequency).

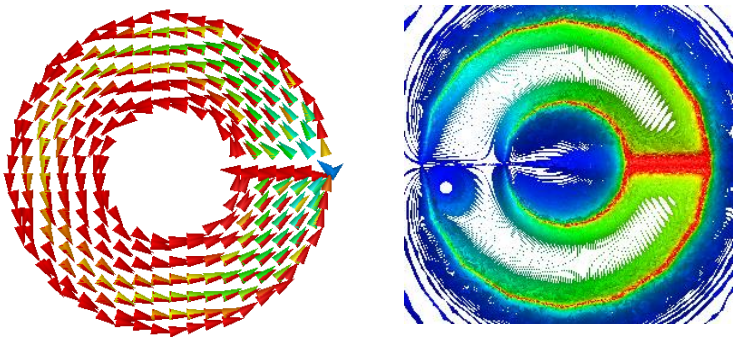

Figure 9.3: (a) The extracted surface current distribution (b) the electric field distribution

For characterizing dielectric materials, the SARR is tested to detect the presence of a solid-dielectric slab with the dielectric constant changing from 1 to 10 with a step of 0.5. Figure 9.6 shows the shift in the resonance frequency (Δf_r) with respect to the free space (the reference). Using the fitting function techniques, the relative permittivity can be related to Δf_r as follows:

$$\epsilon_r = 9.4 \times 10^{-6} e^{(\frac{\Delta f_r}{0.052})} + 3.5 e^{(\frac{\Delta f_r}{0.4})} - 2.5 \tag{9.4}$$

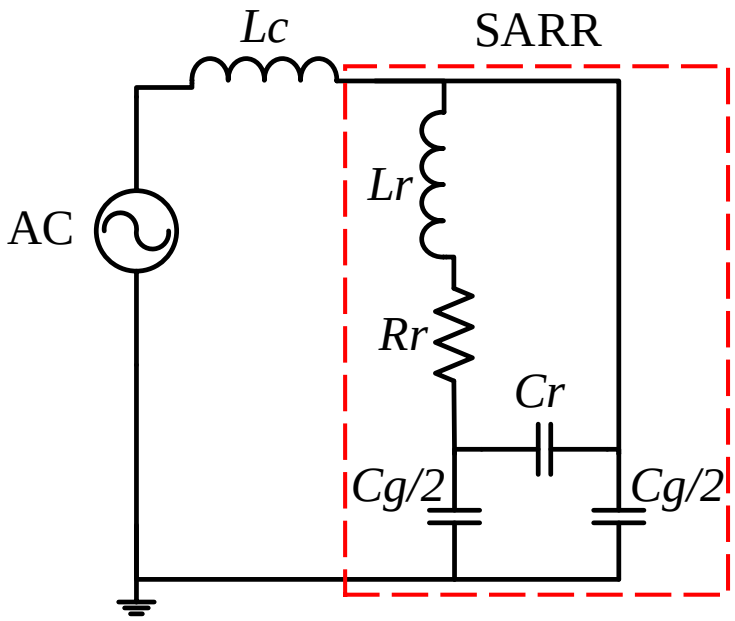

Figure 9.4: The proposed circuit model of the SARR, where L_c is the source coupling inductive element, L_r, C_r; R_r are the inductance, capacitance, and resistance, respectively; C_g is the ground coupling capacitive element.

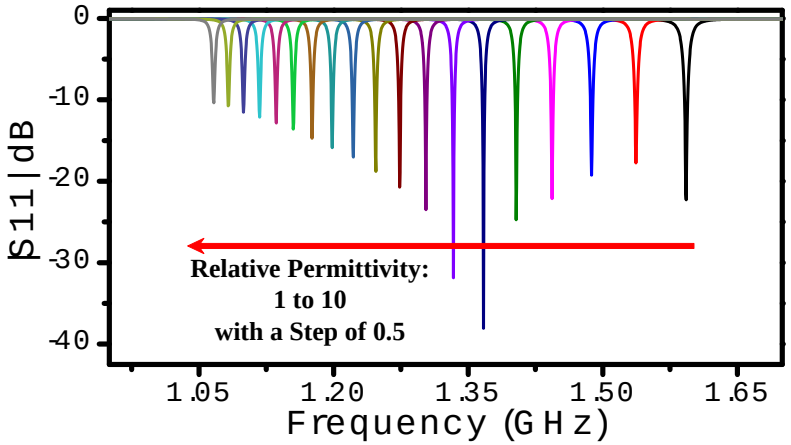

Figure 9.5: The scattering parameter of the sensor detecting changes in a dielectric slab that is varied between 1 to 10 with a small variation of 0.5

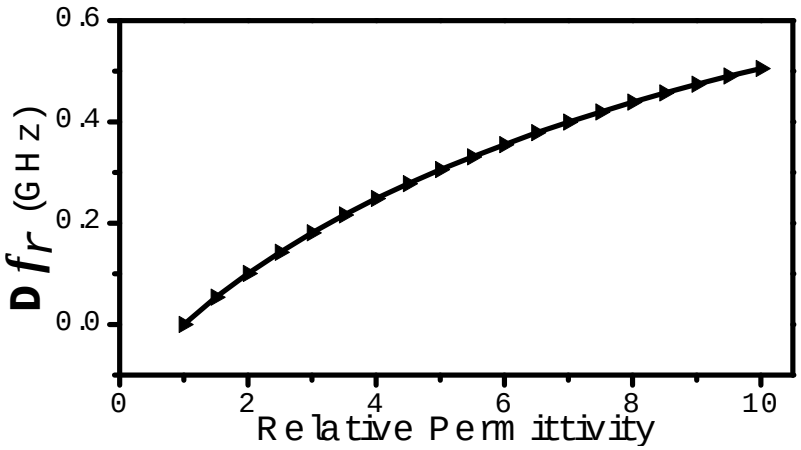

Figure 9.6: The shift in the resonance frequency versus the relative permittivity varied from 1 to 10 with a step of 0.5

9.3 Sensor Fabrication and Experimental Results

For experimental validation, a SARR based sensor is fabricated using the printed circuit board technology (PCB) as shown in figure 9.7. The sensor response is observed using a 50-Ω vector network analyzer. Figure 9.8 shows the response of the sensor extracted using the numerical simulation (HFSS), circuit model, and the experimental result. The sensor was used to characterize two dielectric slabs with the relative permittivity of 2.2 and 9.2 where the dielectric slabs covered the whole SARR. Figure 9.9 presents the response of the sensor detecting the dielectric slabs. The shifts in the resonance frequency due to the presence of the dielectric slabs, 2.2 and 9.2 are 0.119 GHz and 0.464 GHz, respectively. By using equation (9.4), the calculated dielectric constant is 2.2114 and 8.7042, so the accuracy of the extracted results are 0.5164% and 5.3886%. The small errors can be attributed to the air gap effects and fabrication tolerance.

Furthermore, the SARR was utilized to design a microwave near-field sensor for the microfluidic technologies since the split exhibits the highest electric field distribution (see figure 9.3(b)). To contain the fluid, a plastic channel is fabricated as shown in figure 9.7(b), where the thickness of the channel is 0.5 mm. Figure 9.10 shows the sensor detecting the

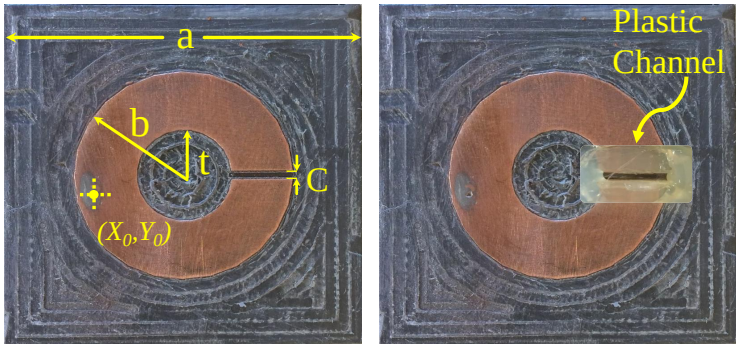

Figure 9.7: The fabricated SARR based sensor, (a) the sensor for solid materials (b) for the fluidic materials

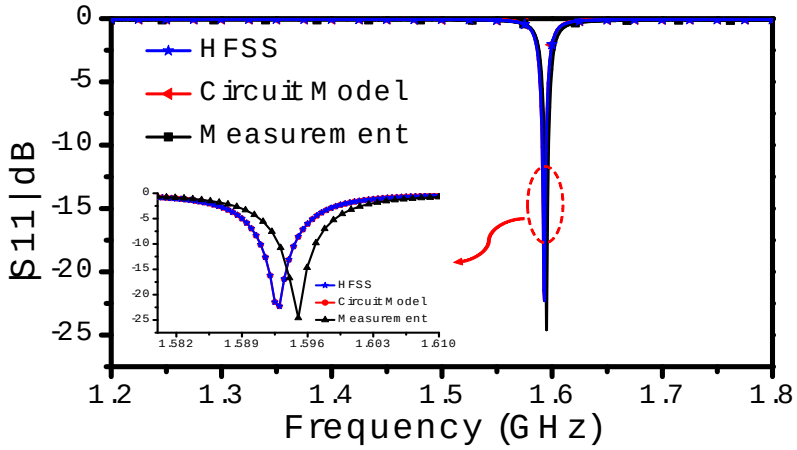

Figure 9.8: The scattering reflection coefficient $|S_{11}|$ dB of the SARR based sensors of the numerical simulation (HFSS), circuit model, and the experimental result.

presence of two-dielectric fluids: chloroform and dichloromethane with permittivities of 4.81 and 8.93, respectively (taken from [61]) with the shift in the resonance frequency of 0.05 GHz and 0.1609 GHz, respectively.

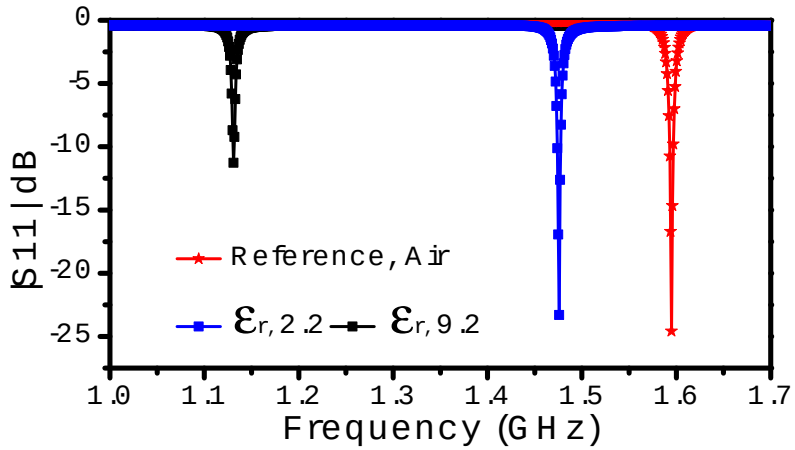

Figure 9.9: $|S_{11}|$ dB of the sensor detecting the change in a dielectric slab with the relative permittivity of 2.2 and 9.2

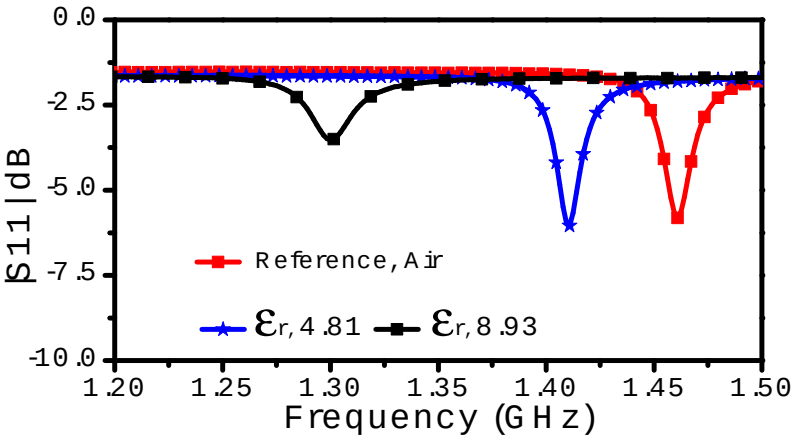

Figure 9.10: $|S_{11}|$ dB of the sensor detecting the change in fluid materials with the relative permittivity of 4.81 and 8.93

9.4 Conclusion

In this chapter, a microwave near-field sensor was reported. The sensor is based on an annular-ring resonator loaded with a split making the resonator compact and miniaturized working at lower frequencies. Although the resonator is based on the planar microstrip line

technology, the resonator shows high-quality factor making it qualify to be used to design near-field sensors for applications including the material characterization and microfluidic technologies. For that, the sensor was tested to characterize two dielectric slabs, 2.2 and 9.2, with the accuracy of 0.5164 % and 5.3886 %, respectively. As a sensor for microfluidic technologies, the sensor was tested to detect the presence of two fluidic materials, dichloromethane and chloroform. So far, for material characterization, the constructed models for characterizing dielectric materials are based on the use of the numerical result and fitting function techniques at a single frequency. Sensing systems based on the measurement at multiple frequency is needed to increase the sensibility of the system.

Chapter 10

Intelligent Sensing Using Multiple Sensors

10.1 Introduction

Planar resonators are unbounded structures which make their analytical models difficult to develop for characterizing the MUT. However, as long as the sensing mechanism is based on measuring the changes in the resonance frequencies, full-wave numerical simulations can be utilized to model the responses of the resonators as functions of the properties of the MUT (e.g., dielectric constant). By using fitting function techniques, the models can then be constructed [31]. Although resonant structures show less sensitivity to noise, other effects such as the air gap between the sensor and the MUT can degrade the performance of the sensors. By using multiple resonances, the effects of the air gap can be taken into account [33]. Nevertheless, since the sensing mechanism is based *only* on single or multiple resonance frequencies, the utilization of the resonators in the sensing systems are still at the preliminary stage. This is due to the limitations and difficulties in constructing either analytical models or models based on numerical results at multiple frequencies.

In this chapter, a concept for designing microwave intelligent sensing (MIS) systems based on modulating the frequency response of multiple electrically-small resonators with

the MUT is introduced. The sensing mechanism of the systems is based on measuring the changes of the transmission coefficients of microstrip lines. When multiple resonators are used, coupling to the resonators will increase the bandwidth of the bandgap. This makes the new system more sensitive for the material characterization. The concept is based on the assumption that the targeted physical parameters are constant over the range of frequencies of the systems. The modulation is based on the interactions between the sensors and the MUT.

Utilizing the information at multiple Extracting more data not only at the resonance frequencies

It can be shown that by utilizing the response of the sensor at many frequencies within the sensitivity of the sensing system, the requirement to have a large number of samples to increase the accuracy of the neural network can be reduced. For validation, an MIS is developed based on utilizing three-identical resonators. The concept was tested using numerical simulation and verified experimentally to characterize the concentration of a fluid mixture.

10.2 The MIS Based on Multiple Resonators

In practical sensing applications, the accuracy of the extracted results can be degraded due to many sources of errors including air gaps between the sensor and the MUT and the background noise. Thus, for characterizing a single physical parameter, such as fluid concentrations or the permittivity or permeability, using the information provided by a single frequency point or the shifts in the resonance frequencies are not sufficient to meet the need for highly reliable sensing systems. If the sensing systems are going to be utilized for characterizing many physical parameters simultaneously, the limitations of models (developed using numerical simulations and fitting function techniques) increase. Of course, the sensing mechanism based on measuring *only* the shifts in the resonance frequencies or the reflection coefficients at a single frequency will make the models construction process easier; however, these models will limit the sensitivity due to measurements' errors or the background noise.

To overcome these limitations, the sensing systems can be designed by utilizing electrically-small resonators where the response over many frequencies can be observed. Microwave planar electrically-small resonators that are based on two-port microstrip line systems terminated by load impedances have an important feature compared to one-port resonant systems such as open-ended coaxial resonator probes and evanescent microwave probes [72,73]. In a two-port system, the MUT affects the resonators but not the terminations (the loads). Hence, the system does not require matching networks to observe the response. For instance, in a 50 Ω system, one designs a microstrip line on a substrate to have a 50 Ω characteristic impedance over a range of frequencies. Then, the system is coupled to a planar resonator and terminated by 50 Ω load impedance. Therefore, observing the transmission coefficient will reveal that the system exhibits a bandgap over a certain range of frequencies. The bandgap is a function of many parameters such as the topology of the resonator and its physical dimensions, the coupling between the line and the resonator, the substrate, and the surrounding environment. Since the sensing system is not enclosed by a perfectly conducting surface, the system will exchange energy with the surrounding environment, namely unbounded structure. The quality of that exchange will determine the system sensitivity, which is limited by the bandgap's characteristic caused by the interaction between the MUT, the resonators and the environment. Therefore, by having multiple resonators, it is expected to increase the sensitivity of the system over a broader bandwidth of the bandgap where each resonator can be modulated with different materials. In fact, some of the resonators can be used to modulate the response with *apriori* characterized materials (i.e., reference materials).

Electrically-small resonators such as CSRRs show higher sensitivity to detect the presence of the dielectric materials compared to SRRs [31]. Figure 10.1 shows an MIS based on a two-port microstrip line exciting three-identical CSRRs (A, B, and, C). Although the MIS is based on three-identical CSRRs, the concept can be generalized to any number of identical or non-identical resonators.

The concept is demonstrated by characterizing the concentration of liquids. For instance, suppose that the MUT (M_m) is a mixture of two pure materials (M_l and M_u) where M_u has a dielectric constant higher than M_l. By loading the resonators A and C with M_u and M_l and resonator B with M_m, figure 10.2 shows the expected qualitative

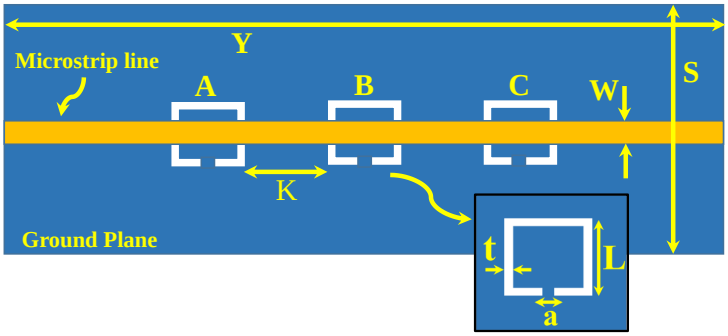

Figure 10.1: A two-port microstrip line exciting three identical CSRRs (A, B, and C) that are etched out in the ground plane of a microstrip transmission line.

response in the form of the transmission coefficient ($|S_{21}|$ dB). The transmission coefficient can be considered as a vector of many components, $|S_{21}(f_1, f_2, ..., f_n)|$. The upper and lower resonance frequencies of M_l and M_u directly depend on their dielectric constants.

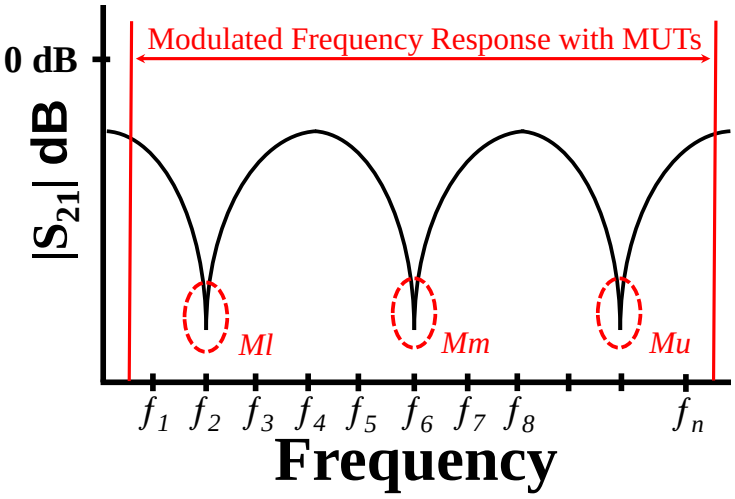

Figure 10.2: A typical qualitative response of the system in terms of the transmission coefficient $|S_{21}|$ dB. M_m is the targeted material whereas M_l and M_u are two reference materials. The M_u has the highest dielectric constant.

The primary objective of the supervised learning algorithms using neural networks is to find the relationship between the input, which is the vector $|S_{21}(f_1, f_2, ..., f_n)|$, and the

output, which is the fluid's concentration. The outcome of the neural network can be depicted in a one-dimensional visualization where the abscissa represents the input (the vector of $|S_{21}(f_1, f_2, ..., f_n)|$) and the ordinate represents the output (the concentration). A qualitative representation of the concentration as a function of the vector ($|S_{21}|$) is depicted in figure 10.3.

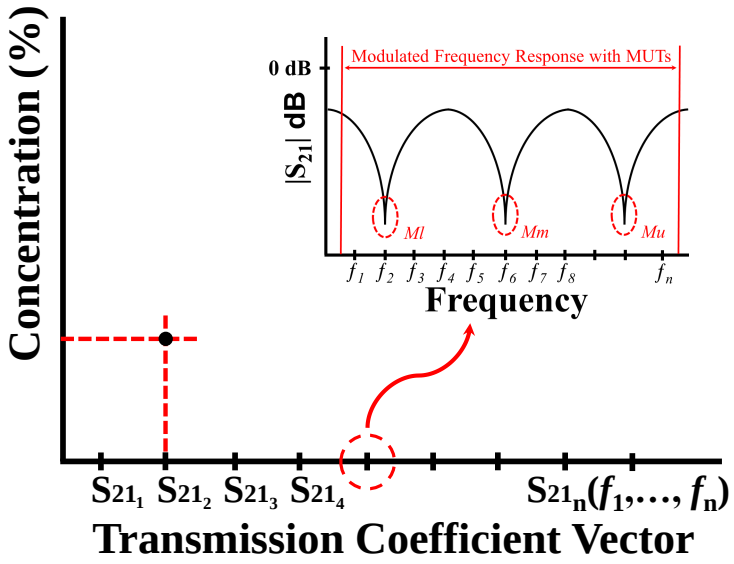

Figure 10.3: A qualitative representation of the concentration as a function of the vector ($|S_{21}|$).

10.3 The MIS Design and Validation

In this work, a two-port microstrip line is used to excite the resonators. Since the response of the MIS ($|S_{21}|$ dB) will be observed by a 50 Ω vector network analyzer (VNA), the microstrip line with a 50 Ω characteristic impedance is designed (line width of 1.63 mm, line thickness of W = 0.75 mm and Rogers RO4350 substrate with the relative permittivity of 3.66 and a loss tangent of 0.0031). The sensitivity of the systems is proportional to the resonators' lengths. This can be confirmed by investigating the shifts in the resonance frequencies versus the dimension of a single CSRR sensor when the MUT is a slab of

the relative permittivity of 4.8 (see figure 10.4). For a system designed to operate at a microwave frequency regime suitable for our measurement setup and taking into account the resonance frequency as a function of the resonators' lengths, the dimensions of the CSRRs are L = 7.5 mm and t = a = 0.5 mm. The MIS system with different values of K is presented in figure 10.5. For K = 10 mm, the MIS system exhibits a resonance frequency of 3.4 GHz.

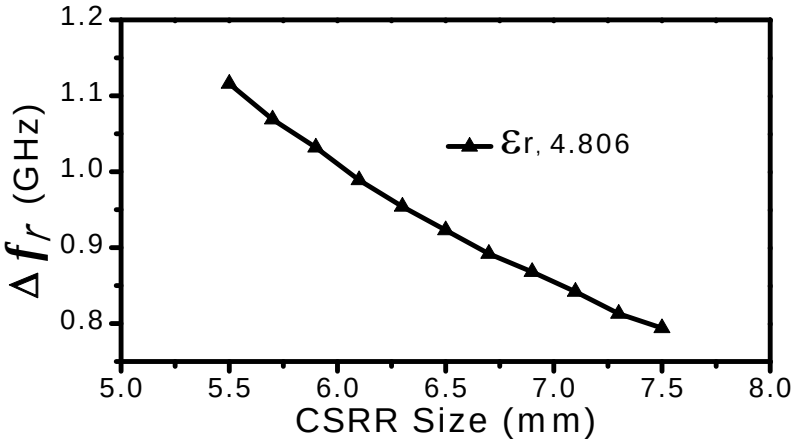

Figure 10.4: The sensitivity of a single CSRR (represented by a shift in the resonance frequency) as a function of the CSRR's dimension when loaded with a dielectric slab having the relative permittivity of 4.8.

The MIS system will be tested by characterizing fluid concentrations. To this end, three-metallic cavities are added to contain the fluids. Figure 10.6 shows the frequency response of the MIS system with and without the metallic cavities. In fact, adding the cavities increased the sensitivity of the system as shown in figure 10.7. This enhancement can be attributed to higher confinement of the electromagnetic field in the sensing area since the cavities are made of metallic material. The fluid concentration of a mixture material (M_m) is prepared by mixing two pure liquids: chloroform (M_m) and cyclohexane (M_l), with permittivities of 4.806 and 2.015, respectively, (taken from [61]).

To study the effect of different liquid concentrations, the resonators A and C are loaded by dielectric materials with the relative permittivity of 4.806 and 2.015, respectively, while resonator B is loaded by a dielectric material with its permittivity varying from 2.015 to

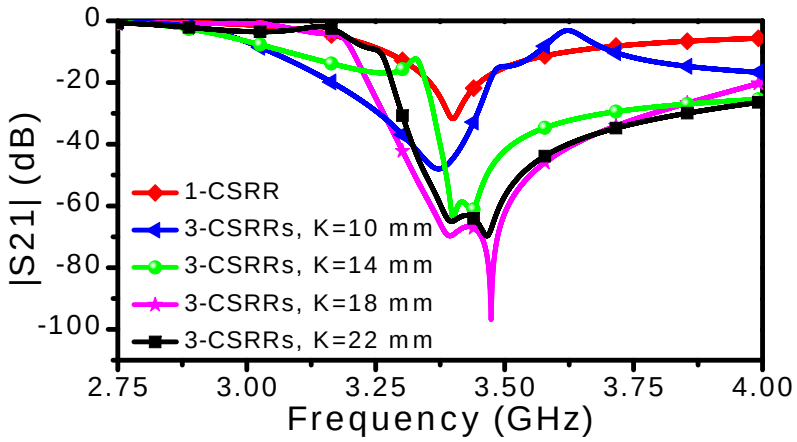

Figure 10.5: The scattering parameter $|S_{21}|$ of a single CSRR and three identical-coupled CSRRs with different values of K.

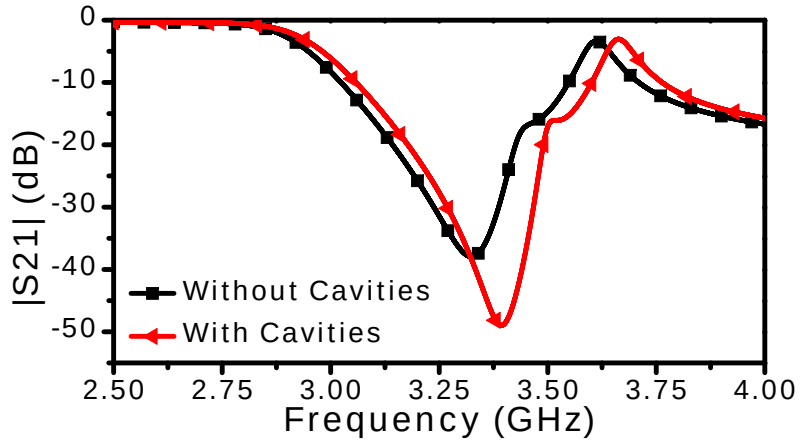

Figure 10.6: The scattering parameter $|S_{21}|$ dB of three resonators system with and without the aluminum cavities.

4.806 with an increment of 0.01. Thus, the response to pure cyclohexane and chloroform will determine the upper and lower frequency limits, whereas the response of the mixture will be presented as a notch in the $|S_{21}|$ located between the two frequency limits. For instance, figure 10.8 shows the response of the MIS where the resonator B is loaded with a material with the relative permittivity of 2.015. Since M_u has the highest dielectric con-

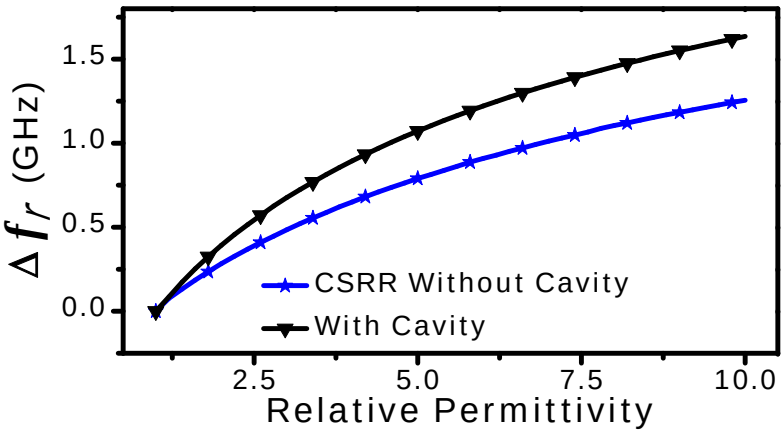

Figure 10.7: The sensitivity of a single CSRR (shift in the resonance frequency) versus the relative permittivity of a dielectric slab with a thickness of 3 mm, with and without a cavity. The relative permittivity of a dielectric slab is varied from 1 to 10 with an increment of 0.2.

stant, the resonance frequency of the resonator A will exhibit the highest shift with respect to free space (upper limit), whereas the resonance frequency of the resonator C loaded with M_l will exhibit the lowest shift (lower limit). Thus, the response of the system interacting with the mixture (M_m) will vary between the upper and lower resonance frequencies. With the dielectric variation of M_m, the response of the system modulated with the reference materials (M_u) and (M_l) and the MUT (M_m) are extracted using the commercial three-dimensional full-wave simulation ANSYS HFSS [34] as shown in figure 10.9.

The response of the MIS system was analyzed and compared to a single CSRR based systems. Both systems were tested to detect materials with dielectric constants of 2.515 and 2.715. The responses of the single-CSRR and three-CSRR sensors are shown in figures 10.10(a) and 10.10(b), respectively. To quantify the sensitivity enhancement of the proposed MIS sensing platform, four parameters, namely, P_1, P_2, P_3, and P_4 (see figure 10.10(b)) were chosen to make the comparison between the two systems. P_1, P_2, P_3, and P_4 represent the shifts in the resonance frequency, changes in the $|S_{21}|$ at the two resonance frequencies (at the notch of the $|S_{21}|$ of the two systems), changes in the $|S_{21}|$ at the first resonance frequency (the presence of M_m with the value of 2.515), and changes in

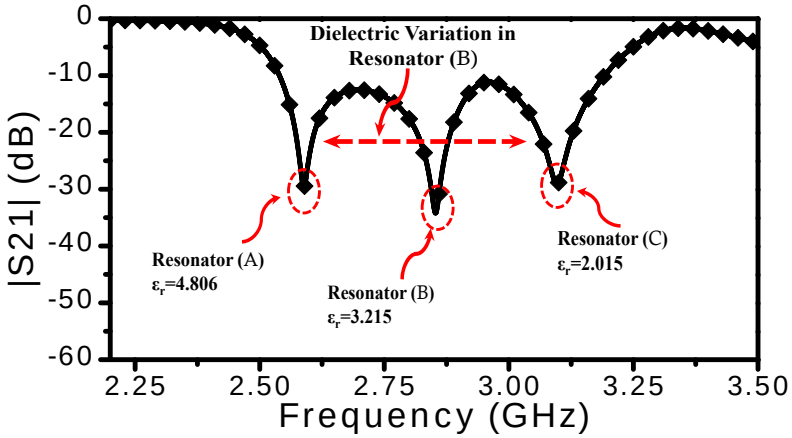

Figure 10.8: The scattering parameter $|S_{21}|$ of the MIS obtained using HFSS, where the resonator A and C are loaded by dielectric materials with the relative permittivity of 4.806 and 2.015, respectively, while resonator B is loaded by the dielectric material with permittivity of 3.215

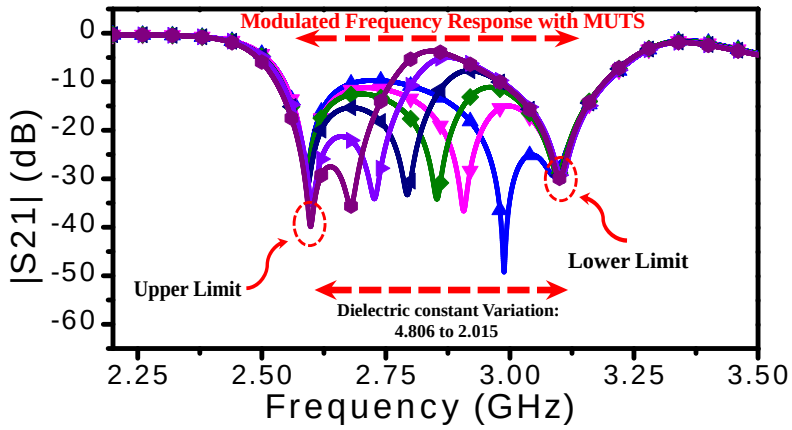

Figure 10.9: The scattering parameter $|S_{21}|$ of the system obtained from the full-wave numerical simulation. The resonator A and C are loaded with 4.806 and 2.015, respectively, while resonator B is loaded with a material having permittivity varying from 2.015 to 4.806 in increments of 0.05 producing 57 curves. The plot is corresponding only to some selected variation for the purpose of making the curves clear.

the $|S_{21}|$ at the second resonance frequency (the presence of M_m with the value of 2.515), respectively. For P_1, the sensitivity is enhanced by 7 MHz or equivalent to 16.5% when the shifts in the resonance frequencies (49.4 and 42.6 MHz) of the MIS system and the single CSRR system, respectively, are compared. For P_2, when compared to the single CSRR system, the sensitivity enhancement in terms of changes in the $|S_{21}|$ of the MIS system when the resonance frequency exhibits a change from 3 to 2.95 GHz, is 14 dB or equivalent to 78.21%. For P_3, the sensitivity enhancement that is evaluated at a single frequency (the resonance frequency of 3 GHz of the MIS system) based on the changes in $|S_{21}|$ is calculated as 21.24 dB or equivalent to 163.38%. Finally, P_4 shows a sensitivity enhancement of 6.38 dB or 46.73% at the resonance frequency of 2.95 GHz. This enhancement in the sensitivity indicates that the overall sensitivity of the proposed MIS system is enhanced over a wide range of frequencies. This enhancement of sensitivity is essential for increasing the accuracy of the entire detection system.

10.4 Fabrication and Experimental Results

The MIS was fabricated using printed circuit board (PCB) technology. Three-aluminum cavities were added to the resonators to hold liquids. The sensing system is shown in figure 10.11. Since the system will be tested to detect the concentration of a fluid material that is a mixture of chloroform and cyclohexane, the mixture was prepared where the chloroform was used as the reference material having a total liquid volume of 1 mL. For instance, 60% is corresponding to 0.6 mL of chloroform and 0.4 mL of cyclohexane.

21 samples were prepared with different concentrations from 0% to 100% with an increment of 5%. The response of the MIS at each concentration is observed as a vector, $|S_{21}(f_1, f_2, ..., f_n)|$ where $f_1 = 2$ GHz and $f_n = 4.50125$ GHz with a step frequency value of 1.88 MHz. Each vector has 1335 components. Therefore, for 21 samples, there are 28035 points of data to be processed. Since the concentration of the fluid is constant over these frequencies, which are going to be enforced by utilizing the supervised learning algorithm, the data points provide new information about the concentration. In fact, extracting more information about the targeted parameter can increase the accuracy of the results if the

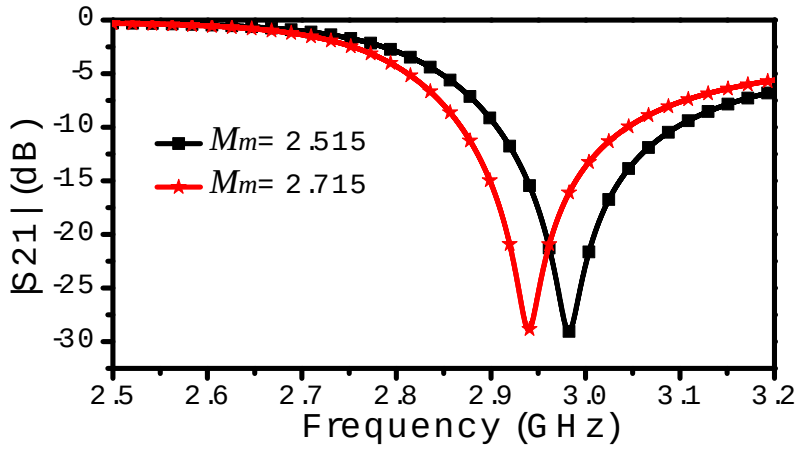

(a)

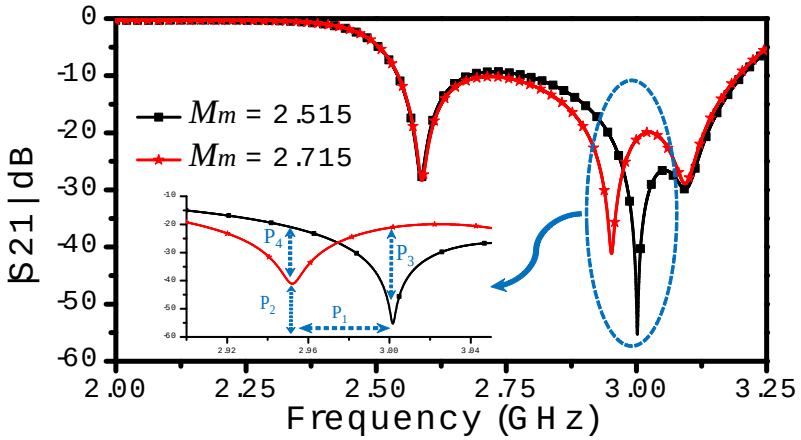

(b)

Figure 10.10: (a) and (b) the scattering parameter $|S_{21}|$ of the single CSRR and three CSRR based sensors, respectively, for M_m having the relative permittivity of 2.515 and 2.715.

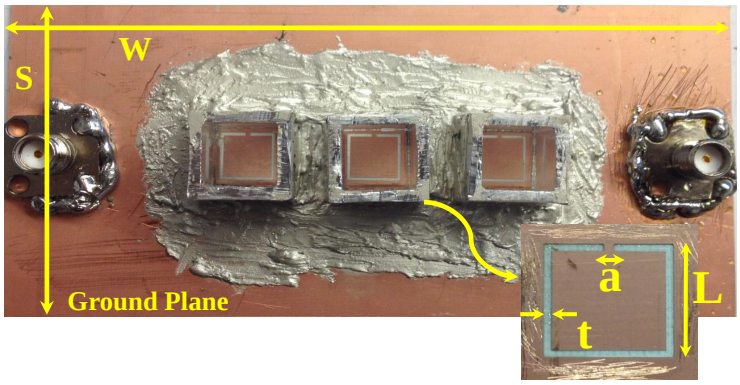

Figure 10.11: The fabricated MIS system, where L = 7.5 mm, t = a = 0.5 mm, W = 100 mm, and S = 50 mm.

collected data has noise since the system will have different sensitivity over the range of frequency considered. For instance, the system might be sensitive to the air gap at a certain frequency but less sensitive at others. Thus, the system will be more robust to overcome the sources of errors that are the result of the experimental setup. In addition, the information can be utilized to extract many parameters simultaneously. Note that if there is a single input (a single frequency response at the resonance frequency), using 21 samples might not be sufficient to train the neural network. The responses of some selected concentrations are shown in figure 10.12. For characterizing M_m using the information contained in the samples, supervised neural networks can be used.

10.5 Demodulation Using Supervised Neural Networks

To find the relationship between the input and the output (the liquid concentration in our case), the multi-layer perceptron (MLP) neural networks with supervisor learning algorithms can be utilized. There are many backpropagation learning algorithms such as Bayesian regulation backpropagation, Levenberg-Marquardt backpropagation, scaled conjugate gradient backpropagation, and resilient backpropagation. Since the datasets are small and limited to only 21 samples, the Bayesian regulation backpropagation algorithm is the best choice to use for the learning process of the neural networks [74]. The Bayesian

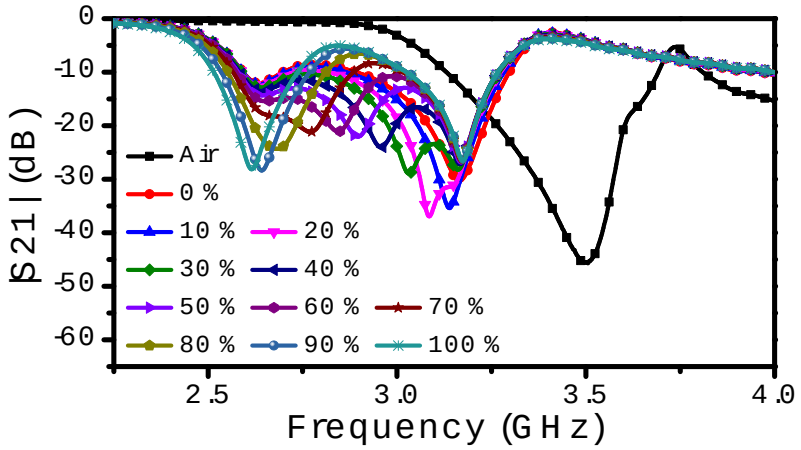

Figure 10.12: The response of the MIS obtained experimentally when using the chloroform as the reference material.

regulation backpropagation artificial neural network (BRANN) can produce robust models without the need of the validation process that is required by other algorithms that need some of the data for validation [74]. In addition, the BRANN overcomes the difficulty of overtraining and overfitting.

The BRANN was tested with different hidden layers since higher number of hidden layers are not necessary to produce higher accuracy. 4 and 5 hidden layers were found to be sufficient for our datasets. In the BRANN, the datasets are divided into training and test (unseen) samples. In particular, the datasets were classified as 1- 70/100 % training 30/100 test (14 samples for training and 6 samples for the test) 2- 85/100 % training 15/100 test (18 samples for training and 3 samples for the test) 3- 90/100 % training 20/100 test (19 samples for training and 2 samples for the test). In the supervisor learning algorithm, the choice of particular samples for training or testing is random to test the performance of the BRANN. Since the datasets are small, it has been found that training the BRANN with 19 samples can result in an accuracy of approximately 99.9 %. The summary of the training and the test samples with different hidden layers and classification of the datasets and the performance in the mean square error (MSE) is presented in table 10.1.

Table 10.1: The bayesian regulation backpropagation artificial neural network (BRANN) for characterizing the concentration of a fluid material

Training Trial	Hidden Layers	Training to Test Samples	Training Performance in MSE	Over All Performance MSE	Test Performance in MSE	Unseen Results (Test)	Results Using the BRANN	Accuracy
1	5	15 to 6	1.06e-20	0.6179	2.1627	10	11.73	82.80 %
						20	21.2172	93.90 %
						30	28.5424	95.00 %
						35	35.9368	97.00 %
						50	52.0599	95.80 %
						95	96.1383	98.80 %
2	5	18 to 3	0.2837	0.0017	1.9754	20	20.0066	99.90 %
						35	35.0105	99.90 %
						40	40.4515	98.80 %
3	5	18 to 3	0.0017	0.1474	1.022	20	20.18	99.10 %
						70	70.59	99.20 %
						75	76.64	97.80 %
4	5	18 to 3	3.31e-15	0.2153	1.5074	75	75.14	99.80 %
						80	78.42	98.00 %
						90	88.58	98.00 %
5	5	18 to 3	7.50e-4	0.1572	1.0962	45	45.61	99.10 %
						50	51.72	96.60 %
						65	65.4	99.40 %
6	5	19 to 2	1.69e-4	0.0539	0.5648	25	25.59	98.40 %
						55	54.12	97.64 %
7	4	19 to 2	2.71e-24	0.2888	3.0322	20	20.4	98.00 %
						100	97.57	97.60 %
8	4	19 to 2	3.67e-4	3.6155e-4	3.0743e-4	40	39.99	99.97 %
						60	59.98	99.96 %
9	4	19 to 2	1.50e-13	0.1053	1.106	20	19.6	98.00 %
						90	88.57	98.00 %
10	4	19 to 2	1.22e-13	0.0718	0.7539	55	54.2	98.50 %
						95	95.93	99.00 %
11	4	19 to 2	0.002	0.0761	0.7803	40	40.08	99.80 %
						75	76.25	98.00 %
12	4	19 to 2	1.91e-14	0.0943	0.9906	15	13.59	90.60 %
						60	59.97	99.60 %

10.6 Conclusion

In this chapter, a microwave intelligent sensing systems was introduced. The system is based on modulating and demodulating the frequency response of multiple closely distanced sensors over a wide frequency range. Under the assumption that the physical parameters to be characterized are constant over the frequency band, the responses, characterized as vectors of multiple dimensions of the transmission coefficients, are then utilized for constructing and testing models that are built using neural networks techniques. Furthermore, to increase the sensitivity of the system over a larger frequency band, multiple identical electrically-small resonators are used. In this work three identical CSRRs were used. The system was tested to detect the concentration of fluids. The sensing part of the system was fabricated using PCB technology and the results were recorded using a vector network analyzer. Then, the results were used to construct models utilizing the Bayesian regulation backpropagation artificial neural network (BRANN). The models were used to characterize the fluids. Although the datasets were relatively small, the utilization of the vectors of many components as inputs provided sufficient information to the BRANN to produce models with an accuracy ranging from 82.8% to 99.97%. An accuracy level of 99.97% was achieved as a result of using 90% of the data to train the BRANN, which shows that larger datasets provide higher accuracy.

Chapter 11

Conclusion and Future Work

11.1 Accomplished Work

1. **In Chapter 2**, the sensitivity of planar CSRRs to their topologies' parameters such as gaps and lengths was analyzed using the approximated circuit model and the eignmode solver of the numerical simulation (HFSS). The result of the analysis was validated numerically by building a system based on CSRRs with different gaps and lengths, with the CSRRs being coupled to two-port microstrip lines. It has been found that the larger the gaps or smaller the length, the higher the sensitivity of the CSRRs sensor to detect changes in dielectric materials. In addition, the analysis shows that the planar CSRRs sensors are suitable for designing near-field sensors for low dielectric materials. The results are validated experimentally by fabricated many prototypes with different gaps and length, where the sensors are utilized to detect the presence of a dielectric slab with the dielectric constant of 2.33.

2. **In Chapter 3**, an ultrasensitive microwave near-field sensor is proposed to design very sensitivity near-field sensors to detect cracks in metallic materials. The proposed sensors shows two advantageous, higher sensitivity and dynamic range, which are essential to detect micrometer cracks. For a crack width of 200 μm and depth of 2 mm, the sensor achieved a resonance shift of 1.8 GHz, which is significantly higher

than what was achieved by any other microwave sensor, including the highly sensitive CSRR sensor, operating in the low microwaves regime. The ultra high sensitivity of the sensor makes it a strong candidate for the detection of sub-millimeter size cracks, and also for other applications such as material sensing and characterization.

3. **In Chapter 4**, a microwave near-field sensor based on planar CSRRs is developed to resolve sub-millimeter cracks in dielectric materials. Design formulae were provided that are based on the numerical simulation that can eliminate expensive full-wave numerical simulations. By analyzing the total electric field on the CSRRs, the position where the maximum field is the sensing element that is most sensitive to changes in the surface of MUTs. The CSRR sensor was found to be highly effective for detecting sub-millimeter cracks in dielectric surfaces.

4. **In Chapter 5**, novel near-field sensors based on coupling multiple resonators to multiple microstrip lines. The resonators are based on planar CSRRs, where the resonators are coupled in perpendicular to the direction of the propagation. Thus, the electrical length of the resonators is kept the same. The multiple resonators increase the sensing areas. Consequently, the sensitivity of CSRRs sensors to detect dielectric materials has enhanced. The sensing system is developed based on splitter-combiner microstrip sections loaded with coupled resonators (CSRRs). The sensitivity of the proposed sensor was validated numerically and experimentally to detect the presence of two dielectric slabs with the dielectric constant of 2.33 and 9.8, respectively. The proposed sensor shows higher sensitivity compared to a single CSRR sensor. Since the rapid growth in the demanding on miniaturized-sensitive sensors with the ease of sample preparation methods [14], microwave near-field sensors based on multiple resonators can open a new degree of freedom to design miniaturized-sensitive sensors.

5. **In Chapter 6**, the new concept was proposed to increase the sensitivity of planar electrically-small resonators as near-field sensors. The concept is based on increasing the overall capacitance of the resonators in the sensing area (the free space), where the resonators can interact with the MUTs. One way of realizing a sensor based on the concept was the placement of a capacitor on top of a planar sensor. For the validation purpose, the sensor was fabricated using PCB technology and verified

experimentally to detect the concentration of fluid materials. The sensor presented here is expected to be useful in the lab on a chip and other quality control and environmental monitoring applications.

6. **In Chapter 7**, the concept of the top capacitors to increase the sensitivity of SRRs was adopted. The capacitors increase the stored-electric field in the sensing areas that interact with the MUTs. Thus, the maximum loaded quality factor of 1555 or 2102% compared to 70.6 of the planar SRR is achieved using the numerical simulation. In terms of the sensitivity, the proposed sensor achieved experimentally 700% sensitivity enhancement when detecting changes in dielectric materials. In addition, the sensor was utilized to detect the level of fluid materials. Since the resonance frequency is a function of the length of the top capacitors, the presented concept can be utilized to design sensors for a large volume of fluids to microfluidic technologies. Thus, applications such as a lab on a chip and other quality control and environmental monitoring can find these type of sensor attractive. Moreover, by analyzing the distribution of electromagnetic field variation over the space, the SRRs with the top capacitance can be used to design microwave near-field microscopy. The sensor is used to image a cylindrical hole (diameter of 4 mm) fabricated into a dielectric material with the dielectric constant of 9.2 and thickness of 6 mm. The resolution of the probe is 0.25 mm.

7. **In Chapter 8**, a novel microwave near-field sensor based on CELCR and three-dimensional capacitors was proposed. The sensing area was shrunk to a micro-scale so that the three-dimensional capacitor can be utilized to design probes for micro-scale based applications such as microfluidic technologies. The sensor was tested using the numerical simulation to detect the presence of fluid materials. In addition, the sensor was utilized to detect the fluid levels of the chloroform, dichloromethane, distilled water, which shows that the sensor can be utilized to detect the presence of high dielectric materials.

8. **In Chapter 9**, a microwave near-field sensor was reported. The sensor is based on an annular-ring resonator loaded with a split making the resonator compact and miniaturized working at lower frequencies. Although the resonator is based on pla-

nar microstrip line technology, the resonator shows high-quality factor making it qualify to be used to design near-field sensors for applications including the material characterization and microfluidic technologies. For that, the sensor was tested to characterize two dielectric slabs, 2.2 and 9.2, with the accuracy of 0.5164 % and 5.3886, respectively. As a sensor for microfluidic technologies, the sensor was tested to detect the presence of two fluidic materials, cyclohexane and chloroform.

9. **In Chapter 10**, a microwave intelligent sensing systems was introduced. The system is based on modulating and demodulating the frequency response of multiple closely distanced sensors over a wide frequency range. Under the assumption that the physical parameters to be characterized are constant over the frequency band, the responses, characterized as vectors of multiple dimensions of the transmission coefficients, are then utilized for constructing and testing models that are built using neural networks techniques. Furthermore, to increase the sensitivity of the system over a larger frequency band, multiple identical electrically-small resonators are used. In this chapter, three identical CSRRs were used. The system was tested to detect the concentration of fluids. The sensing part of the system was fabricated using PCB technology, and the results were recorded using a vector network analyzer. Then, the results were used to construct models utilizing the Bayesian regulation backpropagation artificial neural network (BRANN). The models were used to characterize the fluids. Although the datasets were relatively small, the utilization of the vectors of many components as inputs provided sufficient information to the BRANN to produce models with an accuracy ranging from 82.8% to 99.97%. An accuracy level of 99.97% was achieved as a result of using 90% of the data to train the BRANN, which shows that larger datasets provide higher accuracy.

11.2 List of Publications

[1] **Ali M. Albishi** and Omar M. Ramahi. Sensitivity and Tunability Enhancement of Split-Ring Resonators for Fluidic and Microfluidic Technologies and Fluid-Level Detection Applications. *IEEE Transactions on Microwave Theory and Techniques*. **(To be submitted)**

[2] **Ali M. Albishi** and Omar M. Ramahi. Sensitivity Enhancement Using a Novel Transmission Line Coupling Mechanism to Multiple Resonators. *IEEE Transactions on Microwave Theory and Techniques*. **(To be submitted)**

[3] **Ali M. Albishi** and Omar M. Ramahi. High-Q Split-Annular-Ring Resonators for Detection Applications. *IEEE Microwave and Wireless Components Letters*. **(To be submitted)**

[4] **Ali M. Albishi** and Omar M. Ramahi. Intelligent Sensing Using Multiple Sensors. *IEEE Transactions on Microwave Theory and Techniques*, June 2017. **(Submitted)**

[5] **Ali M. Albishi** and Omar M. Ramahi. Highly Sensitive Microwaves Sensors for Fluid Concentration Measurements. *IEEE Microwave and Wireless Components Letters*, Apr 2018. **(Accepted)**

[6] **Ali Albishi** and Omar M. Ramahi. Intelligent Sensing Using a System of Multiple Microwaves Resonators. In *Antennas and Propagation & USNC/URSI National Radio Science Meeting, 2017 IEEE International Symposium on*, pages 225–226. IEEE, July 2017. **(Conference)**

[7] **Ali Albishi** and Omar M. Ramahi. A high-Q Annular Ring Antenna as a Microwave Near-Field Material Sensor. In *Antennas and Propagation & USNC/URSI National Radio Science Meeting, 2017 IEEE International Symposium on*, pages 1213–1214. IEEE, July 2017. **(Conference)**

[8] **Ali M. Albishi** and Omar M. Ramahi. Microwaves-Based High Sensitivity Sensors for Crack Detection in Metallic Materials. *IEEE Transactions on Microwave Theory and Techniques*, 65(5):1864–1872, March 2017. **(Accepted)**

[9] **Ali M. Albishi** Mohamed K. El Badawe and Omar M. Ramahi. A Microwave Planar Near-Field Sensor Based on Metamaterial Unit Cells for Sensitivity Enhancement. In *The 7th International Conference on Metamaterials, Photonic Crystals and Plasmonics , 2016*, pages 2429–1390. IEEE, July 2016. **(Conference)**

[10] **Ali Albishi** and Omar Ramahi. Ultrasensitive Microwave Near-Field Based Sensors for Crack Detection in Metallic Materials. In *Antennas and Propagation (APSURSI), 2016 IEEE International Symposium on*, pages 1955–1956. IEEE, June 2016. **(Conference)**

[11] **Ali M. Albishi** and Omar M. Ramahi. Surface Crack Detection in Metallic Materials Using Sensitive Microwave-Based Sensors. In *Wireless and Microwave Technology Conference (WAMICON), 2016 IEEE 17th Annual*, pages 1–3. IEEE, June 2016. **(Conference)**

[12] **Ali Albishi** and Omar M. Ramahi. Detection of Surface and Subsurface Cracks in Metallic and non-Metallic Materials Using a Complementary Split-Ring Resonator. *Sensors*, 14(10):19354–19370, 2014. **(Accepted)**

[13] **Ali M. Albishi**, Omar M. Ramahi, and Muhammed S. Boybay. Complementary Split-Ring Resonator as a High Sensitivity Sensor. In *Antennas and Propagation Society International Symposium (APSURSI), 2012 IEEE*, pages 1–2. IEEE, July 2012. **(Conference)**

[14] **A. M. Albishi**, Muhammed S. Boybay, and Omar M. Ramahi. Complementary Split-Ring Resonator for Crack Detection in Metallic surfaces. *Microwave and Wireless Components Letters, IEEE*, 22(6):330–332, June 2012. **(Accepted)**

11.3 Future Work

1. **Extend** the sensitivity analysis of electrically-small resonators by analyzing the spatial variation of the electromagnetic field in the reciprocal space (K-space) that will help to understand the possibility to design sensitive probes with high resolution.

2. **Design** sensors based array for crack detection in metallic and non-metallic materials to cover large surface areas under test.

3. **Apply** the concept of electrically-small resonators and three-dimensional capacitors to sub-micrometer based applications.

4. **Apply** the concept of the integrated system of multi-resonators and the artificial intelligence to applications such as blood glucose monitoring systems.

5. **Analyze and Understand** the possibility to scale down the electrically-small resonators to the radio-wave regime where the fabrication, implementation, and testing are expected to be much easier and cheaper than in the microwave regime.

References

[1] A.M. Albishi, Muhammed S. Boybay, and Omar M. Ramahi. Complementary split-ring resonator for crack detection in metallic surfaces. *Microwave and Wireless Components Letters, IEEE*, 22(6):330–332, June 2012.

[2] Ali Albishi and Omar M. Ramahi. Detection of surface and subsurface cracks in metallic and non-metallic materials using a complementary split-ring resonator. *Sensors*, 14(10):19354–19370, 2014.

[3] J.D. Baena, J. Bonache, F. Martin, R.M. Sillero, F. Falcone, T. Lopetegi, M.A.G. Laso, J. Garcia-Garcia, I. Gil, M.F. Portillo, and M. Sorolla. Equivalent-circuit models for split-ring resonators and complementary split-ring resonators coupled to planar transmission lines. *Microwave Theory and Techniques, IEEE Transactions on*, 53(4):1451–1461, April 2005.

[4] Jonathan S Daniels and Nader Pourmand. Label-free impedance biosensors: Opportunities and challenges. *Electroanalysis*, 19(12):1239–1257, 2007.

[5] Stuart O Nelson, Wen chuan Guo, Samir Trabelsi, and Stanley J Kays. Dielectric spectroscopy of watermelons for quality sensing. *Measurement Science and Technology*, 18(7):1887, 2007.

[6] Claire Dalmay, A. Pothier, P. Blondy, F. Lalloue, and Marie-Odile Jauberteau. Label free biosensors for human cell characterization using radio and microwave frequencies. In *Microwave Symposium Digest, 2008 IEEE MTT-S International*, pages 911–914, June 2008.

[7] Jongchul Kim, Arsen Babajanyan, Artur Hovsepyan, Kiejin Lee, and Barry Friedman. Microwave dielectric resonator biosensor for aqueous glucose solution. *Review of Scientific Instruments*, 79(8):086107, 2008.

[8] Amir Ebrahimi, Withawat Withayachumnankul, Said Al-Sarawi, and Derek Abbott. High-sensitivity metamaterial-inspired sensor for microfluidic dielectric characterization. *Sensors Journal, IEEE*, 14(5):1345–1351, 2014.

[9] Hee-Jo Lee, Jung-Hyun Lee, Hui-Sung Moon, Ik-Soon Jang, Jong-Soon Choi, Jong-Gwan Yook, and Hyo-Il Jung. A planar split-ring resonator-based microwave biosensor for label-free detection of biomolecules. *Sensors and Actuators B: Chemical*, 169:26–31, 2012.

[10] Reza Haghani, Mohammad Al-Emrani, and Mohsen Heshmati. Fatigue-prone details in steel bridges. *Buildings*, 2(4):456–476, November 2012.

[11] Peter J Shull. *Nondestructive evaluation: theory, techniques, and applications*. CRC press, 2002.

[12] Chin-Yung Yeh and Reza Zoughi. A novel microwave method for detection of long surface cracks in metals. *Instrumentation and Measurement, IEEE Transactions on*, 43(5):719–725, Oct 1994.

[13] R Zoughi and Sergey Kharkovsky. Microwave and millimetre wave sensors for crack detection. *Fatigue & Fracture of Engineering Materials & Structures*, 31(8):695–713, August 2008.

[14] Peter RC Gascoyne and Jody V Vykoukal. Dielectrophoresis-based sample handling in general-purpose programmable diagnostic instruments. *Proceedings of the IEEE*, 92(1):22–42, Nov 2004.

[15] Ahmed Salim and Sungjoon Lim. Review of recent metamaterial microfluidic sensors. *Sensors*, 18(1):232, Jan 2018.

[16] David M Pozar. *Microwave engineering*. John Wiley & Sons, 2009.

[17] Fawwaz T Ulaby, Umberto Ravaioli, and Eric Michielssen. *Fundamentals of applied electromagnetics*. Prentice Hall, 2014.

[18] Muhammad Usman Memon and Sungjoon Lim. Review of electromagnetic-based crack sensors for metallic materials (recent research and future perspectives). *Metals*, 6(8):172, July 2016.

[19] Chen Gao and X-D Xiang. Quantitative microwave near-field microscopy of dielectric properties. *Review of scientific instruments*, 69(11):3846–3851, November 1998.

[20] J. Kerouedan, P. Queffelec, P. Talbot, C. Quendo, S. Blasi, and A. Brun. Detection of micro-cracks on metal surfaces using near-field microwave dual-behavior resonator filters. *Measurement Science and Technology*, 19(10):105701, August 2008.

[21] J.B. Pendry, A.J. Holden, D.J. Robbins, and W.J. Stewart. Magnetism from conductors and enhanced nonlinear phenomena. *Microwave Theory and Techniques, IEEE Transactions on*, 47(11):2075–2084, Nov 1999.

[22] F. Falcone, T. Lopetegi, J.D. Baena, R. Marques, F. Martin, and M. Sorolla. Effective negative-ϵ; stopband microstrip lines based on complementary split ring resonators. *Microwave and Wireless Components Letters, IEEE*, 14(6):280–282, June 2004.

[23] Sergei Alexander Schelkunoff and Harald T Friis. *Antennas: theory and practice*, volume 639. Wiley New York, 1952.

[24] Tao Chen, Suyan Li, and Hui Sun. Metamaterials application in sensing. *Sensors*, 12(3):2742–2765, Feb 2012.

[25] Chieh-Sen Lee and Chin-Lung Yang. Single-compound complementary split-ring resonator for simultaneously measuring the permittivity and thickness of dual-layer dielectric materials. *Microwave Theory and Techniques, IEEE Transactions on*, 63(6):2010–2023, 2015.

[26] Hee-Jo Lee, Hyun-Seok Lee, Kyung-Hwa Yoo, and Jong-Gwan Yook. DNA sensing using split-ring resonator alone at microwave regime. *Journal of Applied Physics*, 108(1):014908, 2010.

[27] H Torun, F Cagri Top, G Dundar, and AD Yalcinkaya. An antenna-coupled split-ring resonator for biosensing. *Journal of Applied Physics*, 116(12):124701, 2014.

[28] Ali M Albishi and Omar M Ramahi. Microwaves-based high sensitivity sensors for crack detection in metallic materials. *IEEE Transactions on Microwave Theory and Techniques*, 65(5):1864–1872, March 2017.

[29] Withawat Withayachumnankul, Kata Jaruwongrungsee, Adisorn Tuantranont, Christophe Fumeaux, and Derek Abbott. Metamaterial-based microfluidic sensor for dielectric characterization. *Sensors and Actuators A: Physical*, 189:233–237, 2013.

[30] Humeyra Caglayan, Semih Cakmakyapan, Sarah A Addae, Melissa A Pinard, Deniz Caliskan, Kadir Aslan, and Ekmel Ozbay. Ultrafast and sensitive bioassay using split ring resonator structures and microwave heating. *Applied physics letters*, 97(9):093701, 2010.

[31] M.S. Boybay and Omar M. Ramahi. Material characterization using complementary split-ring resonators. *Instrumentation and Measurement, IEEE Transactions on*, 61(11):3039–3046, Nov 2012.

[32] Muhammed S Boybay and Omar M Ramahi. Non-destructive thickness measurement using quasi-static resonators. *Microwave and Wireless Components Letters, IEEE*, 23(4):217–219, 2013.

[33] Chin-Lung Yang, Chieh-Sen Lee, Kuan-Wei Chen, and Kuan-Zhou Chen. Noncontact measurement of complex permittivity and thickness by using planar resonators. *IEEE Transactions on Microwave Theory and Techniques*, 64(1):247–257, December 2016.

[34] ANSYS HFSS version, 15.0.0, http://www.ansys.com, last access 27-July-2018.

[35] John F O'Hara, Ranjan Singh, Igal Brener, Evgenya Smirnova, Jiaguang Han, Antoinette J Taylor, and Weili Zhang. Thin-film sensing with planar terahertz metamaterials: sensitivity and limitations. *Optics Express*, 16(3):1786–1795, Jan 2008.

[36] Hu Tao, Andrew C Strikwerda, Mengkun Liu, Jessica P Mondia, Evren Ekmekci, Kebin Fan, David L Kaplan, Willie J Padilla, Xin Zhang, Richard D Averitt, et al.

Performance enhancement of terahertz metamaterials on ultrathin substrates for sensing applications. *Applied Physics Letters*, 97(26):261909, Dec 2010.

[37] B Wu, B Li, T Su, and C-H Liang. Equivalent-circuit analysis and lowpass filter design of split-ring resonator DGS. *Journal of Electromagnetic Waves and Applications*, 20(14):1943–1953, Apr 2006.

[38] Koray Aydin, A. Ozgur Cakmak, Levent Sahin, Z. Li, Filiberto Bilotti, Lucio Vegni, and Ekmel Ozbay. Split-ring-resonator-coupled enhanced transmission through a single subwavelength aperture. *Phys. Rev. Lett.*, 102:013904, Jan 2009.

[39] Jordi Bonache, Marta Gil, Ignacio Gil, Joan Garcia-Garcia, and Ferran Martin. On the electrical characteristics of complementary metamaterial resonators. *Microwave and Wireless Components Letters, IEEE*, 16(10):543–545, September 2006.

[40] C Yeh and R Zoughi. Microwave detection of finite surface cracks in metals using rectangular waveguides. *Research in Nondestructive Evaluation*, 6(1):35–55, March 1994.

[41] Reza Zoughi, Stoyan I Ganchev, and Christian Huber. Microwave measurement-parameter optimization for detection of surface breaking hairline cracks in metals. *Nondestructive Testing and Evaluation*, 14(5):323–337, 1998.

[42] Kristen M Donnell, Andrew McClanahan, and Reza Zoughi. On the crack characteristic signal from an open-ended coaxial probe. *IEEE Transactions on Instrumentation and Measurement*, 63(7):1877–1879, May 2014.

[43] A Husain and EA Ash. Microwave scanning microscopy for non-destructive testing. In *Microwave Conference, 1975. 5th European*, pages 213–217, Sept 1975.

[44] Taehwa Yun and Sungjoon Lim. High-q and miniaturized complementary split ring resonator-loaded substrate integrated waveguide microwave sensor for crack detection in metallic materials. *Sensors and Actuators A: Physical*, 214:25 – 30, August 2014.

[45] Bing Hu, Zhao Ren, Muhammed S Boybay, and Omar M Ramahi. Waveguide probe loaded with split-ring resonators for crack detection in metallic surfaces. *IEEE Transactions on Microwave Theory and Techniques*, 62(4):871–878, March 2014.

[46] Amanpreet Kaur and Anupma Marwaha. Crack detection on metal surfaces with an array of complementary split ring resonators. *International Journal of Computer Applications*, 119(10), 2015.

[47] Abdulbaset Ali, Bing Hu, and Omar M. Ramahi. Intelligent detection of cracks in metallic surfaces using a waveguide sensor loaded with metamaterial elements. *Sensors*, 15(5):11402–11416, May 2015.

[48] Ali Albishi and Omar Ramahi. Ultrasensitive microwave near-field based sensors for crack detection in metallic materials. In *Antennas and Propagation (APSURSI), 2016 IEEE International Symposium on*, pages 1955–1956. IEEE, June 2016.

[49] Firas Awaja, Shengnan Zhang, Manoj Tripathi, Anton Nikiforov, and Nicola Pugno. Cracks, microcracks and fracture in polymer structures: Formation, detection, autonomic repair. *Progress in Materials Science*, 83:536–573, Oct 2016.

[50] J.D. Baena, J. Bonache, F. Martin, R.M. Sillero, F. Falcone, T. Lopetegi, M. A G Laso, J. Garcia-Garcia, I Gil, M.F. Portillo, and M. Sorolla. Equivalent-circuit models for split-ring resonators and complementary split-ring resonators coupled to planar transmission lines. *Microwave Theory and Techniques, IEEE Transactions on*, 53(4):1451–1461, April 2005.

[51] J. Nadakuduti, G. Chen, and R. Zoughi. Semiempirical electromagnetic modeling of crack detection and sizing in cement-based materials using near-field microwave methods. *Instrumentation and Measurement, IEEE Transactions on*, 55(2):588–597, 2006.

[52] Taehwa Yun and Sungjoon Lim. High-q and miniaturized complementary split ring resonator-loaded substrate integrated waveguide microwave sensor for crack detection in metallic materials. *Sensors and Actuators A: Physical*, 214(0):25 – 30, 2014.

[53] J.D. Baena, J. Bonache, F. Martin, R.M. Sillero, F. Falcone, T. Lopetegi, M. A G Laso, J. Garcia-Garcia, I Gil, M.F. Portillo, and M. Sorolla. Equivalent-circuit models for split-ring resonators and complementary split-ring resonators coupled to planar transmission lines. *Microwave Theory and Techniques, IEEE Transactions on*, 53(4):1451–1461, April 2005.

[54] L. Yousefi and Omar M. Ramahi. New artificial magnetic materials based on fractal hilbert curves. In *Antenna Technology: Small and Smart Antennas Metamaterials and Applications, 2007. IWAT '07. International Workshop on*, pages 237–240, March 2007.

[55] Mohammad Abdolrazzaghi, Mohammad Hossein Zarifi, and Mojgan Daneshmand. Sensitivity enhancement of split ring resonator based liquid sensors. In *SENSORS, 2016 IEEE*, pages 1–3. IEEE, Oct 2016.

[56] L. Su, J. Mata-Contreras, P. Vlez, and F. Martn. Splitter/combiner microstrip sections loaded with pairs of complementary split ring resonators (csrrs): Modeling and optimization for differential sensing applications. *IEEE Transactions on Microwave Theory and Techniques*, 64(12):4362–4370, Dec 2016.

[57] Lijuan Su, Javier Mata-Contreras, Paris Vélez, and Ferran Martín. Configurations of splitter/combiner microstrip sections loaded with stepped impedance resonators (sirs) for sensing applications. *Sensors*, 16(12):2195, Dec 2016.

[58] Lijuan Su, Jordi Naqui, Javier Mata-Contreras, and Ferran Martín. Modeling and applications of metamaterial transmission lines loaded with pairs of coupled complementary split-ring resonators (*csrr*s). *IEEE Antennas and Wireless Propagation Letters*, 15:154–157, May 2016.

[59] Muhammed S Boybay and Omar M Ramahi. Near-field probes using single and double negative media. *Physical Review E*, 79:016602, Jan 2009.

[60] Ibraheem A Ibraheem Al-Naib, Christian Jansen, and Martin Koch. Thin-film sensing with planar asymmetric metamaterial resonators. *Applied Physics Letters*, 93(8):083507, 2008.

[61] Authur A Maryott and Edgar R Smith. Table of dielectric constants of pure liquids. Technical Report 514, Nat. Bureau Standards Circular, Gaithersburg, MD, USA, Aug 1951.

[62] Kyungjun Song and Pinaki Mazumder. Design of highly selective metamaterials for sensing platforms. *IEEE Sensors Journal*, 13(9):3377–3385, Apr 2013.

[63] Ignacio Gil, Jordi Bonache, Joan Garcia-Garcia, and Ferran Martin. Tunable metamaterial transmission lines based on varactor-loaded split-ring resonators. *IEEE transactions on Microwave theory and techniques*, 54(6):2665–2674, June 2006.

[64] Margarita Puentes, Martin Schüßler, and Rolf Jakoby. 2d sensor array based on split ring resonators for monitoring of organic tissue. In *Sensors, 2011 IEEE*, pages 272–275. IEEE, 2011.

[65] JR Bray and L Roy. Measuring the unloaded, loaded, and external quality factors of one-and two-port resonators using scattering-parameter magnitudes at fractional power levels. *IEE Proceedings-Microwaves, Antennas and Propagation*, 151(4):345–350, Aug 2004.

[66] Ali M Albishi and Omar M Ramahi. Highly sensitive microwaves sensors for fluid concentration measurements. *IEEE Microwave and Wireless Components Letters*, Apr 2018.

[67] Muhammed Shafi KT, M Arif Hussain Ansari, Abhishek Kumar Jha, and M Jaleel Akhtar. Design of srr-based microwave sensor for characterization of magnetodielectric substrates. *IEEE Microwave and Wireless Components Letters*, 27(5):524–526, April 2017.

[68] Jaejin Lee, Yang-Ki Hong, Woncheol Lee, Gavin S Abo, Jihoon Park, Won-Mo Seong, and Seok Bae. Role of small permeability in gigahertz ferrite antenna performance. *IEEE Magnetics Letters*, 4:5000104–5000104, Feb 2013.

[69] C Cotae, O Baltag, R Olaru, D Calarasu, and D Costandache. The study of a magnetic fluid-based sensor. *Journal of Magnetism and magnetic materials*, 201(1-3):394–397, 1999.

[70] Francesco Monticone and Andrea Alù. The quest for optical magnetism: from split-ring resonators to plasmonic nanoparticles and nanoclusters. *Journal of Materials Chemistry C*, 2(43):9059–9072, Sep 2014.

[71] Saeed I Latif and Lotfollah Shafai. Loaded annular ring antennas for multi-frequency operation. In *Antenna Technology and Applied Electromagnetics and the Canadian Radio Science Meeting, 2009. ANTEM/URSI 2009. 13th International Symposium on*, pages 1–4. IEEE, Feb 2009.

[72] Sergei V Kalinin and Alexei Gruverman. *Scanning probe microscopy: electrical and electromechanical phenomena at the nanoscale*, volume 1. Springer, New York, 2007.

[73] Sijia Gu, Tianjun Lin, and Tuami Lasri. Dielectric properties characterization of saline solutions by near-field microwave microscopy. *Measurement Science and Technology*, 28(1):014014, December 2016.

[74] David J Livingstone. *Artificial neural networks: Methods and applications (methods in molecular biology)*. Humana Press, 1 edition, 2008.

[75] Abdulbaset Ali, Mohamed El Badawe, and Omar M Ramahi. Microwave imaging of subsurface flaws in coated metallic structures using complementary split-ring resonators. *IEEE Sensors Journal*, 16(18):6890–6898, 2016.

[76] T Chady, M Enokizono, and R Sikora. Crack detection and recognition using an eddy current differential probe. *IEEE transactions on magnetics*, 35(3):1849–1852, May 1999.

[77] Ali M Albishi, Omar M Ramahi, and Muhammed S Boybay. Complementary split-ring resonator as a high sensitivity sensor. In *Antennas and Propagation Society International Symposium (APSURSI), 2012 IEEE*, pages 1–2. IEEE, July 2012.

[78] Ali Albishi and Omar M Ramahi. A high-Q annular ring antenna as a microwave near-field material sensor. In *Antennas and Propagation & USNC/URSI National Radio Science Meeting, 2017 IEEE International Symposium on*, pages 1213–1214. IEEE, July 2017.

[79] Ali M Albishi and Omar M Ramahi. Surface crack detection in metallic materials using sensitive microwave-based sensors. In *Wireless and Microwave Technology Conference (WAMICON), 2016 IEEE 17th Annual*, pages 1–3. IEEE, June 2016.

[80] Ali Albishi and Omar M Ramahi. Intelligent sensing using a system of multiple microwaves resonators. In *Antennas and Propagation & USNC/URSI National Radio Science Meeting, 2017 IEEE International Symposium on*, pages 225–226. IEEE, July 2017.

[81] AJ Bahr. Nondestructive microwave evaluation of ceramics. *IEEE Transactions on Microwave Theory and Techniques*, 26(9):676–683, Sep 1978.